THE UNIVERSITY *of* EDINBURGH

Arrays of 3D polymer scaffolds for biomedical applications

Antonio Conde González

THE UNIVERSITY *of* EDINBURGH

Doctorate of Philosophy

The University of Edinburgh

2020

Correlación no implica causalidad

Lay Summary

Functional polymeric biomaterials have attracted attention in tissue repair due to their tailorability, low cost, biocompatibility and, in certain cases, ability to promote wound healing. A successful biofunctional polymer needs to either be passive to the host or trigger a beneficial host response and, ideally, requires a matching of the material mechanical properties to that of the tissue it will replace.

However, the design of biofuncional polymers relies on the ability to understand the complex interplay between the material properties and cell/tissue behaviour. The concept of my thesis is the development of “arrays of 3D polymers” as an approach to “scan” polymer–cell interactions and, simultaneously, examine the effect of numerous biomaterial compositions and various 3D microstructures on cellular behaviour. However, despite previous efforts, there is currently no route that efficiently permits control of 3D microstructures with multiple different polymers.

To address these challenges, the work in my thesis set out to develop a new and efficient approach to produce arrays of 3D scaffolds. The scaffolds were constructed with numerous pores (like an Emmental cheese) that permit cells to travel deep into them and promote efficient mass transfer and oxygenation. The pores were obtained and controlled by polymerisation taking place around frozen solvent crystals, which acted as moulds for the formation of pores.

The approach developed was applied here to fabricate porous scaffolds that were used to successfully identify a material that promoted vascularisation (formation of blood vessels) and bone healing with potential application in bone repair.

Abstract

The field of functional biomaterials has seen huge progression with enormous efforts made to discover 3D scaffolds that support and promote tissue formation. Polymer-based 3D scaffolds are used extensively as a consequence of their remarkable tunability and biocompatibility.

However, the scope of possible scaffolds, with respect to their physical and chemical properties, is vast encompassing chemical composition, wettability, 3D structure and mechanical properties to name but a few. In addition, the combined effects of these properties on cellular fate, in association with scaffold/protein binding, leads to highly complex systems with numerous processes occurring simultaneously at multiple levels, which hinders a full understanding of the cell–material interface. Therefore, despite huge efforts to understand how the physical and chemical cues of these 3D scaffolds trigger and control cellular behaviour, the effect of these properties on cells remains vague, yet continues to be a key element of tissue engineering.

2D polymer microarrays have been shown to be an efficient high-throughput technology to discover new functional polymers. However, these polymer features lack the necessary 3D structure and morphologies present within tissues. In this thesis, I present the development of a new strategy to fabricate arrays of 3D polymer scaffolds exploiting photo-polymerisation within a crystallisable solvent (dimethyl sulfoxide, DMSO), which serves as a template for the generation of pores.

Initial studies involved the identification of suitable polyacrylates that were capable of binding and maintaining human bone osteosarcoma cells (SAOS-2 and MG-63). These were then used to optimise a polymerisation process that maximised the formation of pores in addition to analysing the effect of the solvent on the 3D structure of the scaffolds and their mechanical properties. An array of 24 different 3D polymer features was fabricated and screened with SAOS-2 cells as a proof of concept of the applicability of the array, showing that cell attachment, proliferation and morphology could be controlled by the composition of the scaffolds along with their 3D microstructures.

A second project (a collaborative effort with the University of Southampton) used the developed screening platform to identify novel 3D scaffolds that promoted the formation of vascularised bone tissue with 45 different 3D polymer scaffolds (15

different polyacrylates with 3 levels of porosity) and foetal bone marrow stroma cells (FBMSCs). A highly biocompatible scaffold was discovered that promoted osteoblastic phenotype expression and vascularisation - the first time for such phenomena had been observed in polyacrylate scaffolds without externally supplied factors. This was validated *ex vivo*, with a chick chorioallantoic membrane (CAM), and *in vivo*, with a subcutaneous mouse model, confirming biocompatibility and the formation of new tissue/vasculature.

Table of Contents

Acknowledgements

First and foremost, I would like to thank my supervisor, Professor Mark Bradley, for giving me the opportunity to carry out my PhD within his group and for his constant support. It was a fantastic experience full of stimulating opportunities to develop my research career. I would also like to thank Dr Annamaria Lilienkampf for her advice these past four years and the members of the Bradley group, past and present, for helping me and sharing with me all those moments in the lab. All of you made working in the lab an enjoyable experience.

Moreover, I would like to express my gratitude to my collaborators Professor Richard Oreffo and Mr (Dr) Michael Glinka at the University of Southampton for their support on a really exciting project. Also, I would like to extend my thanks to Dr Anthony Callanan, Dr Robert Wallace, Mr Stephen (Steve) Mitchell, Dr Martin Lee and Ms Theresa O'Conner for their kind support and huge help with my (not always easy) scaffolds and the SuRF for their histological service. I would also like to thank Dr Deepanjalee Dutta, who has also been hugely important as a collaborator and a friend this last year. Moreover, I also want to acknowledge the European Research Council for founding my research.

My PhD would have not been the same without some good friends who made my last four years be an unforgettable experience. A special thanks goes to Jess, Andrea/Andronio, Vikki, Kevin, Matt, Gavin, Dan, Paul, Yichuan, Jingjing, Maria, Sonia, Assel, Muhammed and Nestor for uncountable dinners, board game nights, pints, chats and fun. Also, I cannot forget Eva, Carlos, Tere, Matteo, Elisa, Alicia, Jose, Antonio, Lola, Ana, Belen and Fermin. I want to thank all of them for their friendship and for making Edinburgh a place to call home.

On a more personal side, I am really grateful to my parents, brother and sister for their constant love and support. Specially my mother, who always encouraged me to follow my dreams (although I am not sure if a PhD was one of these). I also want to thank my mates Noe, Pablo, Josu and JoseLu along with the people from Salar (I am sure I will forget someone, so I am not even going to try).

Finally, a massive thanks to Laura. Your positivism, support and help make the best of me. What I have achieved would not have been possible without you and I cannot be more grateful.

Declaration of Authorship

The research detailed within this thesis has been carried out by the author during his PhD studentship between the dates of November 2015 and October 2019 under the supervision of Professor Mark Bradley, School of Chemistry, at the University of Edinburgh. The work, data and interpretation presented here is that of the author unless there was a significant collaborative contribution made, in which case this has been clearly recognised/noted in the text. Where published work has been consulted or quotations made, the source has been clearly cited. The work has not been submitted for any other degrees or professional qualifications. Parts of the work presented herein have been published or submitted as:

- A. Conde-González, D. Dutta, R. Wallace, A. Callanan and M. Bradley. *Rapid Fabrication and Screening of Tailored Functional 3D Biomaterials*. **Materials Science and Engineering: C, 2020, 108, 110489**
- A. Conde-González[*], M. Glinka[*], D. Dutta[*], (equal contribution) R. Wallace, D. Norman, A. Callanan, R. O. C. Oreffo and M. Bradley (**2019**). *3D Porous Growth-factor free Scaffolds Supporting Enhanced Vascularization for Tissue Repair*.

The author has also collaborated in the following publications that have not been reported in this thesis:

- L. H. Tucker, A. Conde-González, D. Cobice, G. R. Hamm, R. J. A. Goodwin, C. J. Campbell, D. J. Clarke, C. L. Mackay. *MALDI Matrix Application Utilizing a Modified 3D Printer for Accessible High Resolution Mass Spectrometry Imaging*. **Analytical Chemistry, 2018, 90, 15, 8742-8749**.
- K. Neumann[*], A. Conde-González[*], (equal contribution) M. Owens, A. Venturato, Y. Zhang, J. Geng, M. Bradley. *An Approach to the High-Throughput Fabrication of Glycopolymer Microarrays through Thiol-Ene Chemistry*. **Macromolecules, 2017, 50, 16, 166026-6031**.
- E. López-Ruiz, S. Venkateswaran, M. Perán, G. Jiménez, S. Pernagallo, J. J. Díaz-Mochón, O. Tura-Ceide, J. Melchor, J. Soto, G. Rus, P. J. Real, M. Diaz-Ricart, A. Conde-González, M. Bradley and J. A. Marchal. *Poly(ethylmethacrylate-codiethylaminoethyl acrylate) coating improves endothelial repopulation, bio-mechanical and anti-thrombogenic properties of decellularized carotid arteries for blood vessel replacement.* **Scientific Reports, 2017, 7, 1, 407-420**.

Antonio Conde González
17/04/2020

Abbreviations

β-TCP	β-Tricalcium Phosphate
β-Gly	β-Glycerophosphate
AISI	American Iron and Steel Institute
ALP	Alkaline Phosphatase
ANOVA	Analysis of Variance
APTES	(3-Aminopropyl)triethoxysilane
BHA	4-tert-Butylcyclohexyl Acrylate
BMA	Butyl Methacrylate
BMPs	Bone Morphogenetic Proteins
BSA	Bovine Serum Albumin
BSP	Bone Sialoprotein
CAM	Chick Chorioallantoic Membrane
COL	Collagen
CS	Chitosan
DAPI	4,6-Diamidino-2-Phenylindole
Dex	Dexamethasone
DIB	Diisocyanobenzene
DKKs	Dickkopf-Related Proteins
DMPs	Dentine Matrix Proteins
DMSO	Dimethyl Sulfoxide

DNA	Deoxyribonucleic Acid
ECs	Endothelial Cells
ECM	Extracellular Matrix
EGDPEA	Ethylene Glycol Dicyclopentenyl Ether Acrylate
ELISA	Enzyme-Linked Immunosorbent Assay
FACS	Fluorescence Activated Cell Sorting
FAK	Focal Adhesion Kinase
FBS	Foetal Bovine Serum
FBMSCs	Foetal Bone Marrow Stroma Cells
FTIR	Fourier Transform Infrared Spectroscopy
HA	Hydroxyapatite
HABs	Hydroxyapatite Based Bioceramics
HDOBA	1,6-Hexanediol Diacrylate
HIFs	Hypoxia Inducible Factors
HIPE	High Internal Phase Emulsion
HSCs	Haematopoietic Stem Cells
HUVECs	Human Umbilical Vein Endothelial Cells
IBA	Isobornyl Acrylate
LATS 1/2	Large Tumour Suppressor 1/2
LINC	Linker of Nucleoskeleton and Cytoskeleton
MACS	Magnetic Activated Cell Sorting

M-CSF	Macrophage Colony Stimulating Factor
MDI	4,4'-Methylenebis(phenylisocyanate)
Micro-CT	Micro-Computed Tomography
MKL1	Megakaryoblastic Leukaemia 1
MMPs	Matrix Metalloproteinases
MSCs	Mesenchymal Stem Cells
MST 1/2	Mammalian STE20-like Kinase 1
MTEMA	2-(Methylthio)ethyl Methacrylate
Nf2	Tumour Suppressor Merlin/NF2
NMP	N-Methyl-2-Pyrrolidone
NPC	Nuclear Pore Complex
OCN	Osteocalcin
OPG	Osteoprotegerin
OPN	Osteopontin
OSX	Osterix or Transcription Factor Sp7
PBS	Phosphate Buffered Saline
PCNA	Proliferating Cell Nuclear Antigen
PDI	Polydispersity Index
PEG	Poly(Ethylene Glycol)
PEI	Poly(Ethylenimine)
PEO	Poly(Ethylene Oxide)

PLA	Poly(Lactic Acid)
PLLA	Poly(L-Lactic Acid)
PCL	Poly(ε-Caprolactone)
PI	Photo-Initiator
PVA	Poly(Vinyl Alcohol)
PVAc	Poly(Vinyl Acetate)
RAFT	Reversible Addition Fragmentation Chain-Transfer
RANK	Receptor Activator of Nuclear Factor kappa-B
RANK(L)	Receptor Activator of Nuclear Factor kappa-B Ligand
RBCs	Red Blood Corpuscles or Red Blood Cells
RUNX2	Runt Related Transcription Factor 2
SEM	Scanning Electron Microscopy
TC	Tissue Culture
TGF-β	Transforming Growth Factor Beta
UV	Ultraviolet
VEGF	Vascular Endothelial Growth Factor
VEGFR	Vascular Endothelial Growth Factor Receptor
VICs	Valve Interstitial Cells
WH	Whitlockite
Wnt	Wingless Signalling Pathway
YAP	Yes-Associated Protein

1. Tissue engineering for bone regeneration

Tissue engineering is a field of regenerative medicine that develops new technologies, strategies and materials to promote tissue formation at sites where tissue would otherwise not form (e.g. after a traumatic injury). Tissue engineering involves typically the use of combinations of biomaterials, cells and growth factors.[1] In this context, tissue engineering offers the potential to solve the clinical need for technologies that permits the artificial regeneration of damaged or diseased tissues*. Moreover, tissue-engineering strategies could also improve "real-life" *in vitro* studies with the use of "human-like" tissue assemblies which could increase the robustness of preclinical assessment and success of clinical studies†.

The definition for the term "biomaterial" proposed by the European Society for Biomaterials Concensus Conference II quotes: "a biomaterial is a material intended to interface with biological systems to evaluate, treat, augment or replace any tissue, organ or function of the body". One of the properties of biomaterials is biocompatibility which has been defined by Williams as "the ability of a material to perform with an appropriate host response in a specific application".[2] According to reports, one of the "first" biomaterials may have been a hybrid material (cow tooth and gold wire) used as a tooth replacement and attributed to the Etruscan civilisation (around 2,600 years ago).[3]

The first generation of biomaterials developed during the 1960s and 1970s aimed to be "inert" to the host to "achieve a suitable combination of physical properties to match those of the replaced tissue with a minimally toxic response".[4] By 1980, there were more than 50 implantable devices in clinical use, made from more than 40 different materials and with more than 2 million devices implanted in patients in the US. One of the first really successful biomaterials widely used in temporary devices such as fracture plates and screws was made of stainless steel (AISI 316L) that contained (by wt) 0.03% C, 17-20% Cr, 12-14% Ni and 2-3% Mo.[5] Titanium and its alloys attracted considerable attention since Branemark discovered that these materials integrated

* About 4,000 transplants were undertaken in the UK in 2018 with more than 6,000 people on the transplant waiting list.[225]

† 1.5 million experimental procedures were carried out with animals in the UK during 2018, with 17% having the purpose of addressing diseases such as cancer (28%) and infectious disorders (25%).[226] Although animal models are a tremendously valuable source of information, they cannot mimic the complexity of human physiology which has been identified as a possible source of clinical trial failure.[227,228]

into bones (osseointegration) reducing the risks of implant failure.[6] Resistance to corrosion of titanium alloys is due to the formation of an adhesive oxide layer (TiO_2) in the implant surface and was another beneficial feature. Commercially pure titanium is used in dental implants whereas titanium alloys such as ASTM F67 and ASTM F136 (Ti6Al14V) are applied in orthopaedic applications. However, vanadium (V) cytotoxicity has driven the development of new titanium alloys (e.g. Ti35Nb5Ta7Zr) based on titanium, niobium (Nb), tantalum (Ta) and zirconium (Zr). Acrylate bone cements based on poly(methyl methacrylate) provide excellent primary fixation of prosthesis although they do not promote any biological response and can create thermal damage during curing. Poly(ethylene) is used in combination with ceramics like alumina (Al_2O_3) in hip arthroplasties.[5]

By the mid-1980s, a second generation of biomaterials, “bioactive materials”, had reached clinical use to produce a controlled physiological response with bioactive glasses, ceramics and composites applied in a variety of orthopaedic and dental applications.[4] The most common bioactive ceramics are based on calcium phosphate such as hydroxyapatite (HA, $Ca_{10}(PO_4)_6(OH)_2$) or β-tricalcium phosphate (β-TCP, $Ca_3(PO_4)_2$). Although HA has low physiological solubility and remains integrated into the bone tissue, β-TCP is fully reabsorbed. Bioglasses like silica (SiO_2) are also used to improve the formation of bone tissue and they are usually applied as dopants in orthopaedic devices. Moreover, bioabsorbable polymers such as poly(lactic acid) and poly(glycolide) are used in the fixation of bones (e.g. degradable screws).[5]

The term third-generation biomaterials, also known as functional biomaterials, has been used since the turn of the new millennium and encompasses biomaterials that that produce specific cellular response at the molecular level affecting cellular genetic activation and protein expression.[4] Functional biomaterials also try to integrate with the properties and characteristics of the extracellular matrix (ECM), a collection of extracellular secretions such as proteins, polysaccharides and water that provide the structural and biochemical support to the cells of tissues.[7] Current clinical approaches typically involve the stimulation of the autologous healing in tissues. One example is INFUSE, a bone graft from Medtronic, for spinal fusion that includes bovine type I collagen sponge containing recombinant human bone morphogenetic protein-2.[8] NOVOCART 3D from Aesculap is in phase 3 clinical trials and targets cartilage

regeneration using autologous chondrocytes seeded on type I collagen sponges with chondroitin sulphate.[9]

Functional biomaterials can be shaped as “scaffolds” to promote tissue healing, delivering cells or growth factors in the damaged tissue. Scaffolds are defined as porous structures that serve as substrates to guide tissue regeneration, providing a three-dimensional (3D) microenvironment that produces adhesion focal points distributed in all three dimensions (Figure 1-1).[10,11]

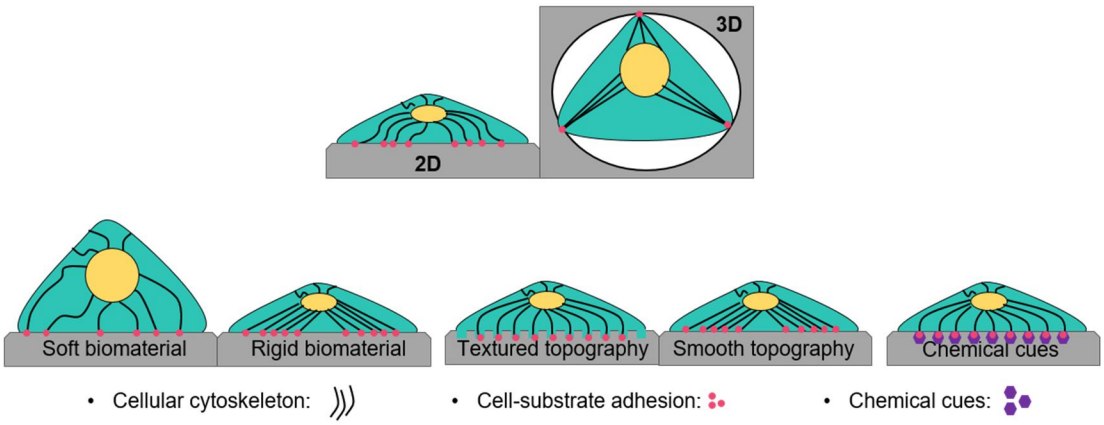

Figure 1-1. Cell-substrate interactions. Differences in the substrate microstructure (2D or 3D), mechanical properties (soft or rigid), topography (textured or smooth) and chemical composition all tune cell behaviour. Substrates and scaffolds are shown in grey, cellular cytoskeleton is represented in black, cytoplasm in illustrated in green with nucleus in yellow. Substrate adhesion points are shown in red with chemical clues in purple.

Mechanical, physical and chemical properties of functional biomaterials all affect cell fate and, ultimately, can stimulate tissue healing or tune tissue characteristics. Cells can also modify their ECM in adaptation to external stimuli, for example, in the absence of gravitational loadings astronauts are known to increase bone resorption processes reducing bone density.[12]

In tissues, external forces and physical loadings produce shear stresses that modify cellular membranes. These forces have a myriad of effects such as allowing calcium ions to flow more easily through stretch-activated ion channels with calcium signalling cascades propagating to neighbour cells through gap junctions.[13] Substrate stiffness, topography and chemical composition can modify the cells binding to them, altering the cellular membrane and cytoskeleton, which can change cell fate and trigger cell differentiation processes (Figure 1-1).[14–16] Outside-in signalling (substrate stiffness

or topography) are typically transmitted through focal adhesion and integrins (transmembrane receptors) that are connected to the cellular cytoskeleton (actin filaments) *via* vinculin (Figure 1-2).[17] At the same time, the cytoskeleton is connected to the nuclear envelope *via* linker of nucleoskeleton and cytoskeleton (LINC) complexes, which changes nuclear membrane tension in addition to nuclear pores and ion channels.[18] The LINC complexes have a variety of functions including DNA repair and the movement of chromosomes within the nucleus during meiosis, which can alter the genetic transcription profile.

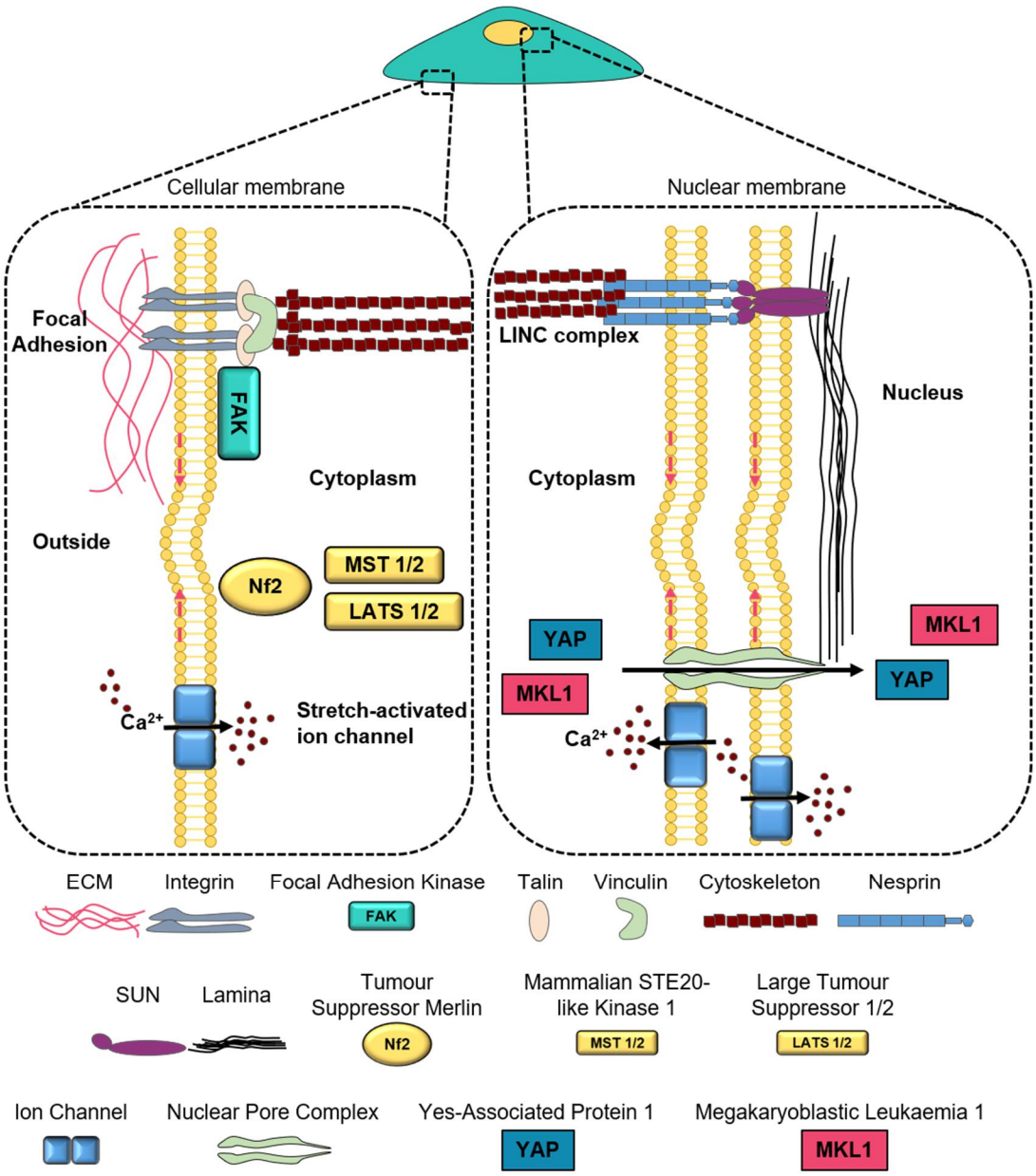

Figure 1-2. Mechanotransduction mechanisms in cells are the processes through which cells sense and respond to external stimuli. These stimuli can activate calcium signalling cascades

that regulate cell motility and proliferation among others or the Hippo signalling pathway that mediates cell proliferation by contact inhibition. Focal adhesions serve as mechanical linkages to the ECM that transmit external stimuli to the cytoskeleton, nuclear envelope and chromosomes *via* linker of nucleoskeleton and cytoskeleton (LINC) complexes. It can also change nuclear permeability to transcription factors such as yes-associated protein (YAP) and megakaryoblastic leukaemia 1 (MKL1).[18]

Current clinical strategies for the repair of large skeletal disorders such as defects produced by tumour resection* involve the use of bone grafts.[19] These grafts can be autogenic bone (autografts), often considered the ideal bone graft because of their osteoconductive properties and absence of immune response. However, these procedures are associated with donor site problems such as pain and infection. Allografts from cadavers or living donors (hip replacement operations being the source of most allogenic bone) is also an alternative. Nonetheless, bone tissue must be decellularised to prevent the host's immune response and be screened to reduce the inherent risk of disease transmission.[20] This has driven the exploration of new biomaterials and tissue engineering principles as an alternative to allow the generation of new bone inspired by the properties of natural tissues (Figure 1-3).

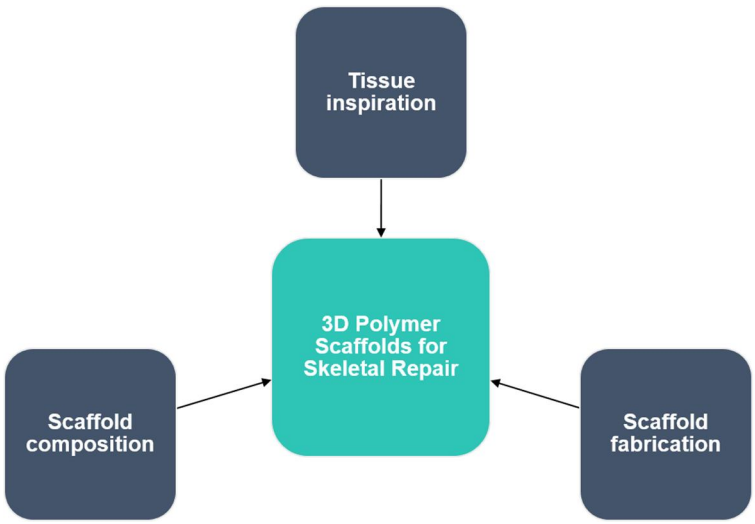

Figure 1-3. Strategy needed to design a 3D polymer scaffold for skeletal repair.

* In the UK there are ~600 new cases of bone sarcoma every year with ~85% of the patients undergoing bone replacements. Patients with bone osteosarcoma have a 55% survival rate of 10 or more years.[229]

1.1 Discovery of synthetic polymeric biomaterials

Considerable efforts have been dedicated to discover materials with improved biocompatibility due to the downsides that many tissue substitutes have. For instance, metals undergo corrosion causing allergic responses, while ceramics lack optimal mechanical properties.[5] As alternatives, bio-inspired materials based on biocompatible polymers have been extensively studied due to their versatile physical and chemical properties along with their ability to mimic the native ECM microenvironment.[21]

Natural materials such as collagen, gelatin and polysaccharides in addition to synthetic polymers such as polyglycolides, polylactic acid, polycaprolactones, polyurethanes and polyacrylates have been investigated as musculoskeletal substitutes.[22–24] Naturally derived biomaterials like collagen, which is the most abundant protein of the ECM, have shown limited success in clinic because of difficulties in fabricating the material on a large scale and the high batch-to-batch variability.[25,26] However, their natural properties allows them to successfully reproduce many physiological processes, for example, mineralisation of collagen fibres.[27]

Synthetic polymers such as polyurethanes and polyacrylates have attracted attention as functional biomaterials because of their remarkable biocompatibility, for example, with hepatocytes, progenitor and mature endothelial cells (ECs), human embryonic stem cells, mesenchymal stem cells (MSCs) or valve interstitial cells.[28–32] Hydrogels based on polyacrylates constitute a group of cross-linked polymers whose hydrophilic structure is capable of “holding” a large amount of water within their 3D network. The high water content of hydrogels as well as their physical and chemical properties matches extraordinarily well the characteristics of many soft natural tissues.[33] For instance, atom transfer radical polymerisation was used to synthesise a thermosensitive hydrogel based on poly(N-isopropylacrylamide) to encapsulate and deliver cardiac progenitor cells.[34] In another example, a hydrogel based on methyl methacrylate, methacrylic acid and poly(ethylene glycol) diacrylate was designed to recapitulate, growth factor-free, the characteristics of human articular cartilage.[35]

The synthesis of novel polymers is in continuous development. In general, two different synthetic techniques can be differentiated to obtain polymers: step growth

polymerisation and chain growth polymerisation/addition polymerisation. Step growth polymerisation, also called polycondensation, consists of reactions carried out between monomers with two functional groups such as bis-amines with bis-acid chlorides or diols with isocyanates.[36] On the other hand, chain growth polymerisations typically refer to polymerisations that occur through activated species such as initiators or actives centres with chains growing sequentially, generating a new reactive site at the terminus of the chain after every new addition.[37] Controlled chain growth polymerisation is extensively used to generate sequence-controlled copolymers and graft polymers e.g. *via* reversible addition fragmentation chain-transfer (RAFT) polymerisation.[38–40]

Microarrays are a platform whereby hundreds or hundreds of thousands of different probes such as DNA, proteins, drugs, tissue samples or polymers are immobilised onto a substrate (typically silica). Microarrays are valuable tools for basic biology and tissue engineering research because they have the capability to evaluate a large number of probes simultaneously, under identical conditions in a single assay. These characteristics give microarrays the ability to conduct experiments with great consistency, little expense and while providing a large amount of information. The first material arrays were reported by Hanak in 1970.[41] The “multiple-sample concept” was introduced to increase the efficiency of the discovery of new superconducting materials by sputter deposition. The fabrication of polymer microstructures achieved by photo-deposition on top of the distal end of an optical fibres reported by Healey in 1995 was another step in the development of microarrays.[42] In 1998, a polymer array with 112 different features (materials spotted on the array) was prepared in order to study physical, mechanical properties as well as fibroblast binding and growth properties.[43]

Polymer microarrays are based on a grid of polymers deposited at defined locations on the substrate (Figure 1-4). The polymers can be pre-synthesized and deposited onto the solid substrate through contact printing* or through *in situ* polymerisation through the deposition of the starting materials using contact printing or inkjet printing†.[44–46] Polymer microarrays have displayed an extraordinary capability to discover polymers for modulating cellular responses. For example, a gradient array

* Contact printing uses metal pins to “collect” and then “deposit” polymer solutions on top of a substrate with direct contact between the pin and the substrate.
† Inkjet printing allows deposition liquid droplets onto a substrate surface, which can turn into a solid as a result of chemical changes (e.g. UV mediated polymerisation).

was designed by Hansen in order to understand and control cellular adhesion with polymer composition.[47]

The design and application of a polymer microarray requires the optimal selection of the substrate, the type of coating, the equipment used to fabricate the array and how the biology will be evaluated. Fluorescence scanners and microscopes are the most commonly used detection instruments for microarray analysis that requires, ideally, an automatic process controlled by appropriate software.[48]

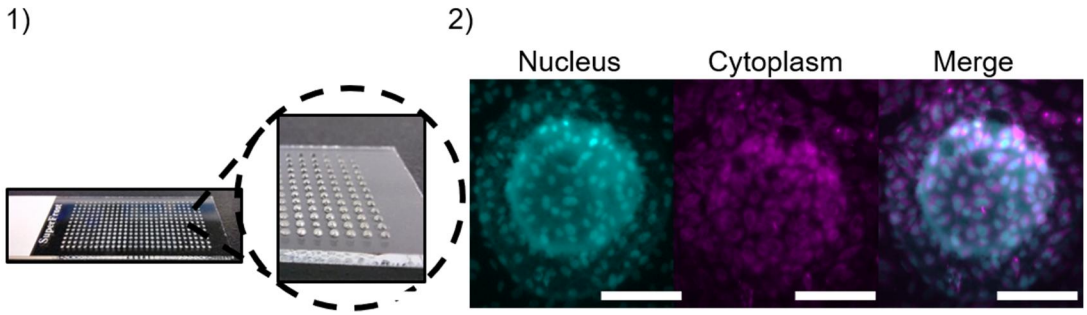

Figure 1-4. 1) Image of a polyacrylate microarray fabricated by *in situ* polymerisation following inkjet mediated printing. The microarray was interrogated with SAOS-2 cells, which binds to selected polymer features. 2) Assessment of cell attachment was carried out using fluorescence and high-content microscopy. In the example, one representative polymer is shown with cell nuclei and cytoplasm stained with DAPI (cyan) and CellMask™ deep red. Scale bar = 200 µm.

1.2 Fabrication of 3D scaffolds

Three-dimensional scaffolds can be defined as porous structures that serve as artificial 3D substrates that support cell culture.[2] As such, ideal scaffolds promote cell stability, enable cell proliferation and provide stimuli for cells that direct the assembly of tissue-like 3D structures.[49] Additive manufacturing prototyping technologies (also known as 3D printing)[50] such as stereolithography,* selective laser sintering,† inkjet

* Stereolithography is based on the selective curing of a photopolymer resin by a laser or light source. The laser polymerises each layer in a point-by-point and line-by-line style and requires a slowly descending platform.
† Selective laser sintering is based on the selective sintering of a fine powder by a high-temperature laser. After each layer is produced, a fresh layer of the powder has to be spread on the bed, following the sintering of a new layer.

printing, fused deposition modelling and extrusion-based techniques* (e.g. 3D bioprinting)[51] allow scaffolds to be directly constructed or printed, and offers an approach within the area of biomedical research to fabricate in a cost-effective and personalised manner medical solutions.[52] These approaches can provide a high level of control of the scaffold microstructure with resolutions in the micrometre scale (1-10 µm) using stereolithography or in the nanometre scale (< 200 nm) using two-photon polymerisation.[53] An extrusion-based approach has been used to construct a gradient scaffold whose pore size changed from the bottom (500 µm) to the top (1100 µm) to enhance osteogenic differentiation.[54] In another example, a soft granular gel was used to print complex structures such as ''blood vessels'' (hollow cylinders). The gel fluidised under high shear stresses, e.g. shear stress produced by a nozzle tip moving in the gel, and it solidified when the high shear stress disappeared. This was used for 3D printing and to trap a pre-polymer solution that was cured upon UV photopolymerisation (Figure 1-5).[55]

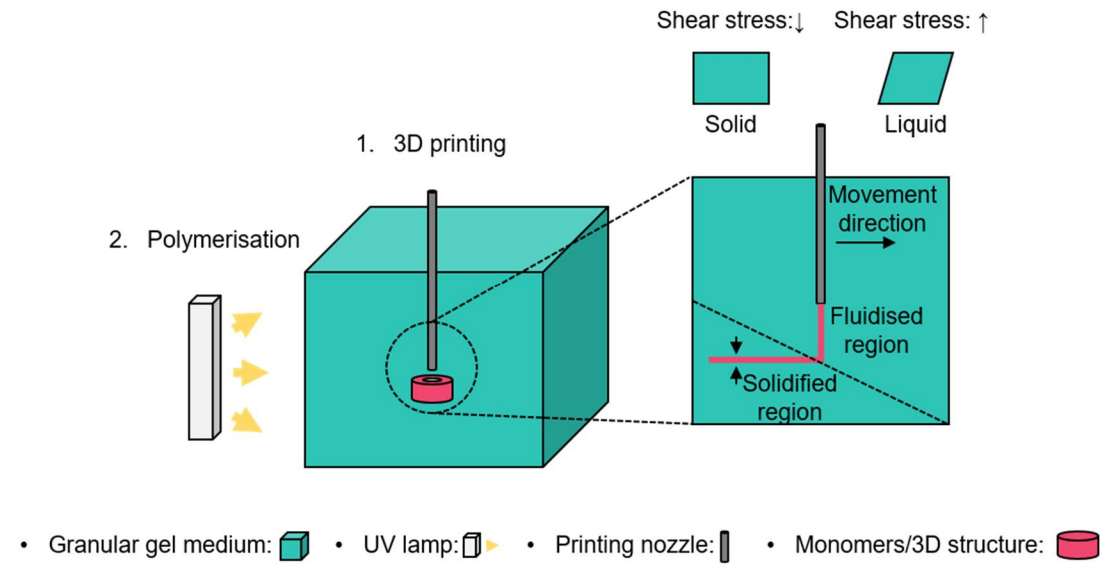

Figure 1-5. 3D printing in a granular gel (0.2% w/v Carbopol in water). As the nozzle moves, the gel fluidises and then gellifies trapping the pre-polymer solution. The structures can then be consolidated upon UV polymerisation.[55]

However, prototyping technologies are material-dependent i.e. properties of the material (viscosity, melting temperature, polymerisation time, etc.) determines the

* Fused deposition modelling and extrusion-based techniques are based on the deposition of melted materials (fused deposition) or deposition of a gel (extrusion-based techniques).

‘‘printability’’. Moreover, all of these approaches are time-consuming and typically require costly equipment.

Electrospinning has risen as an interesting approach to prototyping technologies for transforming polymers into homogenous fibres with diameter that can range from nanometres to micrometres with fibrous microstructures resembling the ECM.[56] Fibres are generated when the electrostatic charge, generated by an electric field between the collector and the jetting needle, overcomes the surface tension of the polymer solution. The polymer solution is dispensed by action of a syringe pump or gravity, and the solvent evaporates when the polymer ‘‘flies’’ to the collector resulting in solid polymer fibres. Characteristics of the fibres are conditioned by properties of the polymer solution such as conductivity, surface tension, viscosity and molecular weight; processing factors such as flow rate, electrical field; and environmental parameters, including humidity and temperature.[57]

The generation of porous scaffolds using sacrificial materials as scaffold templates using solvent casting and particulate leaching or inducing phase separation by means of a porogen, a reaction or a change of temperature e.g. non-solvent induced phase separation, reaction-induced phase separation, gas foaming, thermally-induced phase separation have been shown to be reliable alternatives to prototyping and electrospinning. These approaches permit the generation of many scaffolds simultaneously and tolerate modification of the composition to explore biocompatibility. However, the control of the porous network size, shape, and porosity is not immediate and porous structures are considered ‘‘random’’.

Solvent casting and particulate leaching is based on the creation of a sacrificial material ‘‘mould’’ that acts as a template to generate the pores (Figure 1-6, 1). The sacrificial material (e.g. sugar, salt, polymers) needs to be immiscible with the monomer or polymer solution to allow the generation of pores after polymerisation or drying and removing the template. For example, poly(methyl methacrylate) microspheres (90 μm) were used as “porogenic” solids to create interconnected pores (65 – 85 μm) in scaffolds prepared with ethyl acrylate and hydroxyethyl methacrylate.[58]

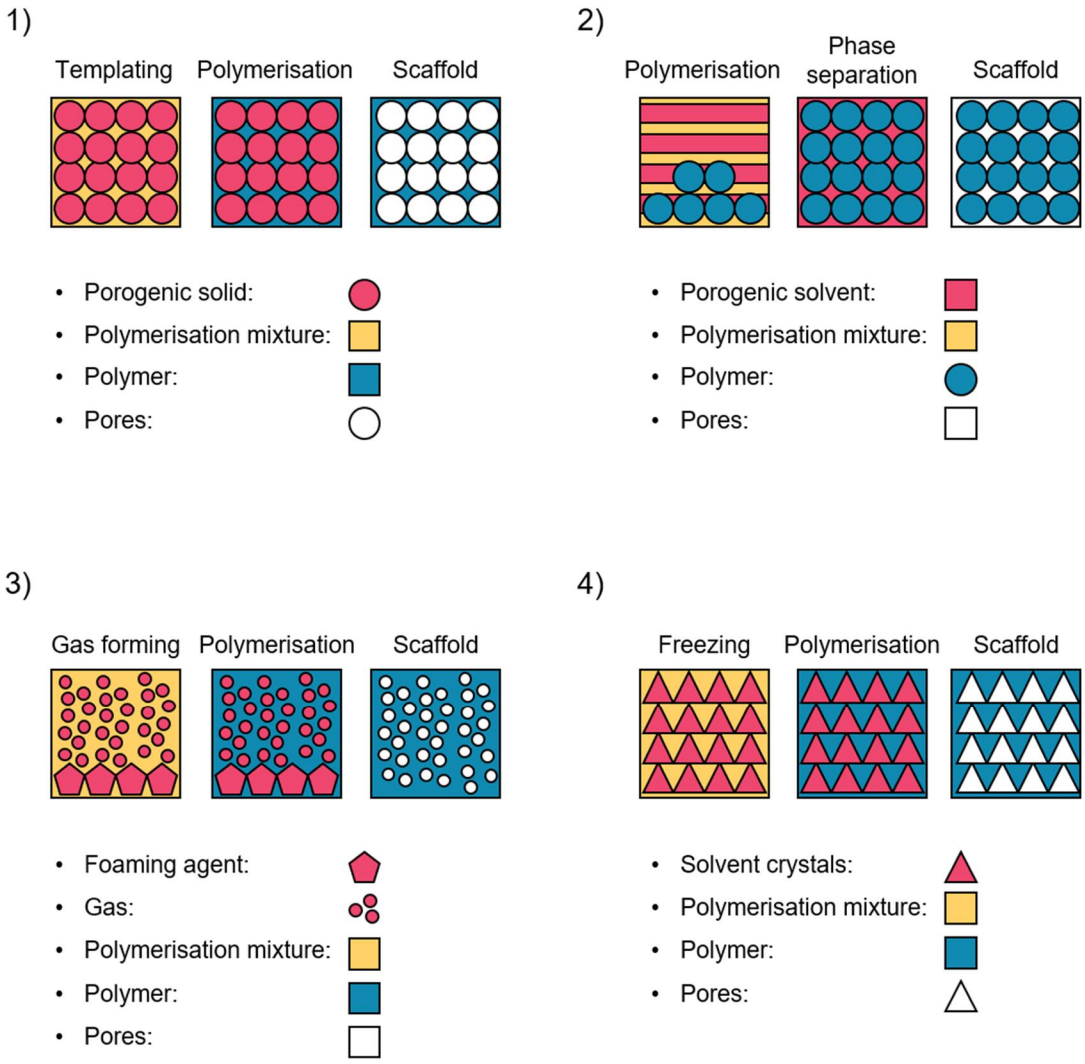

Figure 1-6. Generation of porous scaffolds. 1) Solvent casting and particulate leaching, where a porogenic solid such as salt acts as a template for the generation of pores during polymerisation. 2) Non-solvent induced phase separation uses a poor solvent for the polymer as a porogenic agent to form a porous structure. 3) Gas foaming applies an agent to generate a gas that acts as a template for the formation of pores. 4) Freeze-casting uses a crystallisable porogenic solvent that forms a template for the generation of pores. Porogenic agents are shown in red, polymerisation mixture in yellow, polymer structure in blue and pores in white.

Non-solvent induced phase separation and reaction-induced phase separation involve the use of porogenic solvents that are efficient solvents for the monomers but poor or deficient solvents for the polymers themselves (Figure 1-6, 2). Porogenic solvents such as methanol, ethanol or poly(ethylene glycol) allow the progressive segregation of the polymer from the solution during the polymerisation e.g. aggregation of polymer and formation of pores.[59] For example, highly porous

materials are constructed by high internal phase emulsion polymerisation (HIPEs), where a discontinuous phase consisting of a porogenic solvent is dispersed in a continuous phase of liquid monomers. However, these systems need to be stabilised by a surfactant, which usually remains in the scaffold affecting the cellular behaviour.[60]

Gas foaming approaches utilise the nucleation and growth of gas bubbles dispersed through a polymer with the bubbles either generated *in situ* or by adding a gas to the polymer phase.[61] One of the approaches more extensively studied involves the use of ammonium bicarbonate that decomposes above 36 °C to give ammonia, carbon dioxide and water (Figure 1-6, 3). Porous microspheres for 3D cell culture have been fabricated using poly(lactic acid)-co-poly(glycolide) and double emulsion methods using gas foaming to generate pores.[62]

Thermally-induced phase separation or freeze-casting consists of cooling the polymer solution below the solvent's freezing point to induce the formation of two phases; a polymer-rich and a solvent-rich phase with the formation of solvent crystals that force the polymer into the interstitial space. Pores are created when crystals are removed (Figure 1-6, 4). A variation of this approach is producing scaffolds by freeze-drying where the solvent is frozen rapidly and removed under vacuum. Freeze-casting offers several features:

- Tailorability to form either homogenous or directional microstructures.
- High porosity.
- Large, open and interconnected pores or gradients of pores.
- Complex shapes and fine features.
- Simple equipment requirements.

Characteristics of these porous networks are controlled by the concentration of the porogenic solvent, the freezing point of solvents, cooling rate and cooling time.[63]

The porogenic solvents previously reported include water,[64,65] water-dimethyl sulfoxide (DMSO),[66] camphene,[67] naphthalene-camphor[68] and tert-butyl alcohol.[69] For example, biomimetic scaffolds with interconnected porous microstructures were fabricated using hydroxyapatite and poly(ethylene glycol), with water as the crystallisable porogenic solvent.[65] In another example, a binary system of naphthalene-camphor allowed freeze-casting at room temperature (≈ 30 °C). The

freezing point of DMSO is 19 °C, which enables freeze-casting at moderate temperatures.[70]

Control of the porous structure can be achieved by controlling the freezing rate and the freezing time. Small pores form with a rapid freezing rate as a consequence of crystal nucleation because it is kinetically more favourable than crystal growth. With larger temperature gradients, heat transfer is more efficient and crystals can grow leading to porous structures with larger pore sizes.[71] In the case of a long freezing time, crystals keep growing linking each other, consequently enhancing pore interconnectivity and large pore size.

Among the different alternatives considered to generate arrays of 3D porous scaffolds (Table 1-1), freeze-casting produces highly porous structures with large and interconnected pores, with pore variation tuned by level of porogenic solvent and temperature. By contrast with prototyping approaches, freeze-casting enables the high-throughput fabrication of multiple 3D microstructures, simultaneously, by tuning the level of porogenic solvent (the more porogenic solvent is used, the larger are the pores) and the freezing parameters.

Table 1-1. Summary of the commonly used techniques to produce porous scaffolds and their key features.[21,72–75]

Technique	Resolution (µm) Porogen examples	Porosity (%)	Pore size (µm)	Advantages	Disadvantages
Stereolithography	0.5-10	<90	20-1,000	Accuracy Shape control	Expensive equipment Support structure is needed Limited choice of resins Low resin biocompatibility
Selective laser sintering	50-1,000	<40	30-2,500	Solvent free No support material	Expensive equipment Removing trapped powder
Fused deposition modelling	100-500	<80	100-2,000	Solvent free Fast processing	Needs filament preparation Limited choice of filaments Medium accuracy
Electrospinning	-	<90	<1-10	Simple method Interconnected porosity	Low mechanical integrity Limited scaffold thickness
Solvent casting and particulate leaching	Polymer microspheres NaCl crystals	<50	30-300	Simple method Controlled porosity/pore size	Residual solvent and particles
Non-solvent induced phase separation	Alcohols, hexane, PEG	<90	<1-10	Controlled porosity Interconnected pores	Residual solvent Complex control
Gas foaming	Pressured CO_2, N_2 NH_4HCO_3 + heat	<90	30-700	Simple method Solvent free	Non-interconnected pores Closed pores
Thermally-induced phase separation	Water, DMSO, camphene	<90	5-6000	Interconnected pores High porosity Controlled porosity/pore size	Residual solvent

1.3 Bone biology, an inspiration for the design of 3D scaffolds

The adult human skeleton contains 206 bones with a broad range of functionalities such as protection for vital organs (e.g. brain, heart, lungs and spinal cord), maintenance of homeostasis (source of calcium and phosphate) and production of blood cells and innate immune system cells. Moreover, bones also act as supports for ligaments, tendons, muscles, and cartilage. Although traditionally bones have been seen as a static tissue, they are a highly complex living tissue, for example, the surfaces of bones are covered by a highly vascularised membrane called the periosteum that has osteogenic functions and maintains nutrient and waste exchange.[76]

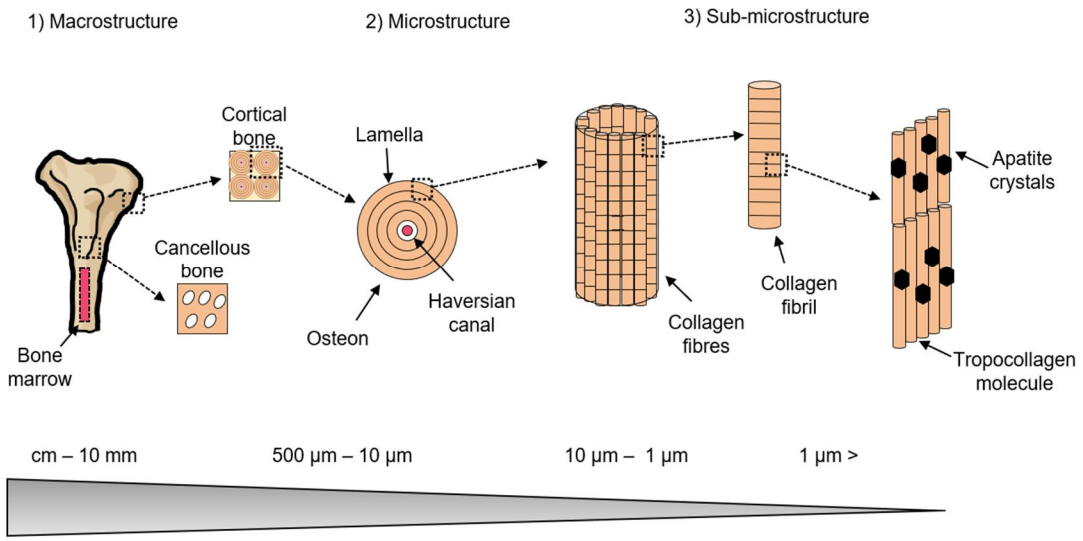

Figure 1-7. Hierarchical bone structure. Bone macrostructure consists of bone marrow, cancellous and cortical sections. Cancellous bone is made of a porous structure filled with bone marrow with cortical bone forming a protective outer surface around the internal structure of bones. Cancellous bone is made of osteons, a *lamellae* or concentric structure (350 to 250 µm) that surround Haversian canals. Collagen fibres determine microstructure of osteons and they are constituted of apatite-mineralised tropocollagen at a molecular level.[77]

Bone is a composite material comprised of an inorganic phase (~ 60%), an organic phase (~ 25%) and water (~ 15%), which confers bone unique mechanical and physical properties such as a compressive strength that exceeds 2,000 kg/cm^2. Structurally, bone can be divided into a smooth surface (cortex or cortical bone) or an internal porous structure (trabecular or cancellous bone). Flat bones such as parietal

bones or hipbones are composed mainly of cortical bone whereas long bones such as the femur and tibia are composed of cancellous bone. Moreover, the internal surface of the long bone contains bone marrow. Red bone marrow (myeloid tissue) is hematopoietic and produces red blood cells (also known as red blood corpuscles or RBCs), white blood cells (leukocytes) and platelets (Figure 1-7). Red bone marrow is gradually substituted by yellow bone marrow (stroma) after the age of 5. The yellow bone marrow contains a higher amount of adipose tissue, as well as skeletal progenitor cells (also known as mesenchymal stem cells or MSCs), adipocytes and endothelial cells.[78] Hematopoietic stem cells (HSCs) are osteoclast progenitors that are believed to generate in yolk sac and aorta-gonad-mesonephros region in embryonic mammals with migration into liver for expansion and maturation, then into bone marrow and subsequently into the spleen.[79]

Cortical bone, 80% bone mass*, has a hierarchical structure of cylindrical osteons (from 10 – 500 μm) with blood vessels in the centre called Haversian canals, which are the basic building block of cortical bone tissue. However, cancellous bone, 20% bone mass, exhibits a network with trabecular roads without Haversian canals.[77] Bone extracellular matrix consists of mineralised collagen fibres (100 to 2000 nm), which are made of collagen fibrils i.e. arrays of tropocollagen molecules (three left-handed helices of peptides).[80] The inorganic component in bone lies in these collagen fibrils, containing calcium phosphate (~ 85%), calcium carbonate (~ 10%) and salts like potassium (~ 5%). Historically, calcium phosphate has been identified as hydroxyapatite, $Ca_{10}(PO_4)_6(OH)_2$, which is a hydroxyl-containing calcium phosphate mineral within the apatite group, $Ca_{10}(PO_4)_6(OH \text{ or } F \text{ or } Cl)_2$.[78] However, properties of this inorganic phase have been shown to vary within the body. For instance, bone apatite† is re-absorbable whereas tooth enamel hydroxyapatite resists

* Mineral mass contents in a bone. The term is usually used to characterise diseases like osteoporosis, a pathological decrease in bone mineral content.

† In this thesis the broader term apatite is used instead of hydroxyapatite for the calcium phosphate mineral/minerals in bones. Current research confirms that the term hydroxyapatite does not reflect the mineral component of bones although it is still broadly used in the literature. Although X-ray diffractograms confirm bone apatite lattice is coherent with geological hydroxyapatite, Raman and FTIR do not show the necessary OH^- bands for bone apatite. Bone apatite has a considerable amount of CO_3^{2-} that can directly displace two OH^- groups. Bone apatite crystallite has been shown to be smaller (from one-tenth to one-hundredth) than the enamel crystallite structure; however, it has been observed than the smaller the crystallite size and the greater the atomic disorder within the lattice unit, the less energetically favourable apatite is to incorporate OH^-.[81] It is also found that when hydroxyapatite is incorporated *in vivo* it is not remodelled.

dissolution; therefore the inorganic component is perhaps more heterogeneous in its composition than typically thought.[81]

The growth of bones, remodelling and repair are controlled by the behaviour of four bone cells (Figure 1-8): macrophage like osteoclasts, osteoblasts, osteocytes and bone lining cells, which are typically characterised using various markers (Table 1-2).

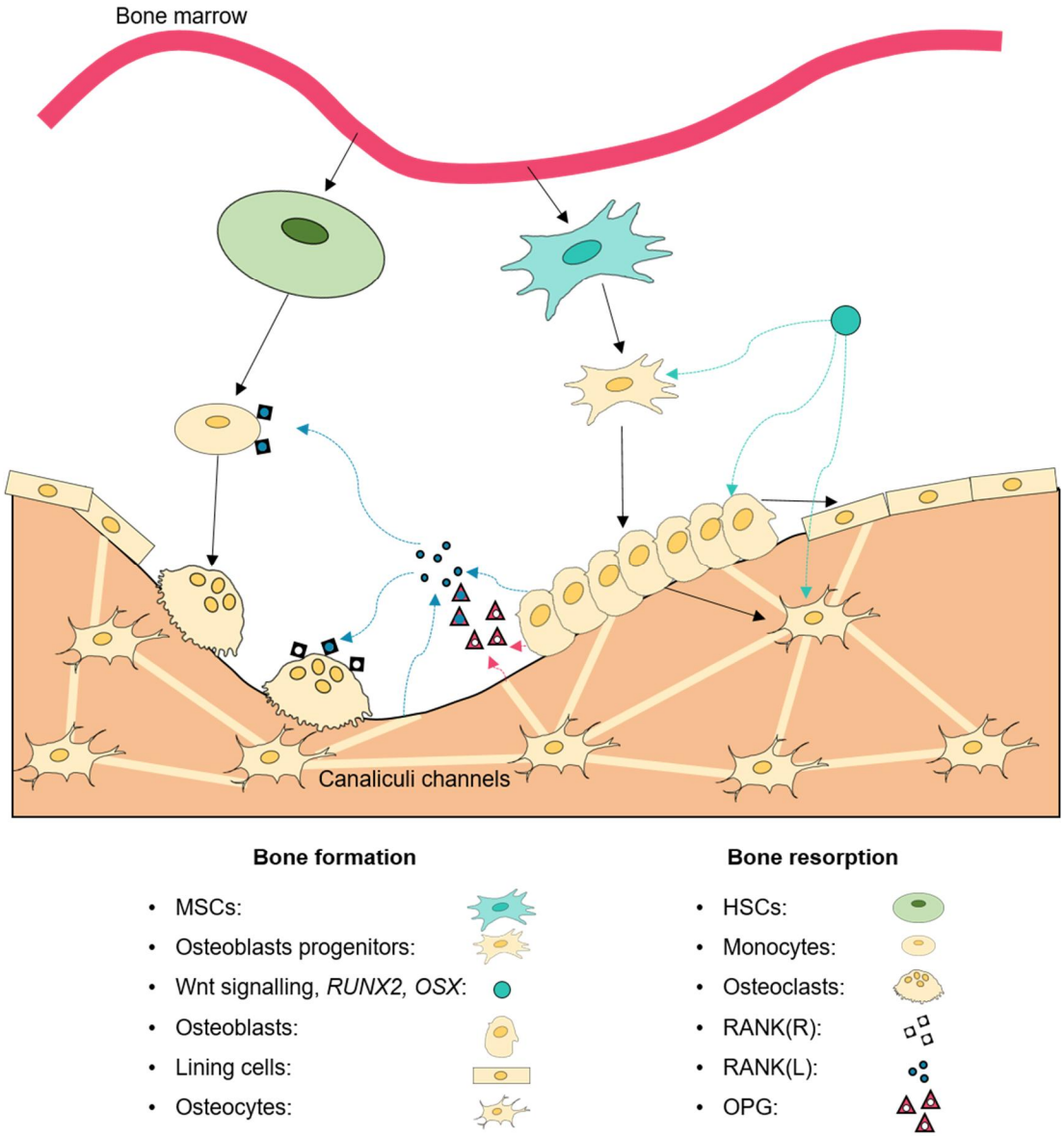

Figure 1-8. Bone cellular biology. Mesenchymal stem cells (MSCs) and haematopoietic stem cells (HSCs) have their origin in bone marrow and their differentiation produces osteoblasts and osteoclasts, respectively. Osteoclasts are in charge of bone resorption processes. Osteoblasts help bone formation along with lining cells (osteoblastic origin) to cover unlined bone surfaces. Osteocytes are differentiated osteoblasts surrounded by mineralised bone

ECM and are part of bone regulatory system. Osteocytes maintain communication between them and other cells through canaliculi channels.[78]

Osteoclasts are multinucleated cells that originate from HSCs and macrophages.[78] The osteoclast differentiation process is triggered/regulated by numerous cytokines with M-CSF, RANK(L) and OPG being the most important (described below).

- M-CSF (macrophage colony-stimulating factor) is secreted by osteoprogenitor stem cells. M-CSF stimulates osteoclast proliferation and inhibits apoptosis (programmed cell death).
- RANK(L) (receptor activator of nuclear factor κB ligand) is secreted by osteoblasts, osteocytes and stroma cells and induces osteoclastogenesis (formation of osteoclasts) when it binds to the RANK(R) (RANK receptor).
- OPG (osteoprotegerin or osteoclastogenesis inhibitory factor) is secreted by osteoblasts, stroma cells and periodontal fibroblasts. OPG binds to RANK(L) inhibiting osteoclastogenesis.[82]

Osteoclasts regulate bone resorption and their malfunction can lead to osteoporosis or osteopetrosis (pathological increase in bone mineral content). During bone remodelling osteoclasts polarise to form a sealing zone in contact with the bone. They then secrete hydrochloric acid (interstitial fluid pH drops to approx. 4.5) and collagen-degrading proteolytic enzymes (e.g. cathepsin K) that dissolves the ECM.[83]

Osteoblasts are differentiated from MSCs and osteoblast progenitor stem cells. The osteoblasts differentiation process is triggered and regulated by the Wnt signalling pathway and key transcription factors (described below).[78]

- Wnt/β-catenin pathway *via* Wnt cell surface receptors LRP5 (low-density lipoprotein-related protein 5) triggers bone formation and stem cells differentiation.
- DKK1/DKK2 (Dickkopf-related protein 1 and 2) and the glycoprotein sclerostin is secreted by osteocytes and downregulates bone formation.
- BMPs (bone morphogenetic proteins) derives from TGF- β (tumor growth factor- β family) and is crucial for bone development, maintenance and fracture healing. BMP is necesasary for RUNX2 (Runt-related transcription factor 2) dependant induction of osteoblast phenotype.[84]

- RUNX2 is involved in a second level of control that regulates the expression of several osteoblast specific genes and the expression of OSX (transcription factor Sp7/Osterix).
- OSX controls the expression of COL1A1 (collagen type I alpha 1 gene), the pre-osteoblast marker ALP (alkaline phosphatase), BSP (bone sialoprotein), OCN (osteocalcin) and OPN (osteopontin).[82]

Osteoblasts are responsible for depositing bone ECM by secreting type I collagen, non-collagenous proteins such as OPN, OCN, BSP and proteoglycan such as decorin and biglycan. Subsequently, mineralisation of the ECM takes place in two phases: a vesicular phase and a fibrillary phase.[82] The vesicular phase begins with osteoblasts secreting matrix vesicles with calcium ions.[85] After that, ALP (a member of the famility of zinc metalloprotein enzymes) mediates dephosphorylation of phosphate-containing compounds like pyrophosphate a mineralisation inhibitor,[86] and phosphate monoesters, which allows phosphate to enter into the matrix vesicles. Fibrillary phase takes place when supersaturation of calcium and phosphate ions in the vesicles leads to apatite nucleation and rupture of the vesicle with apatite crystals spreading on top of the ECM.[83,87]

Osteocytes are mature osteoblasts trapped in bone ECM occupying lacunae cavities. Although osteocytes maintain some similarities with osteoblasts, they are characterised by the following:

- Organelles such as rough endoplasmic reticulum and Golgi apparatus decrease in quantify and osteoblasts markers like OCN, BSP and type I collagen are down regulated.
- DMP1 (dentine matrix protein 1) and sclerostin are highly up-regulated controlling bone formation by osteoblasts.[78]
- OPG is also secreted by osteocytes which regulates osteoclasts behaviour.[88]

Osteocytes maintain cytoplasmic extension through canaliculi channels *via* gap junctions and interstitial fluids that permit osteocytes to ‘‘sense’’ mechanical signals and ‘‘communicate’’ between themselves. Osteocytes response to mechano-stimuli regulates osteoclast and osteoblast behaviour driving bone structure and density.[78,82]

Bone lining cells are a class of flat shaped osteoblasts that cover the bone surface. Bone lining cells play a crucial role in osteoclast differentiation as they produce OPG.

It has been observed that bone lining cells act as a barrier to impede bone resorption/formation processes. However, their role is not yet fully understood.[82]

Table 1-2. Summary of the main cells and factors that drive bone biology.[78,89]

	Osteoclasts 	**Osteoblasts** 	**Osteocytes** 	**Bone lining** 
Origin **Progenitor cell markers**	HSCs PU.1 M-CSF	MSCs STRO-1 COL I CD105 CD73 CD90	Mature osteoblasts	Mature osteoblasts
Differentiation triggered/ regulated by	M-CSF RANK(L) OPG	Wnt RUNX2 OSX		
Markers	TRAP Cathepsin K B3 integrin CIC-7 H^+-ATPase	ALP +++ COL I ++ OCN +++ OPN +++ BSP +++	ALP – COL I – OCN + OPN +++ BSP +++	
Function	Bone resorption	Bone formation	Bone mechanosensing	Control resorption-formation

Bone formation occurs during foetal development by two differentiated mechanisms: intramembranous ossification and endochondral ossification. Intramembranous ossification is typical of flat bones such as calvarian bones. The process starts with layers of MSCs condensing around a vascularised connective tissue to differentiate into osteoblasts and osteocytes. As the tissue grows, osteons develop to make trabeculae interconnected structures forming woven bone*. Long bones like the femur develop through endochondral ossification where MSCs differentiate into chondrocytes and secrete a cartilaginous scaffold for bone formation. Cartilaginous scaffold is substituted by bone after several re-sorption and bone formation processes lead by osteoclasts and osteoblasts, respectively. Moreover, endochondral ossification is the natural healing process of bone fractures.[90]

* Woven bone is characterised by a lack of organisation of collagen fibres and is mechanically week.

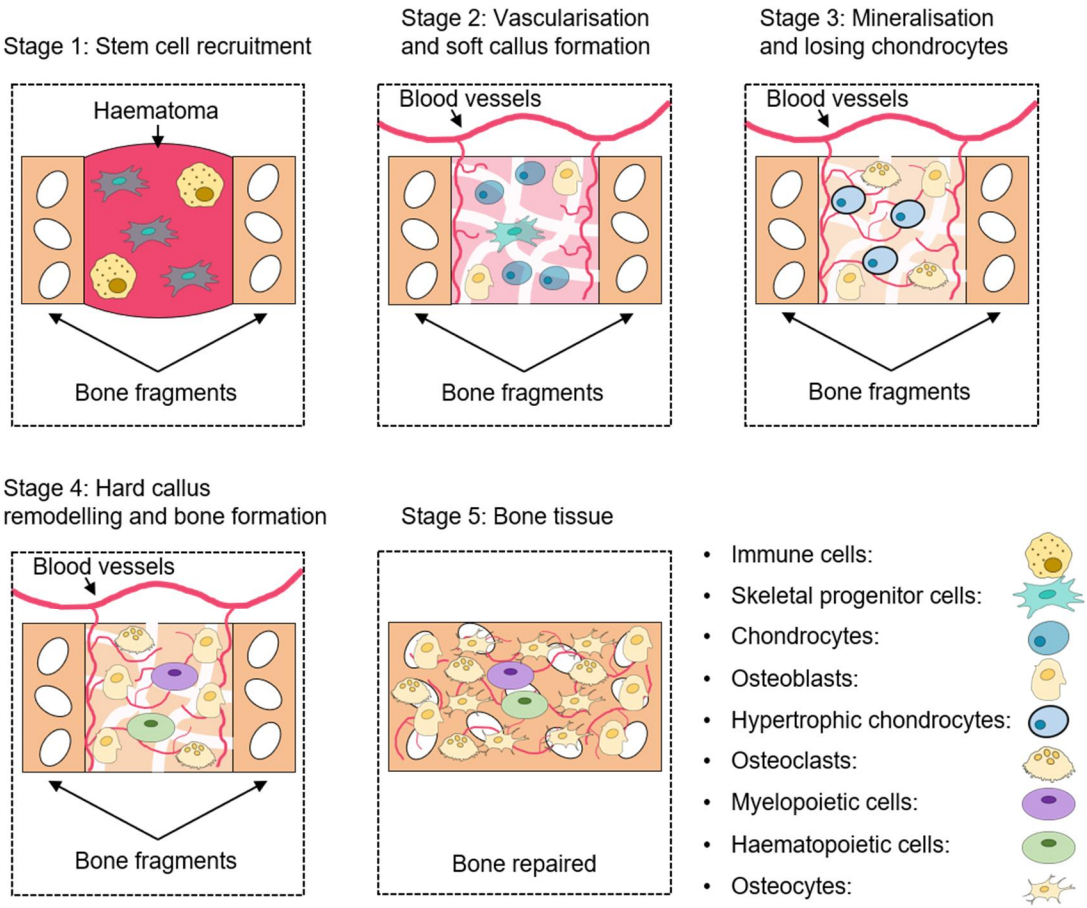

Figure 1-9. Bone fractures are stabilised by endochondral ossification where a soft callus is vascularised and mineralised. The mineralised callus is reabsorbed and substituted by new bone tissue by several bone remodelling cycles.[91]

Bone repair is one of the few postnatal processes that is believed to be truly regenerative i.e. the healing process fully recovers pre-injury cellular composition, structure and mechanical functions.[91] Skeletal tissue repair initially involves an anabolic phase where immune cells remove necrotic tissue and stem cells are recruited to form new bone and vascularised tissue at stage 1 (Figure 1-9). Next to the fracture site a cartilaginous callus forms generated by chondrocytes. Simultaneously to cartilage formation, angiogenesis in the surrounding muscle sheath is promoted to construct new blood vessels that will supply the new bone at stage 2.[92] The healing process progresses with the cartilaginous callus undergoing mineralisation by action of osteoblasts, which results in chondrocyte apoptosis and termination of the anabolic phase at stage 3.[93] Subsequently, a catabolic phase can be identified where cartilage tissue is resorbed. This mineralised tissue is resorbed

by osteoclasts with osteoblasts depositing new bone tissue at stage 4. After several cycles of osteoblast – osteoclast activity, the bone structure (bone remodelling) is completed at stage 5. At this stage, bone morrow tissue is formed with the repopulation of haematopoietic and myelopoietic cells. Bone repair terminates with final vascular remodelling where the vasculature in the surrounding muscle returns to the original level.[94]

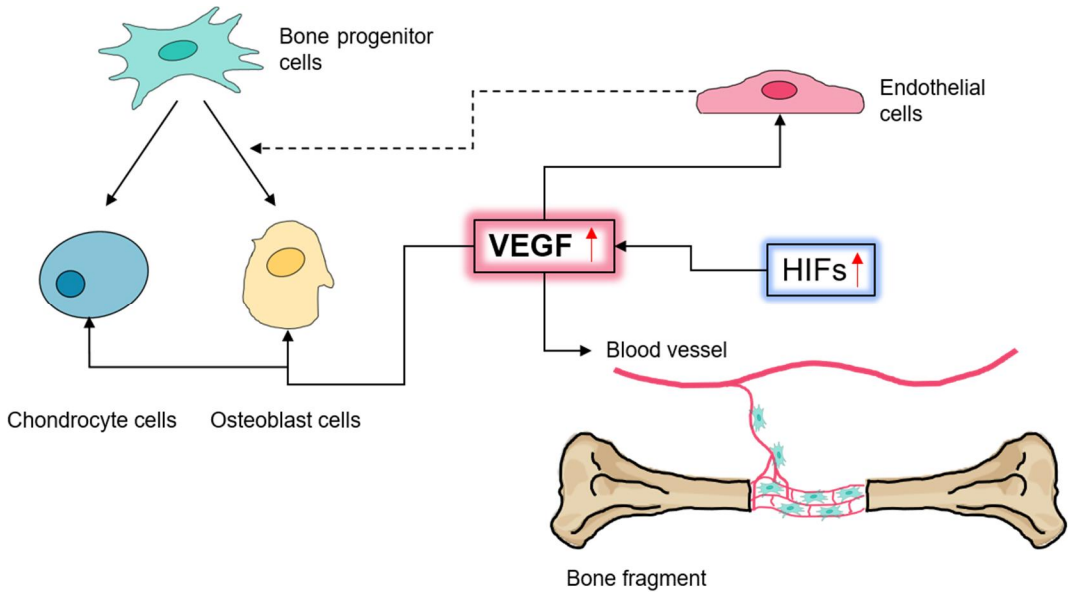

Figure 1-10. VEGF roles during bone regeneration. Hypoxia, as a consequence of fractures, produces an increase of hypoxia inducible factors (HIFs) that activates the increase of vascular endothelial growth factor (VEGF). VEGF stimulates angiogenesis bringing progenitor cells to the fracture callus. VEGF also promotes the differentiation of osteoblast cells and the production of osteogenic cytokines by endothelial cells.[95] Moreover, VEGF regulates the survival of chondrocytes and hypertrophic chondrocytes.[96]

The presence of a functional vascular system is a crucial step for bone formation and repair, with blood vessels playing a pivotal role in supplying oxygen, nutrients and minerals (calcium and phosphate).[95] Bone repair starts when the damaged area becomes hypoxic as a consequence of the rupture of surrounding blood vessels. It activates the hypoxia-signalling pathway with the expression of HIF and stimulating the production of VEGF, which is secreted by endothelial cells, macrophages, fibroblasts, osteoblasts and hypertrophic chondrocytes. VEGF plays several roles in bone repair (Figure 1-10):

- Stimulates the formation of new blood vessels (angiogenesis), which brings skeletal progenitor cells to the fracture.[95]
- Stimulates endothelial cells to produce osteogenic cytokines such as bone morphogenetic proteins (BMPs) that promote progenitor cell differentiation.[97]
- Controls osteoblast chemotaxis, proliferation and differentiation.[98,99]

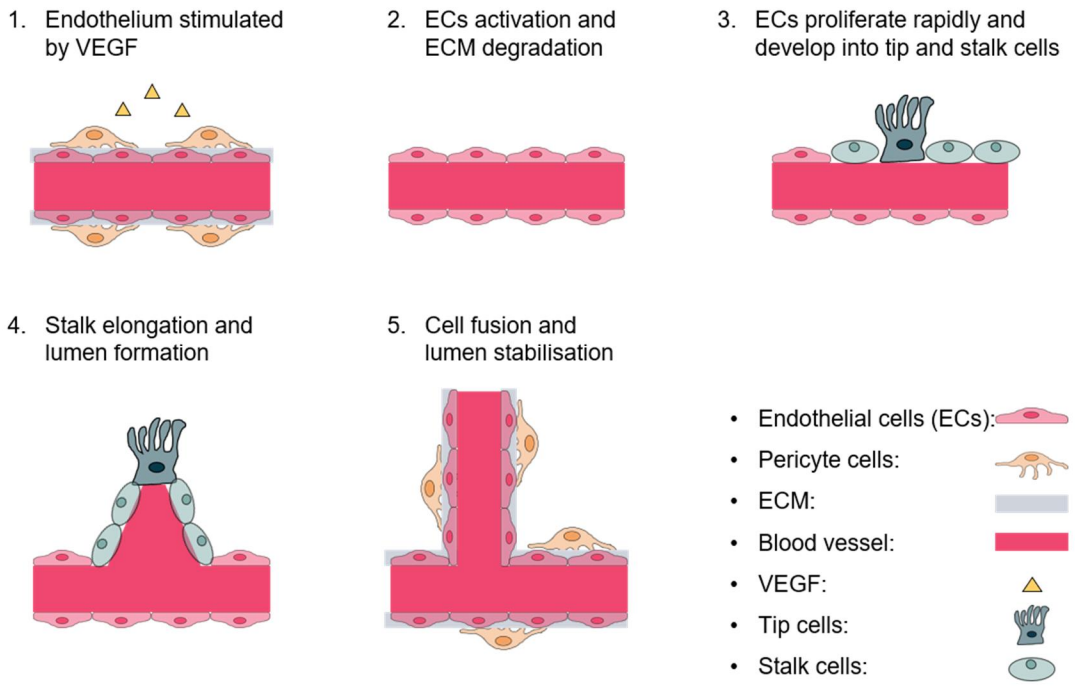

Figure 1-11. Illustration of angiogenesis. Angiogenesis is activated as a response to local tissue hypoxia, which produces the release of endothelial growth factor i.e. VEGF. VEGF triggers the degradation of the ECM and activates endothelial cells, which changed their phenotype to “tip and stalk” cells that are in charge of guiding the new blood vessels and forming the lumen. The new blood vessels stabilise and increase cell – cell junctions, secreting new ECM and repopulating with pericyte cells.[100]

Angiogenesis is the mechanism by which an organism produces new blood vessels. The sequence of events (Figure 1-11) starts with sprouting of endothelial cells where angiogenic growth factors activate endothelial cells to degrade the ECM, a process mediated by matrix metalloproteinases (MMPs).[101] In addition, some endothelial cells start to express filopodia and to increase their motility, which is regulated by the Notch pathway and VEGF. These endothelial cells with filopodia are also called tip cells and act as the leading front of the developing blood vessel. Tip cells “feel” the ECM for attractive cues guiding the sprouts into the stroma. Endothelial cells also change into

stalk cells, which are responsible for forming tubes and branches mediated by their high proliferation rate and their ability to form a lumen. Finally, the new branches are stabilised by deposition of ECM, recruitment of pericyte cells that reduces endothelial cell proliferation and increases cell-cell junction formation.[100,101]

Bone ECM composition along with the bone macrostructure and microstructure confers to bone its unique viscoelastic properties. Bone (macro) mechanical properties are heterogeneous with large variations between cortical and cancellous bone as a consequence of their compact and porous structure, respectively. Additionally, important variability in these mechanical properties has been also identified between different cancellous bones depending of their function. Compressive stress-strain curves of cancellous bone show three different regions:

- The elastic response (linear region identified by the 0.2% strain offset technique).
- The plastic region (where the structure collapses).
- Densification (where the trabeculae structure stack on top of each other).

Cancellous bone presents anisotropic mechanical properties with higher compressive strength than tensile strength both in longitudinal and transversal planes. Moreover, cancellous bone can resist greater deformation in the longitudinal plane than the transversal plane both in terms of compressive and tensile strength.[102] Compressive strength and elastic modulus have been shown to be high in cancellous bone with large variations between different bones according to their anatomical position and needs (Table 1-3).

Table 1-3. Bone mechanical properties depends of their anatomical positions.

Anatomical position	Loading	Ultimate compressive strength (MPa)	Young's modulus (MPa)
Human tibia[102]	Compression	27	211
Femoral head[103]	Compression	-	1700 - 6900
Calcaneus[104]	Compression	3.89	368

A 3D environment that emulates the bone ECM is essential for bone regeneration as the majority of bone physiological phenomena are irreproducible in 2D substrates.[89]

A successful functional biomaterial for skeletal repair must provide the right stimuli that guide the formation of integrated functional bone tissue. Moreover, an ideal scaffold must also stimulate angiogenesis as it improves tissue viability and promotes osteogenesis.

Historically, bone tissue substitutes have tried to match the physical and mechanical properties of bone tissue (e.g. Young's modulus 0.5 – 3 GPa for cancellous bone). However, it has led to aberrant cell behaviour in the host tissue with excessive ossification or bone resorption.[105] Current trends with polymeric biomaterials are in the direction of enhancing endochondral bone regeneration where substrates try to mimic the properties of cartilaginous bone, e.g. young's modulus approximately 100 kPa, and ECM gradients. ECM is a heterogenous microenvironment that can display several gradients such as cell density, chemical cues or composition.[106] For example, in a previous report the fate of myeloid progenitor cells was controlled *in vitro* using polyacrylamide substrates with a stiffness comparable to collagenous bone (~ 44 kPa) and different proteins that mimic the composition of bone marrow. Fibronectin compositions that resembled the endosteal region maintained primitive myeloid progenitors whereas laminin compositions that resembled the vascular region promoted differentiation to an erythroid phenotype.[107]

Micro-porosity (pore size < 10 μm) and macro-porosity (pores > 50 μm) have a strong impact in osteogenesis. Micro-porosity results in larger surface areas that contributes to higher adsorption of bone formation proteins.[108] High porosity results in an increase in cell proliferation due to increased available space/surface and enhanced nutrient diffusion. For example, it was identified that MC3T3 cell proliferation was enhanced in scaffolds made of poly(propylene fumarate) with pores of 350 μm whereas pores of 500 μm inhibited their proliferation[109]. On the other hand, lower pore sizes have been shown to improve osteogenic expression (upregulation of ALP and OCN) as a consequence of suppressing proliferation and increasing cell aggregation.[110] Generally, optimum bone regeneration is considered to happen in pores that resemble the size of trabeculae (100 μm to 400 μm) as demonstrated by the stimulation of proliferation and osteogenesis (100 μm to 200 μm) and angiogenesis (200 μm to 400 μm).[111–113] An interesting approach explored is the co-culture of endothelial and osteoblast cells in a starch-based scaffold, which resulted in the spontaneous formation of blood vessels in the scaffolds.[114] However, little

evidence was found to support that these pre-made vascular-like structures could connect to the host vasculature when implanted *in vivo*.

Overall, an ideal scaffold for bone regeneration would promote osteoinduction, osteoconduction and osseointegration of the functional 3D implant, permitting differentiation of stem cells into bone-forming cells, allowing bone growth into the implant with direct contact between the artificial tissue and the living bone.[115] To do so, a 3D scaffold must:

- Support cell colonisation, proliferation and differentiation.
- Be biocompatible and elicit minimal immune response.
- Provide appropriate surface chemistry to stimulate production and remodelling equilibrium of the ECM.
- Provide appropriate stiffness and mechanical strength.
- Have an interconnected pore structure with large pores, to promote osteogenesis (100 µm to 200 µm) and angiogenesis (200 µm to 400 µm)

To achieve the above, polymeric 3D biomaterials have attracted increasing attention as artificial bone ECM mimetics because of their remarkable physical and chemical tunabilities to match bone characteristics along with their biocompatibilities.[116]

1.4 3D polymer scaffolds for skeletal repair

In the design of graft substitutes, 3D scaffold structure and composition play a pivotal role in determining cell behaviour through surface chemistry and physical properties.[117] Previously, the Bradley group in collaboration with Oreffo's group have successfully explored a number of 3D scaffolds that expand the current space of functional biomaterials for bone repair applications including polyurethanes[118] and hydrogels[119] as well as binary[120] and ternary blends[121] of commercial polymers.

The first approach used polyurethanes and STRO-1(+)* skeletal progenitor cells, which have the ability to differentiate into multiple musculoskeletal cells promoting bone healing.[118] Current approaches for cell enrichment involve time-consuming approaches such as magnetic-activated cell sorting (MACS) and fluorescently-

*Antibody used as a mesenchymal stem cells marker.

activated cell sorting (FACS) both based on immunoselection. As an alternative to these approaches, a microarray constituted of 120 polyurethanes was interrogated with an enriched STRO-1(+) population isolated from adult bone marrow tissue with four polyurethanes selected as a result of their high STRO-1(+) affinity (Table 1-4). These four ‘‘hit’’ polymers were capable of supporting STRO-1(+) cell binding from a heterogeneous population of bone marrow cells where STRO-1(+) cells constituted 11% of the population. Polymer selectivity was further studied by using MG-63 and SAOS-2 cells, osteoblast-like cells with robust STRO-1 expression. Both of the cell lines being unable to bind to the four candidate polymers. Differentiation potential of STRO-1(+) cells cultured on the top polyurethane showed invariance of the osteogenic gene markers RUNX2, ALP and COL1A1 after 25 days in basal medium and an increase of genetic expression in osteogenic medium.

Table 1-4. ‘‘Hit’ polyurethanes discovered for STRO-1(+) binding.[118]

Polyurethane	Polyol	Diisocyanate	Chain extender
PU-16	PEG (2000 Da)	MDI	-
PU-17	PEG (900 Da)	MDI	-
PU-61	PEG (2000 Da)	MDI	1,4-butanediol
PU-71	PEG (2000 Da)	DIB	1,4-butanediol

Although polyurethanes showed their capability to attach skeletal progenitor stem cells, an ideal polymeric scaffold for bone repair also has to promote cell differentiation which these polyurethanes were unable to do without the support of differentiation additives. To address this issue, binary blends consisting of one polymer with good mechanical strength and another polymer with suitable surface chemistry for cell compatibility were engineered and high-throughput screened to identify substrates that successfully promoted skeletal stem cells differentiation.[120] Seven commercially available polymers (Table 1-5) were blended to obtain 135 different substrates. STRO-1(+) cells, foetal skeletal cells and the osteosarcoma cells line MG-63 and SAOS-2 were used to screen these polymer blends. PLLA/PCL (20:80) exhibited remarkable competence binding all these skeletal cell populations. Additionally, 3D porous scaffolds obtained by freeze-drying were used *in vitro* to validate osteogenic differentiation of skeletal progenitors STRO-1(+) into mature osteoblasts. Expression of ALP along with collagenous and non-collagenous bone matrix proteins i.e. COL I, BSP, OPN, osteonectin and OCN were used as differentiation markers. However, osteogenic induction factors such as ascorbate, dexamethasone and human bone

morphogenic protein (BMP-2) were also needed to initiate differentiation. A femur defect model in mice was used to study *in vivo* responses to a PLLA/PCL (20:80) scaffold, which showed bone formation and substantial cell infiltration in the region of the defect by micro-CT with histology confirming the scaffold's osteoinduction ability.

Table 1-5. Commercially available polymers used to generate 135 binary blends for high-throughput screening.[120]

Polymer	Abbreviation	M_w (kDa)
Poly(ethylenimine)	PEI	750
Chitosan	CS	300
Poly-L-lactic acid	PLLA	152
Poly-ε-caprolactone	PCL	120
Poly(ethylene oxide)	PEO	100
Poly(vinyl acetate)	PVAc	260
Poly-2-hydroxyethyl methacrylate	PHEMA	300

This successful attempt in small animals led to the study of the osteogenic potential of the PLLA/PCL (20:80) 3D porous scaffold in large animals (sheep).[122] The osteogenic effect of a scaffold seeded with ovine skeletal stem cells (isolated 2 weeks before surgery) and a scaffold without cells was studied in a long bone segmental defect with an empty defect used as control. Micro-CT revealed modest new calcified bone formation (compared to the control) after 12 weeks post-implantation with histological analysis showed regenerative tissue forming around the scaffolds. However, new tissue was not observed within the central scaffold area indicating the absence of large and interconnected pores that were necessary to allow cell penetration.

The increasing demand for recapitulating properties of the ECM also involved the design of 3D hydrogels due to their ability to incorporate high water content. One approach explored the biocompatibility of chitosan – poly(ethyleneimine) hydrogels (Figure 1-12), which was achieved by mixing an acid solution (1% aqueous acetic acid, pH ≈ 4) of chitosan partially hydrolysed (250 kDa) and poly(ethylenimine) (300 kDa, 10% in water, pH ≈ 11) in various molar ratios.[119] 40:60 CS/PEI showed an interconnected microporous morphology and enabled 3D cell culture by simply mixing cells with the hydrogel before full gelation. Human skeletal cells isolated from cartilaginous foetal femora presented spherical morphology with expression of PCNA (proliferating cell nuclear antigen) and chondrogenic markers, COL2A1 and aggrecan,

when cells were cultured in the 3D hydrogels for 28 days. In contrast, fibroblastic morphology with high levels of type I collagen expression and low levels of chondrogenic markers were observed in cells cultured in 2D tissue culture. However, TGF-β3 supplementation was essential to stimulate the differentiation cascade.

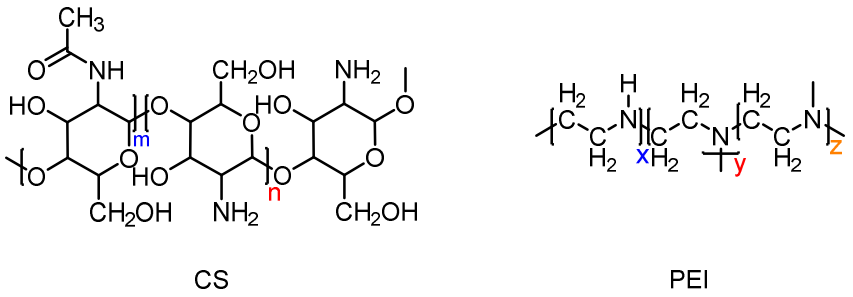

Figure 1-12. Structure of chitosan (CS) and poly(ethylenimine) (PEI) used to obtain the 3D hydrogels.[119]

Despite hydrogels having shown potential in 3D cell constructions, skeletal repair applications demand stiffer substrates capable of withstanding physiological loading. Moreover, a highly porous 3D network that enables vascularisation, cellular activity, and nutrient exchange is also crucial in designing effective biocompatible scaffolds. With this in mind, ternary blends of the commercial polymers previously explored (Table 1-5) were screened to study their ability to bind skeletal cells and subsequently used to obtain libraries of 3D porous scaffolds.[121] A microarray with 19 ternary polymer blends were contact printed and high-throughput screened with skeletal progenitor STRO-1(+) cells, foetal skeletal cells, SAOS-2 cells and MG-63 cells. Following microarray analysis, four polymers (Table 1-6) with high STRO-1 (+) binding were chosen to obtain 3D porous scaffolds. 3D scaffolds were fabricated by mixing the polymers in the appropriate ratio, flash-freezing in liquid nitrogen and subsequent solvent evaporation using freeze-drying. The porous polymer scaffold composed of CS/PVAc/PLLA (50/25/25) showed interconnected pores sized between 5 μm to 10 μm in cross-section with channels between 50 μm to 600 μm, which was selected for further *in vitro* and *in vivo* studies because of its bone-like structure. The *in vitro* evaluation of skeletal stem cells STRO-1(+) in this scaffolds showed ALP expression although osteogenic culture conditions with BMP-2, ascorbate and dexamethasone were needed to promote differentiation to mature osteoblasts, confirmed by the expression of type I collagen, OPN, BSP and osteonectin after 28 days culture. Murine femoral defect models were used to evaluate the *in vivo* response of the selected 3D

scaffold with high resolution micro-CT showing more bone formation in defects with scaffold alone and scaffold with STRO-1(+) cells than the control without scaffold. Histological analysis demonstrated that the scaffold alone was able to generate woven bone within the osteotomy gap whereas scaffold with STRO-1(+) cells presented mature chondrocyte development prior to endochondral ossification. Additionally, endothelial tissue infiltration was identified by immunohistological analysis for the scaffolds with and without cells. However, vascularised tissue in the scaffolds was not observed.

Table 1-6. Ternary blends with high binding of STRO-1(+) cells identified using microarray technology.[121]

Polymers	Blend ratio
CS/PVAc/PEI	50:25:25
CS/PVAc/PLLA	50:25:25
CS/PEI/PLLA	50:25:25
PEI/PHEMA/PCL	50:25:25

The design of functional 3D biomaterials involves a material selection step and a 3D fabrication step inspired by the tissue of interest. For example, bone tissues have tensile and compressive stress in the gigapascal range. Aiming to match these mechanical properties, a solvent, catalyst and photoinitiator-free polyurethane UV-crosslinkable was synthesised with mechanical properties tuned by UV exposure time (Figure 1-13).[123] In addition to biocompatibility, the polymer showed an extraordinary tensile (0.6-2.7 GPa) and compressive (1.5-3.0 GPa) moduli plus the ability to withstand 10,000 cycles of physiological tensile loading.

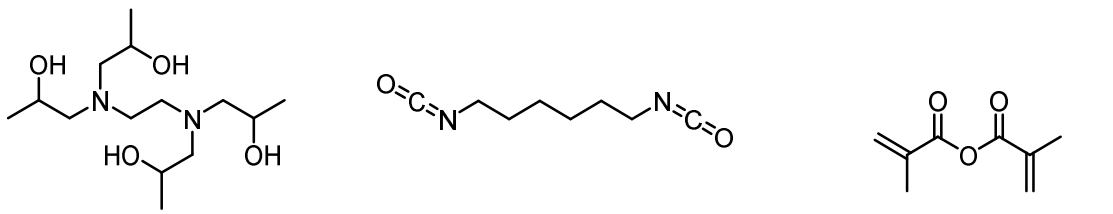

Quadrol (Q) Hexamethylene diisocyanate (H) Methacrylic anhydride (M)

Figure 1-13. UV-crosslinkable polyurethane polymer was synthesised in a 1:0.5:1.5 molar ratio.[123]

The synergistic interplay between inorganic compounds and biocompatible polymers have been explored in order to further mimic some of the characteristic of the bone extracellular matrix, which is composed of apatite crystals embedded within type I collagen fibres. One example that illustrated the potential of these polymer composites was the calcium phosphate polymer induced liquid-precursor (PILP) to treat bone affected by osteoporosis, a disease characterised by the loss of mineral mass in the bone tissues.[124] Calcium phosphate PILP was obtained by mixing polyaspartic acid and polyacrylic acid, negatively charged biocompatible polymers, with high concentration of $CaCl_2$ and Na_2HPO_4. Here, calcium phosphate PILP ability to form mineralised structures were demonstrated *in vitro* and *in vivo* with the large molecular weight of polyacrylic acid (450 kDa) playing a crucial role in the stabilisation of the necessary therapeutic concentration of $CaHPO_4$. In another attempt to mimic human bone composition, gelatin methacrylate was UV photo-crosslinked with methacrylic anhydride to encapsulate hydroxyapatite (HA) and whitlockite (WH) nanoparticles, which is the major human bone inorganic phase.[125] The optimisation of the HA/WH ratio as well as scaffold stiffness (polymerisation time) proved the interdependent effect of these properties in the fabrication of successful scaffolds.

Multi-material and multi-structure scaffolds have been developed as a consequence of the heterogeneity of human bone microenvironment. Examples of these scaffolds were obtained by constructing poly(limonene thioether)/poly(glycerol sebacate) scaffolds with primary and secondary porous structures.[126] The scaffolds composition was chosen to meet design criteria such as slow biodegradability and elastomeric mechanical properties and the double porous structure aimed at producing high cell infiltration and attachment in addition to promoting oxygen and nutrient diffusion. The double porous structure was achieved using a silicon wafer mould etched to obtain microchannels larger than 500 μm as a primary porous structure and poly(methyl methacrylate) spheres (5-20 μm) that served as a porogen for the secondary porous structure. In another example, three-layer scaffolds that tried to imitate the joint between bone and cartilage were obtained *via* thermally-induced phase separation with poly(lactic acid) and sulfate/phosphate cellulose nanocrystals.[127] The approach showed success with high biocompatibility with chondrocyte cultures and differences *in vivo* tissue infiltration that resembled human cartilage. However, scaffolds of both examples needed to be assembled manually layer-by-layer.

Vascularisation regulates the growth, differentiation and reconstruction of bone tissue and its surrounding soft tissue. Composition of 3D biomaterials play a crucial role to stimulate vascularisation and bone tissue regeneration.[128] For example, a 3D scaffolds with potential for therapeutic bone repair was made of polyvinyl alcohol (PVA), PCL and hydroxyapatite based bioceramic (HAB) with electrospinning. PVA-PCL-HBA scaffolds showed growth of stromal stem cells, *in vitro* osteogenic differentiation and *in vivo* vascularised bone formation with the HBA degradation products stimulating the production of VEGF.[129] A biodegradable scaffold composed of polydiolcitrate-gelatin (PPCNG) was fabricated to release cytokines such as BMP-9 *in situ*, one of the most potent known osteogenic differentiation factors.[130] The histological analysis of the subcutaneous injection of PPCNG with MSCs in mice showed the gel resorbed over time, the increase of VEGF expression and the formation of more mature trabecular bone-like structures.

Cell-based pre-vascularised scaffolds showed the potential to repair large bone defects as an alternative to growth factors embedded in polymer scaffolds.[131] MSCs and human umbilical vein endothelial cells (HUVECs) were cultured independently to obtain cell sheets and combined with β-TCP scaffolds. *In vitro* results indicated that seeded HUVECs rearranged the ECM produced by MSCs, which led to rapid formation of functional blood vessels *in vivo*. Moreover, *in vivo* pre-vascularised scaffolds gained attention inspired by autografts, present gold standard for repairing long bones. For example, β-TCP scaffolds with MSCs and pre-vascularised with insertions of femoral vascular bundle showed increasing expression of VEGF.[132]

Despite the huge amount of resources* used to develop successful 3D biomaterials for skeletal repair application, there are consistent limitations of current 3D scaffolds that impede clinical applications (Table 1-7).[13] Although long-term cell viability and biocompatibility has been proven *in vitro* and *in vivo*, cell functionality persists as a challenge. Growth factors and biochemical clues like BMPs have been used to overcome these challenges, however, the high concentrations (mg/ml) required, compared to their physiological concentration (ng/ml), can lead to adverse effect such as carcinogenesis and aberrant bone formation. In addition, efficient nutrient and waste removal has yet to be efficient enough to allow sustained tissue growth. Although angiogenesis occurs spontaneously upon scaffold implantation it is triggered

* 60% of the publications with the term “polymer tissue regeneration” are focused on bone regeneration (ISI Web of Knowledge).

by inflammation, resulting in poor vascularisation of scaffolds and tissue penetration. These are significant and commonly observed limitation. Moreover, a full understanding of scaffold microstructure/mechanical properties and cell behaviour remains incomplete, which hinders the cell selection and the scaffold design. Furthermore, the translation of academic research in the absence of automated and controlled production, and the lack of methods to evaluate potential 3D materials adds real challenges to their clinical development and application.

Table 1-7. Advantages and disadvantages of different 3D polymer for skeletal repair.

Scaffolds	Pros	Cons
Polyurethanes	Isolation and maintenance of skeletal progenitor stem cells. Good mechanical properties.	Poor osteogenic and angiogenic properties. Deficient 3D microstructure.
Polyacrylates	*In vitro* and *in vivo* osteogenic and angiogenic properties. Tailorability and good mechanical properties.	Limited long-term osteogenic properties. Deficient 3D microstructure
Hydrogels	Recapitulation of ECM properties.	Poor osteogenic and mechanical properties. Deficient 3D microstructure.
Composites	Good osteogenic and angiogenic properties.	Limited long-term osteogenic properties. Poor mechanical properties. Deficient 3D microstructure.

2. Aims of the thesis

In the design of 3D biomaterials, scaffold properties such as chemical composition, stiffness, wettability, porosity, pore size or pore distribution all affect cell fate. Given the impossibility of examining all of these variables simultaneously, the majority of current methods try to simplify the analysis studying the effect of one variable at a time on cell behaviour. However, this reductionist approach does not take into account the importance of interplay between these processes.

This thesis aimed to develop a novel approach to generate an array of 3D polymer scaffolds that could be exploited in the identification of yet undiscovered biomaterials for biomedical applications. The premise was that this array would enable the high-throughput analysis of the effect of multiple scaffold features such as composition, porosity, pore size and pore distribution on cellular fate, which would enhance the identification of successful functional biomaterials. Coupled with the classical 2D polymer microarray technology, this approach aimed to reduce the gap between the *in vitro* identification of a biomaterial and its subsequent *in vivo* application.

To address the above, arrays of 3D scaffolds were fabricated *via* freeze-casting and UV photo-polymerisation as a convenient, yet powerful method to tune scaffold composition and 3D microstructure. Polyacrylates were selected as substrates due to their versatility, proven biocompatibility and their ability to support endothelial cells (ECs).[29] After establishing this new method, the applicability of the approach was demonstrated in the selection of 3D scaffolds for bone repair.

3. Material and methods

3.1 Instrumentation

- Plasma generator Zepto O_2 (Diener Electronic GmbH, Germany).
- Microarray printer SciFLEXARRAYER S5 (Scienion, Germany).
- Fridge-Freezer Combi 263L (Lec Medical, UK).
- Ultraviolet cross-linker CL-1000 (UVP, USA).
- Freeze-dryer BenchTop Pro with Omnitronics (SP SCIENTIFIC, UK).
- Fluorescence microscope Nikon Ni-U eclipse equipped with an automated stage and Pathfinder™ Wellscan software (IMSTAR S.A., France).
- Biosafety cabinet HERAsafe KS 18 class II (Heraeus, Germany).
- Incubator HERAcell 150 (Heraeus, Germany).
- Microscope Zeiss LSM880 Airscan equipped with a 20X NA 0.8 air objective (Zeiss, Germany).
- Scanning electron microscopy Hitachi S-4700 (HITACHI, Japan).
- Micro computed tomography Skyscan 1172 (Bruker, Belgium).
- Microplate reader GloMax® Explorer (Promega, USA).
- *In vivo* optical imaging system IVIS Lumina S5 (PerkinElmer, USA).
- Imaging System Odyssey® CLx (LI-COR, USA).
- Universal mechanical testing system Instron (model 3367) equipped with a 50 N load cell for compression and the software Bluehill 3 (INSTRON®, USA).
- Histology slide scanner NanoZoomer XR (Hamamatsu, Japan).
- Thermometer testo 905i (Testo, Germany).
- TGA instrument SDT Q600 (TA Instruments, USA).

3.2 Materials

2-(Methylthio)ethyl methacrylate (MTEMA), butyl methacrylate (BMA), isobornyl acrylate (IBA), ethylene glycol dicyclopentenyl ether acrylate (EGDPEA), 1,6-hexanediol diacrylate (HDOBA) and 2-hydroxy-2-methylpropiophenone (PI), pepsin from porcine gastric mucosa (Roche), Alizarin Red, Sirius red S, picric acid solution (1.3% in H2O), phosphatase substrate (P4744), 1.5 M alkaline buffer solution (A9226), Cellytic M, Igepal CA-630, p-nitrophenol (N7660), dexamethasone, β-glycerophosphate disodium salt hydrate, molybdophosphoric acid (221856), Sirius red F3B (365548), Orange G (O3756), Light green SF (L5382), Dulbecco's modified Eagle medium (DMEM), 2-phospho-L-ascorbic acid disodium and flat-bottom polypropylene 96-well plates (Greiner Bio-ONE) were purchased from Sigma-Aldrich. 4-tert-butylcyclohexyl acrylate (BHA) was obtained from Tokyo Chemical Industry.

Alpha MEM eagle with UGln1 and nucleosides and penicillin/streptomycin/fungizone 10K/10K/25 µg were purchased from Lonza. Fetal bovine serum, L-glutamine, DAPI (62248), Quant-iT™ PicoGreen™ dsDNA assay (Life Technologies), alamarBlue™ (Thermo Scientific), Live/Dead Cell imaging assay (R37601, Invitrogen) and Alexa Fluor™ 568 phalloidin (A12380, Invitrogen) were purchased from Thermo Fisher Scientific. RA Lamb Waxes (12624077, Thermo Scientific), Histo-Clear™, DPX mounting medium (10050080), Weigert's Hematoxylin (10181710) and Alcian blue 8GX (40046-0100, ACROS Organics) were acquired from Fisher Scientific. Herring sperm DNA (D1811) was purchased from Promega. Vitamin D3 was obtained from Cayman Chemical Company.

Anti-Alkaline Phosphatase (ab65834), Anti-Osteopontin antibody (ab8448), Anti-Collagen I antibody (ab34710), Goat Anti-Rabbit IgG Alexa Fluor® 647 (ab150079), BCA assay kit (ab207002) and Human Pro-collagen I SimpleSep ELISA® kit (ab210966) were purchased from Abcam.

OsteoSense® 800 Fluorescent Imaging Agent was acquired from PerkinElmer. IRDye® 800CW BoneTag™ Optical Probe was purchased from LI-COR.

3.3 Cell characteristics and culture methods

SAOS-2 or HTB-85 was purchased from ATCC and it is a human bone osteosarcoma adherent cell line with epithelial morphology. MG-63 or CRL-1427 was purchased from ATCC and it is a human bone osteosarcoma adherent cell line with fibroblast morphology. SAOS-2 and MG-63 were expanded to confluence in DMEM medium supplemented with foetal bovine serum (FBS, 10%), L-glutamine (4 mM) and antibiotics (penicillin/streptomycin, 100 units/mL) and used within 10 passages.

FBMSCs, provided by Dr Stefanie Inglis and Ms Suzanne Renz from the University of Southampton, were isolated as per the ethical approval obtained from Southampton & South West Hampshire Local Research Ethics Committee (LREC296/100). FBMSCs were used within 4 passages. FBMSCs were expanded to confluence in supplemented α-MEM medium with FBS (10%) and penicillin/streptomycin/fungizone (100 units/mL), known as basal medium. Osteogenic differentiation medium was composed of α-MEM medium supplemented with FBS (10%), 2-phospho-L-ascorbic acid (50 μg/mL), calcitriol (10 nM) and penicillin/streptomycin/fungizone (100 units/mL).[133]

3.4 Microarrays

3.4.1 Glass slide silanisation and mask fabrication

Superfrost™ glass slides (ThermoFisher) were cleaned by washing with HPLC grade water and with acetone and dried in anoven at 110 °C for 5 min. O_2-plasma treatment (Electronic diener ZEPTO at 50 NL/h O_2, 10 minutes, 30 W) was then performed.

A previously developed method was adapted to generate a fluorous mask on the surface of the glass slide (Figure 3-1).[30] To do so, 10 drops (≈ 3.50 nL in total) of an aqueous solution of sucrose (20% w/v) was jetted on top of the cleaned glass slides to obtain the microarray pattern (540 polymer features were printed in an array of 12 columns and 45 rows). Inkjet printing was carried out using a microarray printer (sciFLEXARRAYER S5, Scienion, Germany) equipped with a PDC 80 piezoelectric capillary with a 50 μm nozzle aperture.

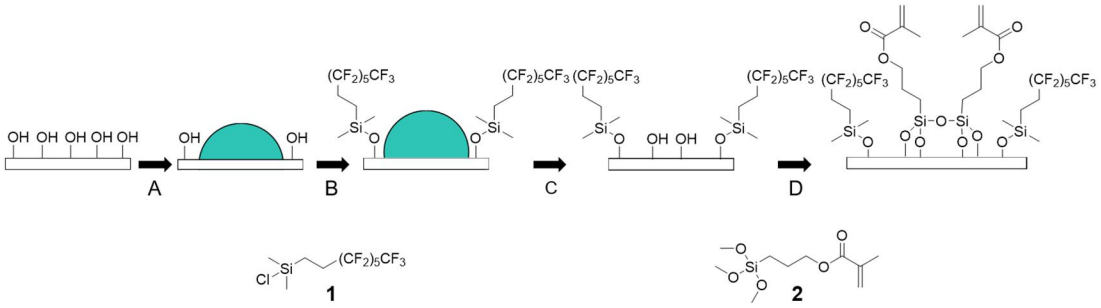

Figure 3-1. Cleaned glass slides (exposed hydroxyl groups) were patterned (A) with sucrose (20% aqueous solution, green sphere). “Fluorosilane” (1) was used to functionalise the remaining areas (B). The sucrose mask was removed with water (C) to expose the hydroxyl groups, which were functionalised (D) with an “acrylatesilane” (2).

“Fluorosilane” (tridecafluoro-1,1,2,2-(tetrahydrooctyl)dimethyl-chlorosilane) was used to functionalise the unprotected surface of the glass slides (where sugar was not printed) to generate a fluorous and cytophobic surface. The glass slides were placed in a high-density polypropylene plastic box (22×11×13 cm) and 10 µL of fluorosilane was dropped around the area printed with sucrose, sealed and reacted for 24 hours. Slides were washed with water (3 x 10 mL) and ethanol (3 x 10 mL) and dried at room temperature to remove excess reagent and the sucrose mask.

Once the slides were dried, 5 µL of the “acrylsilane” (3-(trimethoxysilyl)-propyl methacrylate) was spread on top of the glass slide surface with a pipette tip and reacted for 48 hours with the “acrylsilane” pooling in the “masked” features. Slides were rinsed with acetone, dried at room temperature and kept in a dry atmosphere.

3.4.2 Fabrication of microarrays and cell seeding on the microarrays

Microarrays constituted of 540 polymer features (180 acrylate polymers with 3 replicates) were fabricated by inkjet printing. Solutions of the monomers, UV photo-initiator and cross-linker were prepared in NMP (A for full list of compositions). *In-situ* polymerisation was achieved by depositing 100 drops (≈ 35 nL in total) of the solutions (72 drops of the monomers, 18 drops of the cross-linker and 10 drops of the photoinitiator) on top of the masked glass slide. Photo-polymerisation was carried out using a UV cross-linker (CL-1000L 8W, λ = 365 nm) for 30 min. The printing procedure

was divided into 5 sections to avoid the slides drying out before polymerisation. NMP was removed under vacuum (40 °C, overnight). Subsequently, microarrays were washed with water and ethanol (1:1, 1 h) and water (24 h) before being dried at room temperature.

Microarrays were sterilised under UV light (1 h) and washed with PBS (1 h) before seeding. SAOS-2 and MG-63 cells were expanded, and cell seeding was carried out with a suspension of SAOS-2 and MG-63 cells (1,000,000 cells/microarray in 5 mL of complete medium) in 4-well tissue culture plates at 37 °C and 5% CO_2 in a humidified atmosphere.

After 2 days, microarrays were washed with PBS (2 cycles) and cells were fixed with paraformaldehyde (4% PFA) for 5 min. Subsequently, removing excess fixative solution, cell nuclei were stained with a solution of DAPI (5 µg/mL) in PBS for 10 min (4 mL/microarray). A Nikon Ni-U eclipse fluorescence microscope equipped with an automated stage and the software Pathfinder Wellscan (IMSTAR) was used to acquire fluorescence and bright field images. Cell attachment was assessed by counting the number of cells on each polymer feature and measuring the polymer area with the image processing software ImageJ-Fiji. Results are presented as the number of cells per mm^2 of the polymer.

3.5 Fabrication of 3D polymer scaffolds and characterisation

3.5.1 Fabrication of arrays and scaled-up scaffolds

The fabrication of arrays of 3D polymer scaffolds was carried out through photo-polymerisation with various porogenic solutions at sub-zero temperatures in polypropylene 96-well plates. The polymerisation mixtures (Table 4-1 and Table 5-1) were composed of the photo-initiator (2-hydroxy-2-methylpropiophenone, 10 mol %), the cross-linker (1,6-hexanediol diacrylate, 18 mol %) and the appropriate combinations of acrylate monomers (72 mol %). The polymerisation mixtures with DMSO were placed in polypropylene plates (80 µL/well) and cooled (5 °C for 16 h and -20 °C for 4 h). The arrays were photo-polymerised (UV cross-linker CL-1000L 8W, λ = 365 nm, 30 min) on top of a dry ice bath (Figure 4-5). Following polymerisation, the

scaffolds were washed with water and ethanol (1:1, 3 days) and water (4 days) at 37 °C before freeze-drying (2 days).

The method described above was modified to obtain larger 3D polymer scaffolds (≈ 12 mm length × ≈ 12 mm width × ≈ 1 mm height) with the porogenic solutions (300 µL/scaffold) cooled (5 °C for 16 hours and -20 °C for 4 hours) and UV-cured for 60 min in square polystyrene moulds (12 mm length × 12 mm width × 7 mm height). After polymerisation, scaffolds were removed from the mould and washed with water and ethanol (1:1, 4 days) and water (5 days) at 37 °C before freeze-drying (2 days).

3.5.2 Structural analysis using SEM

Polypropylene plates were cut in sections of 3×6 wells before proceeding with the array fabrication. The sections were coated with gold/palladium alloy (3:2) using a sputter coater (30 mA, 0.75 Torr). A Hitachi S-4700 was employed to perform the image acquisition and the analysis was carried out using ImageJ-Fiji. SEM images were segmented using the thresholding plugin and filtered to separate the porous structure from the polymer. Subsequently the porous segmented areas were quantified (analyse particles plugin) using the pore descriptors porosity (%) and Feret's diameter (the largest distance between the edge of the pores).

3.5.3 Structural analysis using micro-CT

Sections of the array of the 3D polymer scaffolds (2×2 wells) were stacked (3 rows high) to obtain a cuboid of 12 polymer scaffolds that was secured with adhesive tape and enclosed into a polystyrene box (5 cm diameter × 7 cm high), preventing movement of the sample during the scan. The sample was placed in a Skyscan 1172 desktop micro-CT (Bruker, Kontich, Belgium) and scanned through 360° using a step of 0.48° between exposures. Micro-CT parameters were 34 kV source voltage, 210 µA source current with an exposure time of 1.8 s to obtain a voxel resolution of 5.94 µm. Noise was reduced using the average of four frames at each position.

Data was reconstructed using Skyscan NRecon v1.6.9 (Bruker, Kontich, Belgium) applying a reconstruction thresholding window of 0.00 to 0.05 in attenuation coefficient with no beam hardening correction. Volume of interests (VOI) were

selected in each reconstructed micro-CT scans and Fiji-Bonej was used to analyse the porosity of the segmented VOIs.[134] A circular region of interest of 4.75 mm diameter was extended by 0.62 mm (± 0.19 SD) through the structure to define the VOI, binarised (thresholding range of 52 – 255) and speckles removed (< 4 pixels). Morphological analysis of the thickness and connectivity density of the polymer structure in addition to pore diameter and open porosity were carried out using CTAn v1.16.4 (Bruker, Kontich, Belgium).

3.5.4 Mechanical characterisation of the 3D polymer scaffolds

Scaled-up 3D scaffolds (≈ 12 mm length × ≈ 12 mm width × ≈ 1 mm height) were re-hydrated with PBS before mechanical characterisation. Indentation was carried out using an Instron testing system (model 3367) equipped with a 50 N load cell for compression and a flat cylindrical (ø = 1 mm) indenter (made in house). The software Bluehill 3 (INSTRON®, USA) controlled the equipment and digital Vernier callipers were used to measure the height of the samples (≈ 1.7 mm). Compression speed with a strain rate of 5% per minute for 20% of the strain was used.

The indentation moduli were calculated between 0% and 5%, 5% and 10%, 10% and 15%, and 15% and 20% strain percentage using a linear model for semi-infinite media (diameter sample to diameter indenter ≥ 3) as previously described.[135–137] The relaxation load (%) was described as percentage of load redaction after 1 min and 5 min of relaxation.[138,139]

3.5.5 Porosity and density of the 3D polymer scaffolds

Porosity on the 96 well plate was calculated as the ratio between the volume of solvent in the pores (V_P) and total volume of the scaffold (V_T) with volumes determined by weighting the solvent (DMSO). The volume of solvent in the pores was firstly calculated. To do so, 200 µl of DMSO (V_0) was added to the 3D polymers and empty wells (96-well plate, control). After 4 hours (to ensure complete filling of the pores), excess DMSO was removed and weighed. The volume of the pores ($V_p = (M_1 - M_2)/ \rho_{DMSO}$) was calculated as the difference between the mass of DMSO in the empty wells (M_1) and the mass of DMSO recovered from the well with the scaffolds (M_2). Subsequently, the total volume of the scaffolds ($V_T = (M_3 - M_4)/ \rho_{DMSO}$) was measured

as the subtraction between the mass of DMSO needed to completely fill an empty well (M_3) and the mass of solvent needed to entirely fill a well with a 3D porous polymer (M_4).

The method described above was modified to measure the density and porosity of the scaled-up scaffolds (≈ 12 mm length × ≈ 12 mm width × ≈ 1 mm height). Density was determined as the ratio between the weight of a dried scaffold and the volume that the scaffold displaced in a measuring cylinder with ethanol. The porosity was calculated as the ratio between the volume of ethanol in the pores and the total volume of the scaffold.

3.6 Characterisation of cells

3.6.1 Cell seeding on the arrays and 3D polymer scaffolds

The arrays of 3D polymer scaffolds were UV sterilised overnight and pre-conditioned with 50 µL of culture medium for 1 h before cell seeding.

SAOS-2 and MG-63 cells were seeded on the arrays in supplemented DMEM medium (20,000 cells/well in 150 µL). FBMSCs were expanded to confluency and seeded (10,000 cells/well in 150 µL) on the arrays in supplemented α-MEM medium or osteogenic differentiation medium.

The 3D polymer scaffolds (≈ 12 mm length × ≈ 12 mm width × ≈ 1 mm height) were UV sterilised overnight and placed into inserts (Transwell® Ø = 12 mm, Corning®). FBMSCs were seeded in basal medium (40,000 cells/scaffold in 110 µL) forming a drop in the centre of the scaffold. Scaffolds were incubated for 45 min allowing cell attachment before adding 1 mL of medium to cover completely the scaffold.

After seeding, the arrays and scaffolds were kept in a humidified atmosphere at 37 °C and 5% CO_2 with the media changed every two days.

3.6.2 Cell viability and proliferation on the arrays

The number of cells along with their metabolic activity was assessed using so-called alamarBlue™ (also called Alamar Blue or resazurin). At the appropriate time, the

culture medium was removed to add 100 µL of Alamar Blue in medium (10% v/v). Arrays were kept in the incubation chamber (dark) for 4 hours (37 °C, 5% CO_2). Thereafter, the supernatant was collected, and fluorescence intensity was recorded using a microplate reader ($\lambda_{ex/em}$ = 530/590 nm). Alamar Blue excess was removed with PBS and medium was added (150 µL/well) to maintain the cells in culture for the next time point. Scaffolds and wells of a tissue culture plate without cells were used as negative controls to analyse Alamar Blue background fluorescence.

3.6.3 Analysis of cell morphology and scaffolds using SEM

The arrays of 3D polymer scaffolds were seeded as described above. At the appropriate time, the medium was removed before washing the scaffolds and cells with PBS (100 µL, 10 min). Cells were fixed with PFA (4%, 15 min) and washed with sodium cacodylate buffer (0.1 M, 1 h). Polymer scaffolds were removed from the wells using a needle. Post-fixation was carried out by applying osmium tetroxide (0.1M, 45 min) followed by further washing with sodium cacodylate buffer (0.1 M, 15 min). Scaffold dehydration was achieved with increasing concentrations of acetone in a mixture of acetone/water (50%, 70%, 90% and 100% v/v) and critical point drying (liquid CO_2). The scaffolds were coated with a gold/palladium alloy in a sputter coater with image acquisition on a Hitachi S-4700 scanning electron microscope (SEM). Scaffolds without cells were used as controls.

3.6.4 Biomineralisation on the arrays

Array sterilisation and seeding was carried out as described above. Mineralisation medium (culture medium supplemented with 50 µg/mL 2-phospho-L-ascorbate, 1 to 20 mM β-glycerophosphate and 10 nM dexamethasone) was used to promote biomineralisation.[140–142] Scaffolds and wells of a tissue culture plate without cells were used as controls.

Mineralisation assessment using Alizarin red.[143] Medium was removed at the appropriate time points and scaffolds were washed with PBS and fixed with PFA (4%, 15 min). Arrays were washed with water (1 h) at 37 °C to remove free calcium present in medium. Alizarin red (40 mM) was prepared in acetic acid (10% v/v) to give an acidic pH (pH 4.1). The scaffolds were incubated with the stain for 1 h in an orbital

shaker. Excess alizarin red was removed by washing the scaffolds extensively with water (5 h with the water changed every hour). Cetylpyridinium chloride (10% w/v) in an aqueous solution of Na_2HPO_4 (10 mM) was used to extract the stain from the scaffolds and the absorbance recorded using a microplate reader (λ = 550 nm).

Mineralisation assessment using near infrared fluorescence dyes.[144] Medium was removed 24 h before analysis, icubating the cells with a solution of OsteoSense® 800 (20 pmol/mL) and IRDye® 800CW BoneTag™ (2 pmol/mL) in culture medium (80 µL/well). After incubation, scaffolds were washed with PBS (100 µL × 3 times) and fixed with PFA (4%, 30 min). After removing excess PFA, scaffolds were washed with PBS (10 min). Fluorescence intensity was recorded using an *in vivo* optical imaging system IVIS Lumina S5 ($\lambda_{ex/em}$ = 780/805 nm).

3.6.5 Live/dead staining assay on the 3D polymer scaffolds

Cells were stained with live/dead cell imaging assay (R37601) according to the manufacturer's protocol with calcein AM ($\lambda_{ex/em}$ = 488/512 nm) for living cells and a nuclear red fluorescence dye (e $\lambda_{ex/em}$ = 570/602 nm) for dead cells. Culture medium was removed from the wells and cells were incubated for 15 min at room temperature (100 µL/well) with the "live/dead staining solution" diluted 1:1 with additive free medium. Image acquisition in 3D was performed using a Nikon Eclipse 50i microscope and the Pathfinder™ software (IMSTAR, France). Scaffolds without cells were used as controls.

3.6.6 Cell cytoskeleton staining on the 3D polymer scaffolds

Cells were fixed (4% PFA for 15 min), permeabilised (0.1% Triton X-100 in PBS, 15 min) and washed with PBS (10 min). Cell nuclei were stained by applying a solution of DAPI (5 µg/mL, 10 min) in PBS (100 µL/scaffold). After removing excess DAPI and washing the scaffolds with PBS (10 min), the actin filaments were stained with Alexa FluorTM 568 phalloidin (1:40 dilution, 30 min) at room temperature. After three washing cycles, scaffolds were removed from the 96-well plates, sectioned with a scalpel (about 6 mm diameter × 1 mm thick) and mounted on glass slides with cultureWell™ gaskets. Image capture was performed on a confocal microscope Zeiss LSM880 Airscan equipped with a 20X NA 0.8 air objective. Cytoskeleton orientation

was assessed with the ImageJ-FIJI plugin OrientationJ.[145] Scaffolds without cells were used as negative controls to analyse scaffold autofluorescence and non-specific staining.

3.6.7 Total collagen on the arrays

Total collagen content was assed using a colorimetric method.[146,147] At the appropriate time point, medium was removed and 3D polymer scaffolds were incubated with pepsin digestion solution (1 mg/mL pepsin, 0.1 M acetic acid and 0.5 M NaCl) for 48 hours at 5 °C (150 µL/well). Digested solutions (100 µL/sample) were dried in a 96-well plate at 37 °C overnight and treated with Sirius red solution (1 mg/mL) in saturated picric acid (1.3% in water) for one hour. Arrays were washed (3 × 5 min) with HCl solution (0.1 N) to remove excess sirius red before homogenising staining with NaOH (0.1 N, 100 µL/sample). Absorbance was recorded using a microplate reader (λ = 550 nm). Scaffolds and wells of a tissue culture plate without cells were used as negative controls.

3.6.8 ALP quantification on the arrays

Alkaline phosphatase was quantified according to a previously reported colorimetric method.[148,149] Medium was removed and scaffolds were washed with PBS (1 × 5 min) before treating with CelLytic M for 1 hour at 37 °C. Cell lysate (10 µL/sample) was placed in a 96-well plate with ALP substrate (90 µL/sample) solution (0.04 g phosphatase substrate in 10 mL of 1.5 M alkaline buffer solution, Sigma A9226, and 30 mL of distilled water). Reactions were carried out at 37 °C between 10 to 60 min and was stopped by adding NaOH (100 µL/sample, 1 M). A standard calibration curve (0 to 2 µM) was obtained using dilutions of p-nitrophenol (10 mM) in assay buffer (30 µL of Igepal CA-630, 5 mL of 1.5 M alkaline buffer solution A9226 made up to a final volume of 15 mL with distilled water). Absorbance was recorded on a microplate reader (λ = 410 nm) with ALP concentration calculated as nmol p-nitrophenol per mL/hour. Scaffolds and wells of a tissue culture plate without cells were used as negative controls.

3.6.9 DNA concentration on the arrays

DNA concentration was evaluated according to a previously reported procedure.[148,149] Medium was removed and scaffolds were washed with PBS (1 × 5 min) before treating with CelLytic M for 1 hour at 37 ºC. Cell lysate (10 µL/sample) was placed in a 96-well plate with TE buffer (1000 µL/sample) and Quant-iT™ PicoGreen™ dsDNA solution (90 µL/sample) according to the manufacturer's protocol. A standard calibration curve (0 to 1000 ng/mL) was prepared with serial dilutions of herring sperm DNA (10 mg/mL) in TE buffer. Fluorescence intensity was recorded using a microplate reader ($\lambda_{ex/em}$ = 480/520 nm). Scaffolds and wells of a tissue culture plate without cells were used as controls.

3.6.10 Immunofluorescence on the 3D polymer scaffolds

At the desired time point, medium was removed and scaffolds were washed with PBS (1 × 5 min) before fixing the cells (4% PFA) for 30 min. Excess fixative was removed and scaffolds were washed with PBS (3 × 5 min) and treated with appropriate blocking solution and permeabilised (200 µL/sample) for 1 hour if necessary.

- ALP blocking solution in PBS (w/v): 1% bovine serum albumin (BSA) and 10% normal goat serum in 0.1% TWEEN® 20 solution.
- Collagen I blocking solution in PBS (w/v): 5% BSA.
- Osteopontin blocking solution in PBS (w/v): 1% bovine serum albumin (BSA) and 10% normal goat serum in 0.1% TWEEN® 20 solution.

Excess of blocking solution was removed by washing with PBS and scaffolds were treated overnight with the appropriate solution of the primary antibody (200 µL/sample) according to the manufacturer's protocol.

- ALP primary antibody (ab65834, Abcam) solution (1/200) was made in BSA solution (1% w/v) in PBS.
- Type I collagen primary antibody (ab34710, Abcam) solution (1/500) was made in BSA solution (3% w/v) in PBS.
- Osteopontin primary antibody (ab8448, Abcam) solution (1/200) was made in BSA solution (1% w/v) in PBS.

Excess primary antibody was removed and scaffolds were washed with PBS prior to treating with a solution of secondary antibody Goat Anti-Rabbit IgG Alexa Fluor® 647 (ab150079, Abcam) in PBS (1/250 dilution) for 1 hour. After three washing cycles with PBS, scaffolds were sectioned with a scalpel (≈ 6 mm diameter × 1 mm thick) and mounted on glass slides with cultureWell™ gaskets. Image capture was performed on a confocal microscope Zeiss LSM880 Airscan equipped with a 20X NA 0.8 air objective. Scaffolds without cells were used as negative controls.

3.6.11 ELISA on the 3D polymer scaffolds

FBMSCs were seeded (1,000,000 cells/scaffold) onto scale-up 3D scaffolds (12 mm length × 12 mm width × 1 mm height) and maintained for 21 days as described above. At the appropriate time point, scaffolds were washed with PBS, crushed with a scalpel and treated with 1X dilution of cell extraction buffer PTR (Abcam) (400 µL/scaffold) for 15 min on ice. Lysates were centrifuged at 15,000 rpm for 20 min at 4 ºC and supernatants passed through protein concentrators Pierce™ PES (30,000 K MWCO's, 2-6 mL, Thermo Fisher Scientific). Total protein was quantified using a BCA assay kit and ELISA performed using a Human Pro-collagen I SimpleSep ELISA® kit according to manufacturer's instructions. Absorbance was recorded on a microplate reader (λ = 450 nm). Scaffolds without cells were used as negative controls.

3.6.12 CAM assay of the 3D polymer scaffolds

Biocompatibility and angiogenesis of polymer scaffolds were evaluated using a chick embryo chorioallantoic membrane (CAM) model according to previously reported methods.[150] The CAM protocols were conducted by Mr. Michael Glinka from University of Southampton under Home Office Approval UK (Project license – PPL 30/2762).

FBMSCs (40,000 cells/scaffold) were incubated for 7 days on the 3D polymer scaffolds (12 mm length × 12 mm width × 1 mm height) before implantation. 3D scaffolds without cells were used as negative controls.

Fertilised chicken eggs were incubated at 37 °C (60% humidified atmosphere and 1-hour rotation) in a Hatchmaster egg incubator (Brinsea, UK) for 10 days.

Subsequently, a window (5 × 5 mm) was opened in the eggshell with a scalpel under sterile conditions. 3D polymer scaffolds with and without FBMSCs were cut with a scalpel (5 mm length × 5 mm width × 1 mm height) and implanted in the eggs with the windows sealed with sterile parafilm. After 7 days incubation, the samples were harvested and scaffold integration in the CAM inspected with a stereomicroscope with a digital camera (Canon Powershot G2) using a Chalkley score method to quantify angiogenesis (the Chalkley's method uses an eyepiece grid with 25 randomised points that is oriented to permit the maximum number of points overlapping on the microvessels). The process is repeated in three different areas of the scaffolds.[151,152] Gestational process of chick embryos was terminated under Home Office guidelines.

3.6.13 *In vivo* scaffold implantation in mice and micro-CT analysis

The subcutaneous surgeries were conducted by Mr. Michael Glinka from the University of Southampton under Home Office Approval UK (Project license – PPL 30/2762). Athymic BALB/cnu mice were grown until three months old (~33 g) before carrying out the implantation.

3D polymer scaffolds (12 mm length × 12 mm width × 1 mm height) were seeded with FBMSCs (40,000 cells/scaffold) as described above and conditioned in basal and osteogenic media for 7 days before implantation. 3D polymer scaffolds without cells were used as a negative control. 3% (w/v) alginate gels with and without cells in basal and osteogenic media were used as a positive control.

Animals were anaesthetised with an intra-peritoneal injection of a 1:1 mixture of Hypnorm™/Hypnovel™ before surgery. Incision on the back of the mouse skin was followed by implantation of pieces of the 3D polymer scaffolds and alginate gels (5 mm length × 5 mm width × 1 mm height) in the subcutaneous pockets (6 small scaffolds/gels per mouse). The incisions were stitched and animals allowed to recover.

Post-surgery evaluation of scaffolds and gels was carried out using a micro-CT system (Bruker Skyscan, Belgium) equipped with micro-focus X-ray source (20-90 kV, 25 W). Experiments were terminated after 4 weeks with the euthanasia of mice under Home Office guidelines and samples collected.

3.6.14 Histological analysis of 3D polymer scaffolds

Histological sample preparation was conducted by Mr. Michael Glinka from the University of Southampton along with Ms Melanie McMillan and Ms Lyndsey Boswell from the histological service of the University of Edinburgh (SuRF).

Recovered *in vivo* samples (CAM assay and subcutaneous mouse model) were fixed overnight with paraformaldehyde (4%) at 4 °C and dehydrated with increasing concentrations of ethanol in a mixture of ethanol/water (50%, 90% and 100%) for 1 hour each step in an auto-processing machine Shandon Citadel 200 (Thermofisher, UK). Dehydration was completed with Histo-Clear™. Afterwards, samples were embedded twice in hot wax for 1 hour each time and processed with a further embedding under vacuum in a Vacutherm Heraeus oven (Thermofisher, UK) for 1 hour at 60 °C. Samples were sectioned (7 µm) on a microtome Microm330 (Optec, UK) and transferred to a pre-heated histological glass slides (37 °C for 2 h).

Before staining, the tissue sections were treated with 100% Histo-Clear™ (2 × 7 min) and re-hydrated with decreasing concentrations of ethanol in a mixture of ethanol/water (100%, 90% and 50%) for 2 min each step. Cell nuclei in the tissue sections were stained with Weigert's Hematoxylin according to the manufacturer's instructions. Excess was removed by washing with hydrochloric acid (1% v/v) in an aqueous ethanol solution (70% v/v) followed by further washing with water. Tissue sections were stained with Alcian blue/Sirius red and Goldner's Trichrome following a previously described protocol.[153,154]

Alician blue/Sirius red protocol. Proteoglycans were stained with Alician blue 8GX (0.5% w/v) in an aqueous acetic acid solution (1% v/v). Slides were washed with an aqueous molybdophosphoric acid (0.6% w/v) solution before staining with a solution of Sirius red F3B (1% w/v) in saturated picric acid (1.3% in water) for collagen visualisation. Excess of staining solution was removed by washing with water.

Goldner's Trichrome protocol. Cytoplasm were stained with Ponceau-Fuchsin and Axophloxin solution (0.75% xylidine ponceau, 0.25% acid fuchsin and 0.5 azophloxin 0.5% v/v) in aqueous acetic acid (1% v/v). Afterwards, slides were treated with an aqueous molybdophosphoric acid solution (0.6% w/v) prior to treating the tissue sections with Orange G solution (0.4% w/v) to visualise erythrocytes. Collagen was

stained with Light green SF solution in water (0.2% w/v). Excess of staining solution was removed by washing with an aqueous solution of acetic acid (1% v/v).

VEGFR-2 protocol. Tissue sections on histological slides were treated with heated antigen retrieval (BOND Epitope Retrieval Solution 1, pH 6, Leica Biosystems) for 20 min. After peroxidase block for 10 min, the sections were incubated with VEGFR-2 antibody (Millipore 07-1294, 1/100 dilution) at room temperature for 60 min. Slides were then incubated with anti-rabbit horseradish-peroxidase labelled polymer for 10 min before reacting with diaminobenzidine solution (1X) for 10 min. Nuclei counterstaining was performed with hematoxylin (BOND Polymer Refine Detection Kit, Leica Biosystems).

Hematoxylin and eosin protocol. H&E staining of tissue sections was carried out according to a standard operation procedure at the University of Edinburgh (SuRF).

Slides were dehydrated with ethanol and Histo-Clear with the procedure described above prior to mounting with PDX. Imaging acquisition was carried out on a Zeiss Axiovert 200 or histological scanner NanoZoomer XR.

4. Arrays of 3D polymer scaffolds *via* freeze-casting

The work presented in this section was carried out in collaboration with Dr Deepanjalee Dutta and Dr Robert Wallace. Dr Dutta performed the analysis of the orientation of the actin filaments while Dr. Wallace carried out the micro-computed tomography (micro-CT) data acquisition.

Parts of this chapter have published as:

- A. Conde-González, D. Dutta, R. Wallace, A. Callanan and M. Bradley. *Rapid Fabrication and Screening of Tailored Functional 3D Biomaterials*. **Materials Science and Engineering: C, 2020, 108, 110489**

4.1 Introduction

The extracellular matrix (ECM) consists of a vast assembly of materials with the specific predominance of any material typically dependant on the required properties of the tissue. Thus, molecules range from type I collagen to apatite-based minerals in bones, or type II collagen in cartilage often with specific 3D arrangements and, molecular gradients all playing vital roles in cellular function or control. Although significant research has been conducted to unravel this complex physiology, it still remains a key challenge in the field of tissue engineering.[155] It is clear that the conversion of physical and chemical signals into biological responses is a highly complex phenomenon with multiple convoluted factors interplaying, complicating full understanding.

Polymer microarrays have been proven to be an excellent tool for shining light on complex biological systems *via* their application in the discovery of polymeric substrates in addition to deciphering cellular and biomaterial behaviour.[156–158] However, the features of most microarray lack the 3D architectures found in tissues and as such fail to recapitulate cell behaviour in its natural environment.[159]

Arrays of 3D biomaterials have emerged as a method to overcome the limitations of current microarray technology as multiple chemical and physical properties of materials can be explored in a 3D format.[160] For example, a high-throughput approach to fabricate 3D microarrays of polymers using contact printing to spot pre-

mixed solutions of hydrogels and cells was developed to study mesenchymal stem cells (MSCs) osteogenic potential under different conditions and substrates.[161] Additionally, a remarkable array of more than 1500 unique 3D microenvironments was established to study the combined effects of gel elasticity, proteolytic degradability and chemical cues such as fibronectin, E-Cadherin and bone morphogenetic protein 4 on mouse embryonic stem cells.[162] Although hydrogels have been shown to be excellent candidates for repair of soft tissues (e.g. cartilage[35]) their mechanical properties are not suitable for stiffer tissues such as bone.[89]

384 and 96 well plates have been explored as a platform compatible with common laboratory equipment. For example, solvent casting and particulate leaching (sodium chloride) have been used to create arrays of porous polymers in 96-well plate format for the study of osteogenic properties of tyrosine-derived polycarbonates.[163] However, modulation of the quantity or size of the porogen (salt particles) is necessary to generate an array of multiple 3D structures, which is cumbersome in the case of a solid. Gas foaming (ammonium carbonate and heat) has also been shown to be an elegant approach in the fabrication of 3D polymeric scaffolds based on poly-L-lactic acid, targeting the growth of neuronal stem cells.[164] However, gases in an immiscible liquid tend to minimise their interfacial free energy forming isolated bubbles, thus, interconnectivity between pores is compromised.

To address the above challenges, a robust method to fabricate arrays of 3D polymer scaffolds was developed and put into practice, seeking to expand the current chemical and physical space of 3D biomaterials. The aim was to design a practical approach for the fabrication of multi-component polymer scaffolds in addition to tuning their mechanical properties and 3D microstructures. Thus, freeze-casting and photo-polymerisation were utilised to obtain *in situ* porous acrylate polymers in 96-well plates. This approach to fabricate arrays of 96 porous polymers allowed the control and design of a variety of 3D microstructures and offered a wide range of mechanical properties. Sitting alongside the current polymer microarray technology, this novel system reduces the gap between the successful identification of biomaterials *in vitro* and their subsequent application *in vivo*. Moreover, this new platform is not just limited to the discovery of 3D biomaterials for tissue repair but could also be exploited to explore a range of applications such as studying the biomaterial – cell interface, designing tissue models for pre-clinical drug studies and producing artificial transplantable tissue to cite but a few possibilities.

As a proof of concept, the array developed was applied towards the identification of 3D biomaterials using human osteosarcoma cells SAOS-2 and MG-63 with a push to develop vascularisation – a key step in any regeneration process. These cell lines were used as they are well established human osteoblast models that present similar alkaline phosphatase activity, genetic expression and mineralisation processes seen for osteoblasts.[165] Additionally, the high proliferation rate of both immortalised cell lines facilitates *in vitro* assays. As a starting point, "two-dimension" polymer microarrays were used to identify four polymeric substrates that were capable of supporting cell binding. Thereafter, these substrates were converted into 3D scaffolds and physically characterised. Subsequently, cell behaviour was analysed to identify the best 3D scaffolds. Finally, the combined effects of the physical properties of the 3D biomaterials and biological responses were studied to gain a deeper understanding of the cell – material interface.

4.2 Results

4.2.1 Substrates for bone cell attachment

In this chapter, the established polymer microarray technology of the Bradley group was used to fabricate microarrays of 180 different acrylate polymers prepared using inkjet printing and photo-polymerisation.[29–31,166,167] These microarrays included a range of biopolymers successfully identified within the group, and were interrogated using SAOS-2 and MG-63 cells, with polymer "suitability" assessed by counting the number of cells adhered onto each polymer feature.

This initial microarray screening (appendix A, Figure 4-1 and Figure 4-2) allowed selection four co-polymer substrates (**A-D**) that were capable of supporting/promoting cell attachment (Figure 4-3). Thereafter, these four acrylate-based lead materials were used to develop an array of 3D polymer scaffolds (Figure 4-4 and Table 4-1).

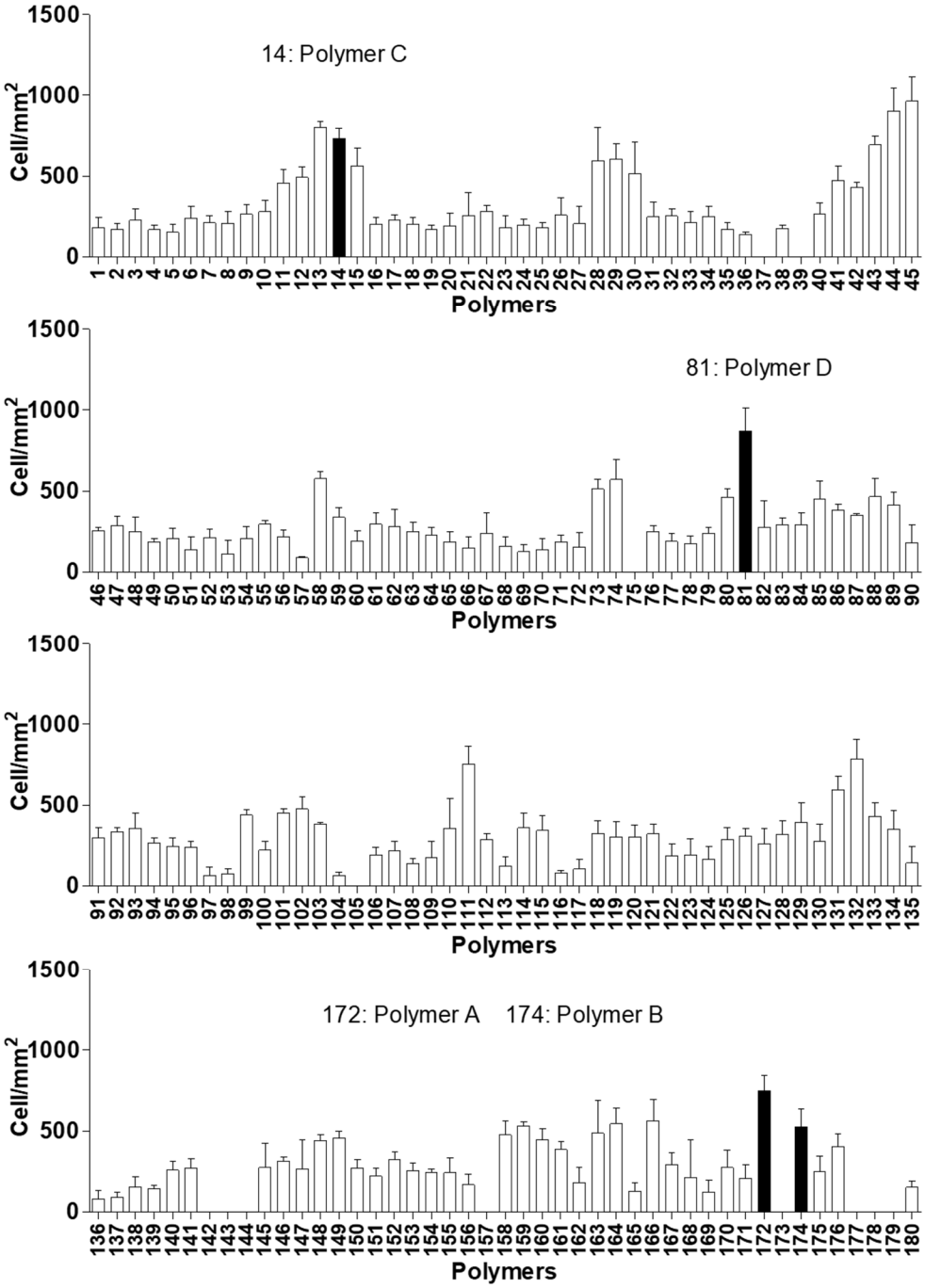

Figure 4-1. Microarray screening with SAOS-2 cells. Two microarrays of 180 acrylate polymers were synthetised *in situ* using inkjet printing and photo-polymerisation. Human osteosarcoma SAOS-2 cells (1,000,000 cells/array) were cultured for two days, fixed (PFA, 4%) and the cell nuclei stained (DAPI). Fluorescence and brightfield images were acquired by high-content microscopy. Cell attachment was analysed as the number of cells per mm^2 of polymer measured with the image processing software ImageJ-Fiji. Hit polymers (Table 4-1) are highlighted. Mean ± SD, n=4.

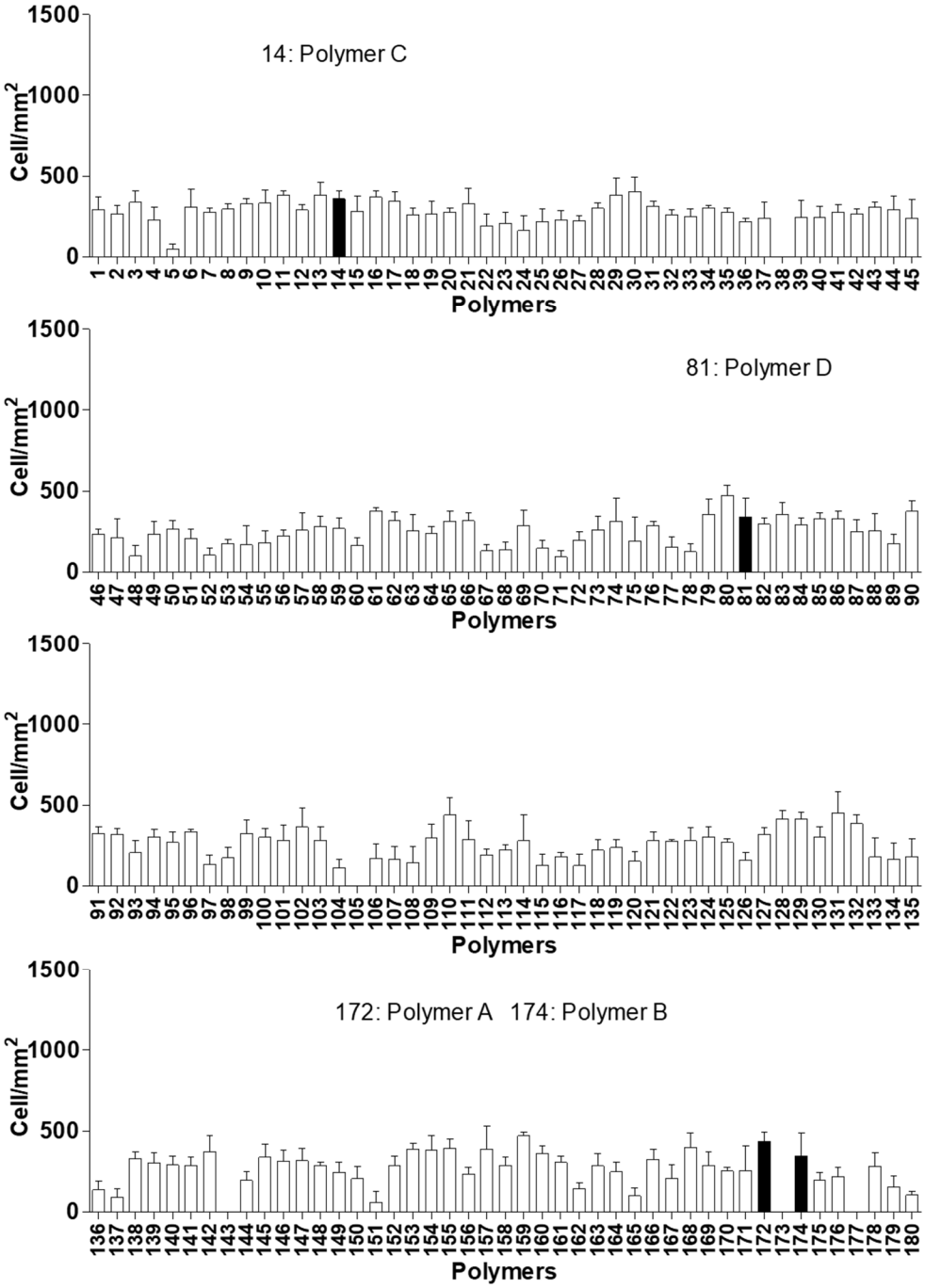

Figure 4-2. Microarray screening with MG-63 cells. Two microarrays of 180 acrylate polymers were synthetised *in situ* using inkjet printing and photo-polymerisation. Human osteosarcoma MG-63 cells (1,000,000 cells/array) were cultured for two days, fixed (PFA, 4%) and the cell nuclei stained (DAPI). Fluorescence and brightfield images were acquired by high-content microscopy. Cell attachment was analysed as the number of cells per mm^2 of polymer measured with the image processing software ImageJ-Fiji. Hit polymers (Table 4-1) are highlighted. Mean ± SD, n=4.

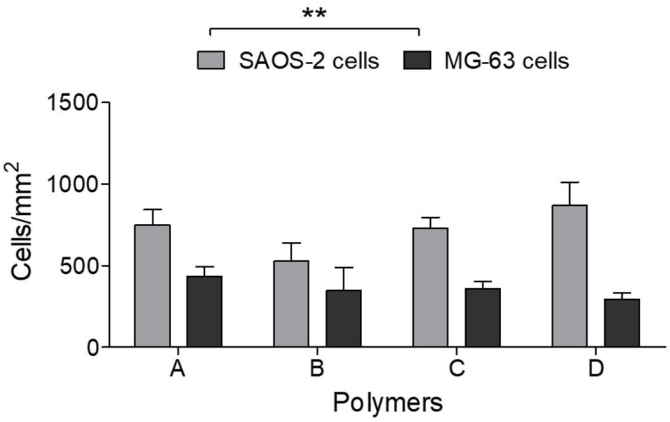

Figure 4-3. The leads selected from the microarray screening of 180 polymers. The number of SAOS-2 and MG-63 cells per mm^2 of polymer after 2 days of incubation (seeding $1x10^6$ cells/array) is seen on the Y-axis. Two tailed t-test (** $p \leq 0.01$). Mean ± SD, n=4.

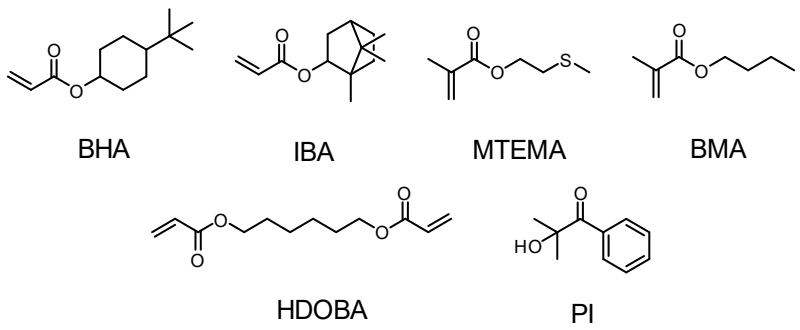

Figure 4-4. Monomers, cross-linker and photo-initiator that were used to fabricate the four co-polymers identified from the microarray screen. 4-*tert*-butylcyclohexyl acrylate (BHA), isobornyl acrylate (IBA), 2-(methylthio)ethyl methacrylate (MTEMA), butyl methacrylate (BMA), the cross-linker 1,6-hexanediol diacrylate (HDOBA) and the photo-initiator (PI) hydroxy-2-methylpropiophenone.

Table 4-1. Polymers selected from the microarray screening.

Polymer	Monomers (mol %)		CL (mol %)	PI (mol %)
	1	2		
A	BHA (72)	-	18	10
B	IBA (72)	-	18	10
C	BHA (36)	BMA (36)	18	10
D	IBA (36)	MTEMA (36)	18	10

4.2.2 Development of a 3D polymer array and characterisation

I. Fabrication strategy

An array of 3D polymer scaffolds was created in flat bottomed 96-well plates *via* UV polymerisation of frozen porogenic solutions. The solutions were obtained by mixing the porogenic solvent (DMSO) with the appropriate polymerisation mixture (Table 4-1). As an example, **P80** scaffolds were obtained by combining DMSO (80% v/v) with the suitable polymerisation mixture (20% v/v).

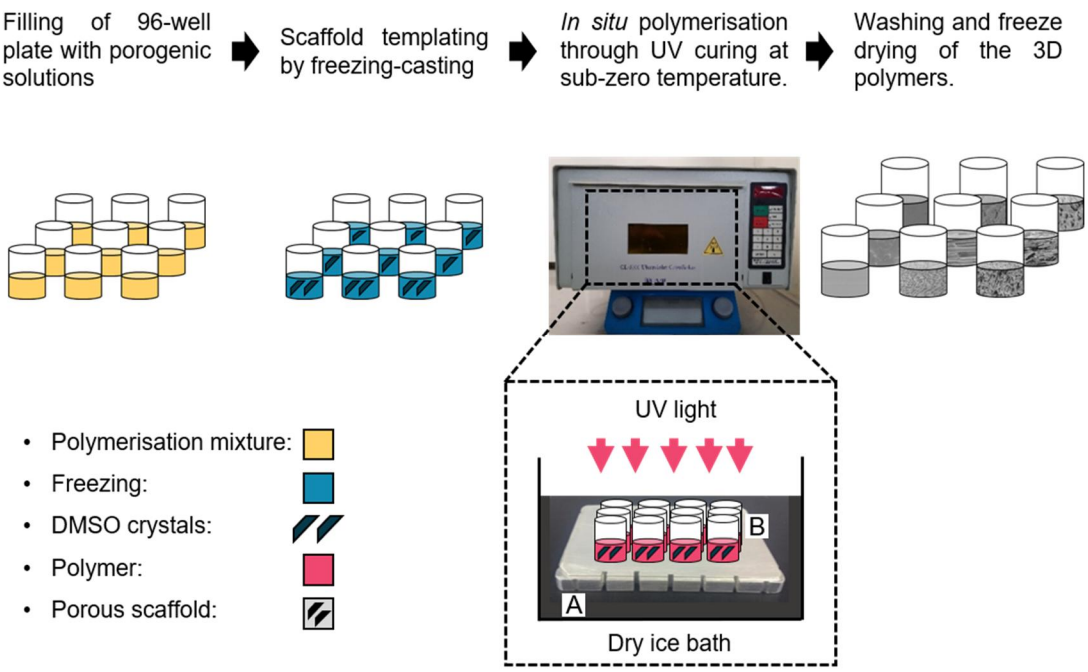

Figure 4-5. Arrays of 3D polymer scaffolds formed *via* freeze-casting. Development of a four-step process to obtain arrays of 3D polymer scaffolds. Templating (formation of a solid phase rich in DMSO), UV polymerisation and drying revealed the porous structure. A dry ice bath and an aluminium cooling block (A) were used to keep the scaffold frozen during the UV-polymerisation of the arrays (B).

The porogenic solutions (80 µL/well) were subjected to freezing (Figure 4-5). Below the melting temperature of DMSO, a phase separation (templating) in the porogenic solution gives rise to two distinct phases: a phase rich-in-solvent (pores) and a phase rich-in-polymer (scaffolds). Subsequent UV polymerisation was carried out on top of a dry-ice-bath and an in-house aluminium-cooling block (127 mm length × 85 mm width × 10 mm height). Washing and freeze-drying revealed the structure of the porous scaffolds.

The array of 3D polymer scaffolds generated was the result of both the combination of different polymer compositions and porosities. Freeze-casting allowed tunability of the 3D architecture using different levels of DMSO or the application of different cooling gradients during templating. For example, **P80-A** scaffolds (**polymer A** from above with 80% v/v DMSO) obtained in the presence or absence of freezing illustrates some of the morphological variations that were explored in the array (Figure 4-6).

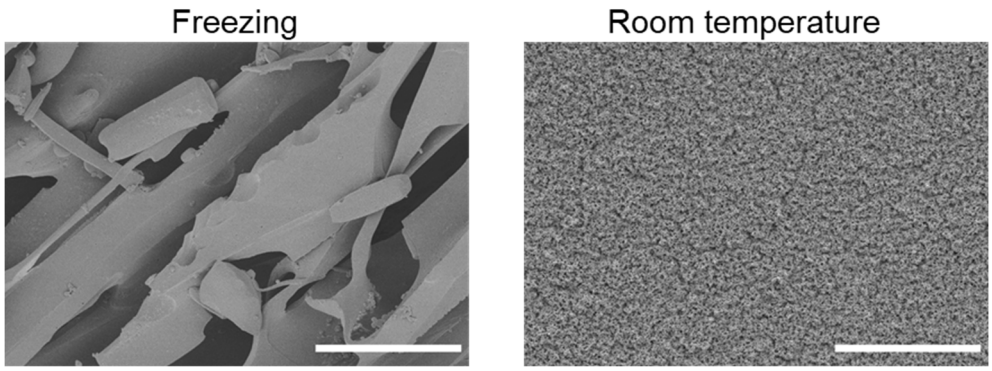

Figure 4-6. Effect of the templating temperature on the formation of pores. Representative SEM images of polymer **P80-A** in case of cooling the sample (freezing) before polymerisation and without cooling. Scale bar = 100 μm.

II. Effect of the cooling gradient on the porous structure

The effect of a cooling gradient was analysed for scaffolds with high porosity (**P80**) for the four **polymers A-D** prepared in the wells of a 96-well plate and analysed using scanning electron microscopy (SEM).

Three different cooling methods (Figure 4-7) were explored so-called: fast, medium, slow with polymerisation at room temperature used as a control.

- Fast cooling: a dry ice bath (-80 °C) for 15 min.
- Medium cooling: a freezer (-20 °C) for 20 h.
- Slow cooling: a fridge (5 °C) for 16 h and a freezer (-20 °C) for 4 h.

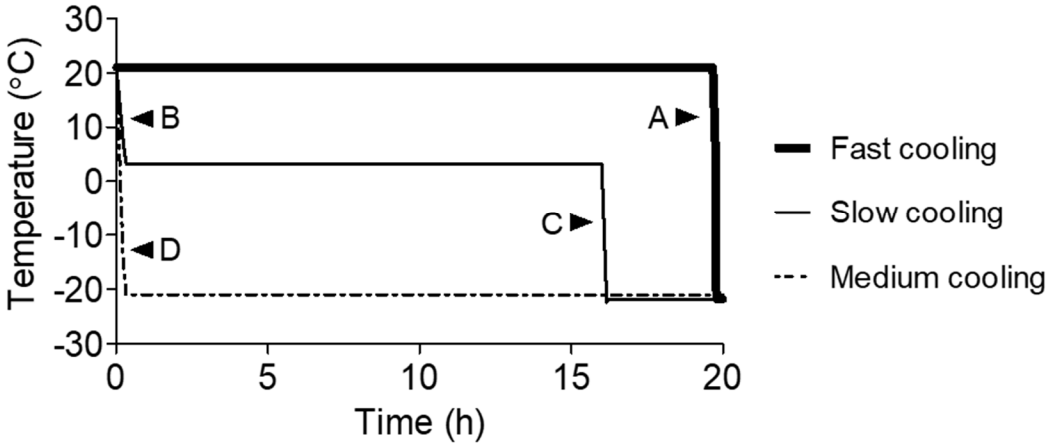

Figure 4-7. Cooling methods explored. A) Fast cooling (cooling gradient 15.6 °C/min). B and C) Slow cooling (1.0 °C/min and 2.6 °C/min). D) Medium cooling (2.5 °C/min). Wireless thermometer (Testo 905i, Germany) was used to record the temperature and time.

After the different cooling stages, the arrays were placed on top of an aluminium cooling block in a dry ice bath and subsequently UV polymerised (30 min). After photo-polymerisation, all the scaffolds were washed and lyophilised (Figure 4-5).

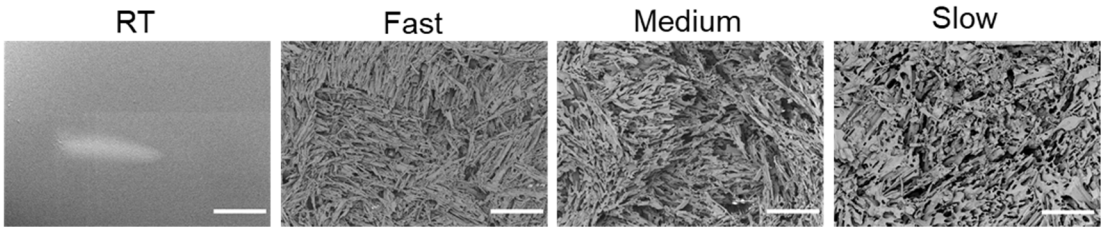

Figure 4-8. SEM images of the scaffolds **P80-B** with the three cooling gradients. Scale bar = 500 µm.

Illustrative images for scaffolds **P80-B** exemplified the morphological changes that the different cooling gradients produced. Scaffolds fabricated at room temperature showed a surface devoid of large pores with no phase separation between the DMSO and the polymerisation mixture. The other scaffolds after the cooling procedure were highly porous (Figure 4-8).

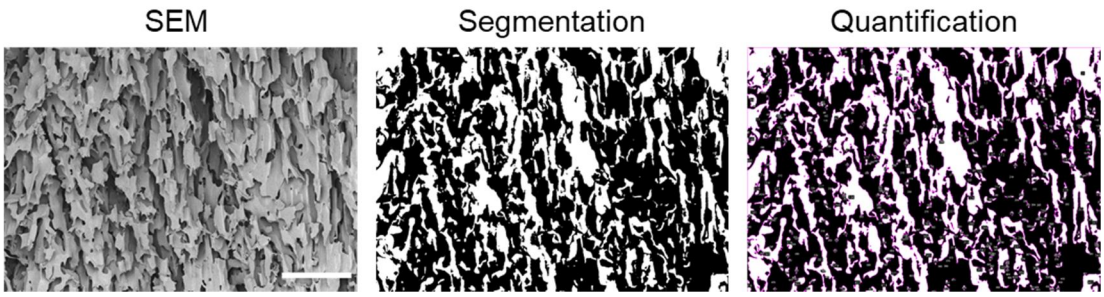

Figure 4-9. Analysis of the SEM images using ImageJ-Fiji. SEM images were binarised (thresholding plugin) and filtered (median plugin, 2 pixels) to separate the polymer from the porous structure. The segmented images were analysed (analyse particles plugin) to quantify the pore descriptors. Scale bar = 500 µm.

ImageJ-Fiji was used to quantify the morphological changes that the different cooling processes produced. To do so, porosity (%), as a percentage of area with pores, and the average Feret diameter (µm) of those pores were used as pore descriptors (Figure 4-9).

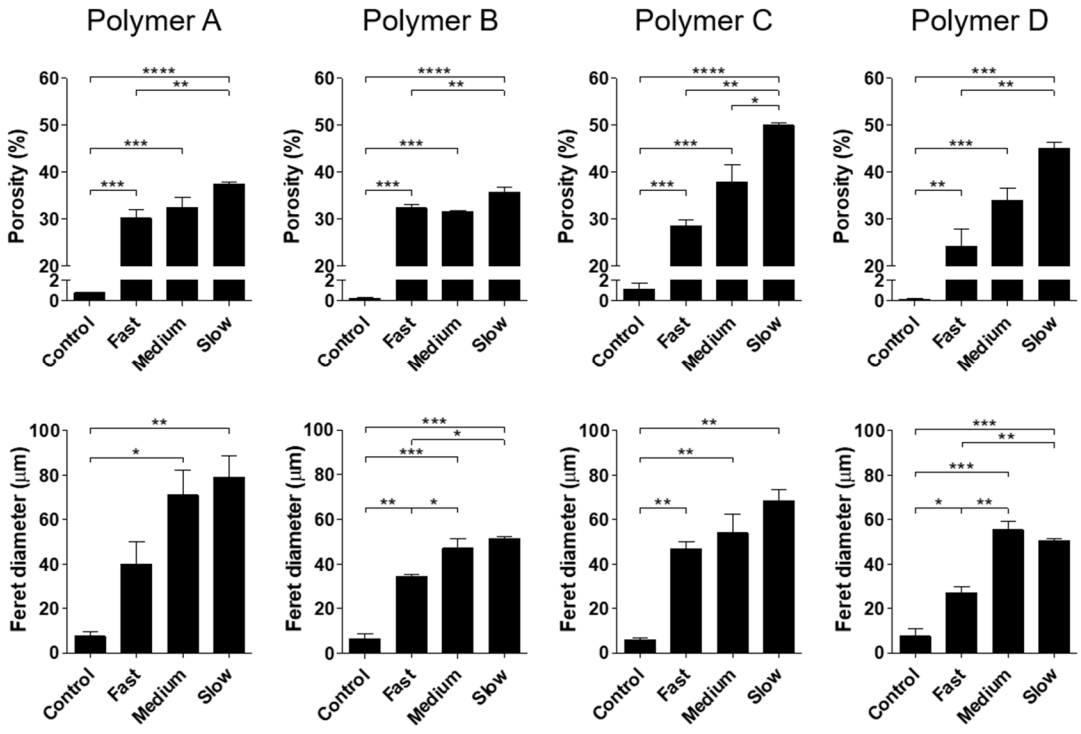

Figure 4-10. Effect of the cooling gradient on the polymer scaffolds. Porosity (%) and Ferret diameter (µm) for **polymers A-D**. Polymerisation at room temperature was used as a control. One-way ANOVA with Bonferroni post-test (* $p \leq 0.05$, ** $p \leq 0.01$, *** $p \leq 0.001$ and **** $p \leq 0.0001$). Mean ± SD, n=2.

Analysis of the effect of the cooling rate on the **P80** scaffolds of **polymers A-D** confirmed that the 3D architecture could be controlled by the templating temperature (Figure 4-10). Generally, the porosity (%) and Feret diameter of the scaffolds increased progressively when the cooling stage changed from “fast” to “slow”. Moreover, very low porosity and Feret diameter were observed in control scaffolds. For example, the porosity for **P80-A** scaffolds with “fast” and “slow” cooling were 30% and 38% ($p \leq 0.01$) and their Feret diameter were 40 µm and 79 µm respectively.

In summary, the “slow” cooling (5 °C for 16 hours and -20 °C for 4 hours) approach was selected going forward in order to maximize the formation of pores.

III. Effect of porogenic solvent on the scaffold structure

The ratio of the porogenic solvent (DMSO) to the polymerisation mixture was also used to control the architecture of the porous polymers with the “slow” cooling method. Three levels of DMSO (0% v/v, 60% v/v and 80% v/v) and **polymers A-D** were combined to give arrays with porous scaffolds (**P60** and **P80**) and their non-porous controls (**P0**).

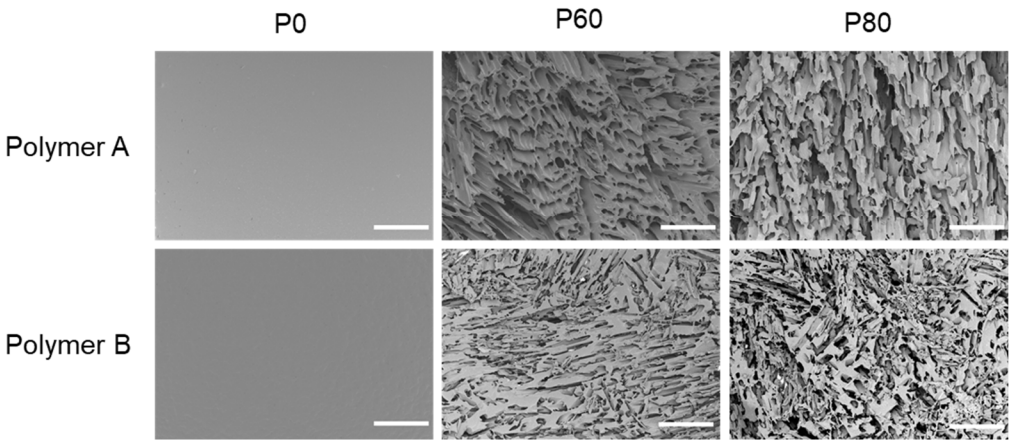

Figure 4-11. SEM images of the **polymers A** and **B** obtained with different concentrations of porogenic solvent: P0 (0% v/v), P60 (60% v/v) and P80 (80% v/v) and the slow cooling method. Scale bar = 500 µm.

SEM images of scaffolds **P0**, **P60** and **P80** of **polymers A** and **B** showed the effect of the concentration of porogenic solvent in the porous structure. The images showed that there were no pores (**P0**) in absence of DMSO and with the increase in the

concentration of DMSO there was a progressive increase in the porous structure (Figure 4-11). Quantification of the morphological descriptors revealed the enhancement of these descriptors when the concentration of DMSO was increased (Figure 4-12). For example, the porosity of scaffolds **P0-A** and **P60-A** increased from approximately 1% to 31% ($p \leq 0.0001$) respectively and further rose to 38% ($p \leq 0.001$) for **P80-A**. Moreover, the Feret diameter increased from 5 µm for **P0-A** to more than 70 µm for **P60-A** and **P80-A** ($p \leq 0.01$).

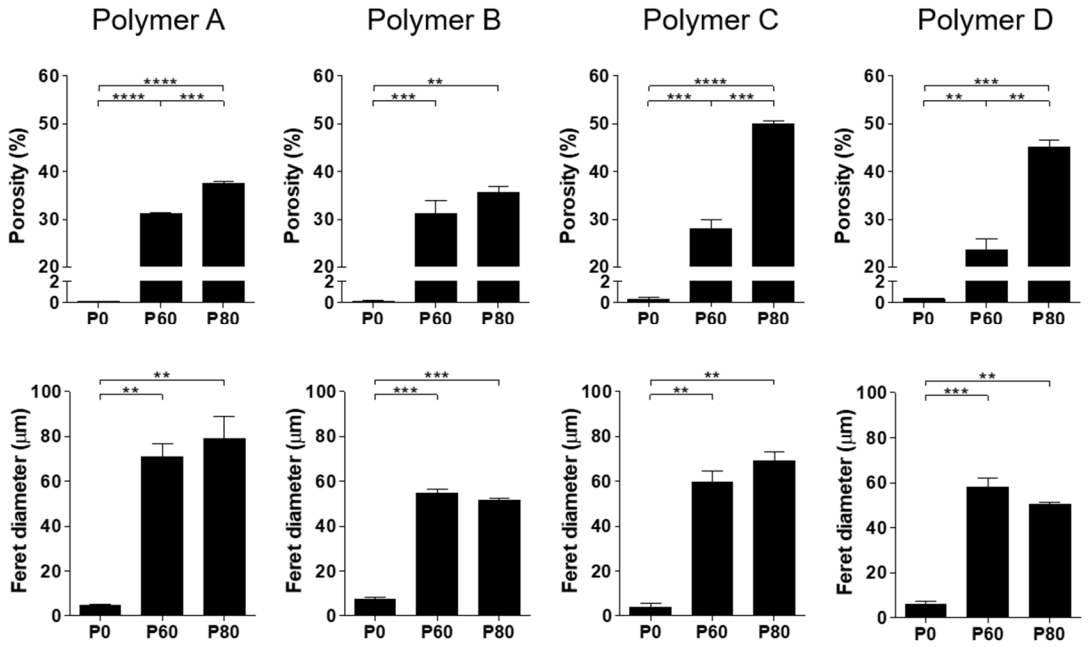

Figure 4-12. Effect of the concentration of DMSO on the array of polymer scaffolds. Analysis of influence of the porogenic solvent (**P0**, **P60** and **P80**) on the porosity (%) and Ferret diameter (µm) for **polymers A-D**. One-way ANOVA with Bonferroni post-test (* $p \leq 0.05$, ** $p \leq 0.01$, *** $p \leq 0.001$ and **** $p \leq 0.0001$). Mean ± SD, n=2.

The analysis of the distribution of the Feret diameter of the 12 scaffolds (**P0**, **P60** and **P80** for **polymers A-D**) allowed a deeper insight into the effect of the concentration of DMSO on the porous structure (Figure 4-13). Although the average size of the pores ranged from 50 µm to 70 µm for medium (**P60**) and high porosity (**P80**) scaffolds, the distribution of the Feret diameter showed the presence of pores larger than 100 µm which is deemed to be important for biological applications. For example, scaffolds **P60-A** and **P80-A** had voids of approximately 750 µm and 1000 µm respectively for 99% of the pores.

The distribution of the size of the pores were classified into three groups namely - pores smaller than 50 µm, pores between 50 µm and 300 µm and pores bigger than 300 µm (Figure 4-14). The first group (< 50 µm) represents pores that are too small to allow cell migration into the scaffolds but could facilitate the diffusion of nutrients and the removal of metabolic waste. The pores from 50 µm and 300 µm include the range of pores that are considered ideal for polymer scaffolds as these pores allow the cells to acquire a “3D morphology”. Pores bigger than 300 µm are viewed as important candidates for allowing cell migration into deeper layers of the polymer scaffolds.[22,112]

Independent of the polymer composition, **P0** scaffolds had no significant pores. **P60** scaffolds showed porosities that varied from 24% to 31 % with about 29% of the pores in the optimal range of pores (from 50 µm to 300 µm) and about 3% of the pores bigger than 300 µm. Moreover, in the case of **P80** scaffolds the porosity varied from 36% to 50% with the optimal range of pores decreasing 22% compared to **P60.** However, a slight increase in the pores larger than 300 µm was also observed.

Generally, it was observed that increasing the concentration of the porogenic solvent 0%, 60% and 80% v/v DMSO produced an increase in the frequency of large pores.

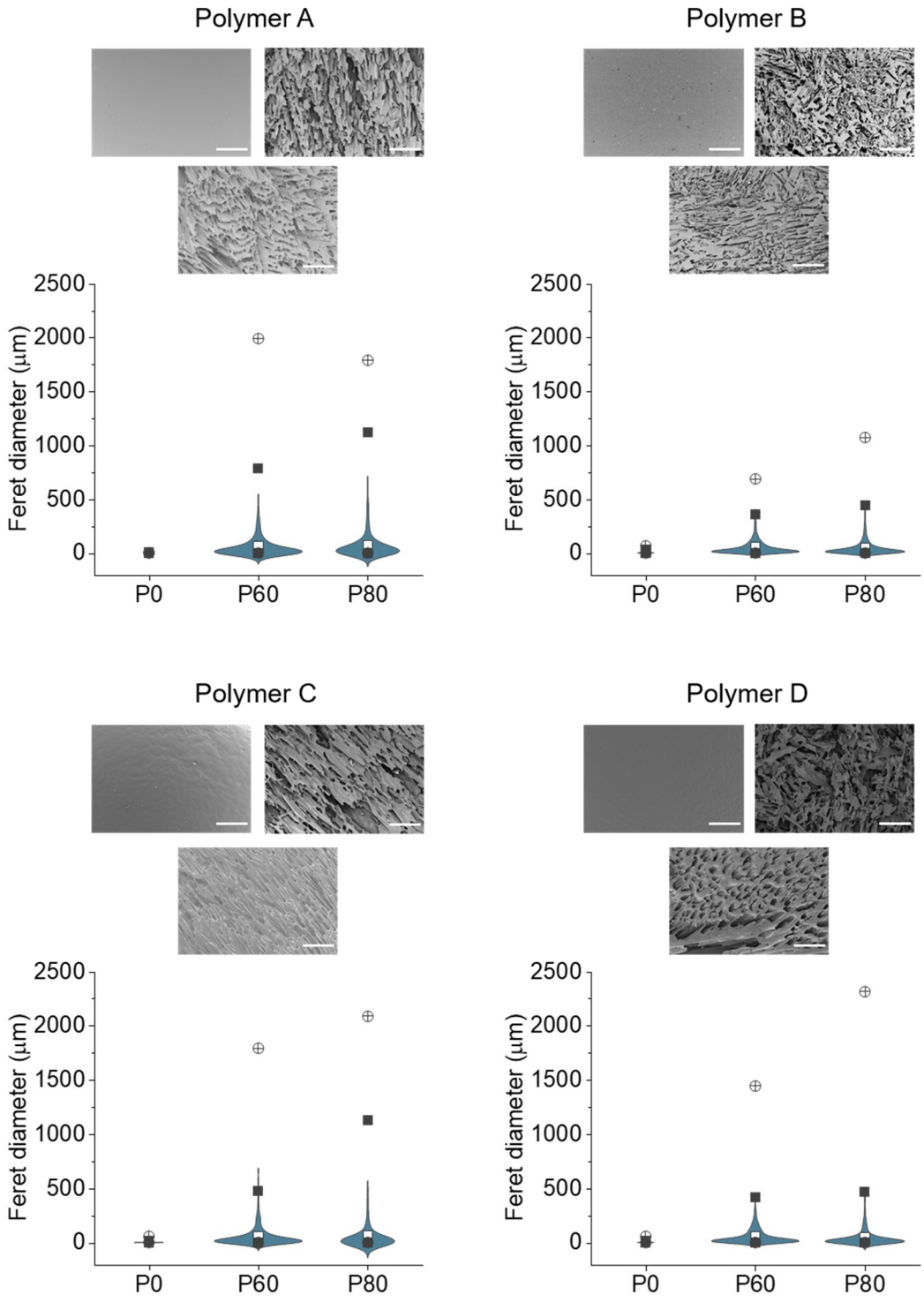

Figure 4-13. Effect of the DMSO level on the polymer scaffolds. Analysis of the distribution of the Feret diameter (µm) for four polymers (**A-D**) and three levels of porogenic solvent (**P0-P80**). Mean (white square), maximum and minimum values (white circles), 1% and 99% percentile (black squares), n=2. Representative SEM images of the scaffolds analysed. Scale bar = 500 µm.

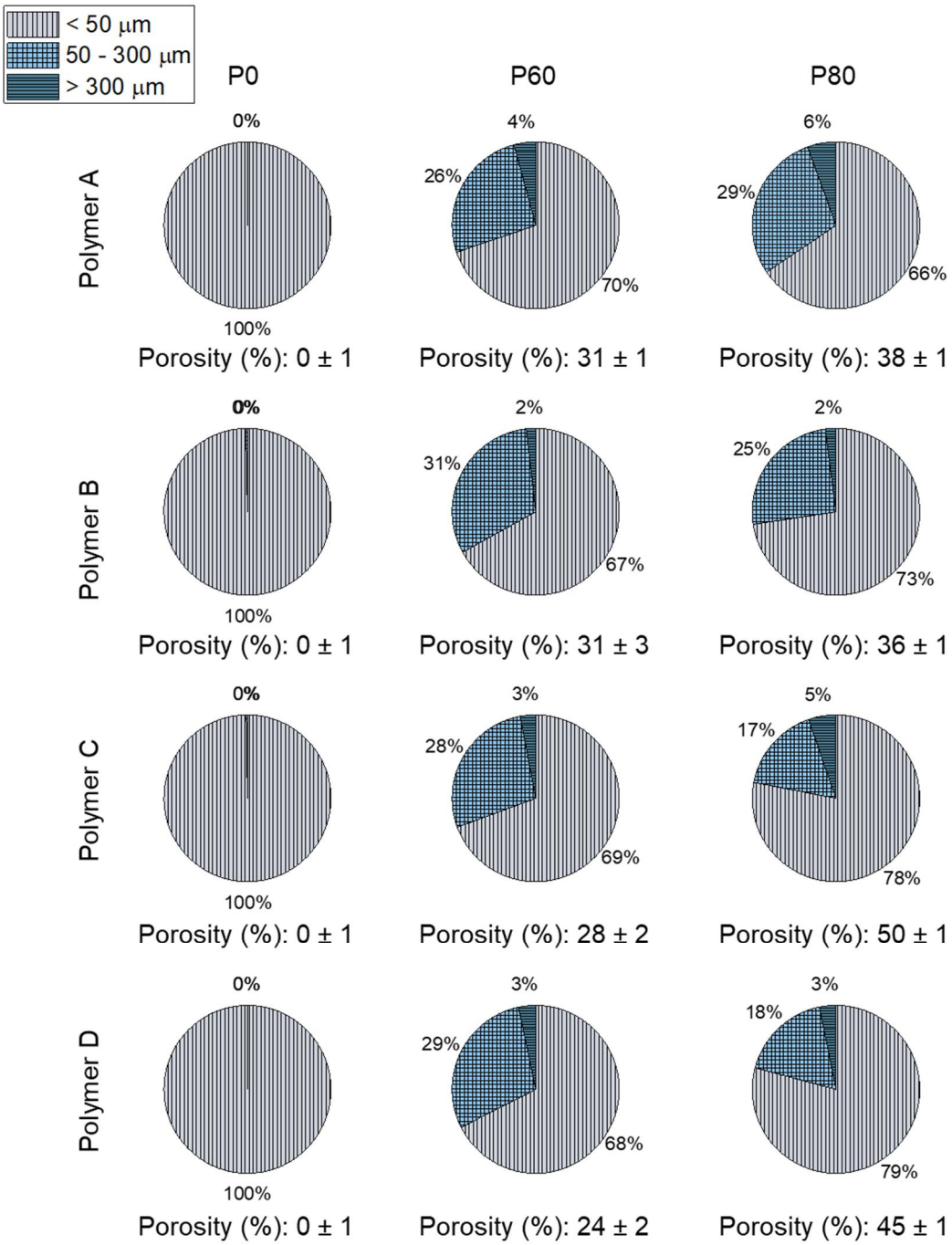

Figure 4-14. Effect of the level of DMSO on the polymer scaffold porosity. Analysis of the combined effect of the porogenic solvent on the porosity (%) and distribution of the Feret diameter (µm) for three concentration of DMSO (**P0-P80**) and four polymers (**A-C**). The size of the pores was grouped to less than 50 µm, between 50 µm to 300 µm and greater than 300 µm, n=2.

IV. Morphological analysis of the array of 3D polymer scaffolds

A high-content screening approach using micro-CT was used to allow the morphological characterisation of 12 polymer scaffolds in a facile manner, while involving minimal sample preparation. An array was prepared in rectangular sections of 96-well plates (2×2 wells) that were stacked together to form a cuboid of 12 polymer scaffolds (2×2×3 wells). The array of 3D polymer scaffolds was prepared with the "slow" cooling approach employing the four **polymers A-D**. Six different concentration of the porogenic solvent (from 0% to 85% v/v) were explored giving the so-called scaffolds **P0**, **P20**, **P40**, **P60**, **P80** and **P85** to gain an understanding of the effect of the DMSO concentration on the morphological characteristics of 3D scaffolds.

Representative stacks of the array of 24 polymer scaffolds displayed the expected reduction of polymer density as a result of the increase of the level of DMSO (Figure 4-15). Abundant quantities of large pores (larger than 100 μm) in the transverse and coronal planes of the scaffolds **P60** and **P80** were observed with patterning of the polymer structure in some scaffolds e.g. **P80-B** and **P60-C**.

3D images of the micro-CT data (rendering of the longitudinal section of wells with polymer scaffolds) were obtained with the software Imaris (Figure 4-16 and Figure 4-17). The scaffolds covered the entire surface of the well and had a concave surface as a consequence of their liquid origin. The majority of the polymers had enlarged pores as the volume of DMSO increased (from 0% to 85% v/v) demonstrating the effect of the porogenic solvent. The micro-CT of **P0** scaffolds showed a compact structure of a polymer without pores. In the case of **P20** and **P40** scaffolds pores were seen at the bottom of the scaffolds. The **P60**, **P80** and **P85** scaffolds had a uniform, open, porous structure; however, **P85** scaffolds displayed a broken and uneven polymer structure suggestive of a fragile nature.

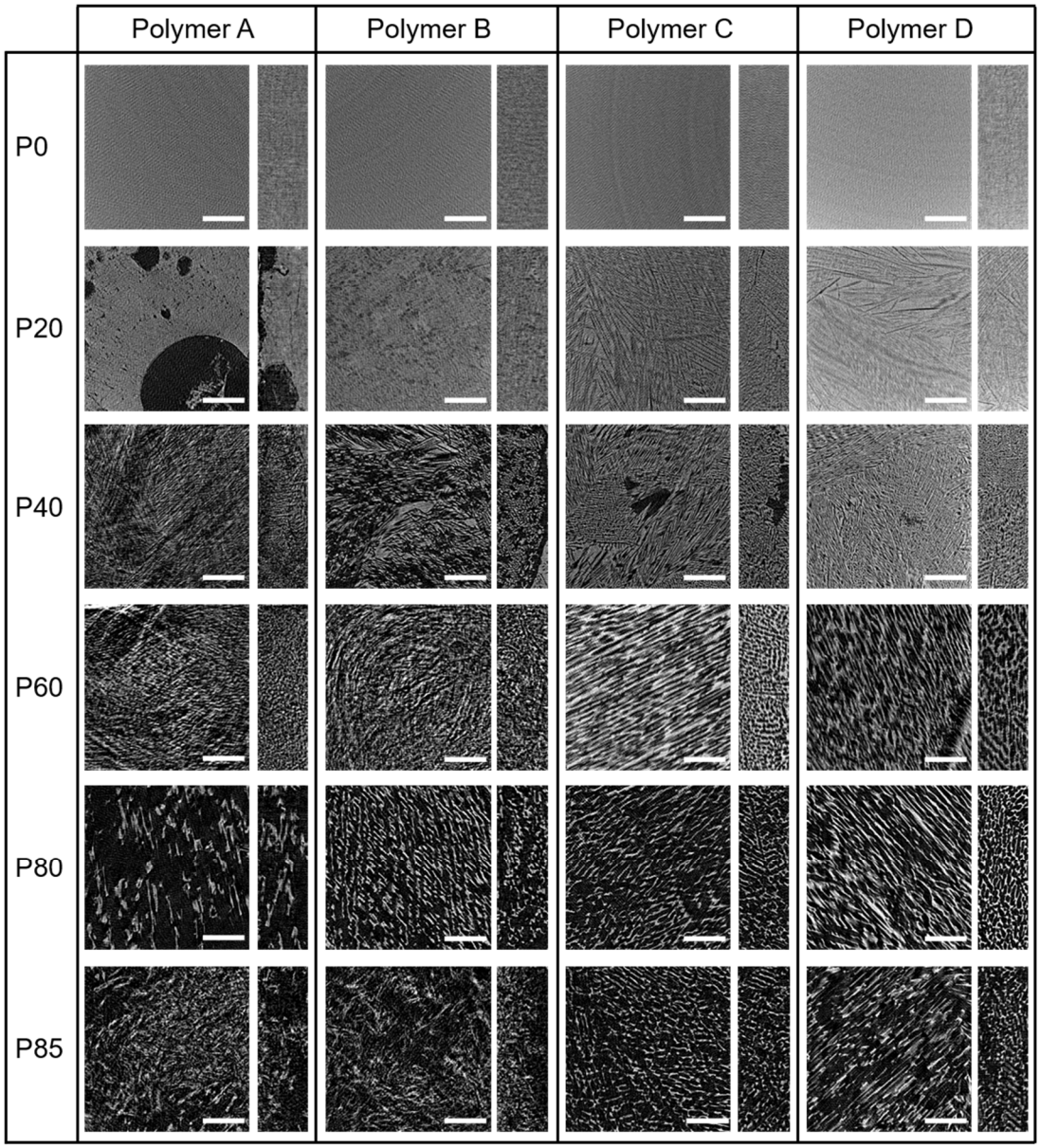

Figure 4-15. Micro-CT analysis of the 24 3D polymer scaffolds. Images of a cross-section (square, left) and longitudinal section (rectangle, right) of **polymers A-D** fabricated with increasing levels of DMSO (**P0-P85**). The polymer is shown in white and grey with the pores in black. Scale bar = 1 mm.

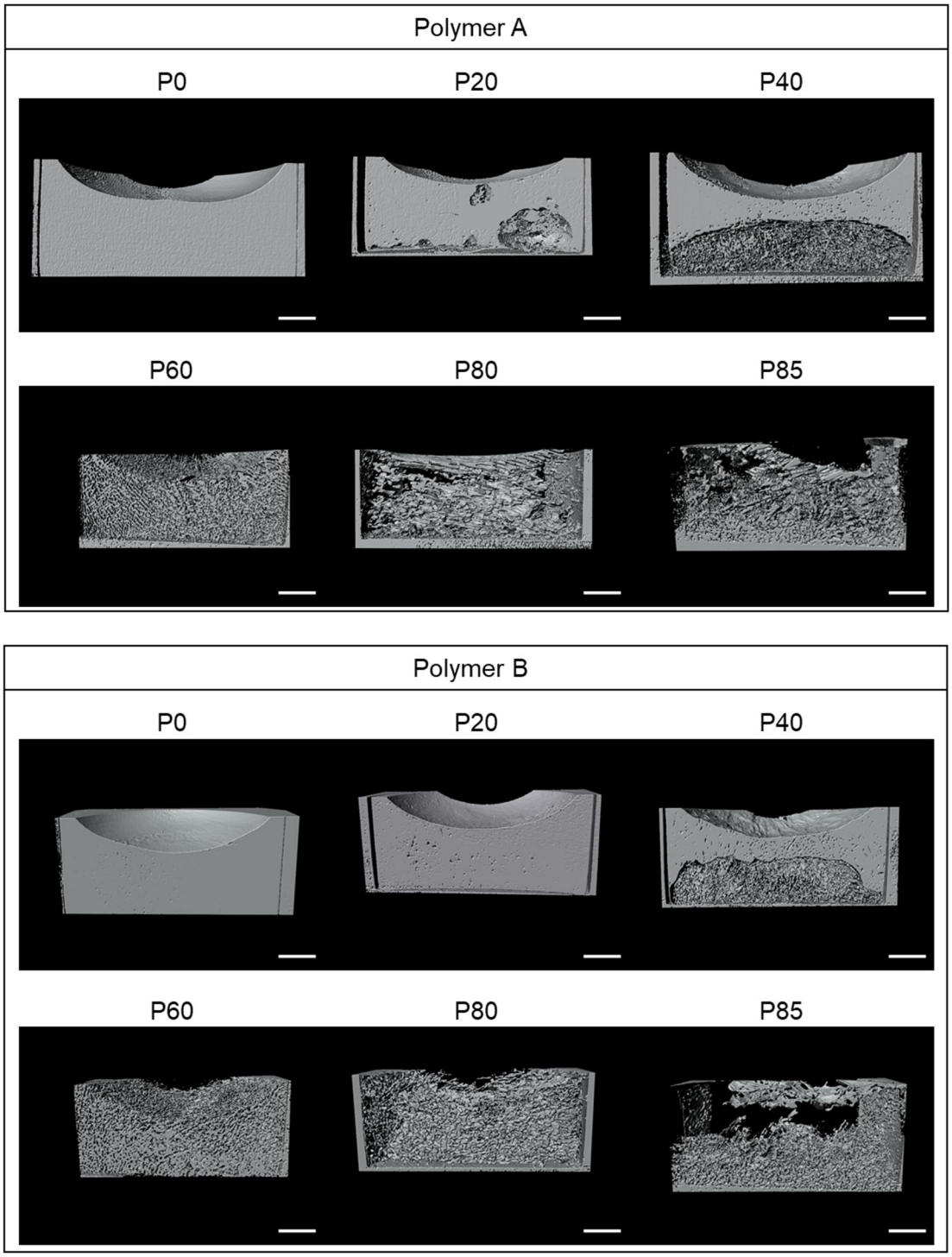

Figure 4-16. 3D images of the micro-CT data of wells of the 3D polymer scaffolds (longitudinal sections) of **polymers A** and **B** varying the level of DMSO (**P0-P85**). Scale bar = 1 mm.

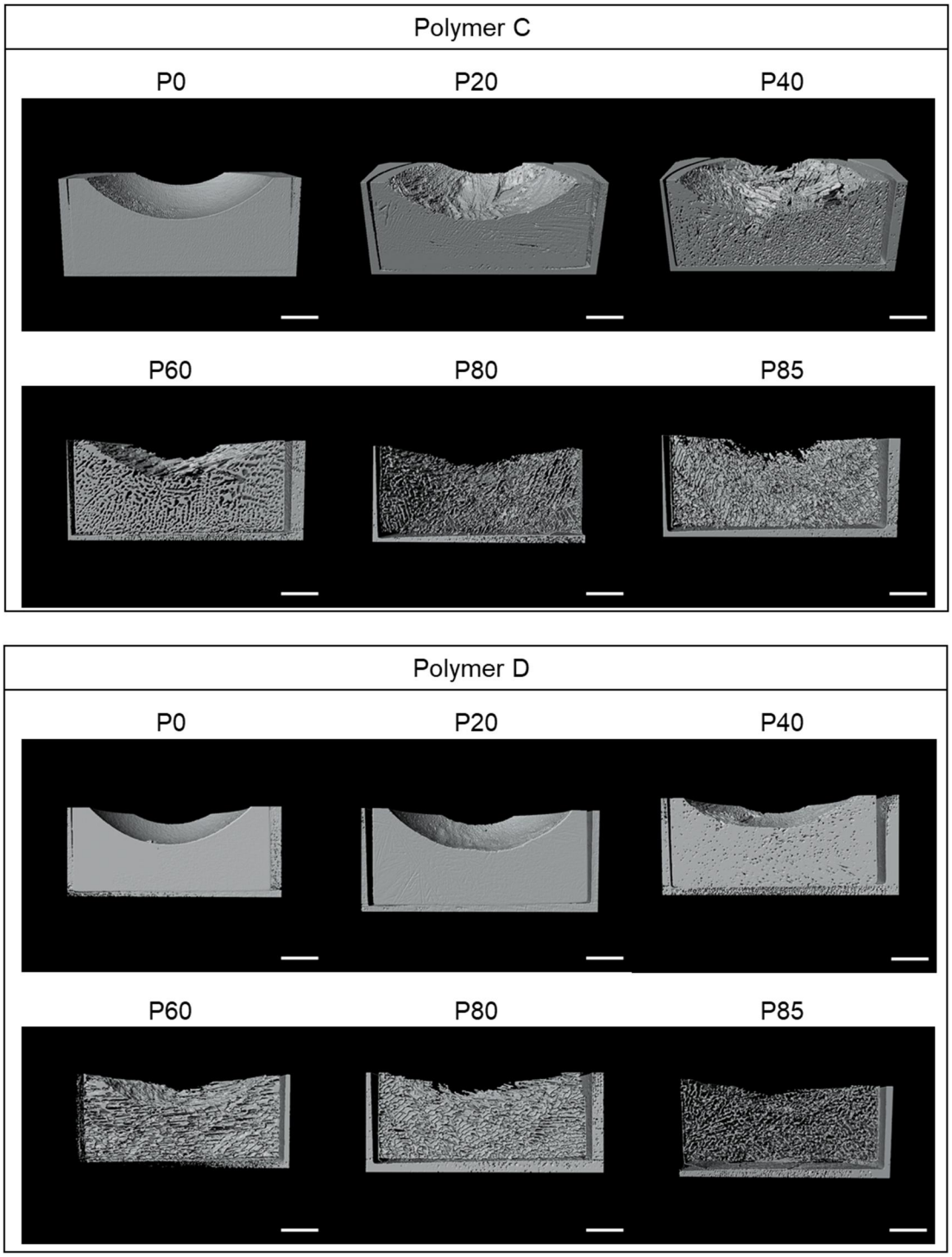

Figure 4-17. 3D images of the micro-CT data of wells of the 3D polymer scaffolds (longitudinal sections) of **polymers C** and **D** varying the level of DMSO (**P0-P85**). Scale bar = 1 mm.

The analysis of the CT data using the ImageJ-Fiji plugin BoneJ[134] (image processing software) of the 3D polymer scaffolds showed the enhancement of porosity with an increase in porogenic solvent independent of the polymer composition (Figure 4-18). For example, **P0** (0% DMSO and 100% polymerisation mixture) had no porosity whereas for **P80** had a porosity of 81% for the four polymers explored.

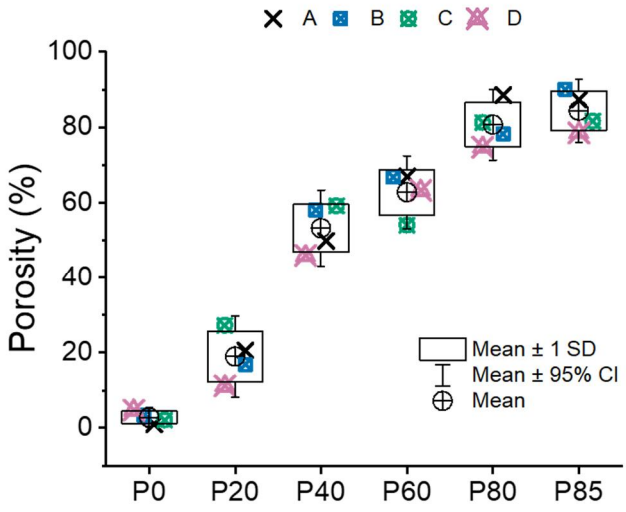

Figure 4-18. Analysis of the 3D polymer scaffolds using micro-CT. Effect of the level of DMSO (from 0% to 85% v/v) on the porosity (%) of **polymers A-D** analysed using ImageJ-Fiji.

The morphological characteristics of the 3D polymer scaffolds were further analysed using the scaffolds having medium (**P60**) and higher porosities (**P80** and **P85**) for the four polymers. The percentage of "open" pores (pores connected to the surface of the volume analysed) and the size of the pores were used to describe the properties of the polymer scaffolds (Figure 4-19).

The "open" porosity analysis defined as pores that were connected to the surface of the volume of interest (volume measured) confirmed that the pores were interconnected (porosity and open porosity were similar) and "open" to the surface. For example, the open porosity of **P60-A** was 66% and increased to 88% for **P80-A** and decreased to 78% for **P85-A**.The largest average diameter of the pores was identified in the **P80** scaffolds (238 μm) with a slight decrease for the **P60** scaffolds independent of the polymer composition. However, the **P85** scaffolds showed an important characteristic in terms of reduction of the average pore diameter (144 μm) which could be attributed to possible collapse of the weaker polymer network.

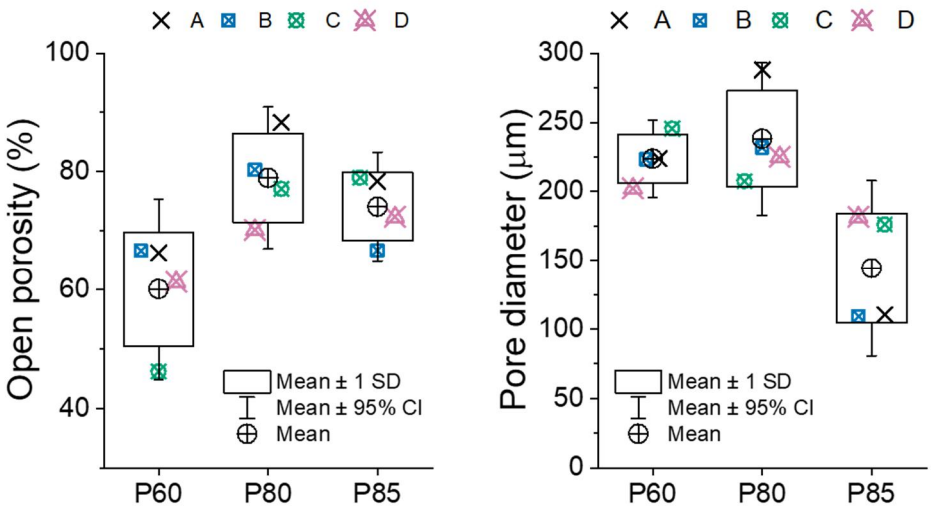

Figure 4-19. Analysis of the 3D polymer scaffolds (**A-D**) using micro-CT. Effect of the level of DMSO (from 60% to 85% v/v) on the open porosity to the edges of the volume of interest and the diameter of the pores (µm) using the software CTAn.

The size of the interconnected pores (throats) is one of the key characteristics in 3D polymer scaffolds. The diameter of the pore throats were modelled (with the software AVIZO) in order to shine light on this complex system.[168,169] 3D images were obtained and polymer/pores were defined (thresholding) using the micro-CT data. Thereafter, the pores were differentiated using a watershed algorithm where continuity of each pore was determined. The position where two adjacent pores narrowed was considered as a throat and its size was the interconnection diameter or throat diameter. These data were visualised constructing a model where the pores were represented as spheres of equivalent diameter to the size of the pore modelled while the position and size of the throats were shown with cylinders of equivalent size. Additionally, a colour map for the throat diameter was also included (Figure 4-20 and Figure 4-21).

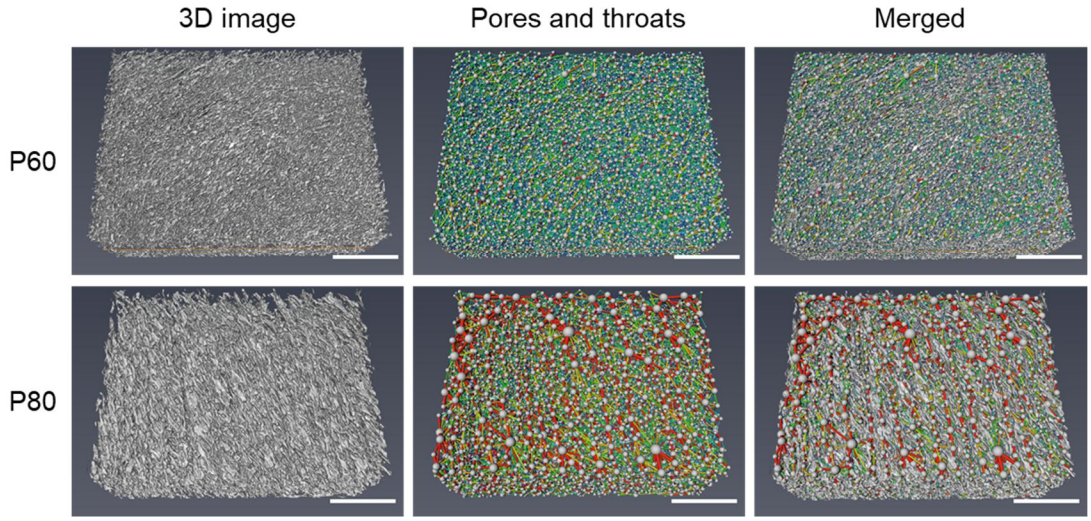

Figure 4-20. 3D images of micro-CT data and the model of pore connectivity for **polymer B** with medium (**P60**) and high (**P80**) porosity. Micro-CT data was modelled to measure the pore diameters and their interconnection pore diameters or throat diameters. Pores and throats are showed as spheres and coloured lines with the sphere diameters and line thicknesses being proportional to the pore and throat sizes. Additionally, a colour scale was used to classify the diameter of the throats (large diameters were represented in red and small diameters in blue). Scale bar = 1 mm.

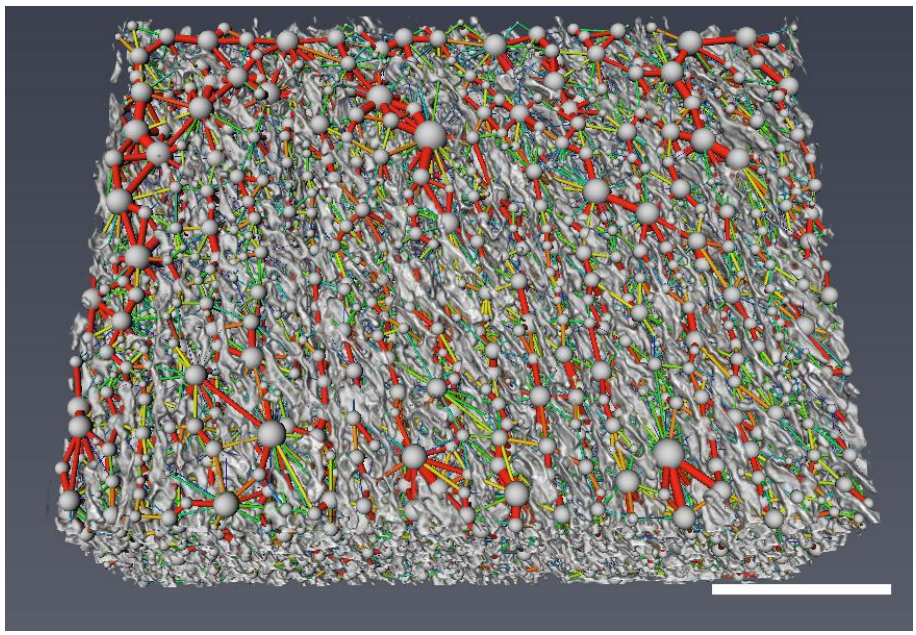

Figure 4-21. Expansion of the pores and throats for the 3D model developed using the micro-CT data of the scaffold **P80-B**. Scale bar = 1 mm.

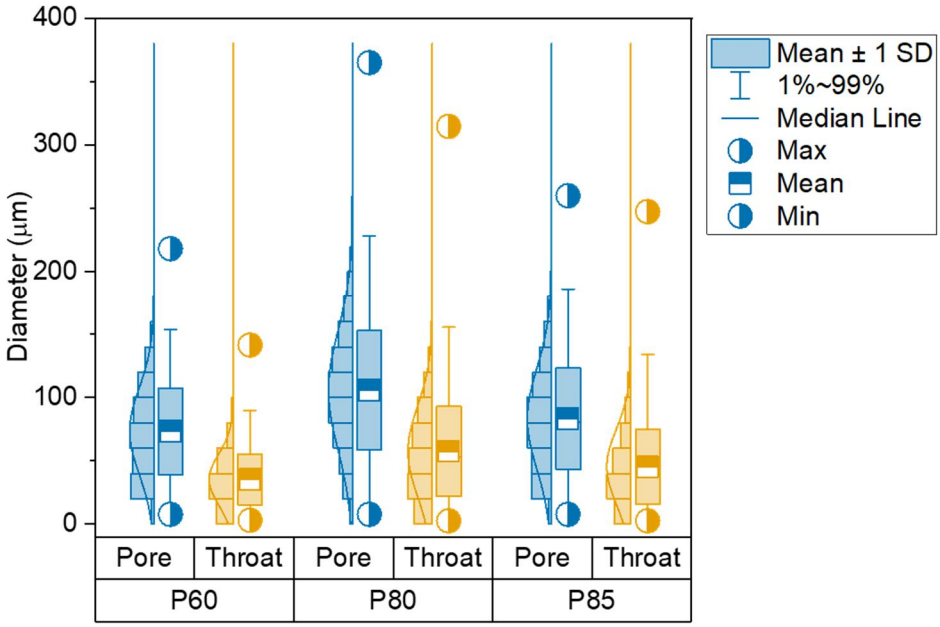

Figure 4-22. Micro-CT analysis of the pore and throat diameter of the 3D **polymer B** (**P60**, **P80** and **P85**).

The analysis of the pore and throat models using AVIZO (Figure 4-22) corroborated previous analysis (Figure 4-19). The largest pore and throat diameters were achieved for scaffolds fabricated with 80% of DMSO (**P80**) in the case of the **polymer B**. The average pore diameter was 100 µm with the 99% of the pores smaller than 200 µm. Pore throats were shown to be around 50 µm with 99% smaller than 150 µm. Pore and throat diameter larger than 100 µm (cut-off target for cells in 3D) were confirmed for the three level of porosity explored (**P60**, **P80** and **P85**) with the largest quantify of in the **P80** scaffold.

Overall, the control of the DMSO level was shown to tune the morphological characteristics of the 3D polymer scaffolds. Scaffolds having an open porosity, adequately interconnected porous network and large pores/throats were obtained by increasing the level of the porogenic solvent. Additionally, the average diameter of the pores in the scaffolds with large porosity was shown to be in the selected target range (100 µm to 300 µm), which can lead to cell migration into the scaffolds (cells in 3D) in addition to efficient nutrient and waste diffusion.

V. Mechanical analysis of the array of 3D polymer scaffolds

Polymers A-D with low (**P0**), medium (**P60**) and high (**P80**) porosity were mechanically characterised using indentation, which allows the mechanical characterisation of a small sample like a scaffold or a piece of bone by applying a force with a punch onto its surface.[103]

The 3D scaffolds formed a meniscus on their surface as a result of their liquid origin. This would produce aberrations in the mechanical testing as the contact between the indenter and the surface would not be homogenous. Thus the 3D polymer scaffolds were thus scaled-up from 80 µL to 300 µL using the slow cooling approach and photo-polymerisation in a polystyrene mould 12×12 mm in order to minimise the meniscus (Figure 4-23).

The scaffolds were then tested, hydrated with PBS in order to mimic physiological conditions. An Instron testing system equipped with a flat cylindrical indenter (ø = 1 mm) used to compress the polymer scaffolds at a strain rate of 5% per minute for 20% of the strain. The characteristics features of each polymer scaffold were obtained from the curves of load-displacement and load-time. Moreover, the relaxation load was also measured for 5 min.[138,139] The indentation moduli (E) were calculated locally for 4 percentages of strain (0% to 5%, 5% to 10%, 10% to 15% and 15% to 20%) using a linear model for semi-infinite materials (diameter sample to diameter indenter ≥3) as previously described.[135–137]

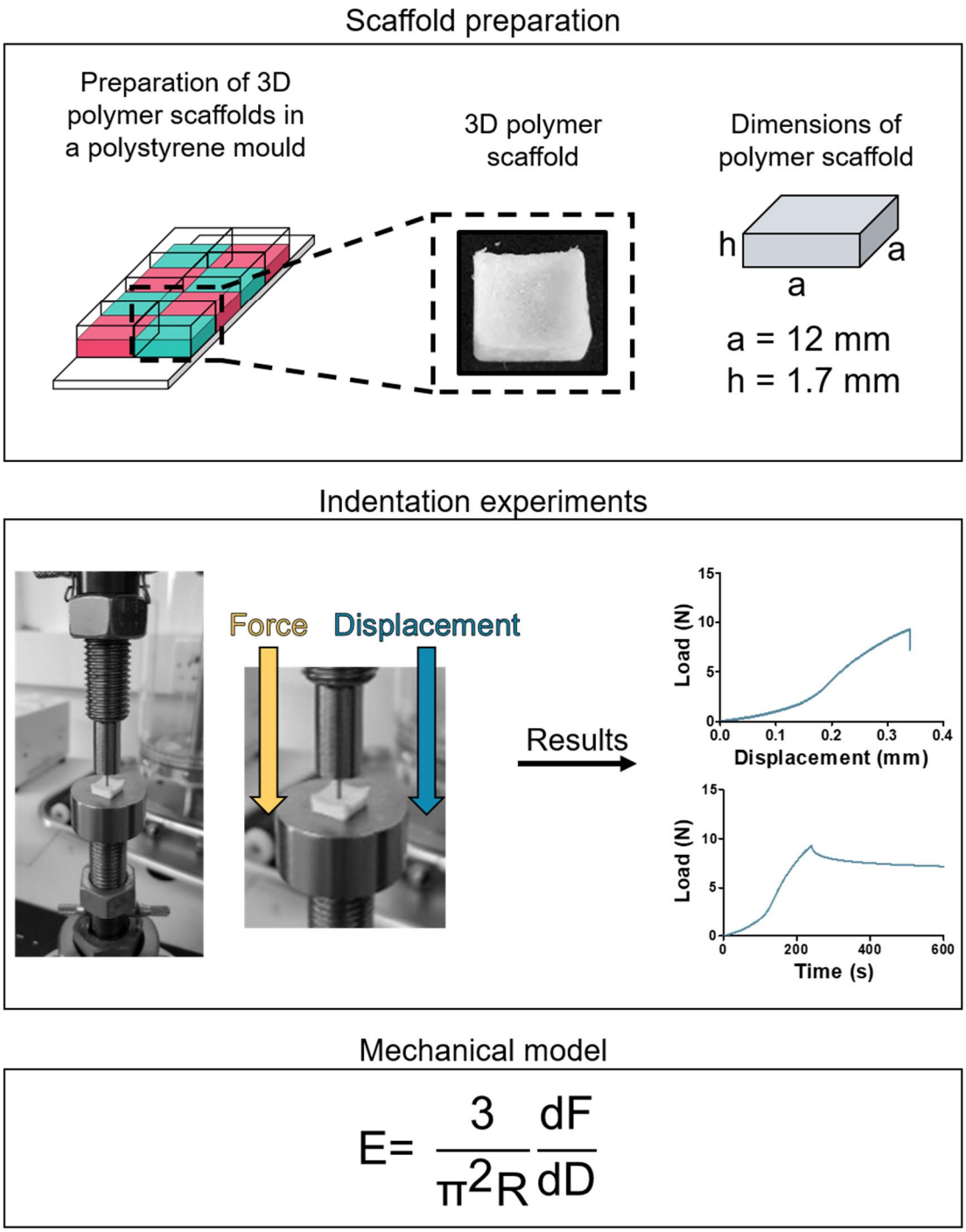

Figure 4-23. Mechanical characterisation of the 3D polymer scaffolds. Scaffolds (12×1.7 mm) were prepared in a polystyrene mould. Indentation was performed using an Instron and a flat indenter (Ø = 1 mm) at a strain rate of 5% per minute for 20% of the strain (340 µm). The indentation modulus (E) was calculated locally using a linear model where the radius of the indenter (R) was fixed and the increment of the load (dF) vs displacement (dD) were calculated from the gradient of the curves of load vs displacement for each polymer.

The analysis of the indentation moduli of control scaffolds (**P0**) revealed the effect of the polymer composition on the mechanical properties (Figure 4-24). Among the four compositions analysed, scaffold **P0-B** presented the highest indentation moduli and **P0-C** the lowest with no significant differences between **P0-A** and **P0-D**. **P0-B** scaffolds were significantly stiffer (40.4 MPa) than scaffolds **P0-A**, **P0-C** and **P0-D** for an initial load (0% to 5% strain). This trend was also observed between 5% – 10%, 10% –15% and 15% – 20% strain although differences between the polymers reduced with the increase of the strain. For example, polymer **P0-B** (55.8 MPa) was again the stiffer polymer when compared with **P0-A** and polymer **P0-C** but significant differences were not observed for scaffolds **P0-D** between 15% to 20% strain.

The porogenic solvent (**P60** and **P80**) produced a reduction in the scaffolds indentation moduli with a further drop in the stiffness when DMSO was increased; for example, indentation moduli for **P0-B**, **P60-B** and **P80-B** were 40.3 MPa, 27.0 MPa and 0.3 MPa between 0% to 5% strain (Figure 4-25).

The porosity, polymer structure and morphological characteristics of the pores are well known to determine the mechanical properties of porous polymers.[170,171] The increase in scaffold porosity is inversely proportional to its density; thus, the density of the scaffolds is representative of their porosity.

The density of scaffolds were calculated by the weight of the dried scaffolds divided by the volume of ethanol that the scaffold displaced after immersion in ethanol for 4 hours (Figure 4-26). The density of **polymer A** in case of the **P0** scaffolds was 631 kg/m^3 which changed to 364 kg/m^3 and 151 kg/m^3 for **P60** and **P80** respectively.

The indentation moduli were normalised to the density of each polymer scaffold (Figure 4-27) in order to elucidate how the scaffold “softened” as the porogenic solvent increased, consequence of the porous network (the more porous the scaffolds, the softer the scaffold).

The differences observed in the normalised indentation modulus between the **P0** and **P80** scaffolds were revealed to be smaller than observed in the original indentation modulus. For instance, normalised indentation moduli between **P0-A and P80-A** showed about a 6-fold decrease whereas their indentation moduli decreased 24-fold for the same change of porosity (from **P0** to **P80**). In the case of polymer **B** scaffolds, normalised indentation moduli decreased about 35-fold for **P0** and **P80**, while their

indentation moduli (not normalised) showed a 119-fold reduction between **P0** and **P80**. Similar behaviour was observed for **P80-C** and **P80-D** with about a 20-fold decrease instead of 100-fold and about an 8-fold reduction instead of 40-fold.

The comparison between the normalised indentation modulus and the indentation modulus directly measured confirmed that the **P80** scaffolds were significantly softer than **P0** and **P60** scaffolds. A more random distribution of the polymer network was expected in the scaffolds with low porosity (**P0**) as the polymer fibres can grow in all the directions.[172] Moreover, decreasing the level of solvent and increasing the concentration of monomers is known to increase polymer stiffness.[173] Perhaps, the presence of DMSO during the polymerisation (incomplete phase separation in the templating stage) could explain the dramatic reduction of stiffness revealed with the increase in DMSO levels.

The relaxation load is the observed reduction in load after applying a prolonged deformation. Two dynamic stress-relaxation mechanisms occur simultaneously in the case of the indentation of hydrated polymer scaffolds; a viscoelastic relaxation related to changes in the structure of the polymer chain and poroelastic relaxation associated with the transport of water out of the scaffolds.[174] Relaxation curves were obtained for the four polymers and three different levels of porogenic solvent (**P0**, **P60** and **P80**). The relaxation load (percentage of decrease of the load) was calculated for the hydrated (PBS) polymer scaffold after 1 and 5 minutes (Figure 4-28). **Polymers A** and **B** exhibited similar decreasing relaxation profiles from **P0** to **P80** whereas **polymers C** and **D** showed the opposite, an increasing trend. Moreover, the scaffolds of polymer **D** displayed significant load relaxation which reduced to 45% for **P0-D** and 57% for **P80-D** after 5 min.

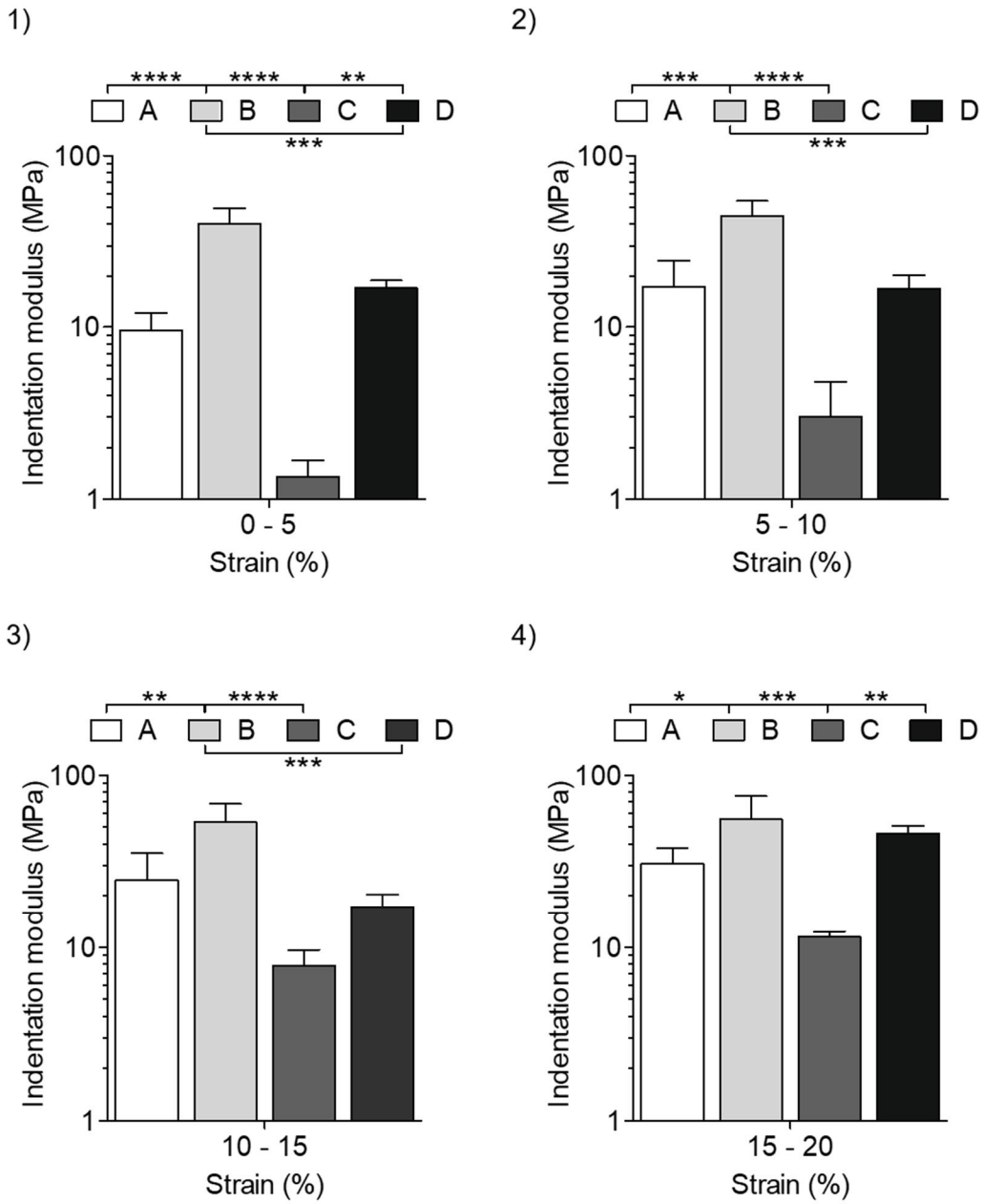

Figure 4-24. Mechanical characterisation of the polymer scaffolds. Indentation modulus for **polymers A-D** with low porosity (**P0**) at 1) 0-5, 2) 5-10, 3) 10-15 and 4) 15-20 strain percentages. One-way ANOVA with Bonferroni post-test (* $p \leq 0.05$, ** $p \leq 0.01$, *** $p \leq 0.001$ and **** $p \leq 0.0001$). Mean ± SD, n=4.

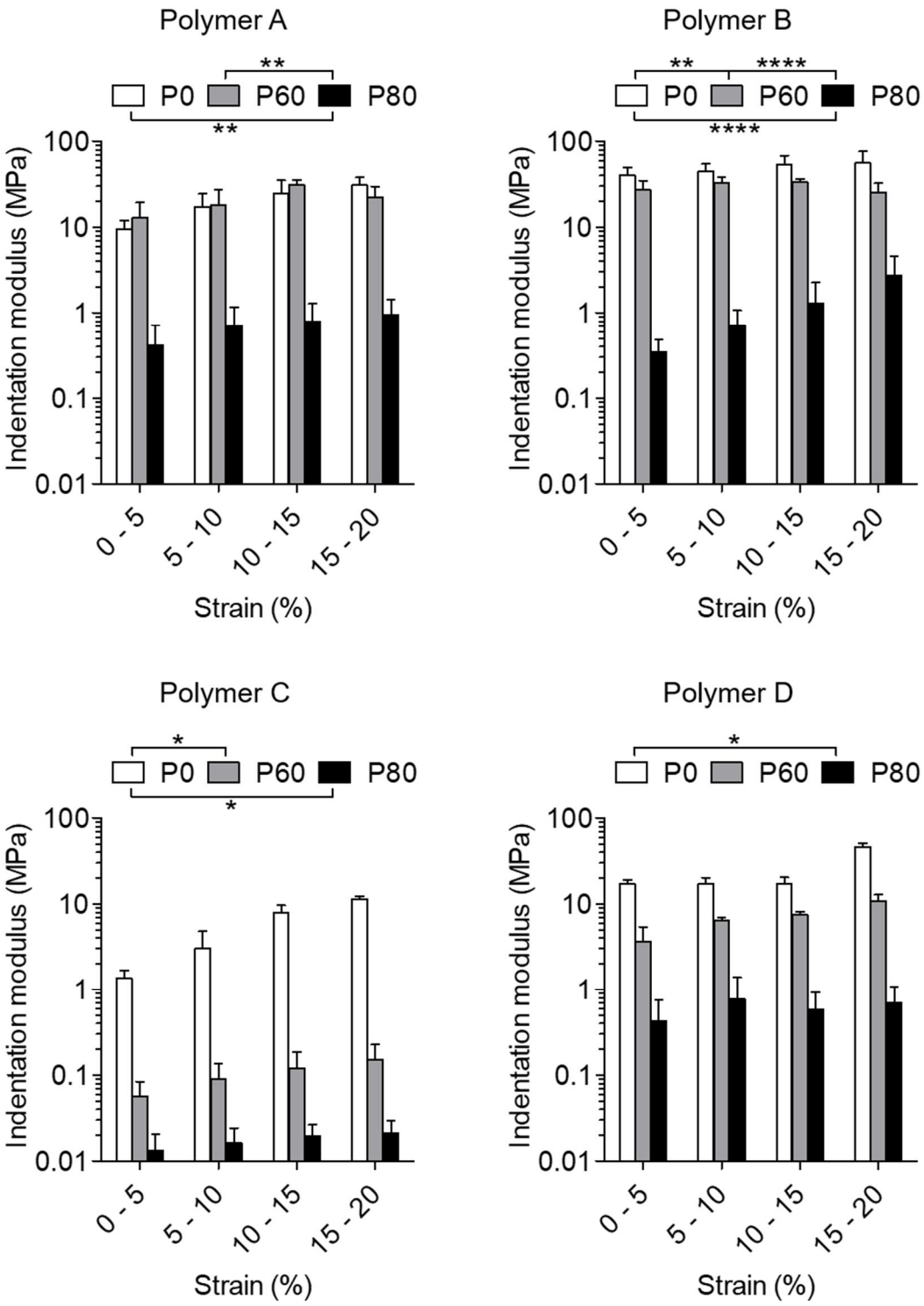

Figure 4-25. Mechanical characterisation of the polymer scaffolds. Indentation modulus for **polymers A-D** with low (**P0**), medium (**P60**) and high porosity (**P80**) at four different strain percentages. One-way ANOVA with Bonferroni post-test (* $p \leq 0.05$, ** $p \leq 0.01$, *** $p \leq 0.001$ and **** $p \leq 0.0001$). Mean ± SD, n=4.

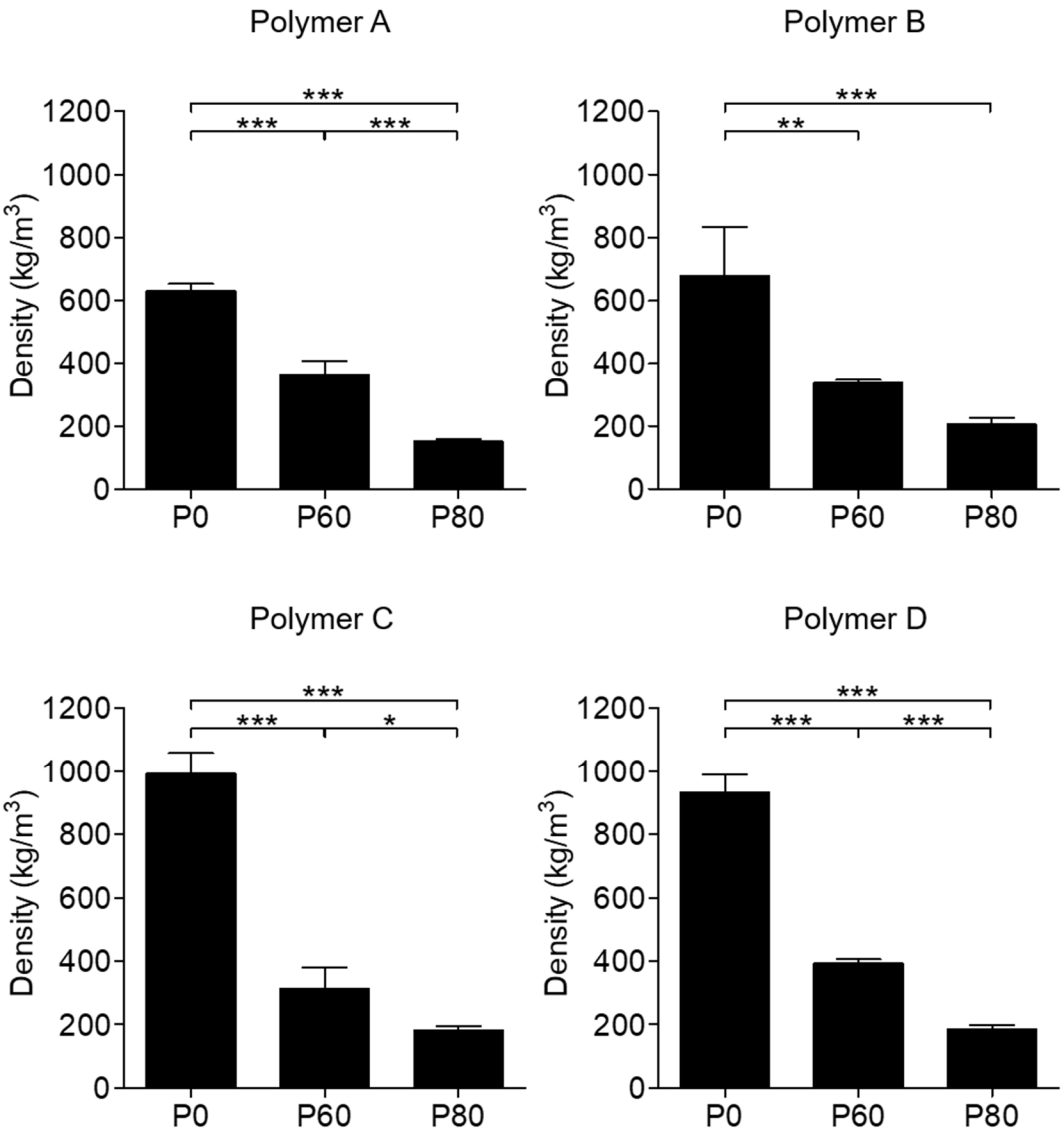

Figure 4-26. Density (kg/m^3) for **polymers A-D** with low (**P0**), medium (**P60**) and high (**P80**) porosity. One-way ANOVA with Bonferroni post-test (* $p \leq 0.05$, ** $p \leq 0.01$, *** $p \leq 0.001$ and **** $p \leq 0.0001$). Mean ± SD, n=4.

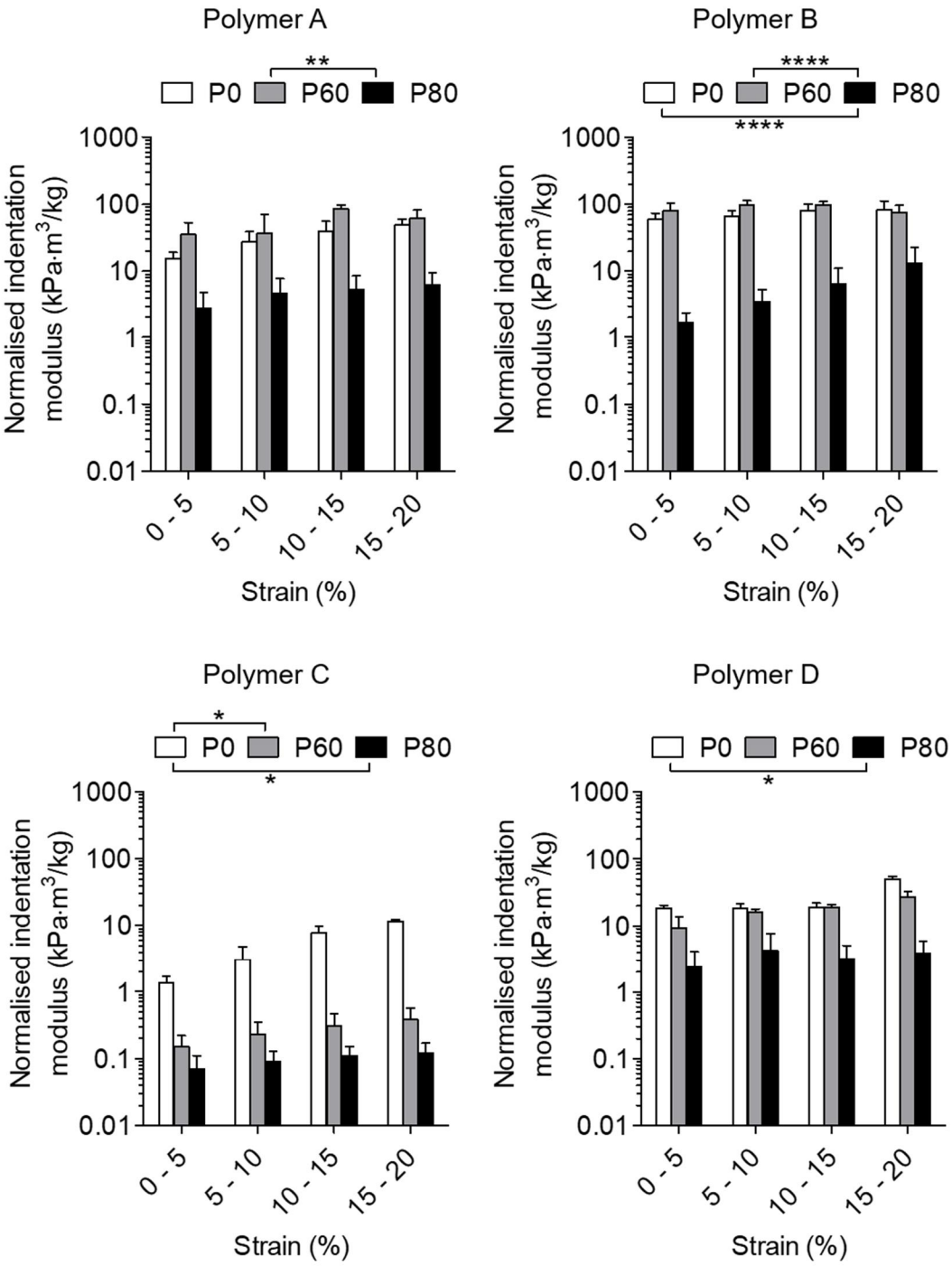

Figure 4-27. Mechanical characterisation of the polymer scaffolds. Normalised indentation modulus at four different strain percentages for **polymers A-D** with low (**P0**), medium (**P60**) and high (**P80**) porosity. One-way ANOVA with Bonferroni post-test (* $p \leq 0.05$, ** $p \leq 0.01$, *** $p \leq 0.001$ and **** $p \leq 0.0001$). Mean ± SD, n=4.

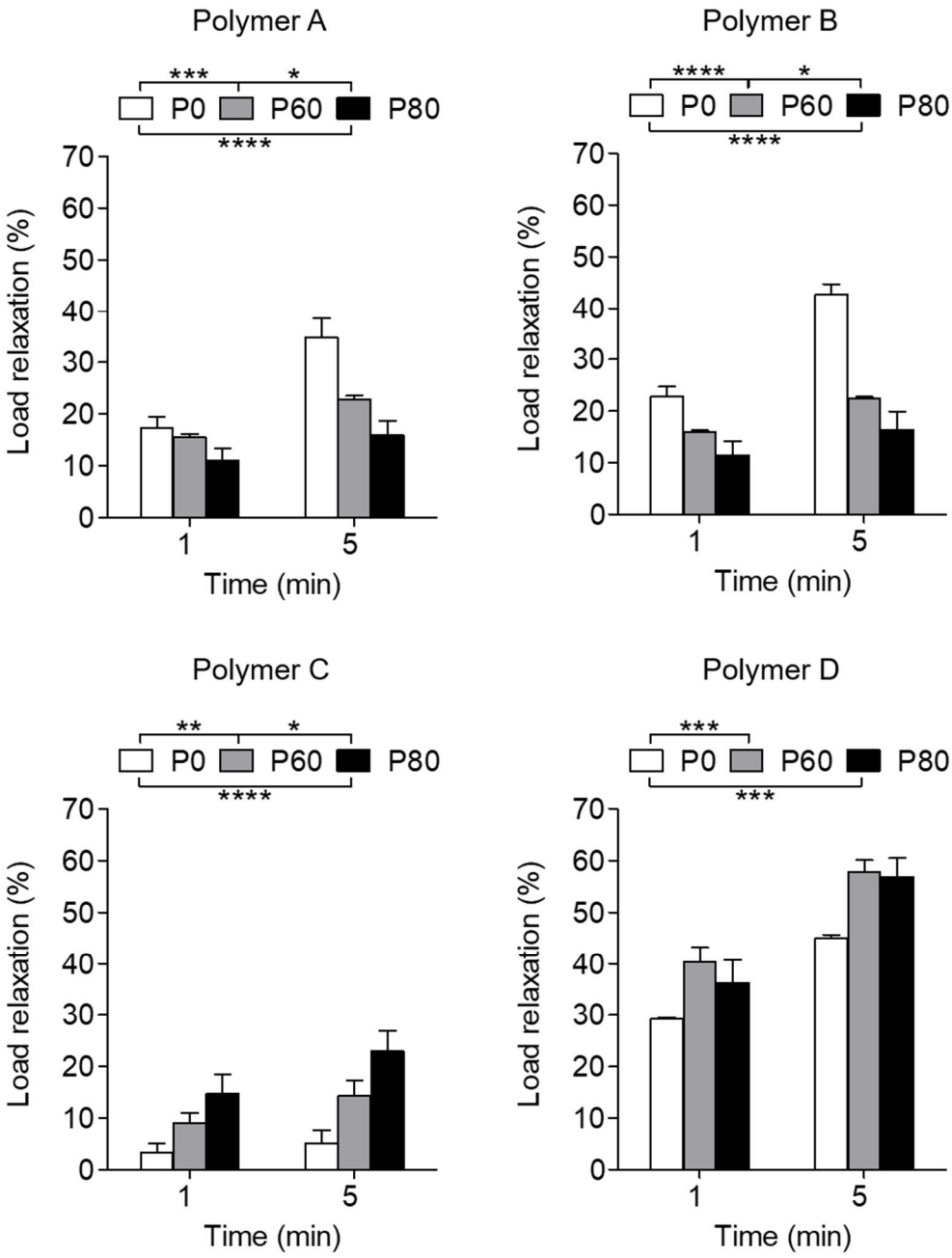

Figure 4-28. Mechanical characterisation of the polymer scaffolds. Load relaxation (%) after 1 and 5 minutes for **polymers A-D** with low (**P0**), medium (**P60**) and high (**P80**) porosity. Statistics were calculated for the final relaxation load (5 min). One-way ANOVA with Bonferroni post-test (* $p \leq 0.05$, ** $p \leq 0.01$, *** $p \leq 0.001$ and **** $p \leq 0.0001$). Mean ± SD, n=4.

VI. Analysis of porosity on the arrays of 3D polymer scaffolds

To analyse the reproducibility of the approach, the entire array was explored using the four different polymer compositions (**A-D**) previously selected (Table 4-1) and six concentrations of porogenic solvent (**P0**, **P20**, **P40**, **P60**, **P80** and **P85**) to give 24 unique polymer scaffolds in the wells of a 96-well plate (Figure 4-29). The array was prepared with the "slow cooling" method, 5 °C for 16 hours and -20 °C for 4 hours, that showed maximum formation of the pores followed by photo-polymerisation for 30 min.

Visual inspection of the array showed evidence of an enlargement of the pore size with an increase in level of DMSO for the four polymer compositions (Figure 4-29). The scaffolds with low porosity (**P0**) were transparent and colourless whereas the porous polymers (from **P40** to **P85**) were opaque and white in colour. Opacity of the polymers being a consequence of light scattering caused by the pores with air and the polymer.[175]

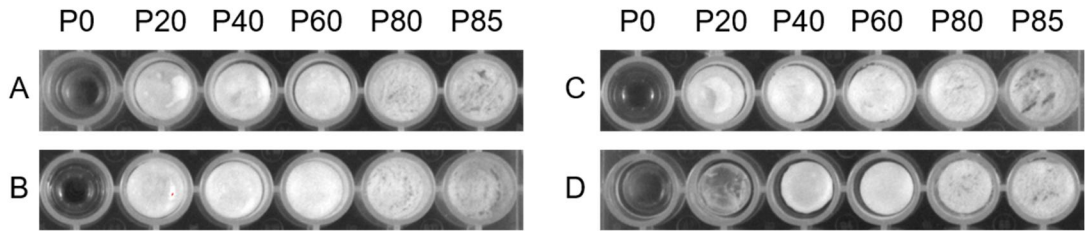

Figure 4-29. The array of 3D polymer scaffolds**. Polymers A-D** were combined with different levels of DMSO, from 0% (**P0**) to 85% (**P85**), to give an array of 24 different polymer scaffolds.

An approach based on solvent displacement was developed to measure the porosity of the scaffolds without extraction. **P0** scaffolds for the four polymer compositions had no porosity as expected while maximum porosity was obtained at 80% with **P80** scaffolds (Figure 4-30).

Comparison of the porosity of the polymers obtained from two independent synthesis allowed a study of intra and inter plate reproducibility in fabrication of the arrays. The measured porosity at each condition in the plate and between plates, batch 1 and batch 2, showed the consistency of the experimental approach (Figure 4-31), moreover, comparison of the porosity measured for the array of polymer scaffolds and the scaled-up scaffolds showed the scalability of the approach (Figure 4-32).

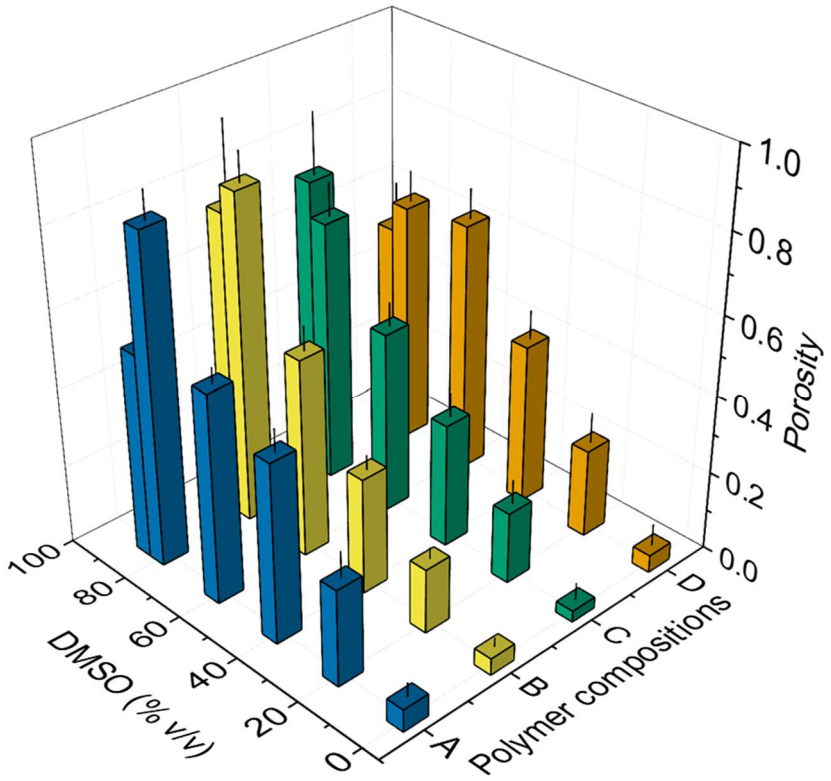

Figure 4-30. Porosity by liquid displacement calculated as the ratio between the volume of solvent inside the pores of the scaffold and the total volume of the scaffold. **Polymers A-D** were combined with six levels of porogenic solvent (**P0**, **P20**, **P40**, **P60**, **P80** and **P85**) to fabricate 24 unique 3D polymer scaffolds. Mean ± SD, n=8

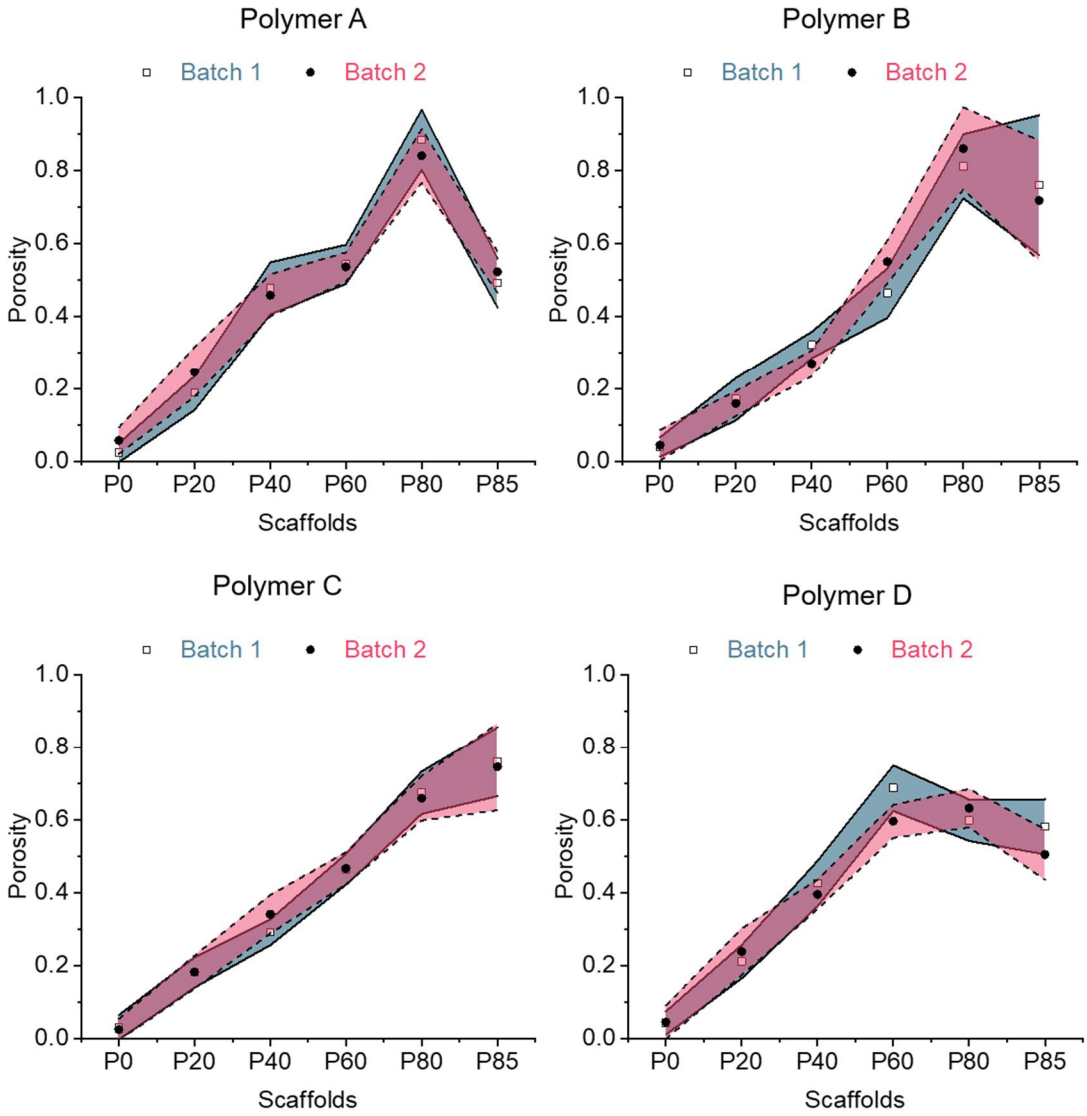

Figure 4-31. Dispersion of the measured porosity between replicates (squares batch 1 and circles batch 2) made at different times (quadruplicate scaffolds, shaded area). The porosity was calculated as the ratio between the volume of solvent inside the pores of the scaffold and the total volume of the scaffold. Mean ± SD, n=4.

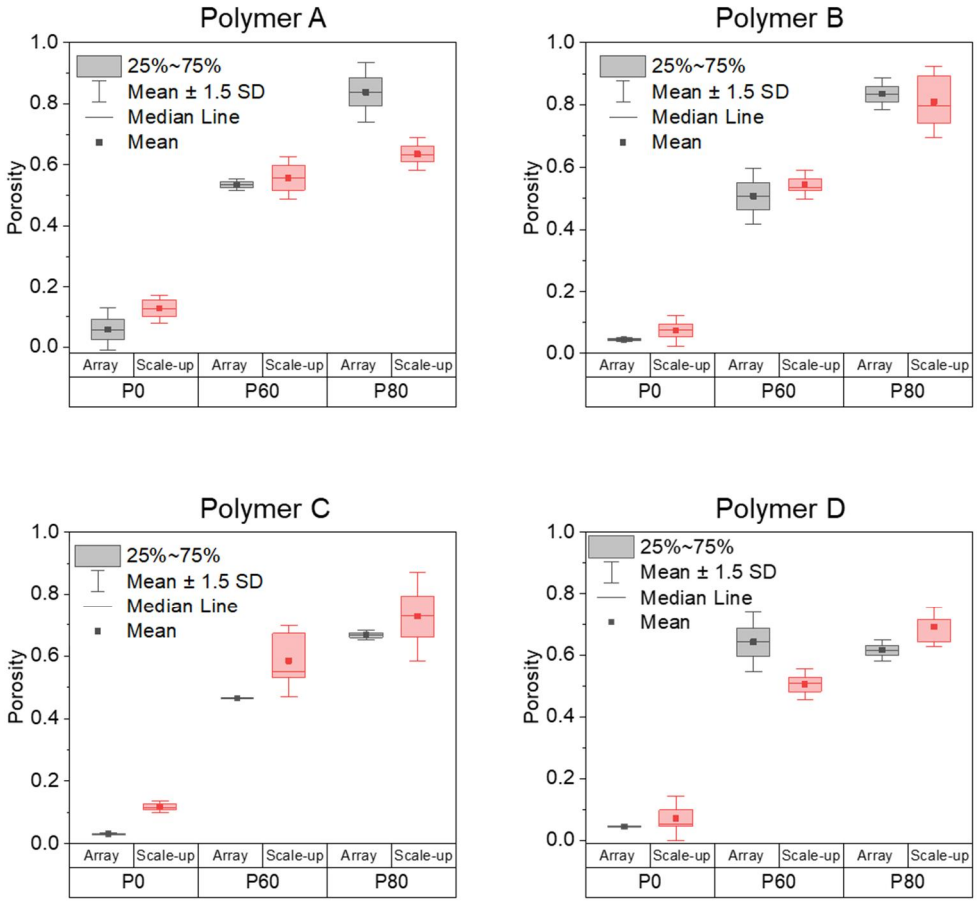

Figure 4-32. Porosity of scaffolds fabricated in the array format (96-well plate, UV-curing 30 min, porogenic solution 80 µL) or scaled-up scaffolds (polystyrene mould, UV-curing 60 min, porogenic solution 300 µL) for **polymers A-D** with three level of porogenic solvent (**P0**, **P60** and **P80**). Mean ± SD, n=8 (arrays) and n=4 (scale-up).

4.2.3 Cell behaviour on the array

I. Seeding conditions in the array

The physical characterisation of the array of 3D polymer scaffolds confirmed that the fabricated scaffolds had close resemblance in terms of the physical properties of bone tissues such as an open porous structure and stiffness.[89] **Polymer A** was used to develop a strategy to screen cell behaviour in the array of 3D scaffolds. First, **Polymer A** fabricated with a range of porosities (**P0**, **P20**, **P60** and **P80**) was used to optimise the seeding conditions and incubation time of SAOS-2 and MB-63 cells seeded at different concentrations (20,000 and 50,000 cells/well) with cell behaviour interrogated at days 2, 7 and 14 (tissue culture well plates were served as a control).

Cellular behaviour in the arrays was studied using alamarBlue™ (also known as the traditional Alamar Blue) as a descriptor of cells viability and proliferation. Alamar Blue relies on the reduction of resazurin (blue and weakly fluorescent) to resafurin (red and highly fluorescent) in living cells, which is related to cellular metabolism in addition to the number of cells (Figure 4-33).

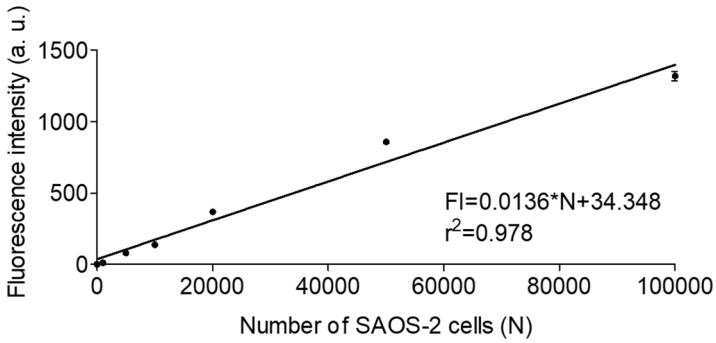

Figure 4-33. Calibration curve of the number of SAOS-2 cells plated and the resulting Alamar Blue fluorescence intensity. Alamar Blue in medium (10% v/v) was added to the wells 2 hours after seeding to ensure cell attachment to the plate. Incubation was performed for 4 hours in a humidified atmosphere (37 °C and 5% CO_2). Supernatant was collected and, subsequently, fluorescence was read in a microplate reader ($\lambda_{ex/em}$ = 530/590). Mean ± SD, n=3.

The seeding of 20,000 SAOS-2 cells on the 3D polymer scaffolds revealed the ability of the 3D polymers to attach and maintain the cells in addition to allowing proliferation (Figure 4-34). **Polymer A** showed a slightly lower cell attachment number and proliferation compared to tissue culture plates. For instance, cells in the control well tissue culture plates peaked at day 7 with about a 2.5-fold increase whereas **polymer A** showed a 1.5-fold increase at the same time. However, when the number of cells increased to 50,000 cells per well no proliferation was observed. MG-63 cells presented similar behaviour as the SAOS-2 cells (Figure 4-35). **Polymer A** allowed cell attachment and proliferation over 14 days in the majority of the 3D scaffolds seeded with 20,000 MG-63 cells while 50,000 cells produced no proliferation. Overall, both cell lines showed attachment and growth on the 3D polymer scaffolds. The seeding density of 20,000 cells per well was favoured as this showed differences in cell behaviour between scaffolds and proliferation over 14 days. The comparison between SAOS-2 and MG-63 cells suggested use of the first cell line over the second

for further studies as SAOS-2 cells were observed to be more selective whereas MG-63 appeared to grow on all the 3D polymers explored.

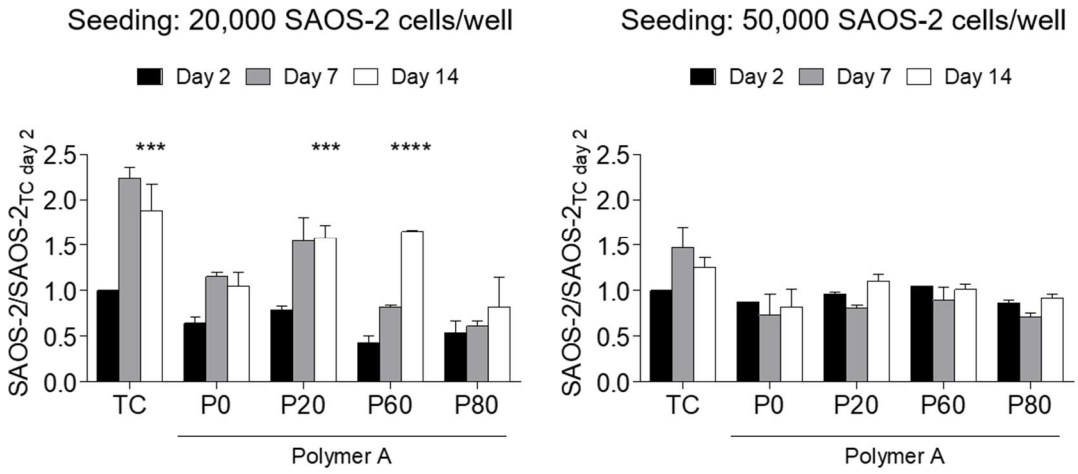

Figure 4-34. Viability of SAOS-2 cells over 14 days and optimisation of the cell seeding. Normalised fluorescence intensity at different time points for each sample (day 2, 7 and 14). Fluorescence intensity was normalised with SAOS-2 cells at day 2 in the control (tissue culture plate). Fluorescence changes were based on the reduction of resazurin (alamarBlue™). The arrays were fabricated using **polymers A** with different porosities (**P0**, **P20**, **P60** and **P80**). Two-way ANOVA with Bonferroni post-test between day 2 and day 14 (* $p \leq 0.05$, ** $p \leq 0.01$, *** $p \leq 0.001$ and **** $p \leq 0.0001$). Mean ± SD, n=2.

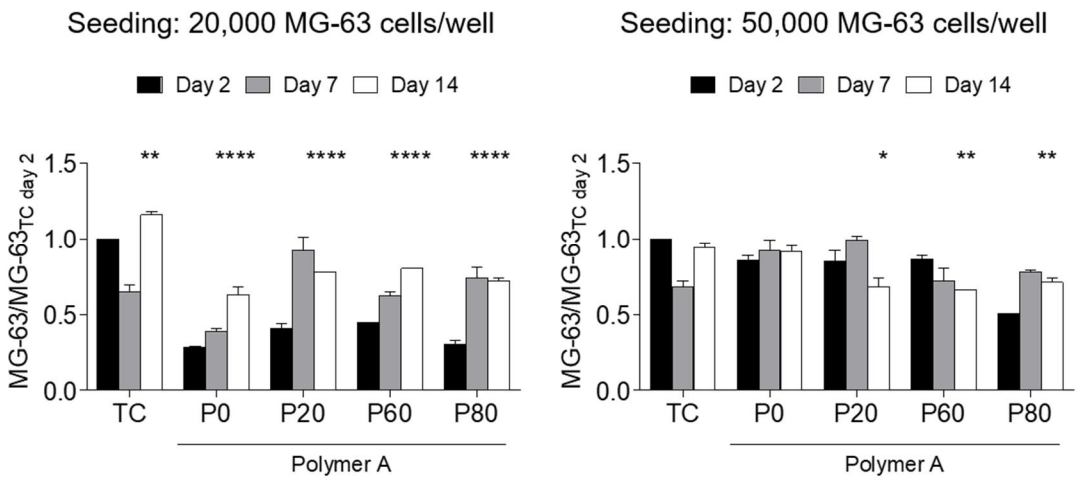

Figure 4-35. Viability of MG-63 cells over 14 days and optimisation of the cell seeding. Normalised fluorescence intensity at different time points for each sample (day 2, 7 and 14). Fluorescence intensity (alamarBlue™) was normalised with MG-63 cells at day 2 in the control

(tissue culture plate). Two-way ANOVA with Bonferroni post-test between day 2 and day 14 (* $p \leq 0.05$, ** $p \leq 0.01$, *** $p \leq 0.001$ and **** $p \leq 0.0001$). Mean ± SD, n=2.

II. Morphology of cells and scaffolds using SEM

The interaction between the polymer scaffold and the SAOS-2 cells was investigated using scanning electron microscopy (SEM). An array of 3D polymer scaffolds was prepared with “slow cooling” with different levels of DMSO. The cells were incubated on the arrays for 3 days (control scaffolds without cells) and fixed. After removing the polymers from the arrays and post-fixation of the cells with osmium tetroxide (OsO_4) to improve contrast, the scaffolds were dried and coated (gold/palladium).

Polymer microstructure in the presence and absence of cells was evaluated with SAOS-2 cells seen to attach and cover the surface of the scaffolds after 3 days (Figure 4-36). A few rounded cells were also observed, which was an indication of poor attachment at some regions leading to cell death. Laminar organisation of the polymer with pores around 50 µm in size were seen in the **P60** scaffolds with medium porosity. Pores of around 100 µm were observed to be populated with cells in the case of the **P80** scaffolds.

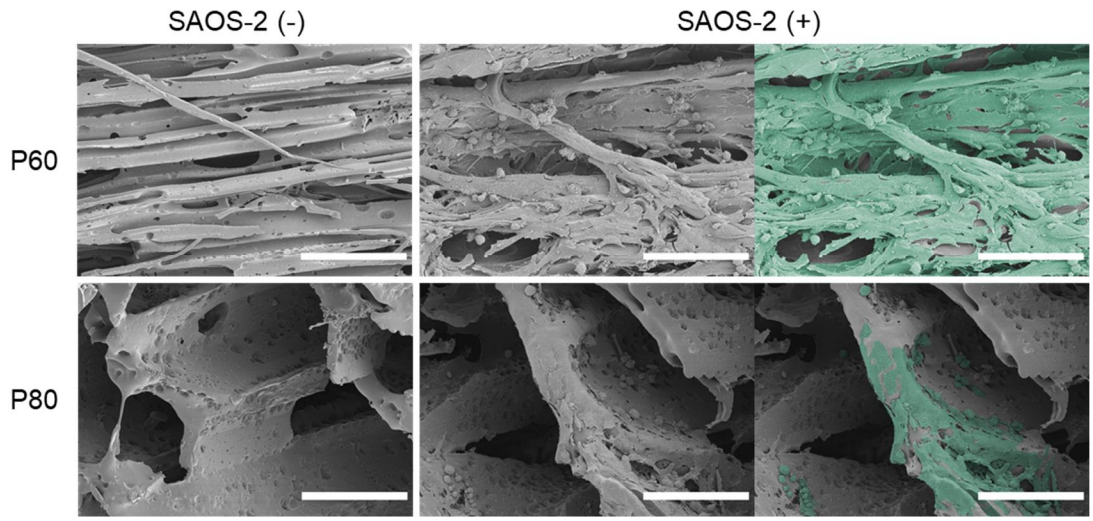

Figure 4-36. SEM images of the scaffolds incubated with SAOS-2 cells. Scaffolds **P60-A** (medium porosity) and **P80-A** (high porosity) with SAOS-2 (+) cells and without cells (-) after 3 days of incubation. Pseudo colour added to the cells (green) to help their visualisation. Scale bar = 100 µm.

III. Cell mineralisation on the array of 3D polymer scaffolds

Biomineralisation is one of key steps in the formation of bones where apatite minerals are formed as part of the extracellular matrix, mediated by osteoblasts.[176] The biomineralisation on the polymer scaffolds was assessed to further examine their functionality. As a preliminary approach, the mineralisation of SAOS-2 cells on the array of 3D polymer scaffolds were interrogated for **polymer A** with 4 levels of porosity (**P0**, **P20**, **P60** and **P80**) over 7 days in mineralisation medium (L-ascorbic acid 2-phosphate and potassium dihydrogen phosphate). Subsequently, SAOS-2 cells were fixed and stained with acid alizarin red.[143]

Microscopy showed the absence of colour for **P0-A** scaffolds and increased intensity of the red stain with increase of porosity (Figure 4-37, 1). The positive control (96-well tissue culture plate) gave a result similar to **P20-A**. Additionally, negative controls (scaffolds without SAOS-2 cells) exhibited red staining with lower intensity compared to their counterparts.

The quantitative data of the alizarin red staining in the scaffolds obtained with **polymer A** were calculated as the difference between an array with SAOS-2 cells and a control without cells. The normalised absorbances were also consistent with the qualitative analysis and the intensity of the alizarin red staining was found to be directly proportional to the increase of porosity (Figure 4-37, 2). For example, **P0-A** did not show any difference to the positive control tissue culture plate (TC) whereas **P60-A** and **P80-A** showed a significant increase with respect to the control. The higher background staining in the control array (SAOS-2 negative) was possibly due to the inherent non-specificity of the stain (alizarin red binds to calcium), which increased proportionately with porosity. Non-mineralised calcium or alizarin red stain could be retained in the polymer scaffolds because of the large surface areas and the extracellular matrix of the SAOS-2 cells. Consequently, a different approach was needed to examine the mineralisation which would be more specific towards apatite rather than just calcium.

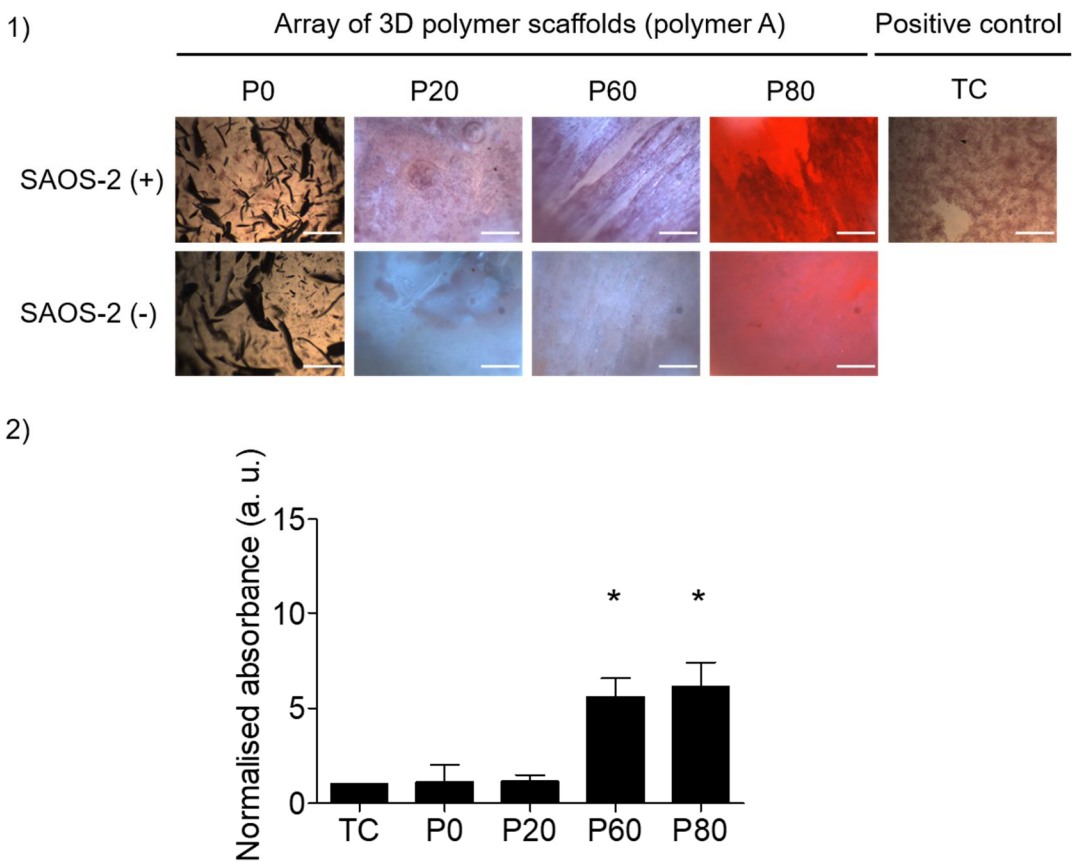

Figure 4-37. Mineralisation of SAOS-2 cells on the 3D polymer scaffolds. 1) Representative images of **polymer A** with different levels of porosity (**P0**, **P20**, **P60** and **P80**) and SAOS-2 cells stained with acid alizarin red after 7 days of incubation in mineralisation medium. Scaffolds without cells and SAOS-2 cells in tissue culture plates (TC) were used as control. Scale bar = 500 µm. 2) Normalised absorbance (A/A_{TC}) between SAOS-2 cells stained with alizarin red on the control plate (TC) and the scaffolds. Absorbance based on the extraction and homogenisation of the alizarin red staining. One-way ANOVA with Bonferroni post-test between tissue culture plate and the scaffolds (* $p \leq 0.05$). Mean ± SD, n=2.

IV. Cell viability assay on the array of 3D polymer scaffolds

The viability of SAOS-2 cells was interrogated on all 24 3D polymer scaffolds fabricated in quadruplicate in 96-well plates (Figure 4-29). SAOS-2 cells were assessed with Alamar Blue at days 1, 3 and 7.

Scaffolds **P0** for polymers **A**, **B** and **D** were observed to allow attachment of SAOS-2 cells whereas the cells did not bind to **P0-C** scaffolds (Figure 4-38). Most of the scaffolds also displayed a reduction in the number of SAOS-2 cells with an increase of porosity (from **P0** to **P85**). Among the four different polymer compositions studied, **polymer B** was able to maintain a good number of cells (little differences compared TC) and promoted proliferation in the scaffolds **P60** and **P80**. For instance, the normalised fluorescence intensity for **P60-B** changed from 0.9 to 1.4 from day 1 to 7 and from 0.6 to 1.1 for **P80-B** in the same period. Contrary, porous scaffolds of **polymers A** and **D** showed a negligible or poor increase in the number of SAOS-2 cells.

Overall, the screening of the scaffolds using SAOS-2 cells revealed the significant influence of polymer composition and the 3D structure on the cellular behaviour of attachment and growth. **Polymers A** and **B** were selected for further experiments because of their ability to maintain SAOS-2 cells (**polymers A** and **B**) and stimulate proliferation (**polymer B**).

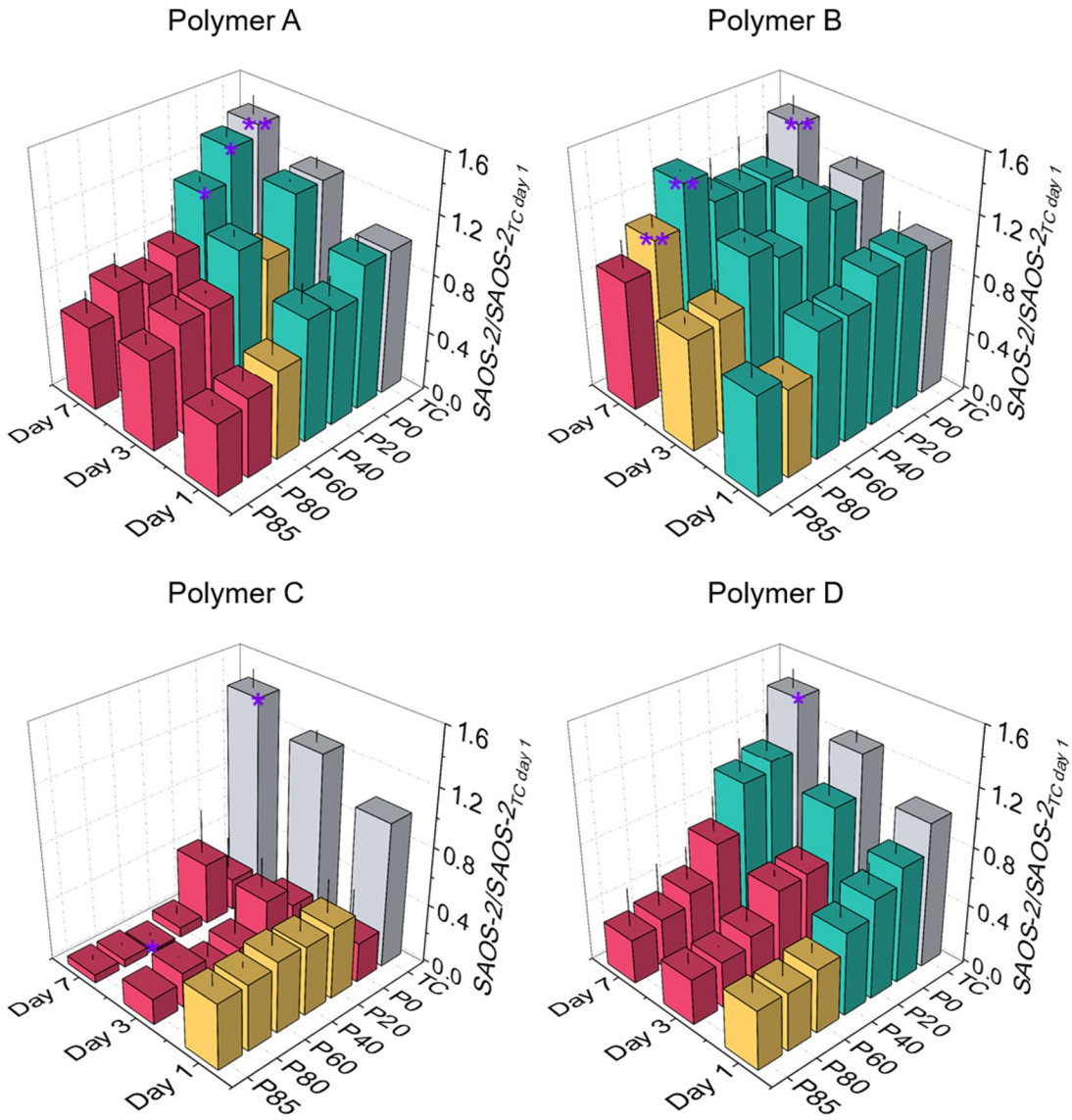

Figure 4-38. Viability of SAOS-2 cell over 7 days on the 3D polymer scaffolds. Normalised fluorescence intensity between the SAOS-2 cells seeded at day 1 in the control (tissue culture plate, 20,000 cells/well) and at day 1, day 3 and day 7. Two-way ANOVA with Bonferroni post-test between tissue culture plate and the scaffolds. Colour scale shows the level of significance representing the differences to TC: No differences (cyan, $p>0.5$), different (yellow, $p\leq0.01$) or very different (red, $p\leq0.0001$). Two-way ANOVA with Bonferroni post-test between day 1 and day 7 (* $p \leq 0.05$ and ** $p \leq 0.01$). Mean ± SD, n=3.

V. Live/dead staining assay on the array of 3D polymer scaffolds

The cell viability assay using Alamar Blue was complemented with a live/dead staining assay. **Polymers A** and **B** were fabricated with four levels of porosity (**P0**, **P60**, **P80** and **P80**) and SAOS-2 cells were incubated for 7 days prior to live/dead staining. Differences in the cell attachment were confirmed between the non-porous **P0** scaffolds and the porous scaffolds **P60**, **P80** and **P85** with **P60-B** showing the highest cell density in the porous polymers (Figure 4-39). Interestingly, it was observed that some cells infiltered or moved into the pores. **P80** and **P85** for polymer **A** and **B** had much of their surface covered by healthy cells (labelled in green) although a few dead cells (labelled in red) were also observed.

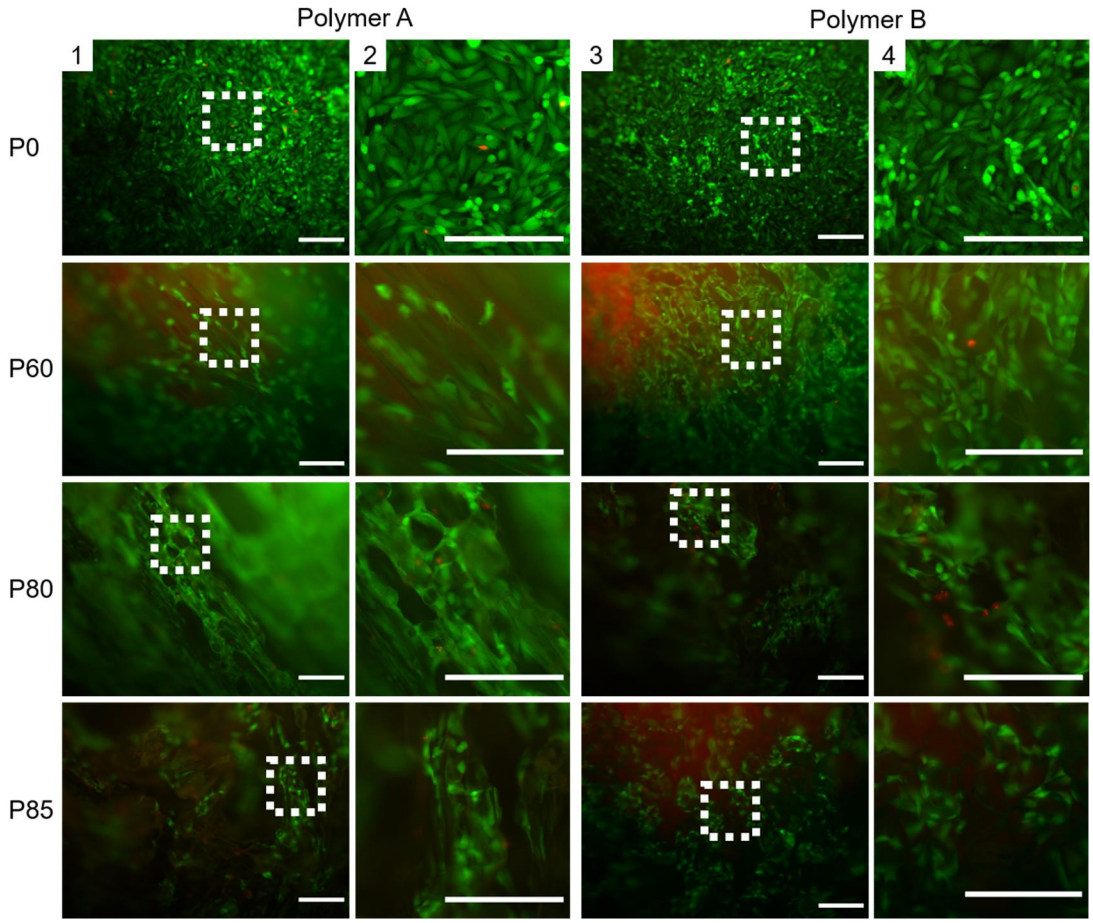

Figure 4-39. Viability of SAOS-2 cells on the 3D scaffolds. Live/dead staining of SAOS-2 cells after 7 days of incubation. **Polymers A** (1-2) and **B** (3-4) with low (**P0**), medium (**P60**) and high (**P80** and **P85**) porosity. Merged images of live (calcein AM, green) and dead cells (nuclear dye, red). White dashed square indicates areas magnified (2 and 4). Scale bar = 200 µm.

The array of 3D polymer scaffolds allowed live cell imaging and high-content screening using an automated imaging capturing systems. The presence of cells in different layers of the scaffolds and the uptake of the dyes by the porous structure, was revealed to be a major challenge of the method as they produced high signal to noise ratios in the images, which hindered quantification (Figure 4-40).

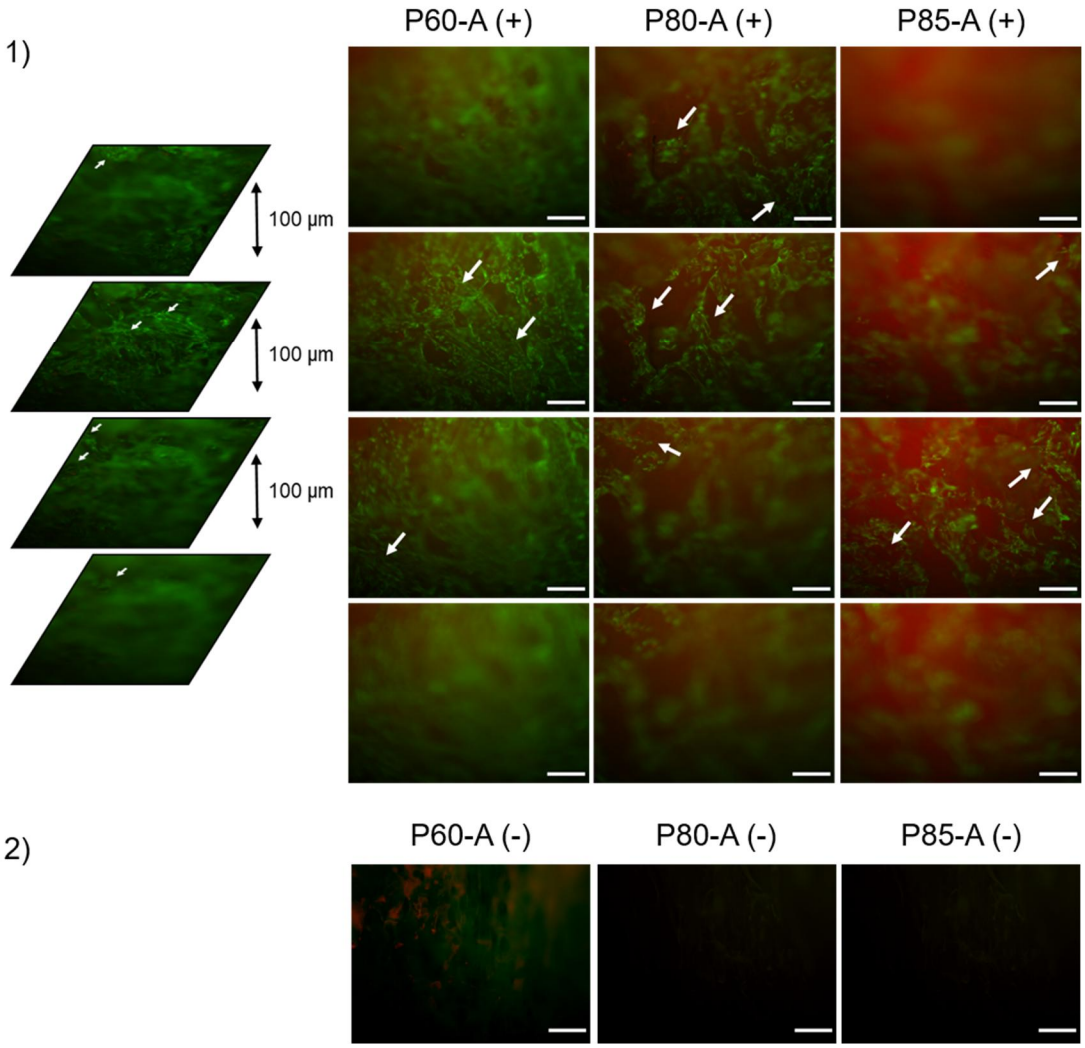

Figure 4-40. Viability of SAOS-2 cells on the **polymer A**. Live/dead staining of SAOS-2 cells after 7 days of incubation. Merged images of live (calcein AM, green) and dead cells (nuclear dye, red). 1) Z-stack (100 µm per image) of SAOS-2 cells (+) in different scaffolds of **polymer A** with medium (**P60**) and high (**P80** and **P85**) porosity. Arrows show the area with cells in the plane. 2) Porous scaffolds without SAOS-2 cells (-) were used as negative control. Scale bar = 200 µm.

VI. Morphology of SAOS-2 cells in the array of 3D polymer scaffolds and analysis of the cytoskeleton orientation

The morphology of SAOS-2 cells and their cytoskeleton orientation was analysed for scaffolds **P60** and **P80** of polymers **A** and **B** as they had shown to be the best 3D polymer scaffolds in the library in terms of biocompatibility. Filamentous actin of SAOS-2 cells on porous scaffolds were stained with a phalloidin staining and scaffolds without cells were used as a control for non-specific staining.

Cells in different layers* of the scaffolds were detected in the **P80** scaffolds after 7 days of culture (Figure 4-41), and observed to spread and grow along the polymer structure. Additionally, large pores (larger than 200 µm) were seen for these scaffolds. On the other hand, poor cell spreading and with a less elongated morphology were observed in case of the **P60** scaffolds with cells growing mostly on top of the materials. Poor penetration of SAOS-2 cells in the scaffolds was a probable consequence of inappropriate pore size (smaller than 100 µm).

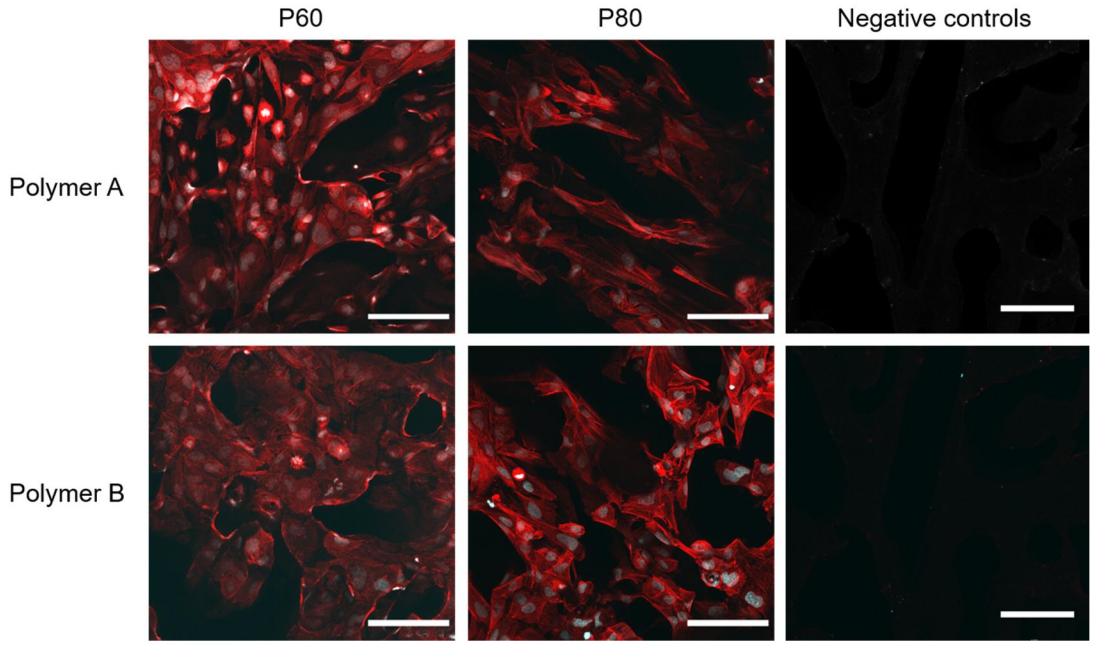

Figure 4-41. Representative images of the actin cytoskeleton of SAOS-2 cells on the 3D polymer scaffolds with medium (**P60**) and high porosity (**P80**). F-actin stained with Alexa Fluor 568 phalloidin is shown in red and nucleus in cyan. Scale bar = 100 µm.

* Videos of SAOS-2 cells in **P60** and **P80** scaffolds are included in the electronic copy. Array of 3D polymer scaffolds: Actin staining of SAOS-2 cells

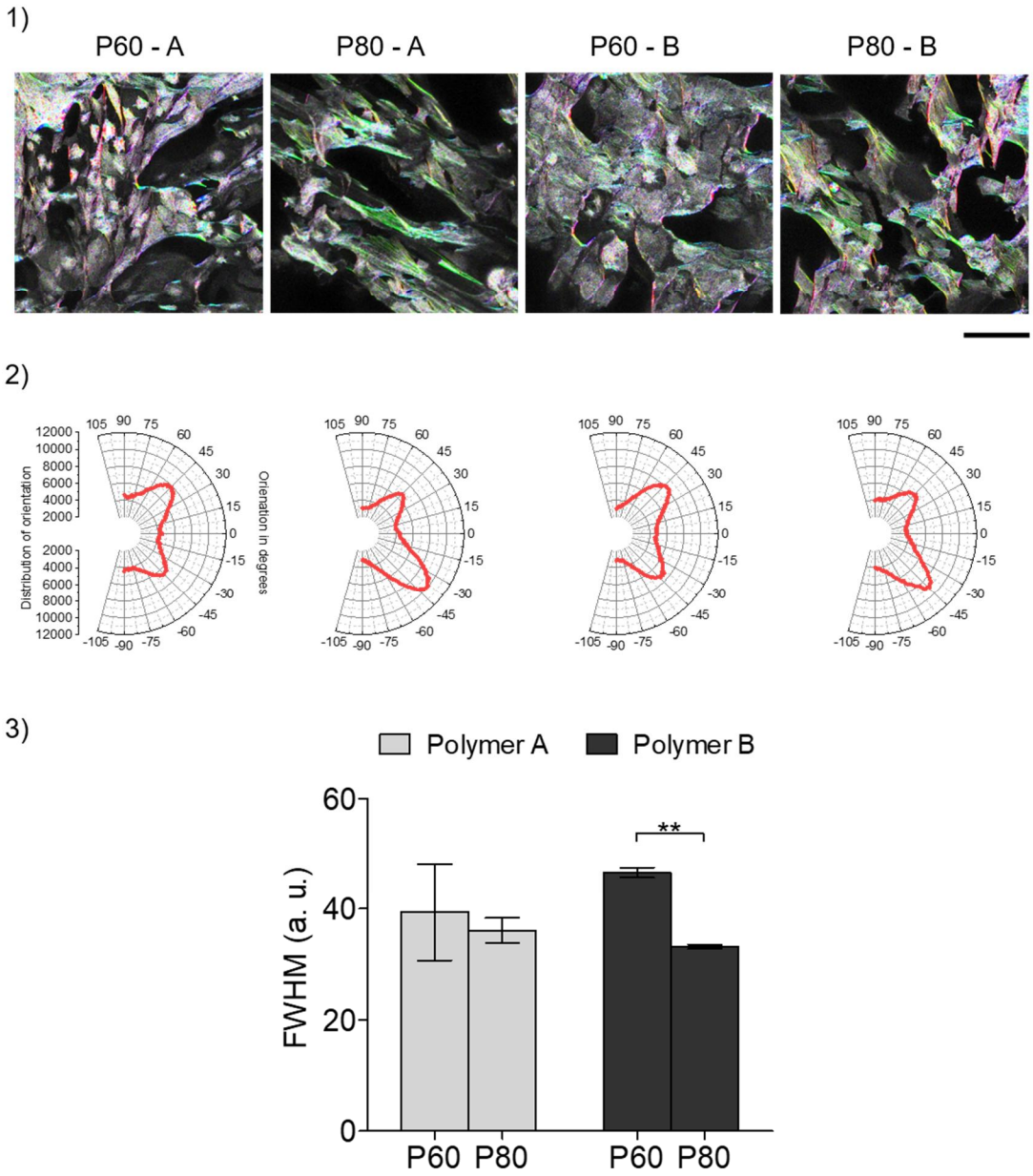

Figure 4-42. Analysis of the orientation of the filaments of the actin cytoskeleton of SAOS-2 cells on the 3D polymer scaffolds after 7 days of incubation. 1) Colour map of orientation of the filaments of the actin cytoskeleton of SAOS-2 cells. Scale bar = 100 µm. 2) Quantification of the distribution of angles (degrees) of the filaments of actin. 3) Full width at half maximum (FWHM) of the distribution of orientations fitted to Gaussian curves for scaffolds **P60** and **P80** (**polymers A** and **B**). Low FWHM indicates orientation of actin fibres. Two tailed t-tests between the paired scaffolds (** $p \leq 0.01$). Mean ± SD, n=2.

The potential organisation of actin filaments of SAOS-2 cells as a consequence of the polymer structure was analysed using the software ImageJ-Fiji (OrientationJ). The

orientation of the actin filament in the scaffolds shown using a colour map (Figure 4-42, 1) and complementary distribution curves (Figure 4-42, 2) suggested the prevalence of one main direction of the actin filaments in the P80 scaffolds compared to the P60 scaffolds. The full width at half maximum (FWHM) of the histogram obtained for the distribution of orientation was used to analyse the orientation of the actin filaments (Figure 4-42, 3). Oriented actin filaments showed narrow histograms and low values of FWHM. The significant reduction of the full width at half maximum for **P80-B** compared to **P60-B** confirmed the change of morphology attributed to the 3D structure of the scaffolds.

4.2.4 The behaviour of SAOS-2 cells is altered by polymer composition, 3D structure and mechanical properties

One of the objectives of developing arrays of 3D polymer scaffolds was to compare the mechanical and structural properties of the scaffolds with cell behaviour. Cell attachment and proliferation, viability for day 1 and day 7 with Alamar Blue, scaffold stiffness with indentation modulus and relaxation were compared. Each property was normalised with the highest property observed. For example, stiffness for the 12 polymer scaffolds exploring **polymers A-D** with porosities **P0**, **P60** and **P80** were normalised to 40.3 MPa, the highest value obtained.

Scaffolds **P0-A** and **P0-B** exemplified two polymer compositions that presented good cell attachment and maintenance (Figure 4-43). The increase of porosity (**P60-A** and **P80-A**) produced a reduction in initial binding and proliferation of SAOS-2 whereas scaffolds **P60-B** and **P80-B** were capable of maintaining proliferation although initial cell attachment was compromised. On the other hand, scaffolds **P0-C** neither showed significant cell attachment nor proliferation and the increase of porosity did not produce variations in this trend.

Generally, the stiffness of the scaffolds was shown to decrease as porosity increased. However, the reduction of stiffness for **P60-A** and **P80-A** scaffolds was more pronounced than in the cases of **P60-B** and **P80-B**. Relaxation of the scaffolds was shown to be closely associated with the polymer composition and was not significantly affected by the porosity, moreover, an effect of relaxation on cell behaviour was not observed.

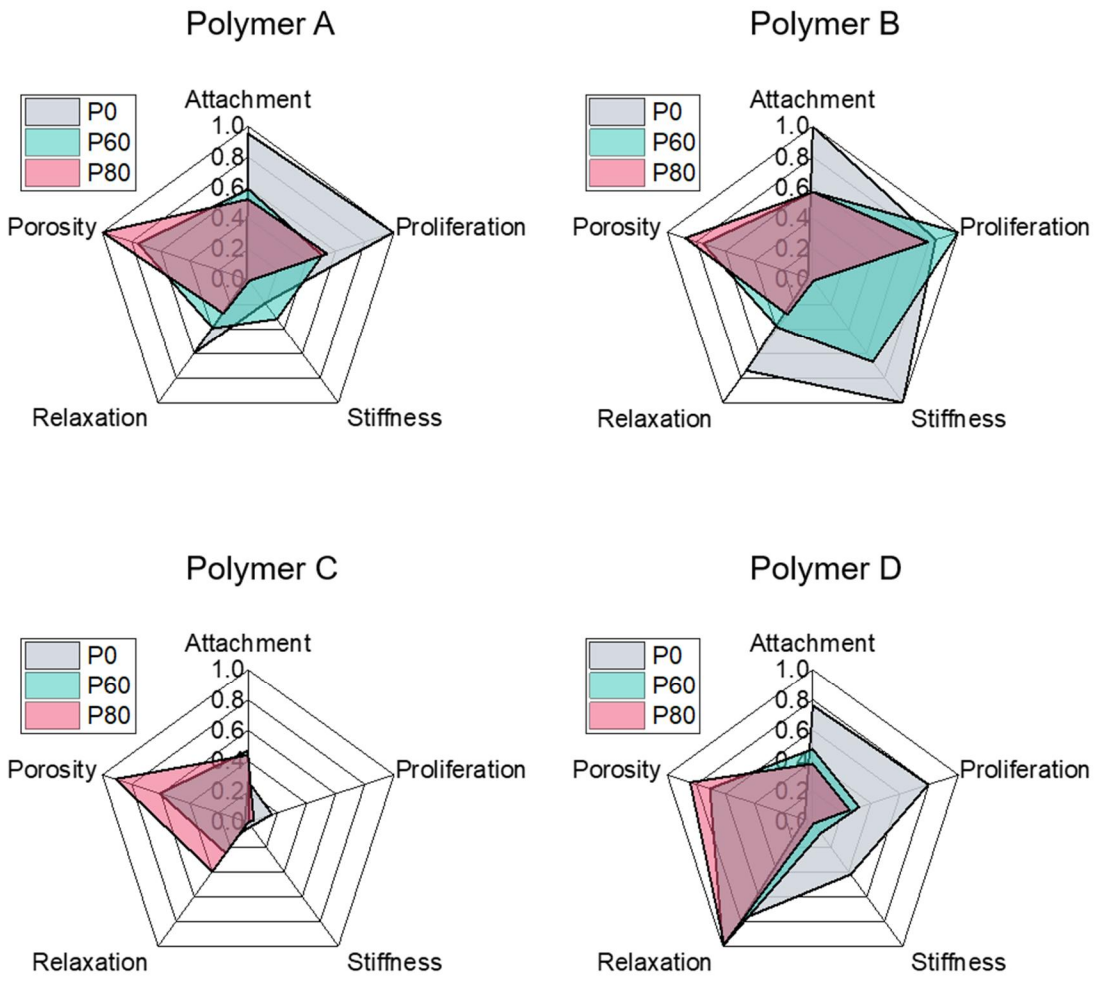

Figure 4-43. Spider plot analysis of the combined effect of the mechanical properties and porosity on the attachment of SAOS-2 cells and their proliferation behaviour. Polymers A - D with low (P0), medium (P60) and high (P80) porosity. Each property interrogated (attachment, proliferation, stiffness, relaxation load and porosity) was normalised with the highest identified value from the 3D screening. The highest and lowest values for each property of the 3D polymer scaffolds were: attachment fold change at day 2 (1.1 – 0.3), proliferation fold change at day 7 (1.4 – 0.1), stiffness (40.3 MPa – 13.4 kPa), percentage of relaxation load (58 – 5) and percentage of porosity (89 – 1).

Overall, polymer composition, stiffness of the polymer and 3D architecture were shown to be closely interconnected and affected cell behaviour. Amongst the various structural properties of the scaffolds analysed, previous reports suggests that mechanical properties of the substrate are crucial for tuning cell behaviour.[177–180] The comparison of stiffness and proliferation exhibit the presence of a working range of stiffness from about 500 kPa to 20 MPa where the SAOS-2 cells were sustained or

proliferated independently of the polymer composition (Figure 4-44). Below or above this range, SAOS-2 cells were found to encounter difficulties in maintaining their growth on the scaffolds. Cell proliferation was optimum in scaffolds produced from **polymer B** even though the stiffness of scaffolds obtained with **polymers A** and **D** were also in the same range. Therefore, it indicates that the polymeric substrate also provides chemical cues and that the mechanical signals alone are insufficient to drive a specific cellular behaviour.

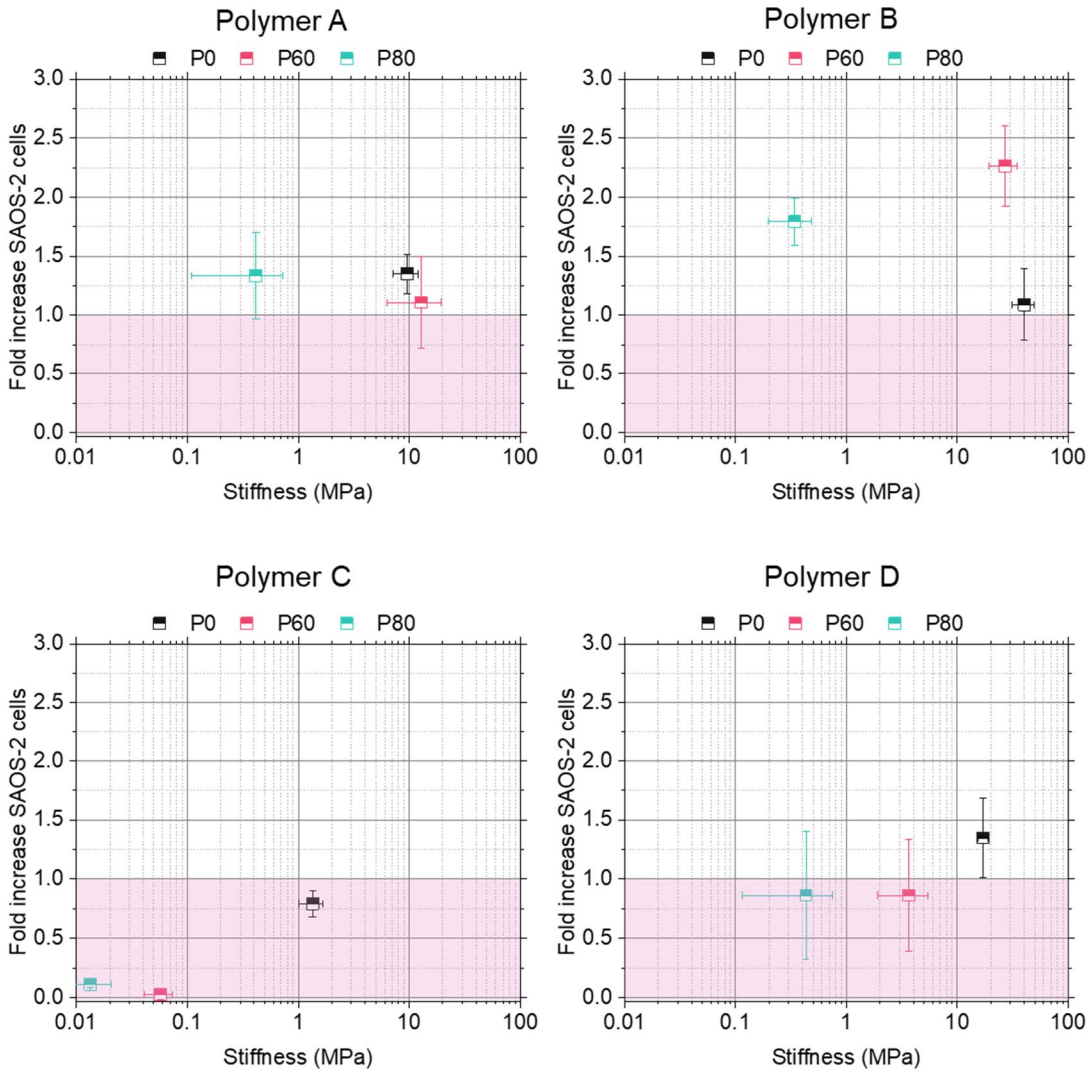

Figure 4-44. Effect of the indentation modulus, "stiffness", on the proliferation of SAOS-2 cells. Proliferation shown as fold increase of fluorescence based on Alamar Blue between day 1 and day 7. Scaffolds with low (P0), medium (P60) and high (P80) porosity were generated with polymers A - D. The indentation moduli of the scaffolds (stiffness) were analysed using a flat indenter for 20% of the strain. Each modulus was calculated using the linear model previously stated. Mean ± SD, n=3.

4.3 Discussion

Microarray technology has been shown to be an outstanding approach to discover new polymeric biomaterials for multiple tissue engineering applications e.g. control the growth of human embryonic stem cells or mesenchymal stem cells.[30,31] These microarrays are generally comprised of thousands of different polymer features on a single glass slide, enabling their high-content screening with cells adhering to the polymers forming a "monolayer". However, the loss of their native 3D microenvironment typically would give aberrant cellular behaviour. The development of an array of 3D polymer scaffolds could overcome these limitations offering variety in terms of composition, 3D architecture and mechanical properties. Previous reports have shown that 3D acrylate polymers are excellent candidates to engineer bone tissues.[120,121] Herein, an array of 3D polymer scaffolds was used to identify porous polymers that maintained human osteosarcoma bone cells, with SAOS-2 and MG-63 cells selected as human osteoblast models.[165,181] Scaffolds and cells were targeted to constitute *in vitro* bone models as some properties of the scaffolds resemble the characteristics of bone tissue in terms of an open porous structure and stiffness.[89]

Initially, four different polymer compositions (Table 4-1 and Figure 4-4) were selected based on standard microarray screening of 180 different polymers using SAOS-2 and MG-63 cells (Figure 4-3).

The approach sought to allow the tuning of the 3D architecture and mechanical properties along with composition of the array features, which can lead to differences in cell behaviour. Herein, photo-polymerisation and freeze-casting were combined to robustly generate different acrylate polymers with 3D porous structures. The process included preparation of the solution, cooling/templating, UV photo-polymerisation and washing enabled the fabrication of multiple 3D scaffolds in a single 96-well plate (Figure 4-5). One of the key steps in the process was to maintain the solution in the frozen state during the photo-polymerisation and to ensure homogenous heat transfer through the polypropylene well plate, which was achieved using a custom-made aluminium cooling block and a dry ice bath.

The porogenic solvent (DMSO) and the polymerisation mixture comprising of photo-initiator, cross-linker and monomers, upon freezing, forms two phases: one rich-in-monomers and another rich-in-solvent. The photo-polymerisation of the frozen

sample after phase separation, templating, produced the porous network, a phase rich-in-solvent, and the polymer scaffold, phase rich-in-monomers. Small pores were evident in the absence of the cooling stage (Figure 4-6) as a consequence of a second mechanism involved, polymerisation induced phase separation. In this second mechanism the cross-linked polymers become insoluble during the polymerisation, which also produces phase separation resulting in formation of porous polymers.[73] Although freeze-casting was shown to be more effective in large pores formation, the interplay of both mechanisms gave rise to the 3D polymer scaffold.

Four cooling stages (Figure 4-7) were explored to maximise the quantity and size of the pores (Figure 4-8). SEM and ImageJ-Fiji (Figure 4-9) were used to analyse as well as quantifying the characteristics of the pores depicting the fact that a gradual change of the temperature (so-called “slow cooling”) in the freezing step produced optimal results (Figure 4-10). SEM and ImageJ-Fiji were also employed to determine the effect of the DMSO level on the polymer’s 3D architecture. Increasing the porogenic solvent was shown to favour the formation of pores, but the Feret’s diameter of these pores were found to be reduced (Figure 4-12). Approximately 30% of these pores were found to be in the range of 50 μm to 300 μm (Figure 4-14), deemed optimal for scaffolds in the case of bone repair.[22]

SEM images are a 2D slice of a 3D structure of the scaffold’s surface thus the data obtained were limited. Moreover, the preparation of the samples for SEM with a conductive coating can modify some of the properties measured. A high-throughput approach using micro-CT was developed to overcome these limitations as well as to acquire the data related to the morphological characteristics of the array of 3D polymer scaffolds.[182] The 3D structure of the scaffolds was positively correlated with the concentration of DMSO (Figure 4-15). 3D images illustrated the gradual increase of pores (Figure 4-16 and Figure 4-17) and porosity (Figure 4-18) with the increment of porogenic solvent. An optimal porous scaffold with large open porosity and big pores was formed with 80% DMSO (Figure 4-19). Increase of porogenic solvent did not produce any additional improvement of the porous structure but weakened the polymer network, causing it to collapse.

The size of the interconnection between pores (Figure 4-20 and Figure 4-21), a critical property to understand cell migration into the scaffolds, showed that a good proportion were larger than 100 μm for the **P80** scaffolds (Figure 4-22). All together, these

findings suggest that the array of 3D polymer scaffolds developed can imitate the wide diversity of 3D microenvironment of bone tissues. For example, the outer layer of the cortical section of bones is highly dense with low number of cells and porosity, similar to the **P40** or **P60** scaffolds. On the other hand, the inner layer of many bones is an extremely porous and vascularised structure, trabecular section, with higher density of cells, comparable to **P80** scaffolds.[89,104] Moreover, the presence of pores larger than 200 μm suggested that **P80** scaffolds could be potential candidates to promote *in vivo* vascularisation.[112]

Deeper insight into the physical properties of the polymeric biomaterials was gained using macro-indentation,[137,183] which allowed measurement of the indentation moduli of the 3D scaffolds (Figure 4-23). Mechanical properties of the polymer scaffolds were shown to be tuned with respect to the polymer composition (Figure 4-24) and the level of porosity (Figure 4-25). For example, scaffolds with large porosity (**P80**) displayed a significantly reduced indentation moduli compared to scaffolds of low and medium porosity (**P0** and **P60**), which were comparable. Scaffold density was used to normalise the indentation moduli in order to elucidate the effect scaffold 3D microstructure has on its mechanical properties (Figure 4-27), confirming that porosity was the main reason for reduced stiffness. These differences between mechanical properties of scaffolds were a result of complex interplay of polymer composition, level of DMSO and 3D architecture characteristics. For example, the formation of an anisotropic material has been shown to increase the stiffness of a scaffold compared to a more randomly distributed structure.[172] Overall, the indentation moduli were found to cover a broad range of tissues such as kidneys or muscles (6 and 16 kPa correspondingly), collagenous bone (≈ 100 kPa) and mineralised bone (from 6 to 14 GPa), which successfully shows that a variety of tissues can be explored in the future.[103,136]

The relaxation load is an important mechanical property for tissues such as bone and cartilage that undergo sustained stress.[184] Healthy bone and cartilage are viscoelastic tissues with relatively good elastic properties that protect the tissues from plastic deformation.[185,186] Cancellous bone exhibits a broad relaxation load that vary from 19% after 7 min and 26% after 100 seconds,[187,188] while human costal cartilage has a relaxation load of about 60% after 2 min.[189] Relaxation load for the polymer scaffolds explored here varied from 16% to 57% after 5 min in the case of scaffolds **P80-B** and **P80-D** (Figure 4-28). Consequently, the polymer scaffolds were observed

in the range of both bone and cartilage which suggests that scaffolds could support either tissue, hence expanding their applicability in the area of both bone and cartilage repair.

24 polymer scaffolds, 4 polymer compositions with 6 levels of DMSO, were constructed in quadruplicate to obtain an array of 96 scaffolds (Figure 4-29). The effect of DMSO level on the porosity was analysed using a liquid displacement approach (Figure 4-30). The reproducibility (Figure 4-31) and scalability (Figure 4-32) of the technique to fabricate arrays of porous polymers was confirmed. Porosity was independent of the polymer composition in agreement with previous SEM or micro-CT analysis. Moreover, thermogravimetric analysis showed polymer stability below 300 °C (appendix B).

An array of 3D polymer scaffolds based on **polymer A** was used to develop an efficient route to screen SAOS-2 cellular behaviour on porous polymers. Alamar Blue, SEM and Alizarin red were used to assess cell viability, cell-scaffold morphology and biomineralisation. Alamar Blue showed that SAOS-2 cells were more selective to the scaffolds than MG-63 (Figure 4-34 and Figure 4-35), which was also consistent with the results of the microarray. The integration of SAOS-2 cells within the scaffolds and formation of ECM on the polymer structure was shown for scaffolds **P60-A** and **P80-A** using SEM (Figure 4-36). The mineralisation of SAOS-2 cells in the model array of 3D polymer scaffolds was tested using a colorimetric assay based on acid alizarin red after 7 days of cell incubation in mineralisation medium.[143] The scaffolds based on **polymer A** (**P0** to **P80**) showed an increase of mineralisation with increase of porosity (Figure 4-37). However, negative controls showed a strong non-specific binding.[190]

Among the three different assays performed in the array of **polymer A** (cell viability with Alamar Blue, cell morphology with SEM and mineralisation with alizarin red), Alamar Blue was chosen to further screen the 24 3D polymer scaffolds (Figure 4-29). Alamar Blue was non-destructive as several assessments on the same scaffold can be performed. Moreover, reagents and products, resazurin and resorufin, are highly soluble in water.

From the four polymer compositions explored in the array only the scaffolds of **polymer B** were shown to be successful candidates to fabricate porous biomaterials (Figure 4-38). These scaffolds presented little differences in the number of SAOS-2 cells compared with the tissue culture plate (control) and showed a significant

increase in the number of cells between days 1 and 7 suggesting robust cell proliferation. By contrast, **polymer A** could maintain SAOS-2 cell for the same length of time, but cell proliferation was not observed.

SAOS-2 cell viability and scaffold toxicity were further evaluated by a live/dead staining (Figure 4-39). Polymers **A** and **B** with low (**P0**), medium (**P60**) and high (**P80** and **P85**) porosity were selected as they represented different cell behaviour in the previous screening. The assay showed high cell viability for these scaffolds with few dead cells in the 3D scaffolds which was corroborated by Alamar Blue. Automated microscopy and high-content screening allowed live 3D cell imaging in the porous scaffolds, however, it was revealed as one of the challenges of the approach as the presence of cells in different layers and the uptake of dyes by the porous structure increased background fluorescence, compromising the quality of the imaging (Figure 4-40).

Distribution of SAOS-2 cells on the 3D scaffolds of **polymers A** and **B** with medium (**P60**) and high (**P80**) porosity showed the cells in different layers of the 3D structure (Figure 4-41). Polymers with the largest pore size (**P80**) had cells in deeper layers of the scaffolds in comparison with the **P60** scaffolds, demonstrating the vast potential to construct tissue-like 3D structures. The analysis of the cytoskeleton orientation of SAOS-2 cells on the 3D scaffolds indicated that polymer scaffolds with large porosity changed the orientation of the filament of actin from disorganised (**P60**) to more organised (**P80**) distributions (Figure 4-42). The potential reorganisation of the actin filaments because of the polymeric structure, geometric cues, can promote differences in mechanotransduction mechanisms that guides differences in the cellular fate as previously described.[16,159]

The analysis of the combined effect of mechanical properties (stiffness and load relaxation) and porosity on SAOS-2 cell behaviour (attachment and proliferation) allow for a deeper understanding of cell – biomaterial interactions (Figure 4-43) in the case of polymer scaffolds with low (**P0**), medium (**P60**) and high (**P80**) porosity. Stiffness of the 3D scaffolds in the range of 500 kPa to 20 MPa were shown to be the driving force for attachment of SAOS-2 cells and their maintenance over seven days in culture (Figure 4-44). Moreover, cell proliferation obtained on **polymer B** scaffolds highlighted the importance of providing the right chemical as well as physical cues.[191]

4.4 Conclusions

Successful functional biomaterials need to provide the right collection of mechanical, physical and chemical signals that enhance or drive cell behaviour. However, the enormous variety of different cues that act simultaneously hinder a full understanding of these processes. High-throughput approaches have played a crucial role to untangle these mechanisms as they allow screening of multiple combinations simultaneously. However, current combinatorial technologies still struggle to take into account the material signals found in 3D architectures.

Herein, a method to fabricate arrays of 3D polymer scaffolds was developed where the chemical composition of acrylate polymers in addition to their 3D structure and mechanical properties were controlled. Multifunctional 3D structures in the form of arrays of 96 polymer scaffolds were fabricated *via* freeze-casting in a standard cell culture platform. Characteristics of the porous polymers were tuned using different gradients of temperature and concentration of the porogenic solvent i.e. DMSO. A high-throughput micro-CT approach was developed to analyse the effect of DMSO concentration on the 3D structure, revealing the majority of the quantified pores and throats were larger than 100 μm. Additionally, the mechanical characteristics of these scaffolds were tuned using different levels of DMSO to cover a wide range of compressive properties that mimic the mechanical properties of a variety of tissues from muscles to collagenous bone.

Bone tissue was selected as a proof of concept for understanding the applicability of developed method. The osteosarcoma bone cells, SAOS-2, were used to screen and select the scaffold composition in addition to exploring the limitations of the 3D platform. Proliferation was found to be maximal in porous scaffolds of **polymer B**, poly(IBA_{72}-*co*-$HDOBA_{18}$), fabricated with DMSO as the porogenic solvent *via* cryo-polymerisation. Overall, the array of 3D scaffolds was shown to provide different polymer compositions, 3D structures and mechanical properties allowing a detailed study of the combined effects of these characteristics on cell behaviour.

5. Discovery of 3D polymer scaffolds with enhanced vascularisation for bone repair

The work presented in this section was carried out in collaboration with Dr Deepanjalee Dutta and Mr Michael Glinka. Dr Dutta supported the immunofluorescence analysis of osteogenic markers while Mr Glinka carried out the in vivo implantation of scaffold in choriallantoic membrane (CAM) and mouse subcutaneous models.

Parts of this chapter have been submitted as:

A. Conde-González[*], M. Glinka[*], D. Dutta[*], (equal contribution) R. Wallace, D. Norman, A. Callanan, R. O. C. Oreffo and M. Bradley (**2019**). 3D Porous Growth-factor free Scaffolds Supporting Enhanced Vascularization for Tissue Repair.

5.1 Introduction

Stem cell-based transplantation therapies have shown huge potential in the treatment of diseased tissues. For example, human tracheal replacement therapy was explored using a decellularised trachea obtained from a cadaveric donor seeded *ex vivo* with MSCs.[192] However, these approaches need to artificially isolate and expand stem cells. Additionally, these approaches had a limited effect for an extended period. Synthetic polymer scaffolds have been successfully applied to support stem cell growth and function in stem cell transplantation strategies.[193] For example, Atala *et al.* successfully engineered an autologous bladder as an alternative to current end-stage disease bladder therapy.[194] The approach used engineered scaffolds based on homologous decellularised donor bladder submucosa and a collagen-poly(glycolic acid) composite. Autologous urothelial and muscle cells were seeded into these scaffolds and implanted during cystoplasty as an alternative to current therapies using gastrointestinal tissue.

Bone is known to be a highly challenging tissue to repair, owing to the complexity of its physiological microenvironment, which includes a mineralised extracellular matrix, a soluble phase of growth factors and multiple cellular components such as osteoblasts, osteoclasts and osteocytes. Additionally, bone tissue is also metabolically active with supply of oxygen and nutrients by an extensive vasculature. One particularly demanding aspect for 3D biomaterials is the ability to promote

vascularisation, which triggers a cascade of molecular and cellular events leading to bone healing processes.[89] In order to induce successful bone tissue, scaffolds need to promote substantial vascularisation to avoid tissue necrosis. Angiogenesis is controlled by host endothelial cells in the blood vessel inner lining, secreting growth factors such as VEGF, vascular endothelial growth factor, triggered by hypoxia. Moreover, VEGF is known to control skeletal progenitor cell differentiation and osteoblast behaviour, which is considered to be a prerequisite for osteogenesis to occur.[95] On the other hand, a previous report suggests that primary human osteoblasts guide host endothelial cells to proliferate and migrate into silk fibroin scaffolds promoting vascularisation.[195] To enhance vascularisation, previous 3D scaffold approaches have also explored the use of calcium phosphate and metal ions as well as osteogenic dopants with the release of growth factors such as BMP-2 and VEGF.[196–199] For example, Oreffo demonstrated the release of encapsulated vitamin C (2-phosphate-L-ascorbic acid) and VEGF from poly(lactic-co-glycolic acid) nanoparticles covalently bonded to 3D porous scaffolds *via* biotin-avidin conjugation.[150]

Microarray technology has enabled the high-throughput screening of biomaterials. However, these polymer biomaterials have been selected based on cells in “2D” (monolayer of cells adhered to the polymer surface) and current available approaches are not able to recapitulate the requisite “3D” in a multi-material and multi-microstructure design.[160] In order to become truly outstanding alternatives, “3D” biomaterials need to recapitulate the complex physicochemical and mechanical space of native tissues.[180,200] In this chapter, a 3D screening method was established to study the effect of 3D polymer scaffolds on foetal bone marrow stromal cells (FBMSCs). FBMSCs were isolated as per the ethical approval obtained from Southampton & South West Hampshire Local Research Ethics Committee (LREC296/100). These cells were selected for 3D screening because of their ability to drive osteoblastic differentiation and their highly proliferative behaviour.[201] Subsequently, the top 3D polymer candidates were validated *in vitro*, to assess FBMSCs differentiation state. Additionally, *ex vivo* validation was performed with chick chorioallantoic membrane (CAM) and an *in vivo* mouse subcutaneous model was employed to evaluate scaffold biocompatibility and angiogenic potential (Figure 5-1).

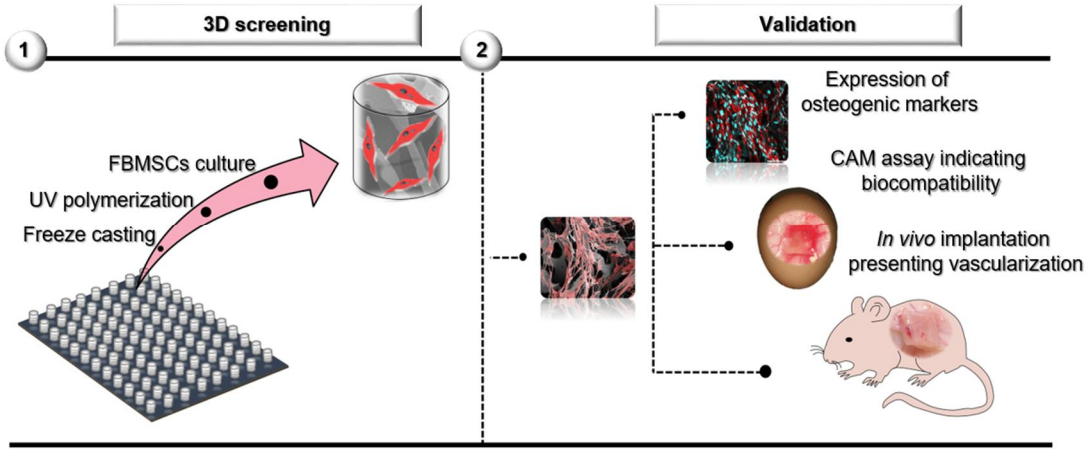

Figure 5-1. 3D screening and validation approach to develop 3D polymer scaffolds with enhanced vascularisation for bone repair. An array of 3D polymer scaffolds based on porous and non-porous polyacrylate substrates was prepared through freeze-casting and photo-polymerisation. FBMSCs were used to interrogate the 3D polymer scaffolds and identify optimal polymer composition and 3D microstructure. Selected candidates were scaled-up to assess osteogenic markers, biocompatibility and angiogenesis.

5.2 Results

5.2.1 Screening of 3D polymer scaffolds and characterisation

I. Substrate selection and 3D array fabrication

Five acrylate-based monomers were selected to fabricate 3D polymer scaffold arrays (Figure 5-2). These acrylates monomers were chosen on the basis of their ability to produce polymers that promoted bone cell line attachment (appendix A and section 4.2.1) and control stem cell fate.[30] Moreover, polymers of EGDPEA were used as a control with low bone cell line attachment. These five monomers and their combinations were used to obtain 15 different co-polymers (Table 5-1).

Arrays of 3D porous scaffolds in flat-bottomed polypropylene 96-well plates were obtained *via* freeze-casting and photo-polymerisation, using DMSO as the porogenic solvent and the slow cooling approach (5 °C for 16 h followed by -20 °C for 4 h) as previously established. FTIR fingerprints were used to characterise the scaffolds after cryo-polymerisation and to ensure the efficiency of the washing step in removing unreacted components (Figure 5-5).[202,203] The 15 different polymer mixtures were combined with three levels of DMSO to obtain scaffolds **P60** with “medium” (60% v/v

DMSO), **P80** with “high” (80% v/v DMSO) porosity and their non-porous control **P0** (0% v/v DMSO). These combinations resulted in an array containing 45 different 3D structures.

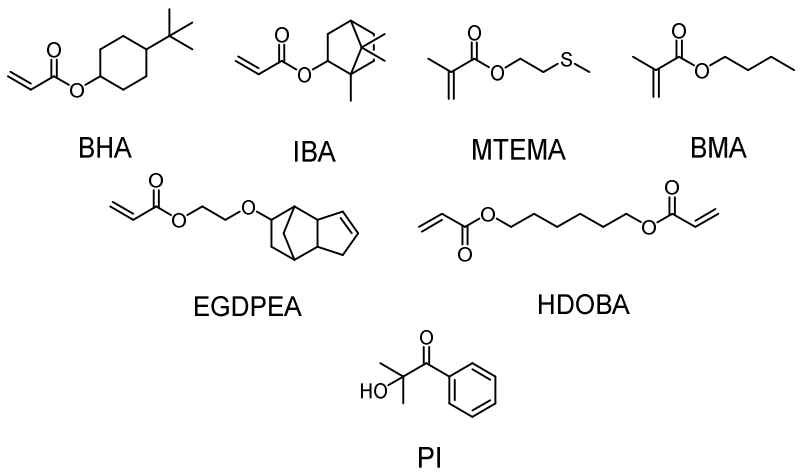

Figure 5-2. Monomers, cross-linker and photo-initiator that were used to fabricate the selected co-polymers. 4-*tert*-butylcyclohexyl acrylate (BHA), isobornyl acrylate (IBA), 2-(methylthio)ethyl methacrylate (MTEMA), butyl methacrylate (BMA), ethylene glycol dicyclopentenyl ether acrylate (EGDPEA), the cross-linker 1,6-hexanediol diacrylate (HDOBA) and the photo-initiator (PI) hydroxy-2-methylpropiophenone.

Table 5-1. The polymerisation mixtures/monomer ratios were obtained by mixing the acrylate monomers A and B, the cross-linker (18 mol %) and the photo-initiator (10 mol %).

Polymer	Monomers		Monomers (mol %)	
	A	B	A	B
1	IBA	-	72	-
2	MTEMA	IBA	36	36
3	MTEMA	EGDPEA	36	36
4	BMA	BHA	36	36
5	BMA	IBA	36	36
6	BMA	EGDPEA	36	36
7	BHA	IBA	36	36
8	BHA	EGDPEA	36	36
9	IBA	EGDPEA	36	36
10	MTEMA	BMA	36	36
11	MTEMA	BHA	36	36
12	MTEMA	-	72	-
13	BMA	-	72	-
14	BHA	-	72	-
15	EGDPEA	-	72	-

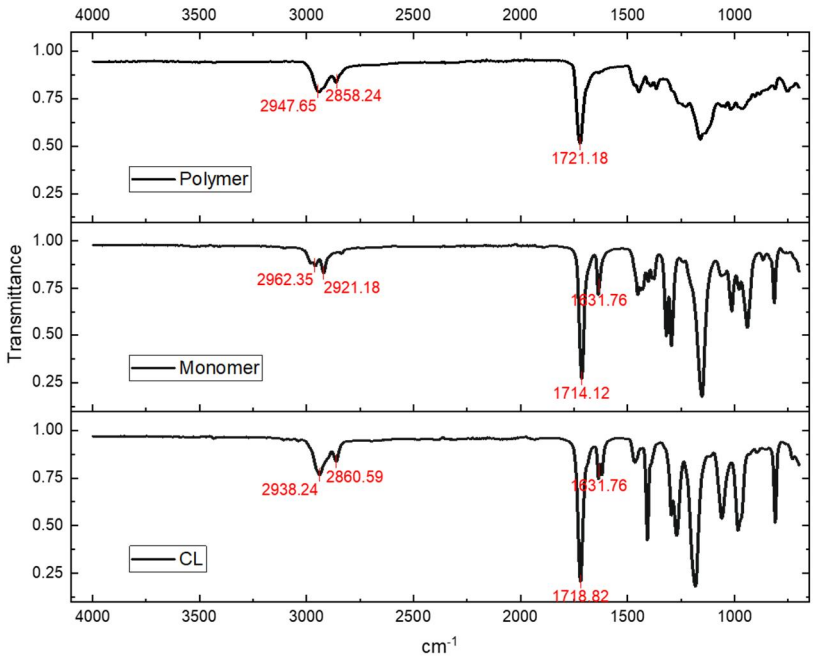

Figure 5-3. FTIR spectra of **polymerisation mixture 12** (Table 5-1) before and after polymerisation. The scaffolds were obtained using DMSO (80% v/v) as the porogenic solvent and UV photo-polymerisation carried out on top of a dry-ice-bath (– 70 ºC) to maintain the samples in a frozen form. Ester IR fingerprints were seen in the monomer, cross-linker and polymer spectra between 1714 and 1721 cm^{-1}. Vibrational peaks of the uncured monomer and cross-linker revealed the presence alkenyl stretching vibration at 1632 cm^{-1}, which were absent after polymerisation.

II. Screening of 3D polymer scaffolds with FBMSCs

Arrays of 3D polymer were used to assay FBMSCs behaviour with proliferation assessed with Alamar Blue (Figure 5-4) over 21 days on the 45 scaffolds obtained by combining **polymers 1-15** with three levels of porgenic solvent (**P0**, **P60** and **P80**).

Control, non-porous scaffolds (**P0**), showed a rapid increase in the number of FBMSCs in the majority of the polymers between days 0 and 2 followed by a stationary phase between days 7 and 21 (Figure 5-5 and Figure 5-6). FBMSCs on scaffolds **P60** and **P80** had slower proliferation rates reaching a plateau in cell proliferation at day 7 for the majority of the polymers. These observations suggested that FBMSCs covered all the available surfaces on the 3D scaffolds during the first

week of culture. Moreover, large differences between FBMSCs on scaffolds and on tissue culture well plates (control) were not observed at day 21 (Figure 5-9).

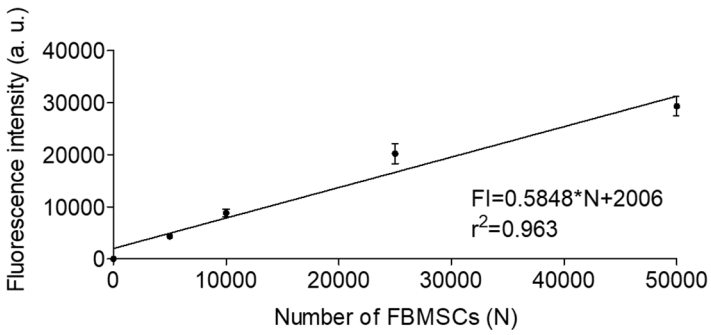

Figure 5-4. Calibration curve of the number of FBMSCs plated and the resulting Alamar Blue fluorescence intensity. Alamar Blue in medium (10% v/v) was added to the wells 2 hours after seeding to ensure cell attachment to the plate. Incubation was performed for 4 hours in a humidified atmosphere (37 °C and 5% CO_2). Supernatant was collected and, subsequently, fluorescence was read in a microplate reader ($\lambda_{ex/em}$ = 530/590). Mean ± SD, n=3.

Based on these initial results, **polymers 1-6** were selected for further analysis as **polymers 1**, **2** and **4-6** had a high proliferative rate, while **polymer 3** was included as a control as FBMSCs showed lower proliferative behaviour on this material. **Polymers 7-15** were discarded as they showed large error bars (indicating poor reproducibility in the polymer characteristics) or had lower proliferation rate than the candidates selected.

Total collagen deposition was quantified on a 3D array of **polymers 1-6** with “medium” (**P60**) and “high” (**P80**) porosity along with their non-porous control (**P0**) using the picro-sirius red assay.[146,147] Increased collagen expression at day 21 was observed in the porous scaffolds (**P60** and **P80**) of **polymers 2** and **3** compared to non-porous scaffolds and tissue well plate controls (Figure 5-7). Overall, the majority of the porous polymer scaffolds exhibited larger total collagen deposition than controls, suggesting that the 3D microenvironment supports the formation of extracellular matrix (Figure 5-9).

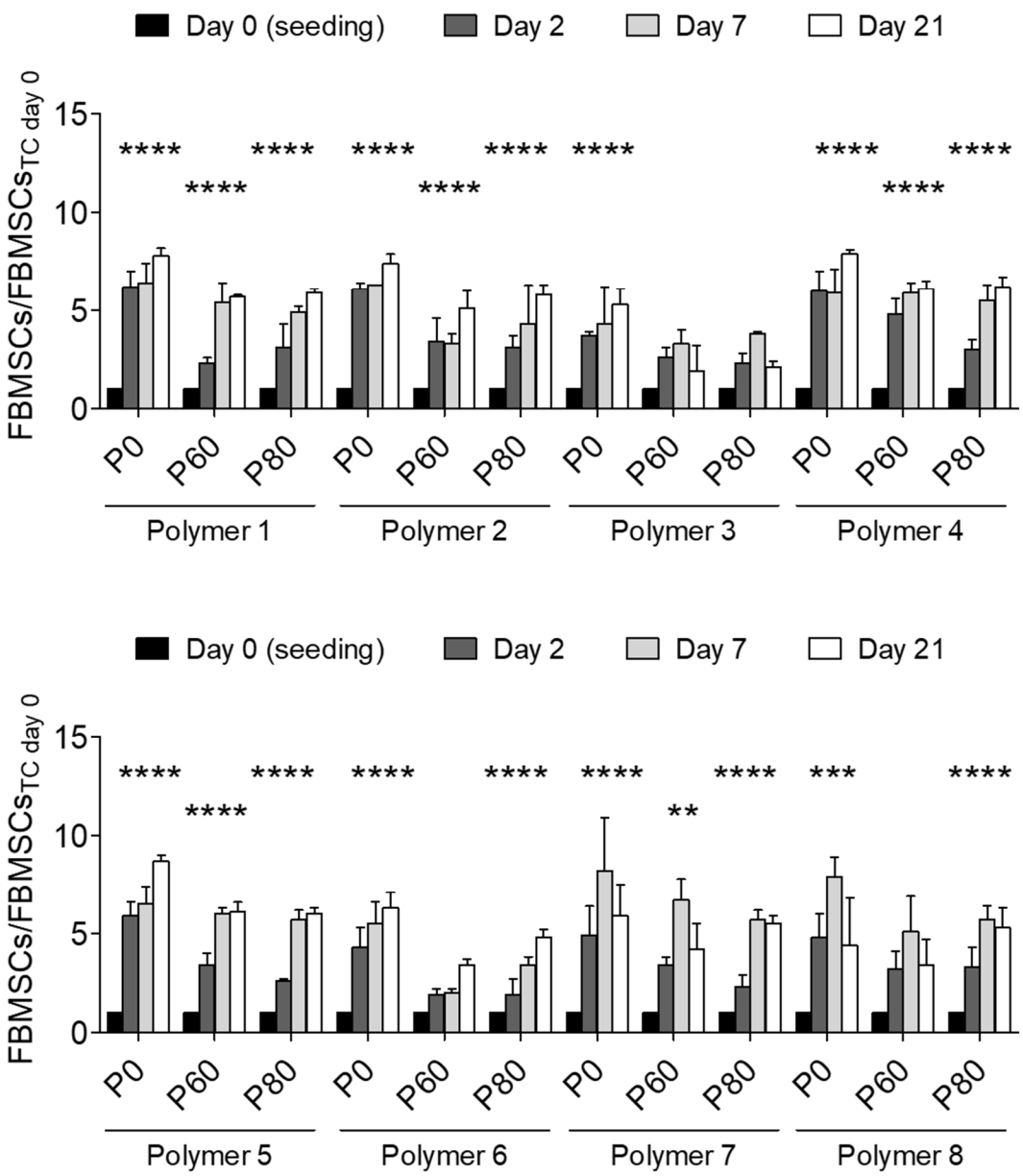

Figure 5-5. FBMSCs proliferation on the 3D arrays. Fold change of fluorescence (based on Alamar Blue) between day 0 (seeding 10,000 FBMSCs/well) and the scaffolds of **polymers 1-8** with medium (**P60**) and high (**P80**) porosity and their non-porous controls (**P0**) at days 2, 7 and 21 (n=3). Two-way ANOVA with Bonferroni post-test (** $p \leq 0.01$, *** $p \leq 0.001$ and **** $p \leq 0.0001$) was carried out between day 0 and day 21. Mean ± SD, n=3.

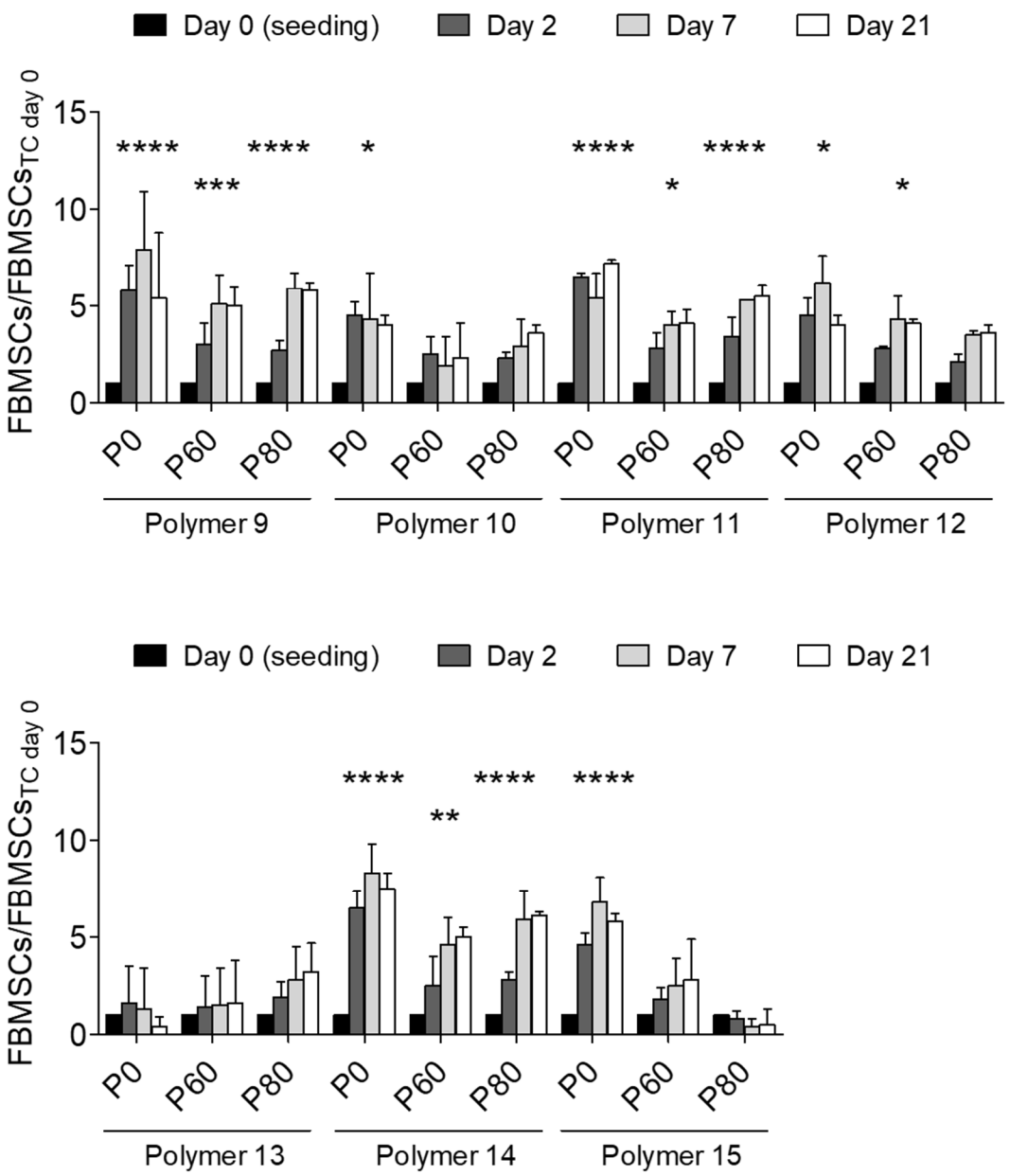

Figure 5-6. FBMSCs proliferation on the 3D arrays. Fold change of fluorescence (based on Alamar Blue) between day 0 (seeding 10,000 FBMSCs/well) and the scaffolds of **polymers 9 -15** with medium (**P60**) and high (**P80**) porosity and their non-porous controls (**P0**) at days 2, 7 and 21 (n=3). Two-way ANOVA with Bonferroni post-test (* $p \leq 0.05$, ** $p \leq 0.01$, *** $p \leq 0.001$ and **** $p \leq 0.0001$) was carried out between day 0 and day 21. Mean ± SD, n=3.

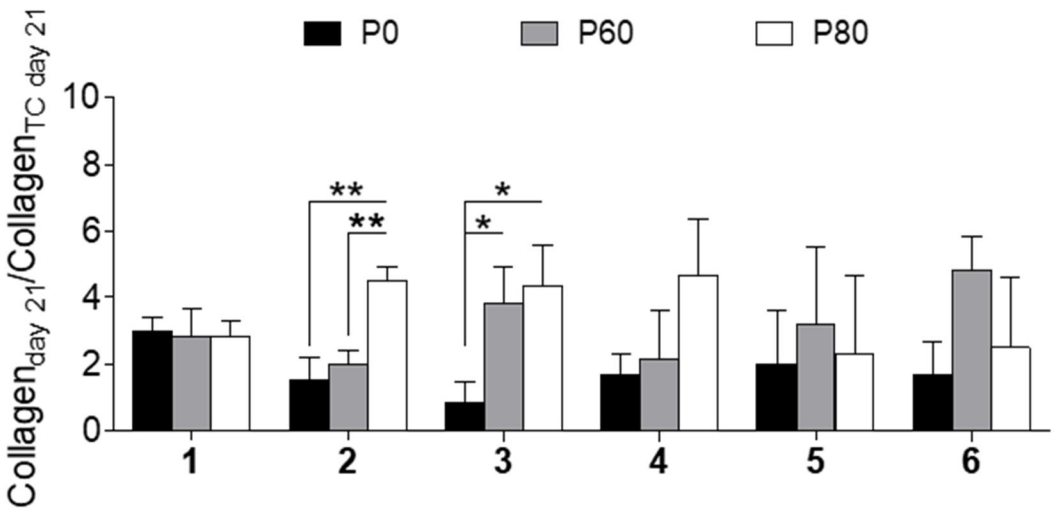

Figure 5-7. FBMSCs total collagen on the 3D arrays. Fold change of absorbance (picro-sirius red staining of collagen) between the TC control and the scaffolds of **polymers 1-6** with medium (**P60**) and high (**P80**) porosity and their non-porous controls (**P0**) after 21 days of incubation. One-way ANOVA with Bonferroni post-test (* $p \leq 0.05$ and ** $p \leq 0.01$) was carried out between the control P0 and the porous scaffolds P60 and P80. Mean ± SD, n=3.

An array of 18 polymer scaffolds (versions **P0**, **P60** and **P80** of **polymers 1-6**) was prepared to assess alkaline phosphatase activity (ALP), an early osteoblast differentiation marker. ALP activity was quantified at days 2, 7 and 21 and normalised to total DNA concentration and control tissue well plates using a previously published chromogenic approach.[148,149] FEBMSCs seeded into 3D polymer scaffolds showed an increase of ALP activity at day 7 followed by a subsequent reduction in ALP levels at day 21 across the majority of the conditions (Figure 5-8). However, TC control show reduced variation of ALP in the same period. **P0** and **P60** scaffolds of polymer **1**, **2**, **5** and **6** did not showed large differences with TC control and followed the same trends. On the other hand, **P0** and **P60** scaffolds of polymers **3** and **4** displayed more ALP than TC control. FBMSCs expressed high levels of ALP on **P80** scaffolds of polymer **1** to **3**, **5** and **6** at day 7 than at day 2 with a decrease of ALP at day 21. The highest change of ALP was produced on **P80-3** scaffolds that showed a fold increase over 4 decreasing to 0 at day 21. However, FBMSCs on constructs of **polymer 4** displayed a delayed ALP activity at day 21. Overall, ALP levels were higher in the majority of the polymer scaffolds with high porosity than the control tissue culture (TC) well plate at day 7 (Figure 5-9)

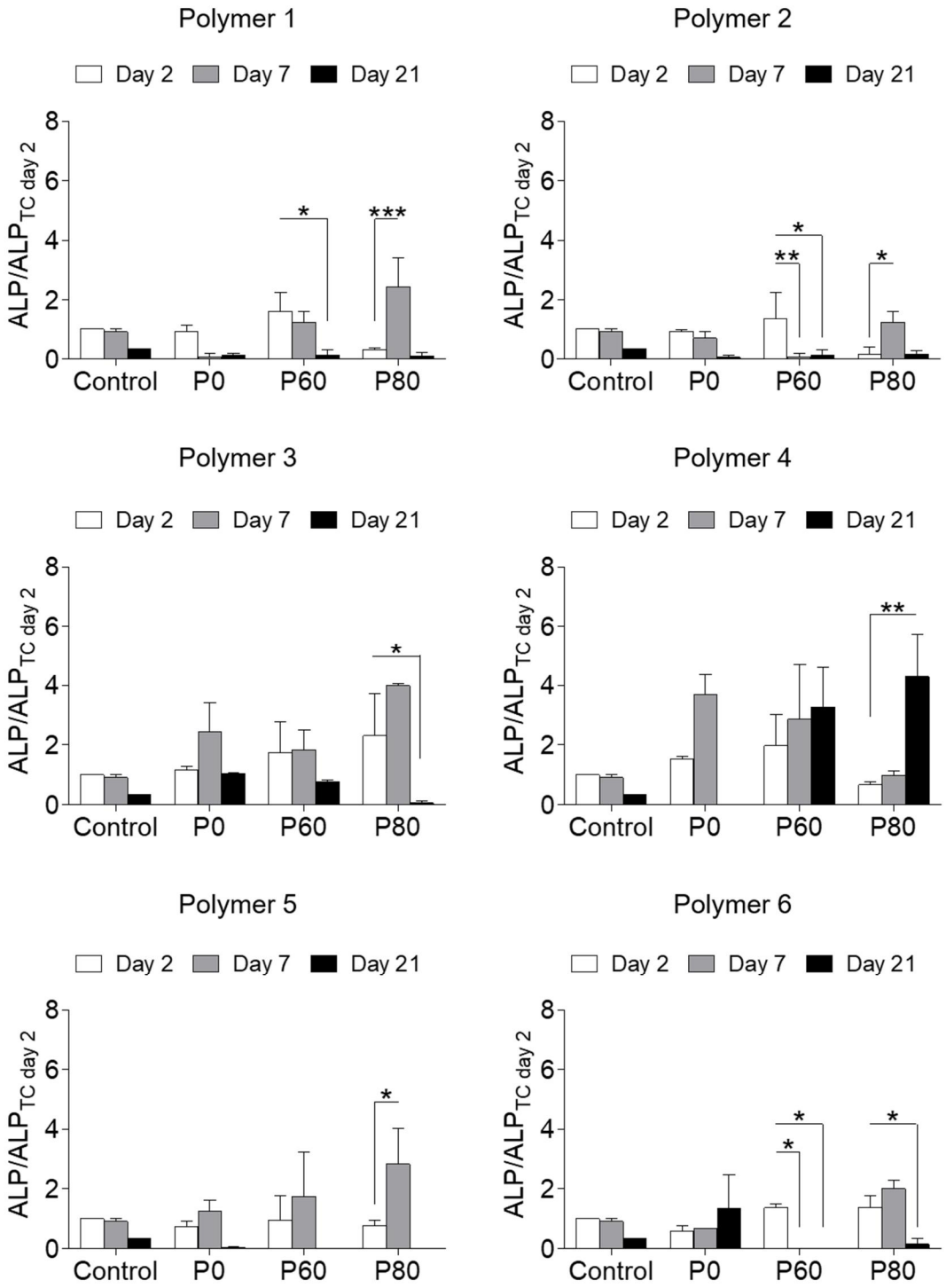

Figure 5-8. FBMSCs alkaline phosphatase (ALP) quantification on the 3D arrays. Fold change of absorbance (chromogenic enzymatic cleavage of phosphatase substrate) between the TC control at day 2 and the scaffolds of **polymers 1-6** with medium (**P60**) and high (**P80**) porosity and their non-porous controls (**P0**) at days 2, 7 and 21. Two-way ANOVA with Bonferroni post-test (* $p \leq 0.05$, ** $p \leq 0.01$ and *** $p \leq 0.001$) was carried out between day 2, day 7 and day 21. Mean ± SD, n=2.

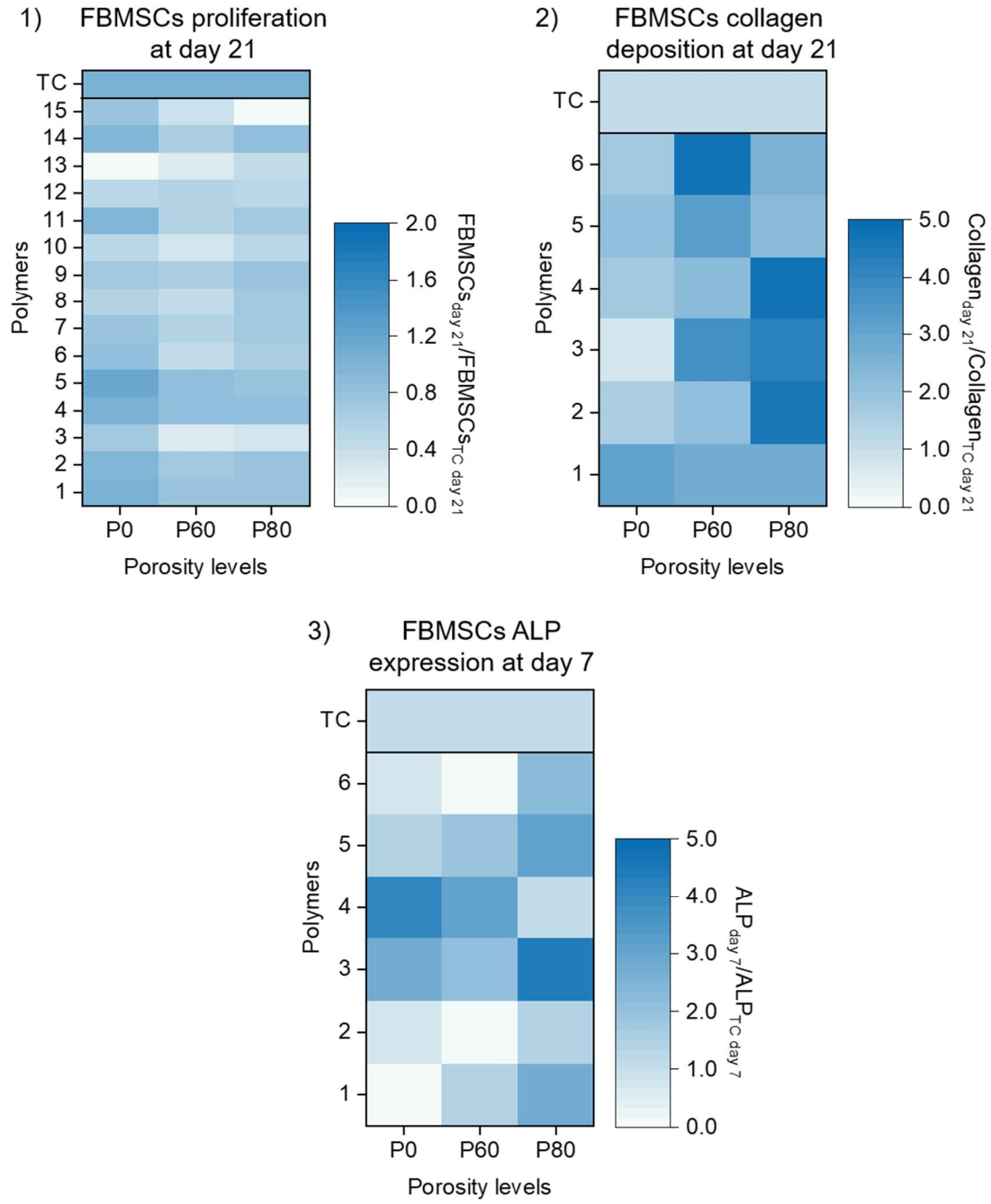

Figure 5-9. Summary of FBMSCs behaviour on the arrays of 3D polymer scaffolds (**P0-P80**) normalised with control FBMSCs on tissue culture well plates (TC). 1) FBMSCs proliferation on scaffolds of **polymers 1-15** at day 21 (FBMSCs $_{\text{day 21}}$/FBMSCs $_{\text{TC day 21}}$). 2) FBMSCs total collagen on scaffolds of **polymers 1-6** day 21 (Collagen $_{\text{day 21}}$/Collagen $_{\text{TC day 21}}$). 3) FBMSCs ALP quantification on scaffolds of **polymers 1-6** at day 21 (ALP $_{\text{day 7}}$/ALP$_{\text{TC day7}}$).

III. 3D microstructure and mechanical characterisation of the 3D scaffolds

Analysis of the scaffold 3D microstructure was achieved using micro-computed tomography (micro-CT). The high-throughput screening method employed rectangular sections of 96-well plates to obtain cuboids of twelve 3D polymer scaffolds (2×2×3 wells) that were scanned simultaneously. It allowed rapid assessment of the 3D structure of 18 polymer scaffolds (versions **P0**, **P60** and **P80** of **polymers 1-6**).

Representative images illustrate the changes in porosity and pore size with different DMSO levels (Figure 5-10). Representative longitudinal and transverse section for scaffolds **P60-2** and **P80-2** demonstrated the highly interconnected porous structure of **P80** scaffolds with high porosity (Figure 5-11, 1). In contrast, **P60** scaffolds contained fewer interconnected pores as a consequence of having higher polymer density. The porosity and pore size distribution of the 3D polymer scaffolds were quantified using the BoneJ plugin in ImageJ-Fiji.[134] The level of DMSO in the polymerisation mixture (from 0% to 80% v/v) was shown to control the degree of porosity in the scaffolds as expected (Figure 5-11, 2). The porosity for **P0** scaffolds of polymer **1** to **6** were below 1% whereas **P60** scaffolds varied between 55% and 70%. The highest porosity was achieved for **P80** scaffolds of polymer **1** to **6** which excided 80%. 3D distance modelling, using BoneJ, showed that the average pore size of the **P80** scaffolds was close to 100 µm independent of polymer composition. Moreover, pore size distribution of several scaffolds, such as **P80-2**, was spread out much more than 200 µm.

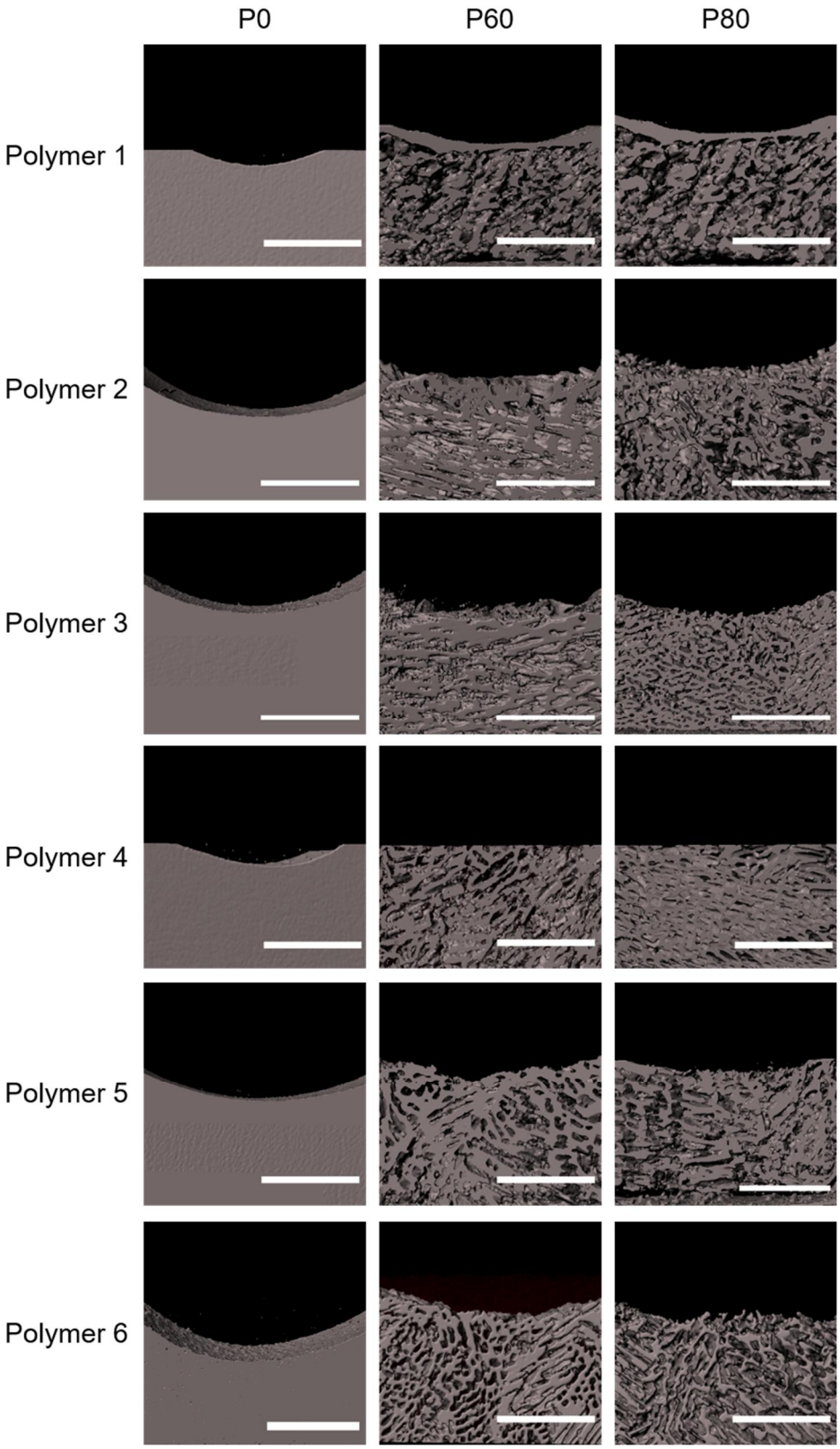

Figure 5-10. 3D images of the porous scaffolds. Longitudinal section constructed using the micro-CT data of the array of 3D porous scaffolds for scaffolds with medium (**P60**) and high (**P80**) porosity and their non-porous control (**P0**) for **polymers 1-6** (scale bar = 1.5 mm).

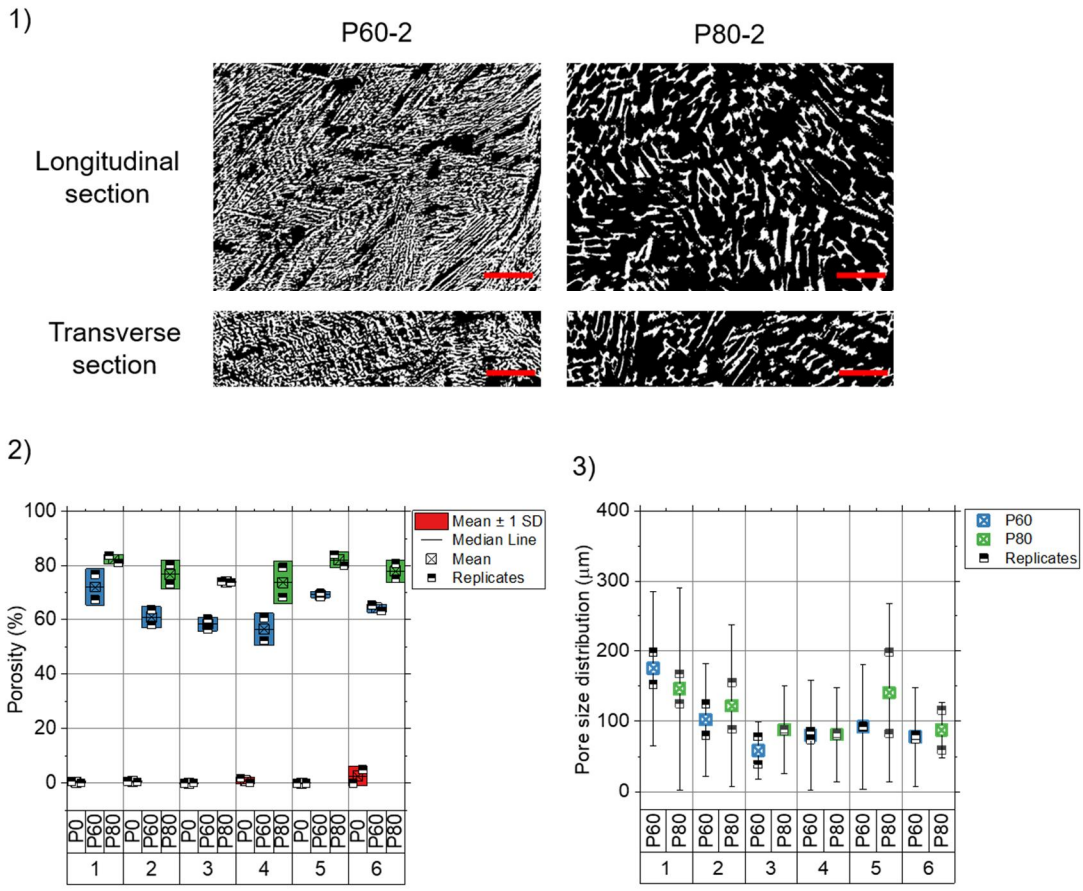

Figure 5-11. Morphological characterisation of the 3D polymer scaffolds using micro-CT. 1) Binary images (white polymer and black pores) of the longitudinal and transverse section for representative scaffolds **P60-2** and P80-2 (scale bar = 1.0 mm). 2) Scaffold porosity (%) and pore size distribution (µm) calculated with computed spheres that fitted the pore space (using the ImageJ-Fiji plugin BoneJ). Red for **P0**, blue for **P60** and green for **P80**. Mean ± SD, n=2.

Indentation moduli, also known as stiffness, of the 3D polymer scaffolds was assessed using indentation. Scaled-up polymer scaffolds (≈ 12 mm length × 12 mm width × 1 mm height) of **polymer 1-6** with medium and high porosity (**P60** and **P80**) and their non-porous control (**P0**) were prepared using polystyrene moulds (12 mm length × 12 mm width × 7 mm height). The indentation moduli were calculated locally for 4 ranges of strain percentages (0-5, 5-10, 10-15 and 15-20) using a linear model for semi-infinite samples, ratio sample area to indenter diameter ≥3, as previously described.[135–137] In addition, the relaxation load for the 3D polymer scaffolds was measured after 5 min.[138,139]

The indentation moduli were shown to be reduced with an increase of DMSO. **P0** scaffolds had higher indentation moduli than scaffolds **P60** and **P80** with the exception of **P60-2**, which was shown to be stiffer than P0-2 (Figure 5-12). Strain range between 5% - 10% were determined to be suitable for reducing the effect of the surface properties. In this range, **P80-2** and **P80-3** were observed to be 3 MPa and 22 kPa, which illustrates the broad range of mechanical properties provided by these high porosity scaffolds.

Relaxation load of the 3D scaffolds was governed by scaffold composition, showing an increase in the load relaxation with the increase in porosity with the exception of **polymer 1** scaffolds that displayed the opposite behaviour (Figure 5-13). Generally, **P80** scaffolds achieved relaxation loads around 40%, for example, relaxation was 47% in the case of **P80-2**.

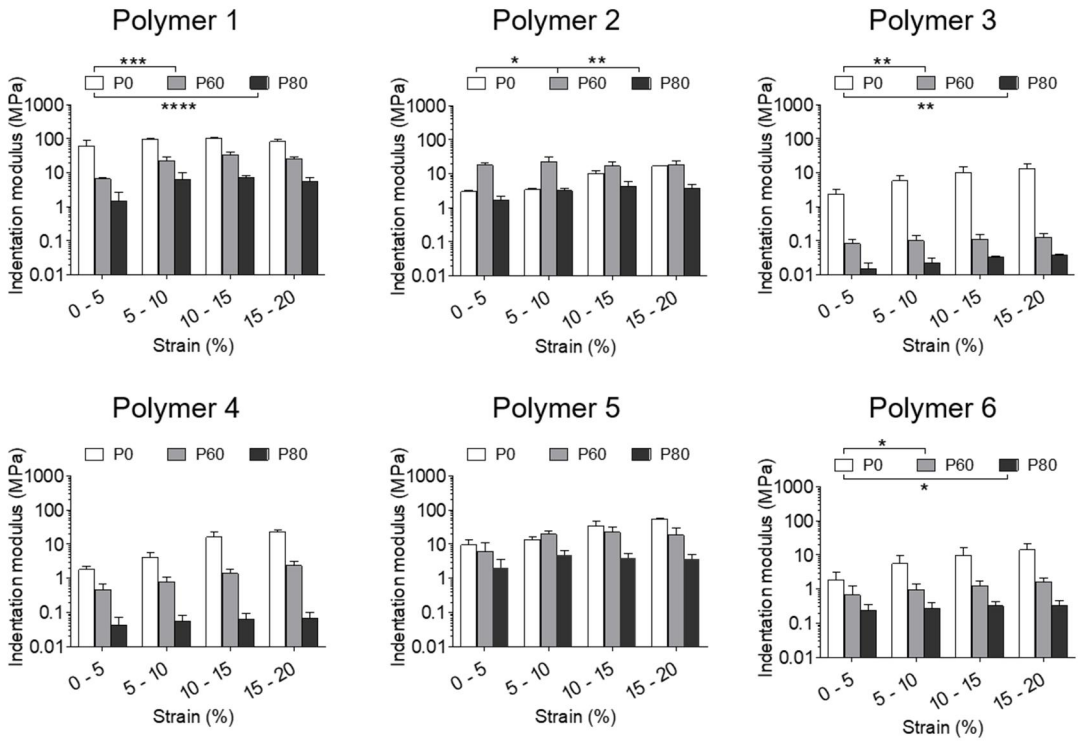

Figure 5-12. Indentation moduli for porous scaffolds (**P60** and **P80**) and their non-porous control (**P0**) for **polymers 1-6**. Macro-indentation approach using a mechanical system for compression (Instron) equipped with a flat indenter (Ø = 1mm). Indentation moduli were calculated from the gradient of the load-displacement curves between 0%-5%, 5%-10%, 10%-15% and 15%-20%. One-way ANOVA with Bonferroni post-test (* $p \leq 0.05$, ** $p \leq 0.01$, *** $p \leq 0.001$ and **** $p \leq 0.0001$). Mean ± SD, n=4.

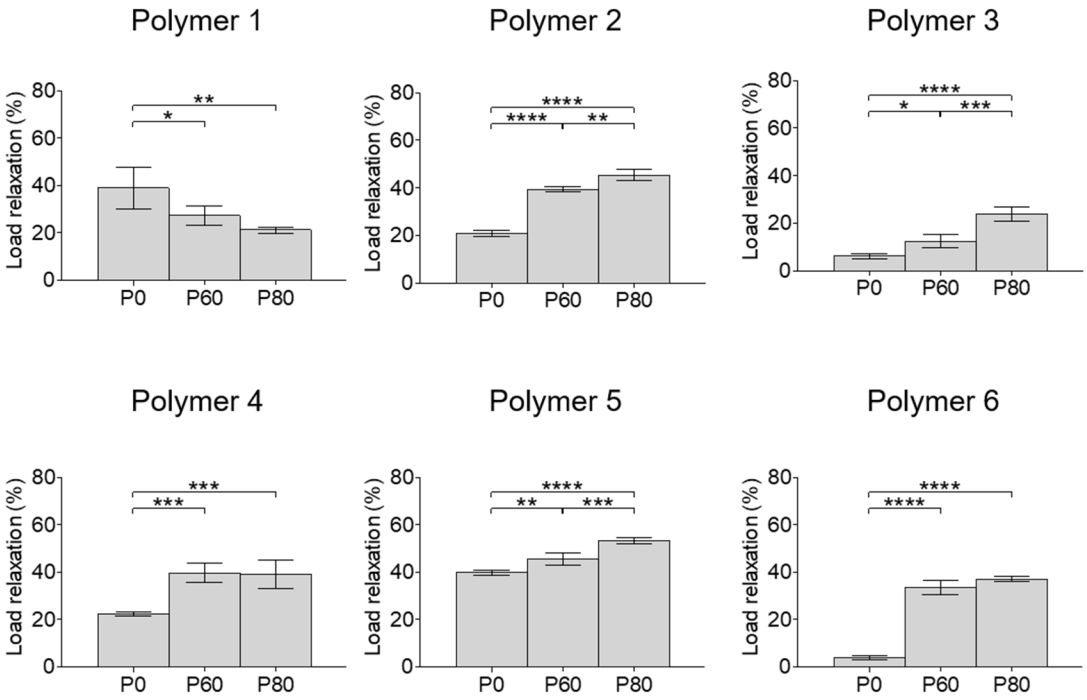

Figure 5-13. Load relaxations for porous scaffolds (**P60** and **P80**) and their non-porous control (**P0**) for **polymers 1-6**. Load relaxation (%) was calculated as the percentage reduction of load at maximum strain (20% strain) for 5 min from the load-time curves obtained by macro-indentation. One-way ANOVA with Bonferroni post-test (* $p \leq 0.05$, ** $p \leq 0.01$, *** $p \leq 0.001$ and **** $p \leq 0.0001$). Mean ± SD, n=4. Mean ± SD, n=4.

IV. Selection of 3D polymer scaffolds

Understanding how the behaviour of FBMSCs is altered by polymer composition, 3D structure and mechanical properties is crucial to allow selection of a successful porous scaffold for tissue repair applications. Proliferation, total collagen deposition, alkaline phosphatase activity, mechanical properties and 3D microstructure were used to compare the 3D polymer scaffolds. Each property was described as a percentage of the highest parameter observed, for instance, the highest proliferation rate was achieved by **P0-5** (8.7-fold increase between day 0 and 21) and thus its normalised value was set to 100%. The proliferation rate on scaffolds **P0**, **P60** and **P80** of **polymers 1-6** is shown as a percentage relative to **P0-5** proliferation.

This analysis allowed us to determine that total collagen and ALP increased with porosity and pore size, although the proliferation rate was also slightly reduced (Figure

5-14). Overall, **P80** scaffolds were observed to maximise osteoblastic markers in comparison to their non-porous control **P0** scaffolds.

To further proceed in scaffold selection, FBMSCs behaviour (proliferation, collagen deposition and ALP levels) with indentation modulus and pore size as scaffold descriptors were compared using the highest value obtained within the **P80** scaffolds. For instance, the highest proliferation rate on **P80** scaffolds was obtained for **P80-4** (6.2-fold increase between day 0 and 21) and its normalised value was set to 1. The proliferation rate of scaffolds **P80** of **polymer 1-6** is thus shown relative to **P80-4** proliferation. **P80-2** scaffolds were identified as a well-balanced material able to support proliferation and to enhance collagen deposition and ALP in “3D” (Figure 5-15). Moreover, **P80-2** exhibited an excellent indentation modulus, even in the presence of large pores. **P80-3** scaffolds were also observed to promote remarkable collagen deposition and ALP expression despite the limited cell proliferation. This phenomenon could indicate that **P80-3** perhaps supports osteoblastic differentiation.

3D microstructure and mechanical properties of scaffolds **P80-1** and **P80-5** were shown to be similar to **P80-2**; however, their lower collagen deposition suggested reduced extracellular matrix formation. Scaffolds **P80-4** and **P80-6** showed properties comparable to **P80-2** although their lower ALP expression at day 7 suggested lower osteoblastic differentiation. Given all of the above, **P80-2** and **P80-3** were chosen for further studies.

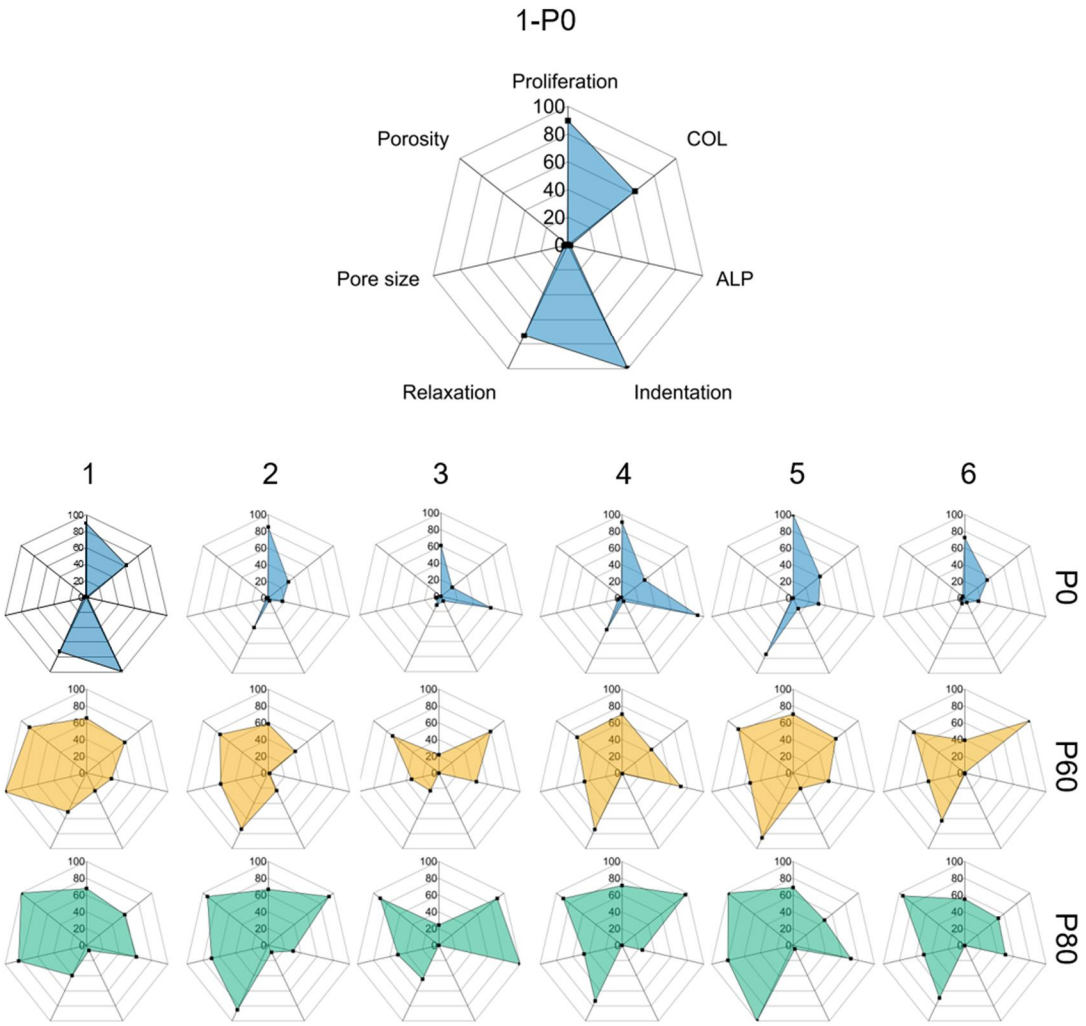

Figure 5-14. Spider plots of FBMSCs behaviour on the scaffolds **P0** (blue), **P60** (yellow) and **P80** (green) were compared with mechanical properties (indentation and relaxation load) and scaffold 3D structure (pore size and porosity). Each property interrogated was normalised (%) with the highest identified value from the 3D screening. The highest and lowest values for each property of the 3D polymer scaffolds were: proliferation fold change at day 21 (8.7 – 1.9), total collagen fold change at day 21 (4.8 – 0.8), ALP fold change at day 7 (4.0 – 0), indentation moduli (96.4 MPa – 22.8 kPa), percentage of relaxation load (53 – 4), pore size (175 – 2 μm) and percentage of porosity (82 – 0).

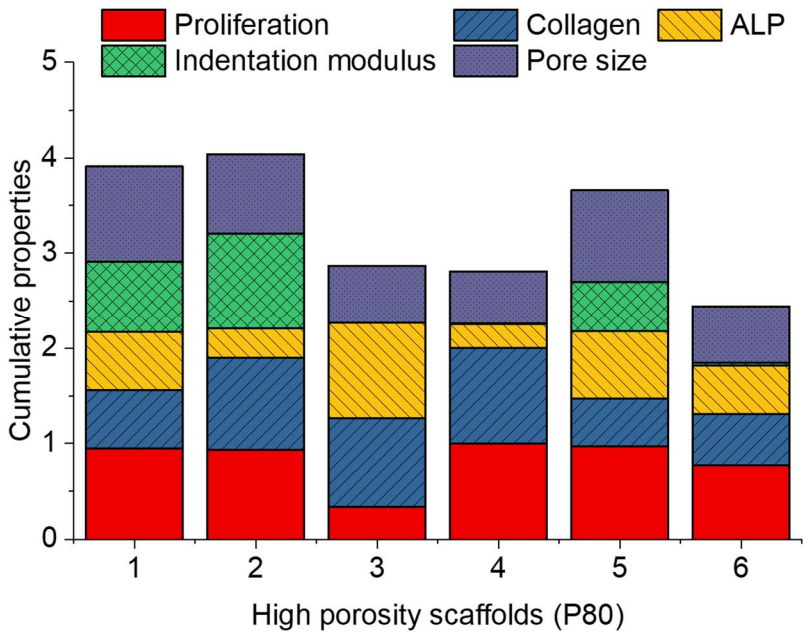

Figure 5-15. Scaffold cumulative analysis: FBMSCs behaviour on the P80 scaffolds (proliferation rate at day 21, total collagen at day 21 and alkaline phosphatase at day 7) were compared with mechanical properties (indentation modulus) and scaffold pore size. Each property was normalised with the highest identified value on **P80** scaffolds (proliferation 6.2-fold, collagen 4.7-fold, ALP 4.0-fold, indentation modulus 9 MPa and pore size 146 µm).

5.2.2 Validation of osteogenic differentiation on 3D polymer scaffolds

I. FBMSCs morphology on the 3D polymer scaffolds

FBMSCs were cultured on the scaled-up scaffolds (12 mm length × 12 mm width × 1 mm height) **P80-2** and **P80-3**, obtained with the "slow cooling" approach and photo-polymerisation, for 7 and 21 days with scaffolds without cells used as a control. FBMSCs morphology and microstructure of the 3D polymer scaffolds were analysed using SEM (Figure 5-16), which showed cells attached to the scaffolds occupying the available surface as well as the intraporous space forming 3D assemblies (arrows). The absence of rounded cells (an indication of poor cell attachment and death) along with the presence of ECM deposition were identified as indicators of a healthy cell population. The control scaffolds showed interconnected pores larger than 100 µm which was in accordance with allowing cells in "3D".

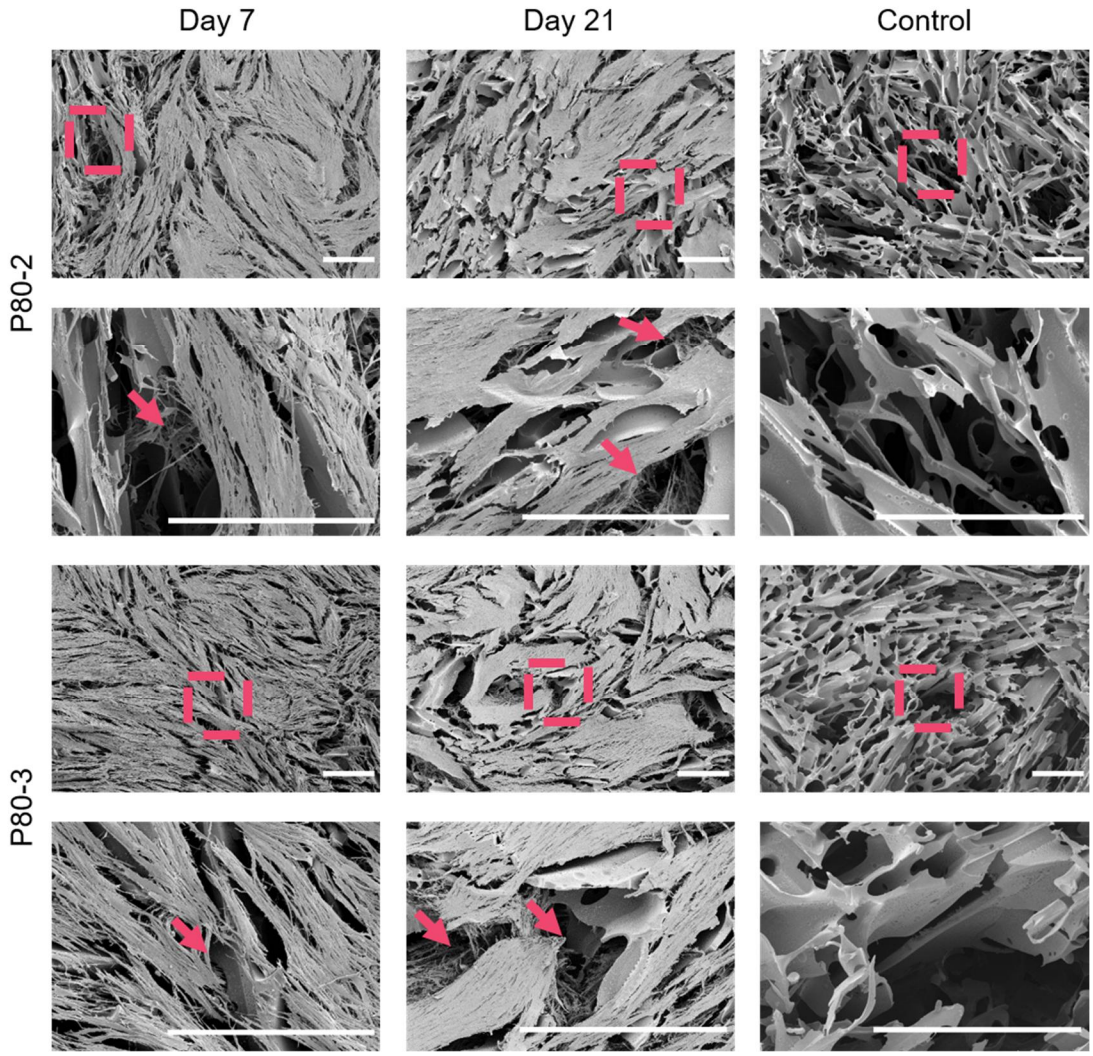

Figure 5-16. Representative SEM images of FBMSCs in 3D polymer scaffolds. FBMSCs were incubated on P80-2 and P80-3 scaffolds for 7 and 21 days. Scaffolds without cells were used as a control. Dashed squares and arrows showmagnified areas and cells in pores respectively. Scale bar = 400 µm.

II. FBMBSCs osteogenic markers on 3D polymer scaffolds

In vitro expression of biomarkers was evaluated by immunofluorescence staining to determine the differentiation state of FBMSCs. Cells were incubated in scaled-up scaffolds **P80-2** and **P80-3** for 2 and 7 days and ALP levels was used as an early osteoblast differentiation marker. Scaffolds **P80-2** and **P80-3** without FBMSCs were used as a negative control to assess non-specific antibody binding (Figure 5-17).

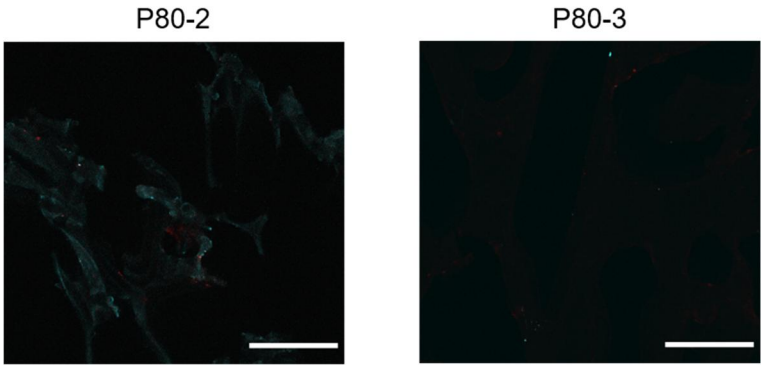

Figure 5-17. Assessment of non-specific ALP antibody staining in scaffolds **P80-2** and **P80-3** without FBMSCs. Immunofluorescence was carried out in parallel with the scaffolds with FBMSCs using the same concentration of dyes and incubation times. Image acquisition and analysis was performed with the same parameters as the scaffolds with FBMSCs using a confocal microscope Zeiss LSM880 Airscan and the image analyse software Imaris. Scaffolds were kept in culture for 7 days with ALP stained red and nuclei stained cyan (DAPI nuclear staining). Scale bar = 100 µm.

ALP activity of FBMSCs was confirmed on the 3D polymer scaffolds with a significant increase in cell numbers between day 2 and 7 (Figure 5-18). Analysis software Imaris was used to quantify the number of cell nuclei and the fluorescence intensity of the ALP images obtained by confocal microscopy (appendix C). Quantification for **P80-2** and **P80-3** showed about a 5 to 6 fold increase in cell number with a decrease in normalised ALP expression (ALP fluorescence intensity per cell) between days 2 and 7, which suggested a progression towards a more osteoblast-like stage (Figure 5-19).

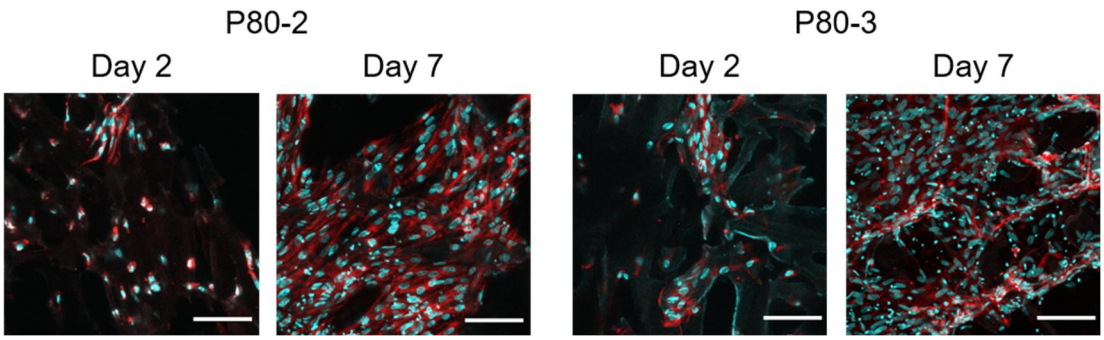

Figure 5-18. Immunofluorescence assessment of FBMSCs ALP expression on the 3D polymer scaffolds. FBMSCs were cultured on scaffolds **P80-2** and **P80-3** for 2 and 7 days. ALP was stained red and nuclei were stained cyan (DAPI nuclear staining). Scale bar = 100 µm.

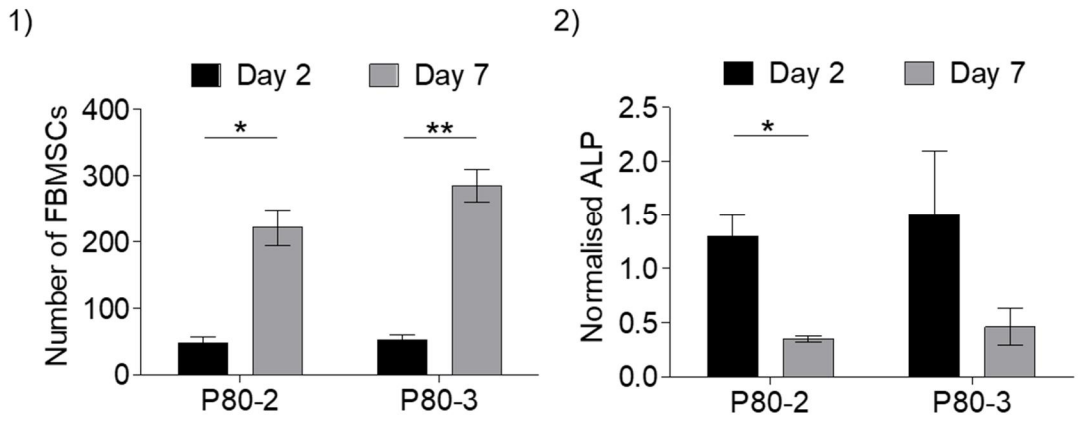

Figure 5-19. Quantification of the immunofluorescence assessment of ALP expression of FBMSCs on the 3D polymer scaffolds **P80-2** and **P80-3**. 1) Number of FBMSCs nuclei and 2) fluorescence intensity normalised by number of FBMSCs at days 2 and 7. Two tailed t-test (* $p \leq 0.05$ and ** $p \leq 0.01$). Mean ± SD, n=2.

The osteogenic markers type I collagen and osteopontin were evaluated after 7 and 21 days of culture in basal, α-MEM medium supplemented with FBS and antibiotics, and osteogenic media, basal medium supplemented with calcitriol and vitamin C.[204,205] FBMSCs cells in tissue culture plates (TC) for 21 days were used as a positive control. Scaffolds **P80-2** and **P80-3** without FBMSCs were used as a negative control to assess non-specific antibody binding (Figure 5-20**Figure 5-17** and Figure 5-21). FBMSCs in osteogenic medium showed more type I collagen at day 7 and 21 than FBMSCs in basal medium. However, little effect was observed in the expression of osteopontin where both conditions showed a decrease after 21 days (Figure 5-22).

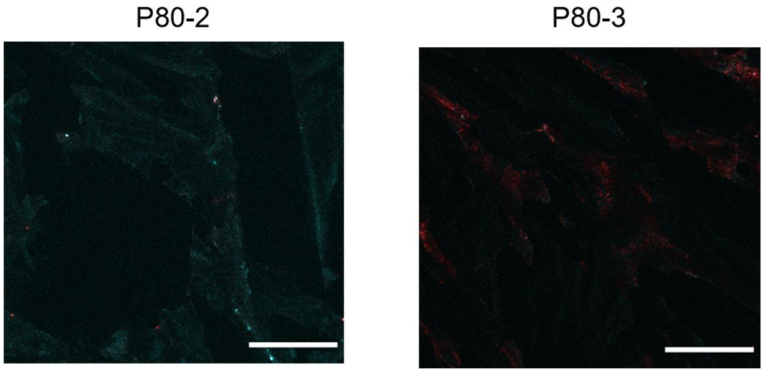

Figure 5-20. Assessment of non-specific type I collagen antibody staining in scaffolds **P80-2** and **P80-3** without FBMSCs. Scaffolds were kept in culture for 21 days with type I collagen stained red and nuclei stained cyan (DAPI nuclear staining). Scale bar = 100 µm.

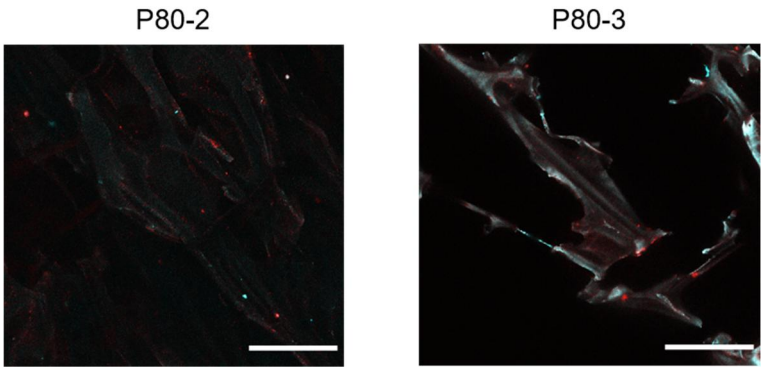

Figure 5-21. Assessment of non-specific osteopontin antibody staining in scaffolds **P80-2** and **P80-3** without FBMSCs. Scaffolds were kept in culture for 21 days with osteopontin stained red and nuclei stained cyan (DAPI nuclear staining). Scale bar = 100 µm.

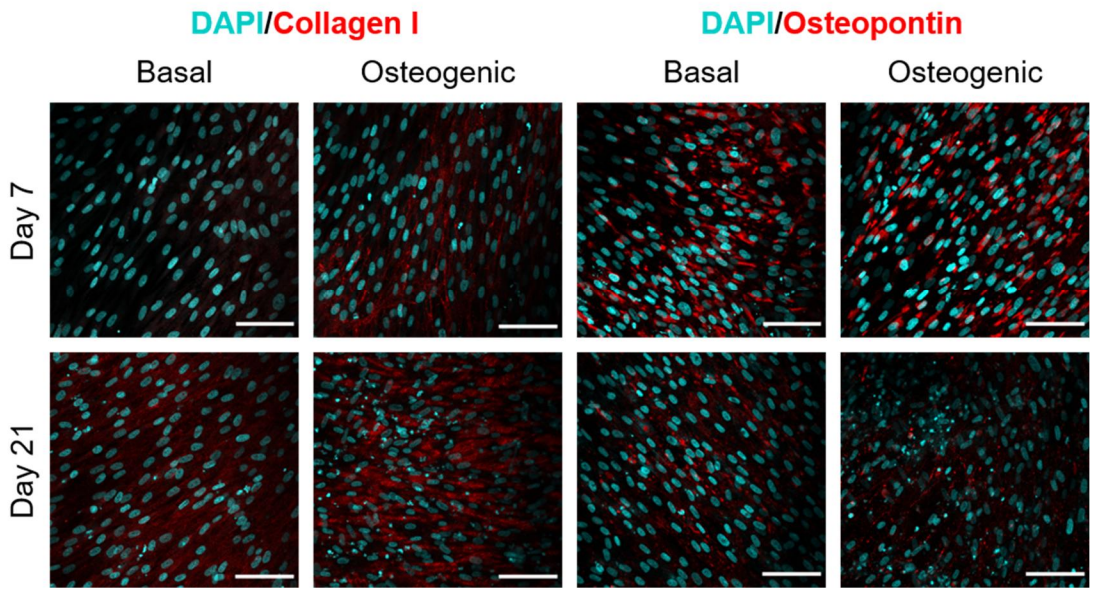

Figure 5-22. Evaluation of the effect of basal and osteogenic media on FBMSCs osteogenic markers in tissue culture plates (TC). Immunofluorescence analysis for expression of type I collagen and osteopontin (stained red) and nuclear staining (DAPI, stained cyan) after 7 and 21 days of culture. Scale bar = 100 µm.

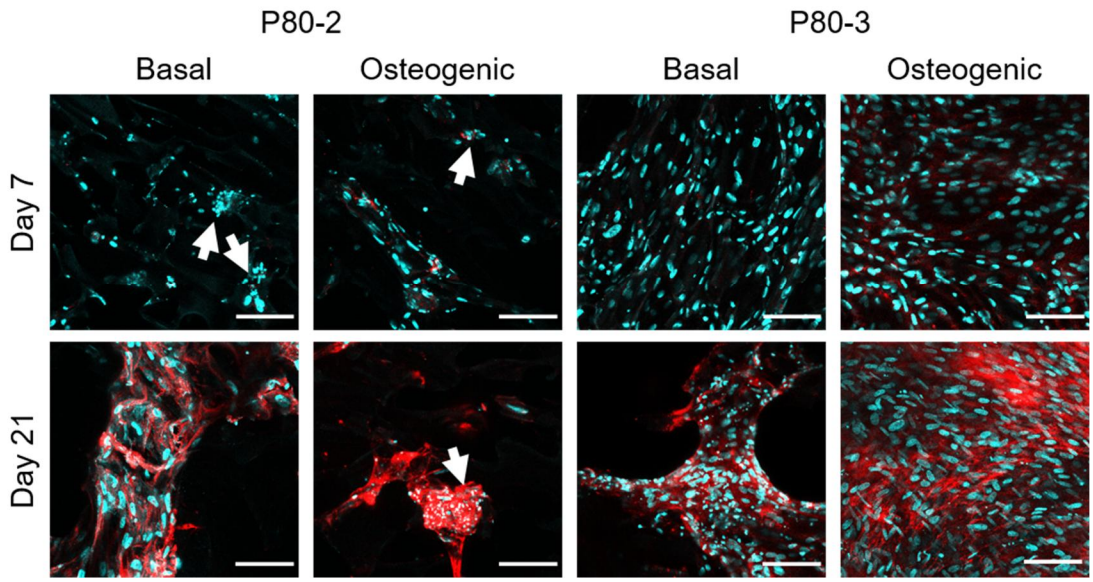

Figure 5-23. Immunofluorescence analysis of FBMSCs type I collagen expression on 3D polymer scaffolds. FBMSCs were cultured on scaffolds **P80-2** and **P80-3** with basal and osteogenic media for 7 and 21 days. Type I collagen was stained red and nuclei were stained cyan (DAPI nuclear staining). Arrows show cell aggregation. Scale bar = 100 μm.

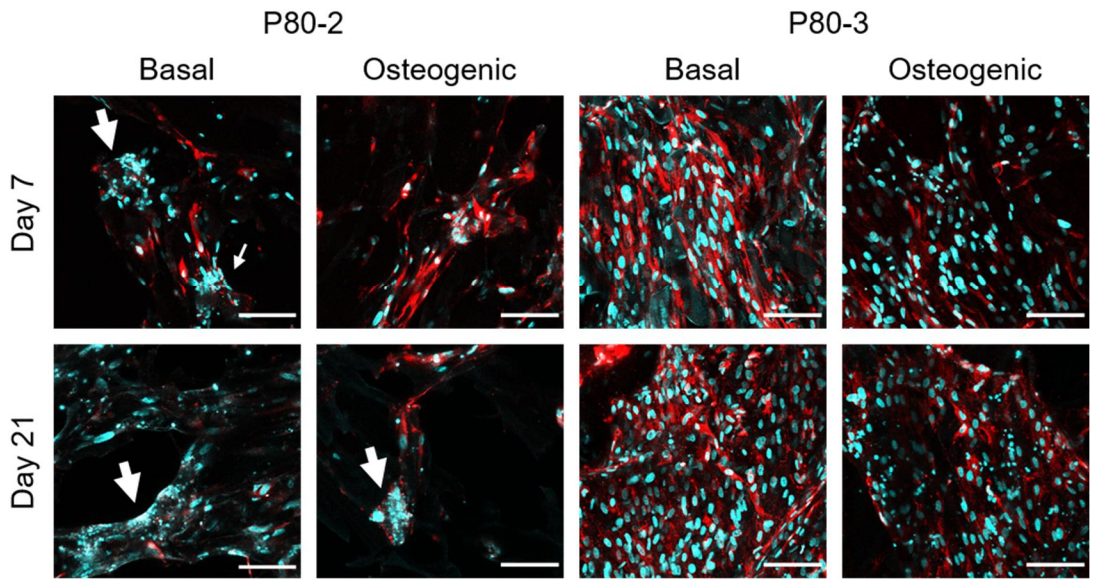

Figure 5-24. Immunofluorescence analysis of FBMSCs osteopontin expression on 3D polymer scaffolds. FBMSCs were cultured on scaffolds **P80-2** and **P80-3** with basal and osteogenic media for 7 and 21 days. Osteopontin was stained red and nuclei were stained cyan (DAPI nuclear staining). Arrows show cell aggregation. Scale bar = 100 μm.

Scaffolds **P80-2** and **P80-3** exhibited an increase of type I collagen from day 7 to 21 in basal and osteogenic media with no need to supplement the medium to have strong expression (Figure 5-23). Moreover, type I collagen expression was significantly higher in the 3D polymer scaffolds than the 2D control. On the other hand, FBMSCs osteopontin expression was retained at 21 days in the **P80-3** scaffolds whereas osteopontin decreased in **P80-2** scaffolds. It could suggest that **P80-3** maintained cell phenotype and **P80-2** promoted differentiation into a more osteoblast-like phenotype.[206] Scaffolds without cells used as a control showed low levels of non-specific staining (Figure 5-21). Interestingly, FBMSCs on scaffolds **P80-2** formed cell aggregates (arrows) with the expression of high content of type I collagen whereas this behaviour was not observed on **P80-3** scaffolds or the TC control.

A live/dead staining assay was carried out to have a better understanding of the FBMSCs aggregates on **P80-2** scaffolds. The assay revealed that cells were alive after 21 days despite the compact cell structure (Figure 5-25, 1 and 2). FBMSCs on **P80-3** were used as a control with the absence of dead cells in both cases. Moreover, the morphology of the cell aggregates (arrows) showed cytoplasm and nuclei staining (Figure 5-25, 3).

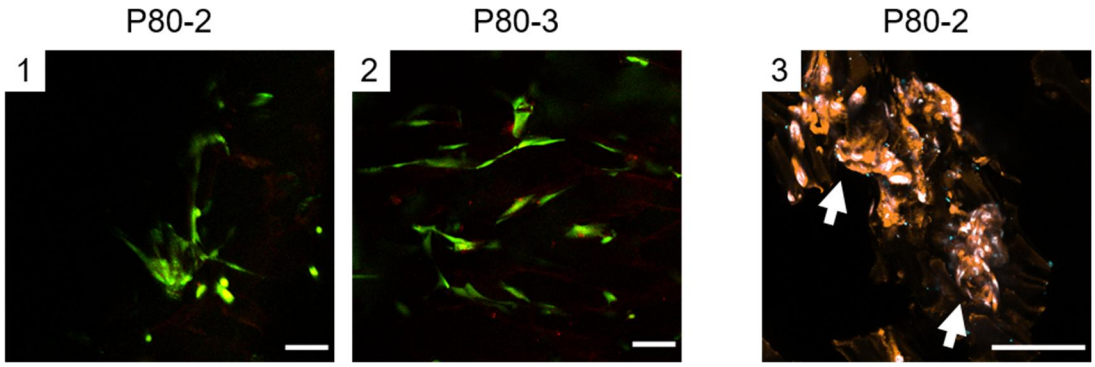

Figure 5-25. FBMSCs viability and aggregation on 3D polymer scaffolds in basal medium. 1) and 2) Representative images of live/dead staining of FBMSCs after incubation on scaffolds **P80-2** and **P80-3** for 21 days. Merged images of live (calcein AM, stained green) and dead cells (nuclear dye, stained red). 3) Representative image of cytoplasm (CellMask™, stained orange) and nuclei (stained cyan) of FBMSCs on a **P80-2** scaffold. Arrows show cell aggregation. Scale bar = 100 μm.

Enzyme-linked immunosorbent assay (ELISA) was used to quantify FBMSCs type I collagen secretion in scaffolds **P80-2** and **P80-3** after 21 days cell culture in basal

medium. FBMSCs total protein content (BIC assay) and DNA concentrations (PicoGreen assay) were used to normalise type I collagen secretion. Scaffolds without FBMSCS and cells on culture plates were also used as controls. Type I collagen of FBMSCs was found significantly higher on scaffolds **P80-3** than **P80-2** (Figure 5-26) while type I collagen of FBMSCs on the TC control was observed below detection limit (range 39 pg/mL to 2000 pg/mL). Moreover, the normalised total protein showed that FBMSCs on **P80-2** secreted more proteins per cell than **P80-3**, which could illustrate the effect of the scaffold characteristics on FBMSCs behaviour.

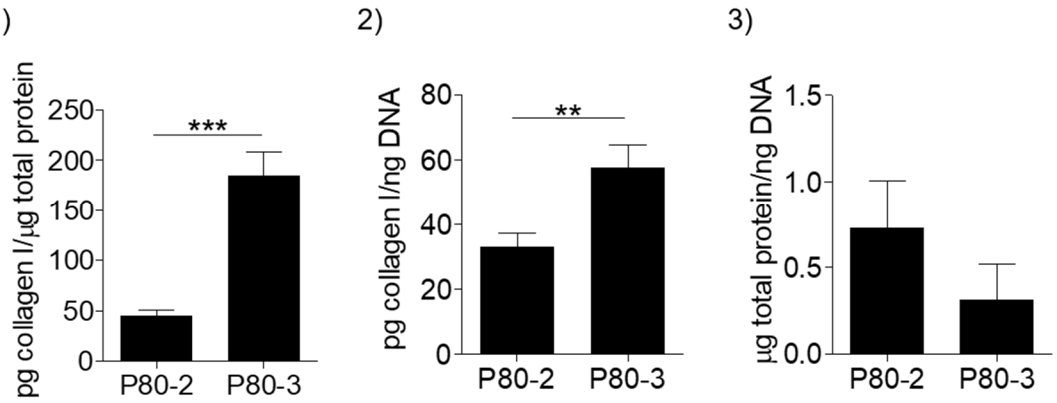

Figure 5-26. ELISA assay for type I collagen. FBMSCs were incubated on the 3D polymer scaffolds **P80-2** and **P80-3** for 21 days. Type I collagen was shown as: 1) collagen I per total protein content (pg/µg) and 2) type I collagen per total DNA content (pg/ng). 3) BIC and PicoGreen assays were used to quantify total protein and DNA concentration. Two tailed t-test (** $p \leq 0.01$ and *** $p \leq 0.001$). Mean ± SD, n=3.

III. Biomineralisation on the 3D polymer scaffolds

Mediated by osteoblast cells, biomineralisation is one of the latest events in bone formation and healing process.[86] Therefore, it was used as a late FBMSCs osteogenic differentiation marker. The following supplemented media were used to accelerate the biomineralisation processes:

- Basal medium: α-MEM medium supplemented with FBS (10% v/v) and penicillin/streptomycin/fungizone (1% v/v).
- Mineralisation medium: basal medium supplemented with 2-phospho-L-ascorbate (50 µg/mL), β-glycerophosphate (1 to 20 mM) and dexamethasone (10 nM).[140–142]

- Osteogenic medium: basal medium supplemented with 2-phospho-L-ascorbate (50 µg/mL) and calcitriol (10 nM).[204,205]

The effect of the osteogenic and mineralisation media and their combinations were explored on FBMSCs cultured on tissue culture well plates (TC) using basal medium as a control (Table 5-2 shows the 10 conditions studied). FBMSCs were kept in culture for a total of 21 days before assessing mineralisation: 7 days in basal medium and 14 days in experimental media. Mineralisation was analysed with a colorimetric approach using acid alizarin red and cetylpyridinium chloride, as previously published.[143] Alternatively, the near-infrared fluorescent dye OsteoSense® 800, for image bone growth *in vivo*, was used as a specific mineralisation dye since alizarin red is a calcium chelating agent.[144]

Table 5-2. Media optimisation for inducing biomineralisation in 3D polymer scaffolds. Basal medium was supplemented with different combinations of β-glycerophosphate (β-Gly), dexamethasone (Dex), Vitamin D (calcitriol) and 2-phospho-L-ascorbate (L- ascorbate).

Media	Code	β-Gly (mM)	Dex (nM)	Calcitriol (nM)	L-ascorbate (µg/ml)
Basal (control)	1	0	0	0	0
Osteogenic	2	0	0	10	50
Mineralisation	3	1	10	0	50
	4	5	10	0	50
	5	10	10	0	50
	6	20	10	0	50
Mineralisation + Osteogenic	7	1	10	10	50
	8	5	10	10	50
	9	10	10	10	50
	10	20	10	10	50

FBMSCs biofilms showed positive staining with alizarin red (Figure 5-27). Staining quantification showed a significant increase for the majority of the conditions in the presence of mineralisation media. However, statistically significant differences were

not observed between the mineralisation media explored. Smaller differences compared to basal control were found in the case of combinations between mineralisation and osteogenic media. On the other hand, OsteoSense® was not able to show significant differences for any condition (Figure 5-27).

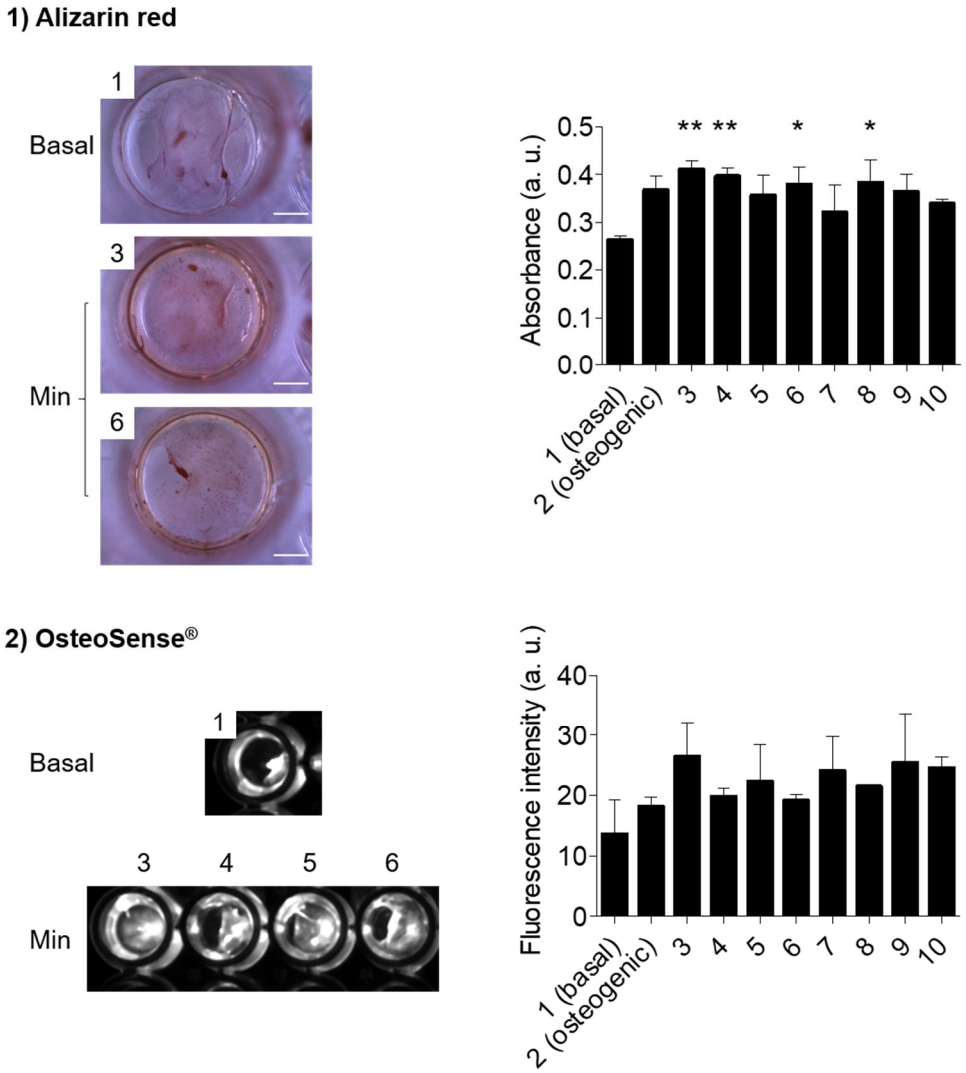

Figure 5-27. FMBSCs biomineralisation on tissue culture well plates (TC). FBMSCs were incubated for 7 days in basal medium and 14 days in mineralisation (min) media (Table 5-2). 1) Representative images of FBMSCs on the bottom of a well stained with acid alizarin red (scale bar = 2 mm). Absorbance based on the extraction and homogenisation of the alizarin red staining recorded in a plate reader (λ = 550 nm). 2) Representative images of FBMSCs on a well stained with OsteoSense® 800. Fluorescence intensity was recorded in near-infrared Odyssey® CLx imaging system ($\lambda_{ex/em}$ = 780/805 nm). One-way ANOVA with Bonferroni post-test (* p≤0.05 and ** p≤0.01) was carried out between basal control (1) and the supplemented (2 – 10) media. Mean ± SD, n=3.

Previous experiments of mineralisation staining in 3D polymer scaffolds with alizarin red (see 4.2.3) were shown to be highly non-specific. Therefore, a high-throughput approach based on the near-infrared dyes OsteoSense® and BoneTag™ (Figure 5-28) was developed using an array of 3D polymer scaffolds and the *in vivo* imaging system IVIS. FBMSCs were cultured on scaffolds for 7 days before switching to medium 6 (Table 5-2) and were kept in culture for a total of 28 days. Medium 6 showed statistically significant differences with basal medium and it was composed of the highest concentration of β-glycerophosphate, which was thought to accelerate biomineralisation. Moreover, differences between medium 6 and media 3 and 4 were not observed. **P80-2** and **P80-3** without FBMSCs in basal medium and on tissue culture well plates (TC) were used as controls. Optical inspection of the polymer scaffolds **P80-2** and **P80-3** with cells showed higher fluorescence intensity than control scaffolds without cells, which was also confirmed by fluorescence quantification (Figure 5-29). In contrast, FBMSCs in 3D polymer scaffolds with basal and mineralisation media did not show significant differences. The differences observed between BoneTag™ and OsteoSense® were perhaps a consequence of the emission intensity of the dyes as total fluorescent radiant efficiency of BoneTag™ was higher than OsteoSense® in all the conditions.

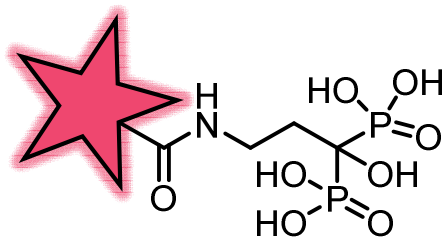

Figure 5-28. OsteoSense® and BoneTag™ uses a bisphosphonate conjugated to proprietary near-infrared dyes (star) to image bone apatite.[207]

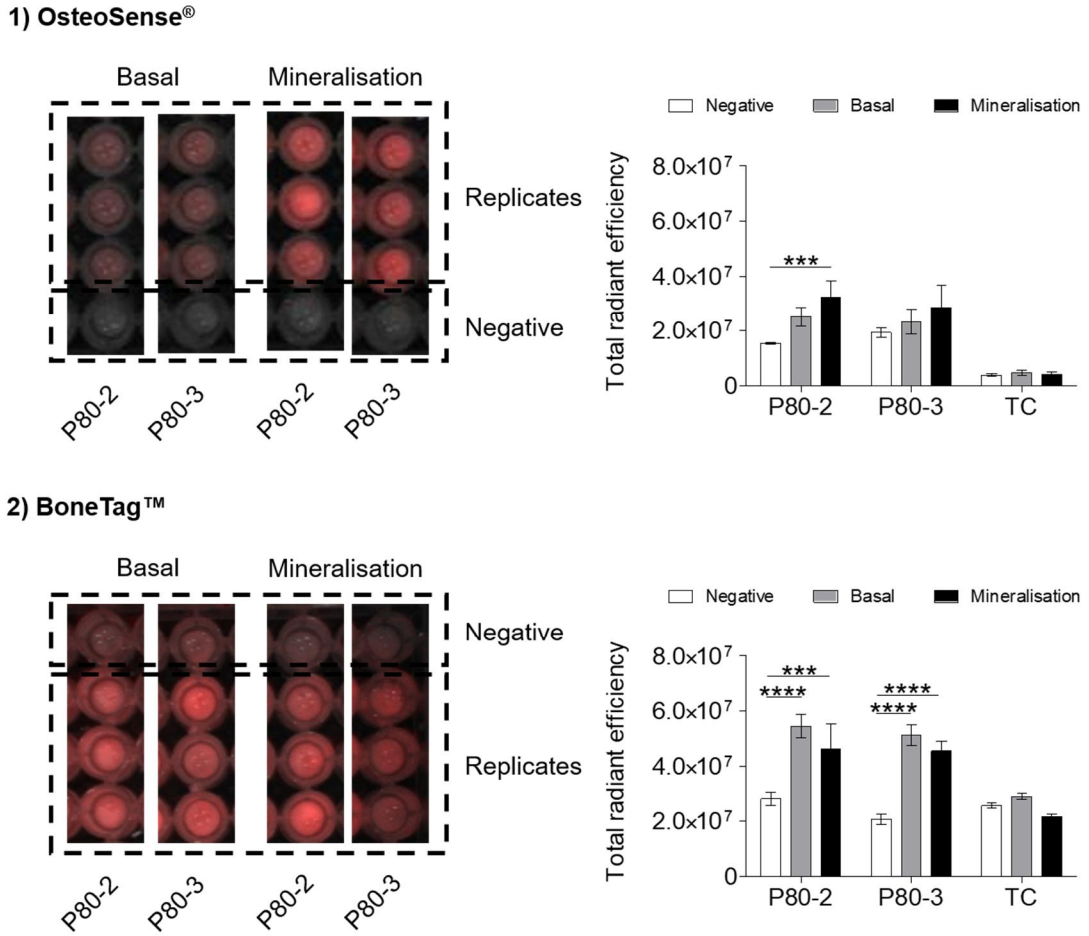

Figure 5-29. Analysis of FBMSCs biomineralisation on arrays of 3D polymer scaffolds. FBMSCs on scaffolds P80-2 and P80-3 were incubated for 7 days in basal medium followed by 21 days in mineralisation medium. Biomineralisation was assessed using the near-infrared dyes Osteosense® and BoneTag™. Scaffolds without cells (negative), FBMSCs cultured in basal medium on scaffolds (basal) and FBMSCs cultured on tissue culture well plates (TC) were used as controls. Images of the arrays and total fluorescent radiant efficiency ([photons/s/cm^2/steradian]/[μW/cm^2]) were recorded using an *in vivo* imaging system (IVIS). Two-way ANOVA with Bonferroni post-test (*** $p \leq 0.001$ and **** $p \leq 0.0001$). Mean ± SD, n=3.

5.2.3 Biocompatibility and angiogenesis assay in the CAM model

The chick choriallantoic membrane (CAM) model was used as a model to assess scaffold compatibility and angiogenesis. Scaffolds **P80-2** and **P80-3** with and without FBMSCs were implanted in 10 day fertile chick eggs following a previously described procedure.[208] After 7 days post-implantation scaffold integration with the CAM was analysed and the amount of blood vessels in the scaffolds quantified following the Chalkley score method (Figure 5-30).[151,152] Eggs without scaffolds were used as a control.

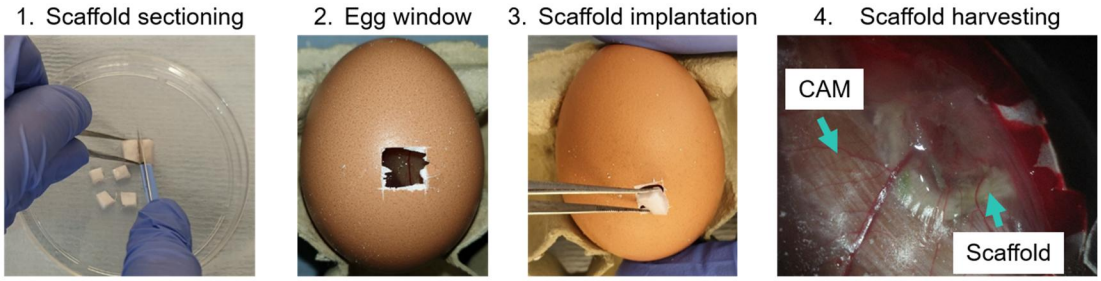

Figure 5-30. CAM experimental design. 1) Scaffolds **P80-2** and **P80-3** with and without FBMSCs were incubated for 7 days before being sectioned (5 mm length × 5 mm width × 1 mm height). 2) Eggshell was removed (5 mm length × 5 mm width) to expose the CAM. 3) Scaffolds were implanted in the CAM and incubated in the chick eggs for 7 days. 4) Scaffolds were harvested and their integration with the CAM inspected by microscopy.

High integration into the chick CAM with ECM deposition was observed for scaffolds P80-2 and P80-3 (Figure 5-31). Angiogenesis was quantified using a Chalkley score method which uses a 25 randomised grid to count microvessels. Scaffolds **P80-2** and **P80-3** were shown to significantly enhance angiogenesis compared with the negative control, empty eggs without scaffolds inside (10.5 ± 2.4, $p \leq 0.0001$). Differences between **P80-2** scaffolds with FBMSCs and **P80-3** scaffolds with and without cells were observed, which suggested that these scaffolds were capable of stimulating angiogenesis.

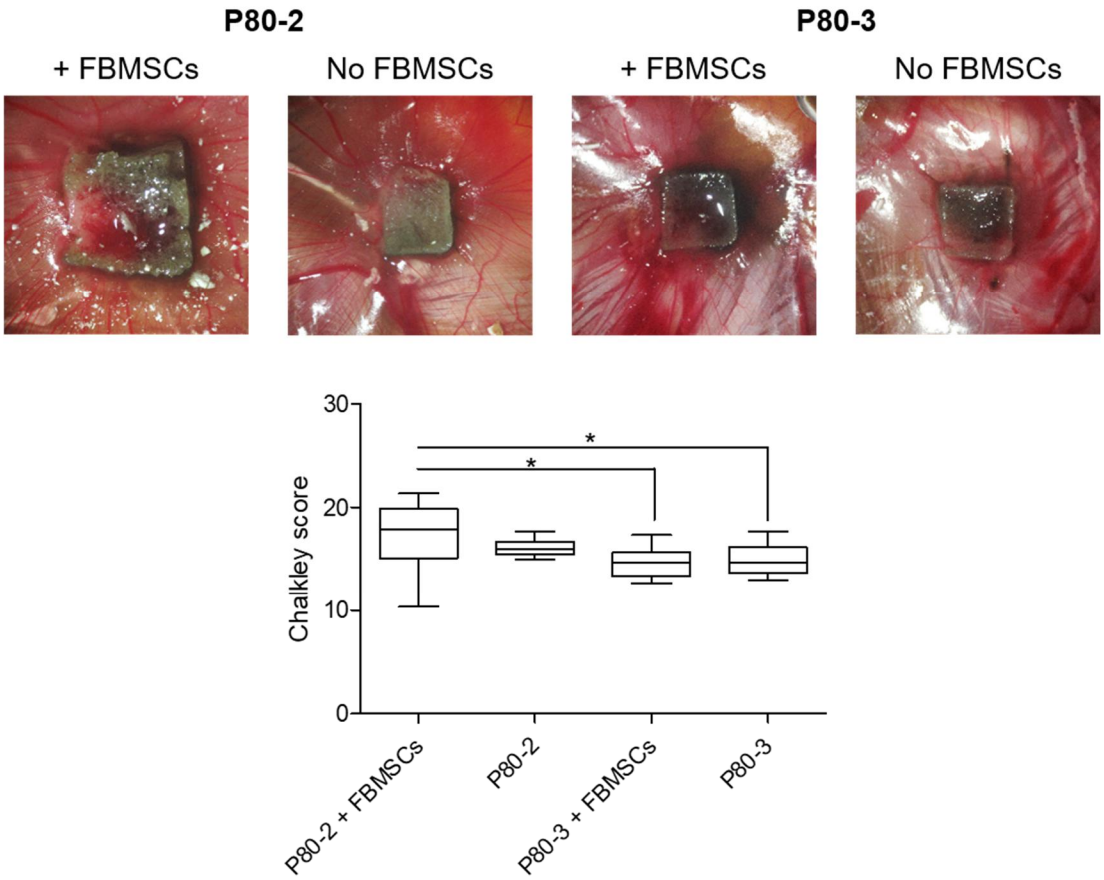

Figure 5-31. Analysis of the scaffolds **P80-2** and **P80-3** with and without FBMSCs implanted in the CAM model. Representative images of scaffolds implanted with (+FBMSCs) and without (no FBMSCs) cells. Quantification of the CAM vasculature in the **P80-2** and **P80-3** scaffolds by Chalkley score. One-way ANOVA with Bonferroni post-test (* $p \leq 0.05$). Mean ± SD, n=10.

Histological analysis using Alician blue and Sirius red (A/S) and Goldner's Trichrome (GT) of scaffolds **P80-2** and **P80-3** showed high integration into the chick CAM with ECM deposition (Figure 5-32 and Figure 5-33). Proteoglycans, stained blue in A/S, were observed to present with high prevalence in all the conditions. However, significant differences between **P80-2** and **P80-3** scaffolds, with and without FBMSCs, were not observed (Figure 5-32). Presence of collagen, stained red in A/S and marked with red arrows, was also identified across all the conditions. The presence of cells in all the samples, stained black in A/S, even in scaffolds without pre-seeded FBMSCs, suggested chick cellular penetration and recruitment as a consequence of the enhanced scaffold's pore size. Goldner's Trichrome staining also showed presence of collagen, stained green and marked with black arrows, across all the conditions (Figure 5-33). Avian erythrocytes, stained orange in GT and marked with blue arrows,

were observed for all the conditions suggesting vasculature network infiltration through the scaffolds. However, appreciable differences of collagen deposition between **P80-2** and **P80-3** scaffolds with and without FBMSCs were not identified.

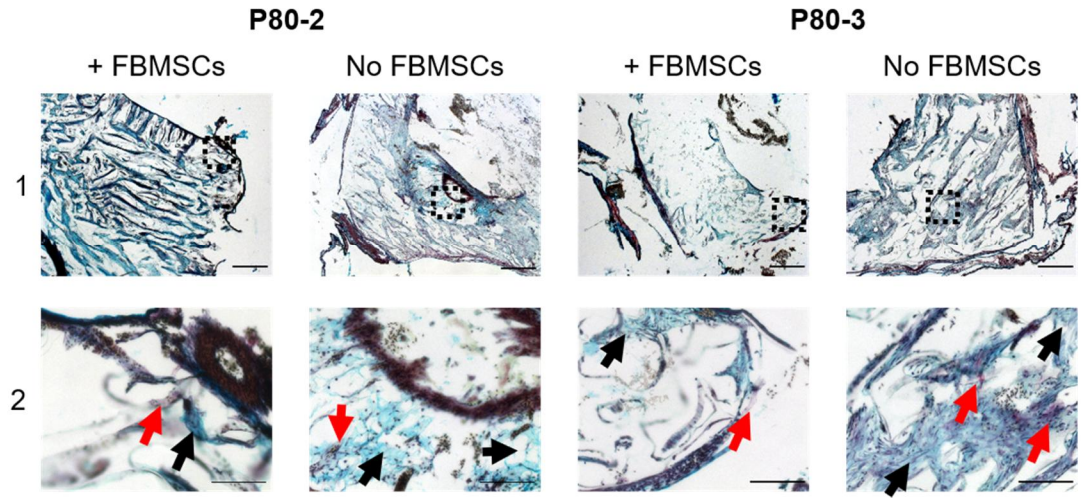

Figure 5-32. Histological analysis with Alician blue and Sirius red staining where blue shows proteoglycans, red shows collagen and black shows nuclei. Black dashed square, black and red arrows indicate areas magnified, proteoglycans and collagen respectively. Scale bar 500 µm (1) and 100 µm (2).

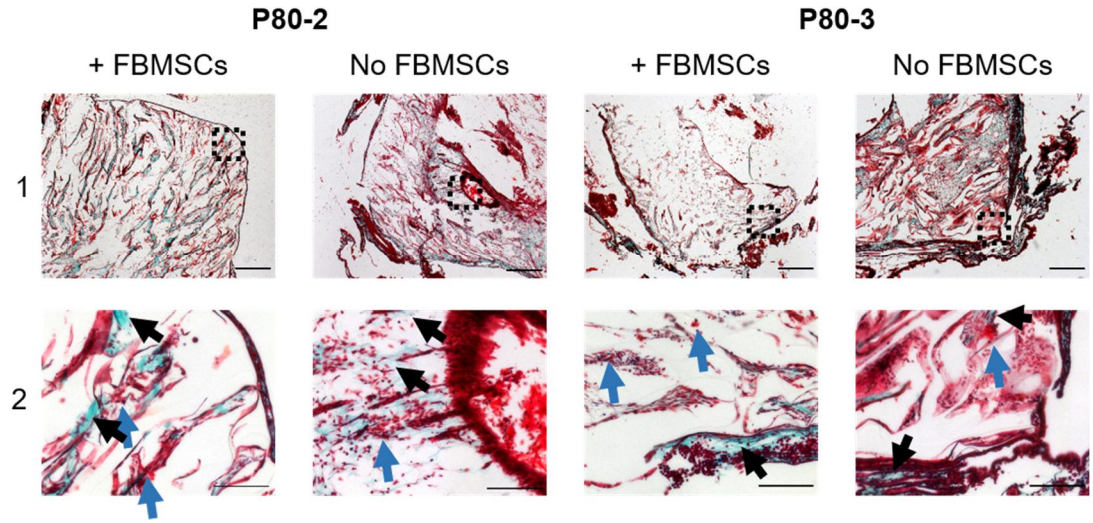

Figure 5-33. Histological analysis with Golner's trichrome where green shows collagen, red shows cytoplasm, black shows nuclei and orange shows erythrocytes. Black dashed square, black and blue arrows indicate areas magnified, collagen and erythrocytes respectively. Scale bar 500 µm (1) and 100 µm (2).

5.2.4 Angiogenesis analysis after subcutaneous implantation in mice

Scaffold **P80-2** was selected for in vivo analysis based on its osteoblastic phenotype expression with higher biomineralization than scaffold **P80-3**. Scaffold **P80-2** displayed enhanced angiogenesis compared to **P80-3** scaffolds. Moreover, large pore size and high stiffness were also identified in **P80-2** scaffolds, which can enhance angiogenesis and osteogenesis.

An *in vivo* subcutaneous murine model was used to further investigate the angiogenesis and bone forming potential of **P80-2** scaffolds in the presence of FBMSCs pre-conditioned in basal and osteogenic media for 7 days before implantation. The *in vivo* procedure took a total of 4 weeks and two controls were used: **P80-2** scaffolds without FBMSCs in basal medium and bulk alginate gel (3% w/v). Micro-CT reconstruction assessed mineral deposition in the scaffolds after 4 weeks post-implantation showing that **P80-2,** in all the conditions, did not form any detectable mineralised tissue in contrast to the alginate control, irrespective of implantation site (Figure 5-34).

Extensive levels of integration with the scaffolds was seen with scaffolds near-indistinguishable from the surrounding tissue independent of the use of FBMSCs or supplemented medium. Poor integration was seen for alginate gels four weeks post-implantation (Figure 5-34 and Figure 5-35). Histological analysis using Alician Blue and Sirius red showed extensive collagen around the **P80-2** scaffolds with FBMSCs compared with **P80-2** without cells and alginate negative controls (Figure 5-35). Lumen-like vascular structures were also identified in some conditions at scaffolds boundaries (yellow arrows). On the other hand, alginate controls showed high levels of proteoglycans staining with low infiltration of murine cells. Goldner's Trichrome stained confirmed extensive collagen around and within the porous scaffolds (Figure 5-36). Moreover, scaffold **P80-2** pre-seeded with FBMSCs displaying elevated levels of collagen staining in comparison to control **P80-2** scaffolds without FBMSCs and alginate gels. Murine erythrocytes blood vessels infiltration (blue arrows) were in concordance with a highly biocompatible material.

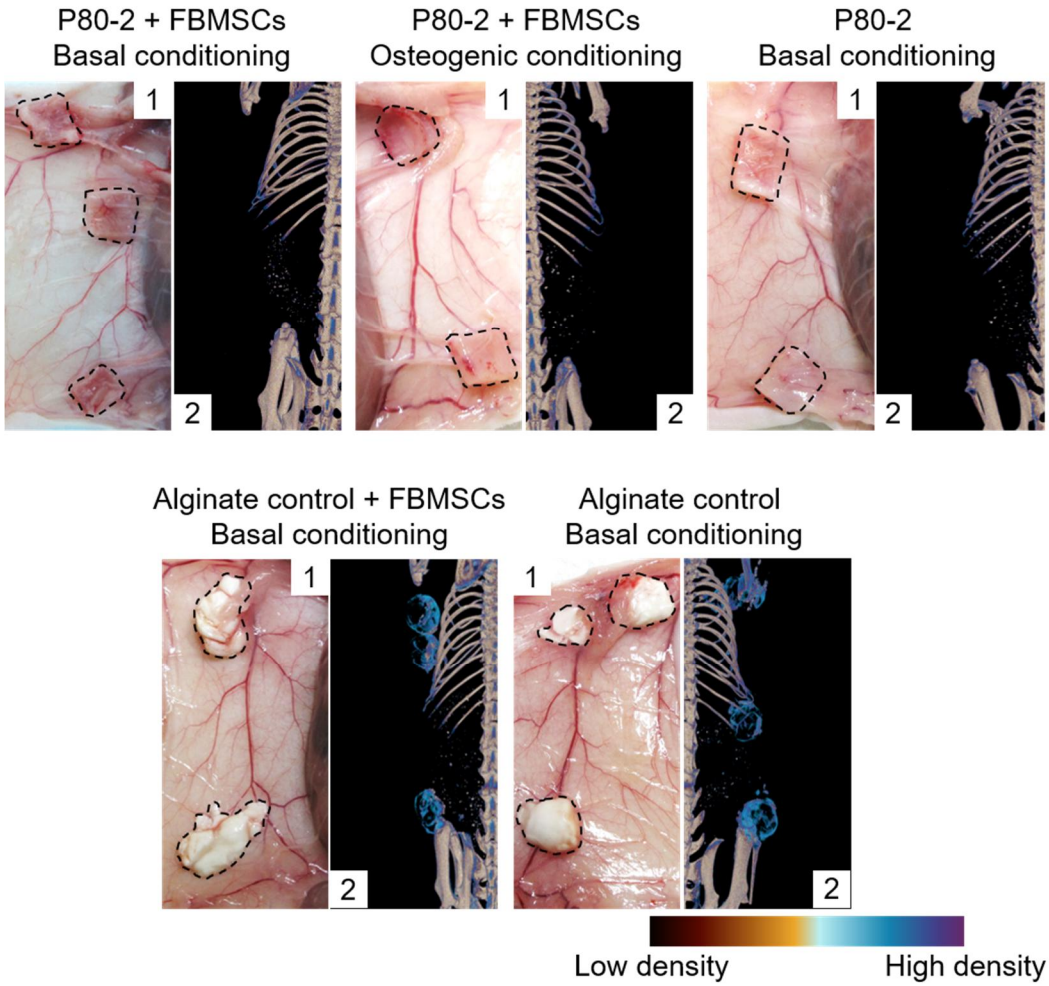

Figure 5-34. *In vivo* evaluation of subcutaneous implantation of scaffolds P80-2 and 3% (w/v) bulk alginate control. 1) Macrographs of scaffolds integration and 2) micro-CT reconstructions of **P80-2** with FBMSCs after basal conditioning, **P80-2** with FBMSCs after osteogenic conditioning, **P80-2** without cells, 3% (w/v) bulk alginate scaffold with FBMSCs after basal conditioning and 3% (w/v) bulk alginate scaffold without cells. Black dashed squares show the scaffolds. New highly dense tissue (mineralization) is shown in blue.

The histopathological analysis of the **P80-2** scaffolds using H&E staining confirmed the presence of lumen-like vascular structures in scaffolds boundaries and scaffold inner structure (Figure 5-37). Infiltration of scaffolds by murine host cells, such as red blood cells (blue arrows) and multinucleated giant cells (yellow arrowheads), was evidenced from the presence of cells in **P80-2** without pre-seeded FBMSCs. The presence of vascular structures throughout **P80-2** scaffolds, including the centre of the constructs, confirmed extensive vascularisation. Quantification of blood vessels

revealed that **P80-2** scaffolds with FBMSCs conditioned with osteogenic media enhanced angiogenesis ($p \leq 0.05$), in comparison with **P80-2** scaffolds with cells conditioned with basal media and **P80-2** scaffolds without cells (Figure 5-38). Although blood vessel in the inner structure of the scaffolds were identified for all the conditions, It may suggest that FBMSCs with more differentiated osteoblastic phenotype can promote further angiogenesis.[195]

Angiogenesis was further evaluated using immunohistochemistry (Figure 5-39) to assess the expression of the vascular endothelial growth factor receptor-2 (VEGFR-2). VEGFR-2 expression was predominant at scaffold boundaries and connective tissue as a consequence of endothelial cells infiltration. Moreover, VEGFR-2 markedly reduced in scaffolds **P80-2** without cells, in comparison to **P80-2** with FBMSCs.

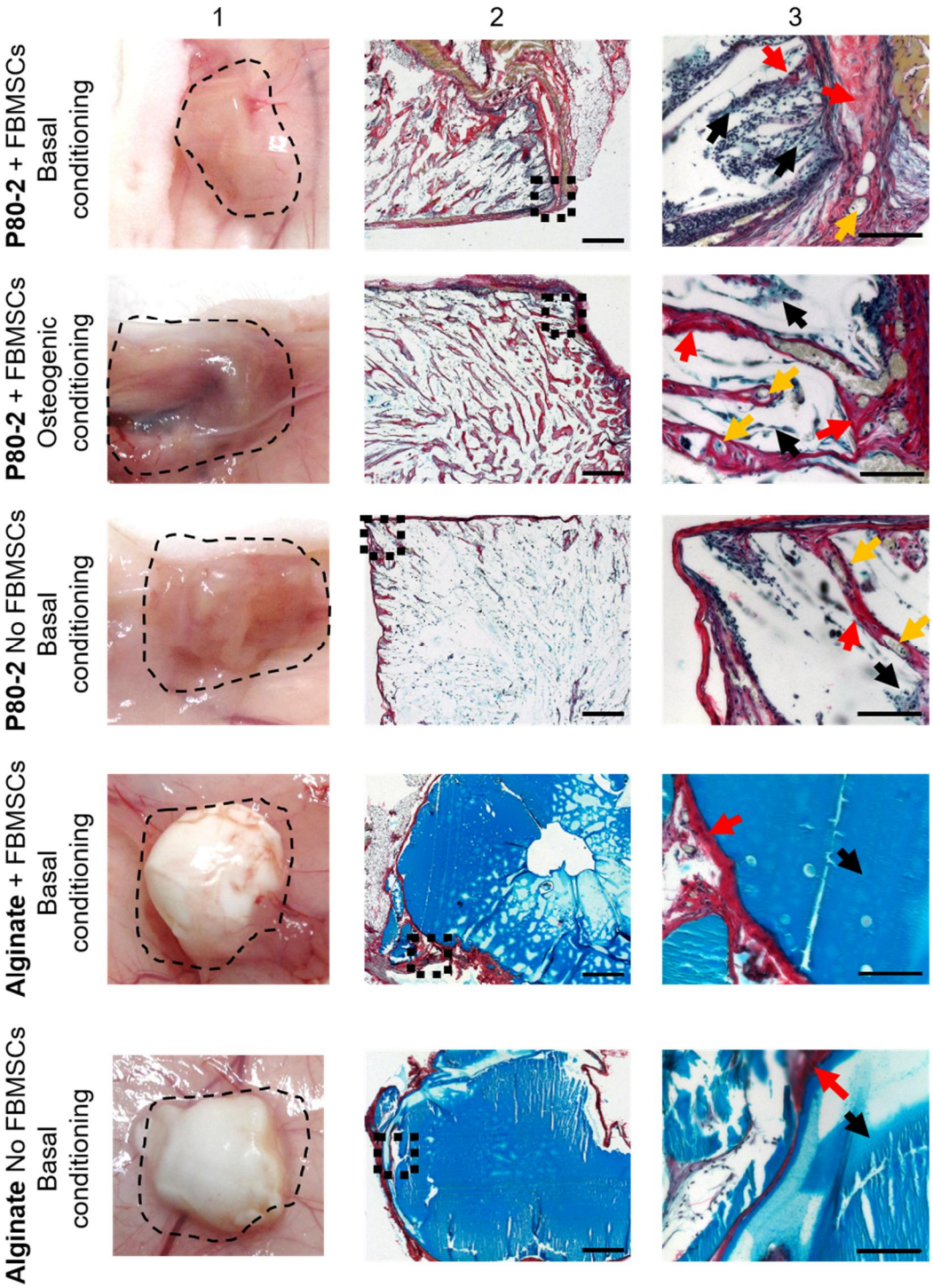

Figure 5-35. *In vivo* evaluation of subcutaneous implantation of scaffolds **P80-2** and 3% (w/v) bulk alginate control. 1) Macrographs of scaffold integration. 2) and 3) Histological analysis with Alician blue and Sirius red (A/S) staining where blue shows proteoglycans, red shows collagen, black shows nuclei and yellow shows muscles. Dashed squares show magnified areas with black, red and yellow arrows indicate proteoglycans, collagen and lumen-like vascular structures respectively. Scale bar in (2) = 500 μm and (3) = 100 μm.

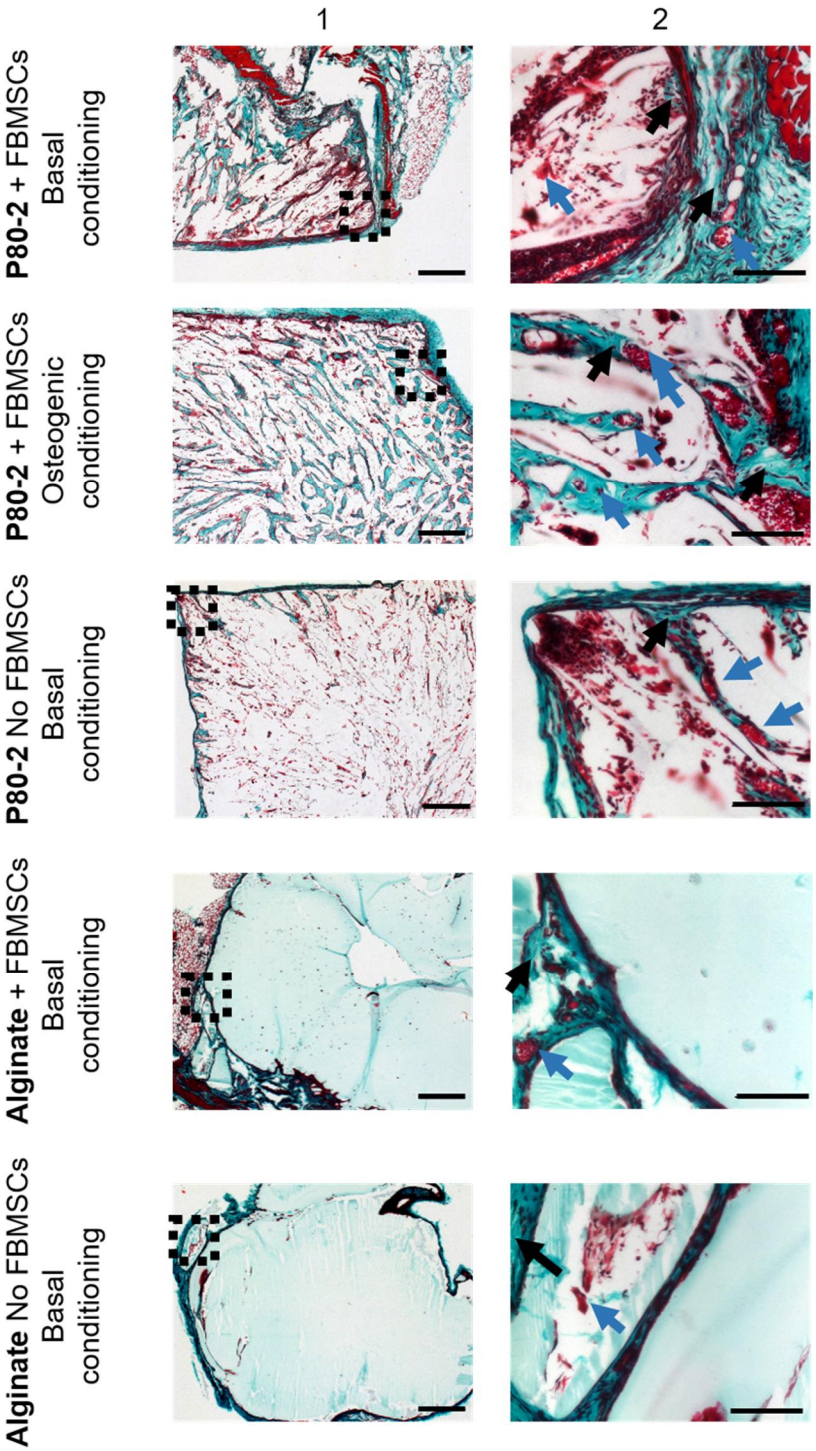

Figure 5-36. *In vivo* evaluation of subcutaneous implantation of scaffolds **P80-2** and 3% (w/v) bulk alginate control. Histological analysis with Golner's trichrome (GT) where green shows collagen, red shows cytoplasm, black shows nuclei and orange shows erythrocytes. Dashed squares show magnified areas, blue and black arrows indicate erythrocytes and collagen respectively. Scale bar in (1) = 500 μm and (2) = 100 μm.

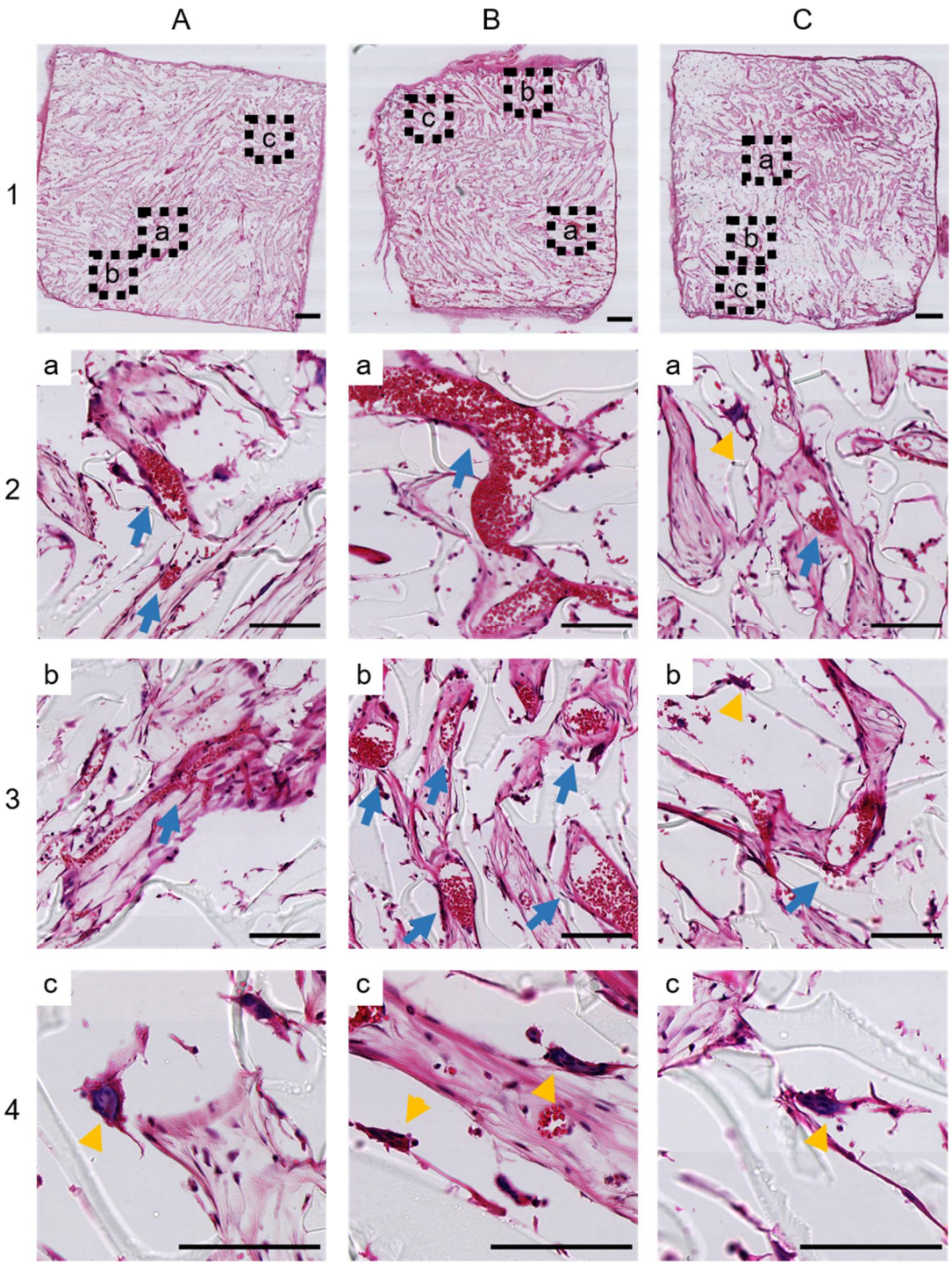

Figure 5-37. Histological evaluation of scaffolds **P80-2** by H&E. **P80-2** with FBMSCs in basal conditioning (A), **P80-2** with FBMSCs in osteogenic conditioning (B) and **P80-2** without FBMSCs in basal conditioning. Dashed squares (a-c) show magnified areas, blue arrows show RBCs and yellow arrowheads shows multinucleated giant cells. Scale bar in (1) = 500 µm and (2-4) = 100 µm.

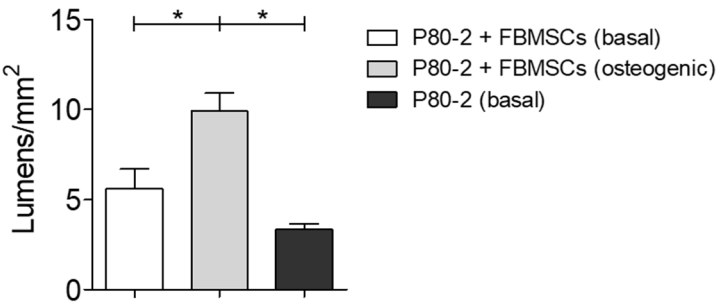

Figure 5-38. Evaluation of the number of lumens/vascular structures per mm^2 of scaffold **P80-2** with FBMSCs after basal conditioning, **P80-2** with FBMSCs with osteogenic conditioning and **P80-2** without any cells. Analysis was performed manually using the software QuPath on the histological sections stained with H&E. One-way ANOVA with Bonferroni post-test (* $p \leq 0.05$). Mean ± SD, n=2 biological replicates.

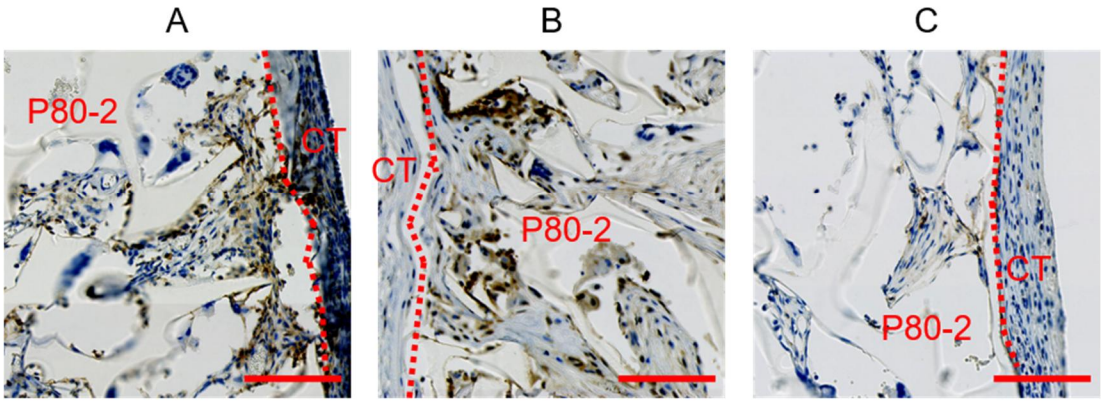

Figure 5-39. Analysis of VEGFR-2 by immunohistochemistry. **P80-2** with FBMSCs in basal conditioning (A), **P80-2** with FBMSCs in osteogenic conditioning (B) and **P80-2** without FBMSCs in basal conditioning. Dashed lines indicate interface between connective tissue (CT) and scaffolds (**P80-2**). Scale bar = 100 µm.

5.3 Discussion

Scaffold composition, mechanical properties and 3D microstructure have shown to be capable of controlling stem cell behaviour to promote tissue healing. For example, porous scaffolds based on chitosan, poly(vinyl acetate) and poly(L-lactic acid) (50:25:25) have been shown to promote skeletal stem cells differentiation with *in vivo* osteogenic potential.[121] Substrate stiffness of porous scaffolds also play a crucial role in stem cell behaviour, for instance, by controlling osteogenic or adipogenic

differentiation of mesenchymal stem cells (MSCs).[209] Moreover, bone marrow stroma cells showed enhanced migration capabilities when cultured on stiffer porous substrates, a crucial event in bone tissue repair processes.[210] Scaffold porosity and pore size have been observed to control and promote osteogenic differentiation.[22] However, in the quest to design an optimal 3D polymer scaffold for tissue repair applications, the combined effects of scaffold properties on cell fate need to be deconvoluted.

In the context of bone repair, one of the major unsolved challenges associated with the successful integration of implanted scaffolds is their capability to associate with the host vasculature. *In vivo* angiogenesis and scaffold viability are promoted in structures that contain a highly interconnected porous network with large pores (200 to 400 μm).[111–113] However, the currently available approaches for screening and designing 3D polymer scaffolds are limited in their ability to assay multiple polymers, 3D microstructures and mechanical properties simultaneously.

Herein, a method was developed to obtain arrays of 3D polymer scaffolds with freeze-casting and photo-polymerisation to explore and assess foetal bone marrow stroma cells (FBMSCs) behaviour in libraries of porous polymer scaffolds (Figure 5-1). Aiming to discover an optimal candidate for bone repair applications, FBMSCs were used to screen the scaffold candidates because of their potential to differentiate into osteoblasts. Acrylate-based monomers were chosen due to their proven ability to provide polymers capable of binding embryonic stem cells[30] and bone cells (appendix A), moreover, the *in vivo* pro-angiogenic potential of acrylate-based polymers was suggested in a previous report.[29,211]

To analyse FBMSCs proliferation on the 3D polymer scaffolds, an array of 45 polymers in a flat-bottomed 96-well plate was obtained combining 15 different polymerisation mixtures (Figure 5-2 and Table 5-1) with three levels of porogenic solvent (DMSO) to give so-called scaffolds with “medium” and “high” porosity, **P60** (60% v/v DMSO) and **P80** (80% v/v DMSO), and their non-porous controls **P0** (0% v/v DMSO). Pores were generated as a consequence of the “slow” cooling procedure (5 °C for 16 h and – 20 °C for 4 h) explored above (section 0), which produces a phase separation between DMSO and polymerisation mixtures as well as a crystalline mould. Scaffold structure was consolidated by UV photo-polymerisation (30 min).

Proliferation on the scaffolds was assed using Alamar Blue over 21 days and FBMSCs (Figure 5-5 and Figure 5-6). **Polymers 1-6** with porosity **P0**, **P60** and **P80** were selected for further analysis due to their higher proliferative rates. FBMSCs total collagen deposition (Figure 5-7) and ALP activity (Figure 5-8) on these 3D polymer scaffolds were used as markers for ECM formation and osteoblastic differentiation respectively.[212] The investigation of FBMSCs behaviour on porous scaffolds (**P60** and **P80**) against non-porous scaffold (**P0**) and tissue culture well plate control (TC) showed an increase of ECM deposition and ALP levels on the porous constructions (Figure 5-9). Among the 18 different scaffolds screened, **P80-2** and **P80-3** were the most outstanding materials.

Scaffold microstructure was observed to be controlled by the level of DMSO as expected (Figure 5-10), with porosities greater than 60% and the abundant presence of interconnected pores larger than 100 µm (Figure 5-11). Moreover, pores larger than 200 µm were observed for the **P80-2** scaffolds, associated with the potential for promoting osteogenesis as well as angiogenesis.[111,113] Indentation moduli (stiffness) for scaffolds with “medium” and “high” porosity along with their non-porous controls showed the broad range of mechanical properties that these materials were able to cover (Figure 5-12). For example, **P80-2** was considered a “stiff” scaffold (3.0 MPa) while **P80-3** was “soft”. Additionally, the relaxation load (the ability to withstand loads without breaking) determined after 5 min relaxation (Figure 5-13) confirmed scaffolds displayed a range of mechanical properties similar to collagenous bone, articular cartilage or trabecular bone.[188,189,213,214]

The comparison of FBMSCs behaviour with physical properties of the scaffolds allowed light to be shone on the complex interplay between cells and scaffolds (Figure 5-14). Overall, scaffolds **P80-2** and **P80-3** were observed to be the top candidates among **polymers 1-6** due to their optimal physical properties and osteogenic potential (Figure 5-15).

Version **P80** of **polymers 2** and **3** were validated using FBMSCs biomarker signatures, which are determinant of cell phenotype. Three stages are distinguished in the osteogenic differentiation of skeletal progenitor cells.[212]

1) Proliferative stage characterised by ALP and type I collagen expression.

2) Maturation stage characterised by increasing levels of type I collagen, osteopontin, osteocalcin and bone sialoprotein with decreasing ALP expression.
3) Mineralisation stage with reduction of collagen and osteopontin expression.

The SEM images of FBMSCs laden scaffolds demonstrated cells across the surface and the pores forming a "3D" cell microenvironment (Figure 5-16). Immunofluorescence analysis confirmed FBMSCs ALP expression (Figure 5-18), which is an early osteoblast differentiation marker responsible for the mineralisation of the extracellular matrix.[215] The immunostaining quantification showed the significant decrease of ALP expression on **P80-2** between day 2 and 7, suggesting FMBSCs progressed towards a more differentiated osteoblast phenotype, with a FBMSCS proliferation rate comparable to the 3D array data (Figure 5-19).

Type I collagen and osteopontin expression on scaffolds **P80-2** and **P80-3** seeded with FBMSCs were compared to cells on control tissue culture plates (TC) using basal medium, α-MEM medium supplemented with FBS and antibiotics, and osteogenic medium, basal medium supplemented with calcitriol and vitamin C) (Figure 5-22.[204,205] FMBSCs maintained in 2D controls displayed less type I collagen expression to cells on 3D scaffolds after 21 days in basal and osteogenic supplemented media (Figure 5-23). FMBSCs osteopontin expression was maintained on the scaffolds **P80-3** in both media conditions, however, a decrease of osteopontin expression was observed on scaffolds **P80-2**, which suggested progression towards a more differentiated osteoblastic phenotype.[206]

In support of the enhanced differentiation, aggregates of FBMSCs on scaffolds **P80-2** were observed to be composed of viable cells attached to the polymer matrix (Figure 5-25). Perhaps, aggregates of FBMSCs could be evidence of an intramembranous ossification process where MSCs form dense clusters of cells, with high type I collagen expression, to generate cortical bone.[216] Moreover, type I collagen production quantified by ELISA showed **P80-3** increased collagen expression compared to **P80-2** (Figure 5-26). However, both porous scaffolds had higher collagen expression than the TC control, which was below the assay detection limit (human pro-collagen I, abcam, range 39 pg/mL to 2000 pg/mL). This supported excellent osteoblastic differentiation as evidenced by high type I collagen matrix production.

Mineralisation is a slow biological mediated process that involves apatite minerals deposition into collagenous ECM and it is used to confirm bone formation as a late osteoblastic differentiation marker.[86] To accelerate biomineralisation, 2-phospho-L-ascorbate, β-glycerophosphate and dexamethasone are commonly used as supplements although their effects are not always fully understood.[140,141,182] 2-phospho-L-ascorbate has been shown stable under culture conditions and it is a source of ascorbic acid *via* enzymatic hydrolysis mediated by ALP, which promotes osteoblastic differentiation upregulating type I collagen expression.[217] Dexamethasone has been shown to induce osteoblastic differentiation by activating WNT/β-catenin signalling and RUNX2 expression with β-glycerophosphate acting as a second phosphate source upregulating osteogenic gene expression; however, β-glycerophosphate concentration presents large variations (1 to 20 mM) in the literature and its use has been identified with non-osteogenic dystrophic mineralisation.[218]

Hypothesising that FBMSCs differentiate to osteoblastic phenotype before mineralising, the effect of osteogenic and mineralisation media along with their combinations (Table 5-2) on FBMSCs culture on TC well plates was assessed using alizarin red (non-specific to bone apatite minerals) and OsteoSense® 800 (*in vivo* near-infrared bone staining).[144] Mineralisation medium was stablished as basal medium supplemented with 2-phospho-L-ascorbate (50 μg/mL), β-glycerophosphate (20 mM) and dexamethasone (10 nM) based on alizarin red staining although significant differences between media were not observed for the near-infrared dye (Figure 5-27).

FBMSCs biomineralisation on scaffolds **P80-2** and **P80-3** was assayed with OsteoSense® 800 and BoneTag™ (Figure 5-28) as a consequence of alizarin red non-specificity (high in porous materials) and to improve specificity of mineralisation assessment.[207,219] FBMSCs mineralisation was observed for porous scaffolds **P80-2** and **P80-3** in comparison to the controls, scaffolds without cells and FBMSCs on tissue culture well plates, even though differences between basal and mineralisation media were not identified (Figure 5-29). These results suggest mineralisation could happen on the scaffolds in the absence of supplemented medium; however, mineralisation needs to be evaluated further.

Chick chorioallantoic membrane (CAM) *ex vivo* model provides a highly vascularised bed to evaluate scaffolds **P80-2** and **P80-3** biocompatibility and angiogenesis before experimentation in more advanced models (Figure 5-30).[208] Angiogenesis on scaffolds **P80-2** and **P80-3** with and without FBMSCs was quantified with the Chalkley score method with **P80-2** scaffolds displaying the highest level of vasculature (Figure 5-31). Moreover, the scaffold integration in the CAM with vasculature network formation and infiltration of avian host cells supported scaffold biocompatibility (Figure 5-32).

Scaffold **P80-2** were selected for *in vivo* analysis on the basis of their capacity to promote FBMSCs aggregation, indicative of biological functions and improved cell-cell communications,[220] osteoblastic phenotype expression and enhanced angiogenesis. Furthermore, **P80-2** had an excellent interconnected porous structure with pore size larger than 200 μm and mechanical properties in matching with musculoskeletal needs.

In vivo angiogenesis of the scaffold, a necessary step in bone repair applications,[95,221] was assessed using a subcutaneous murine model.[222] **P80-2** scaffolds were shown to be highly integrated in the host tissue four weeks post-implantation with an absence of abnormal mineralisation in the subcutaneous pocket (Figure 5-34). The observation of extensive collagen deposition (Figure 5-35) and vasculature (Figure 5-37) within the scaffolds, an uncommon observation in the absence of exogenously supplied VEGF factors or endothelial cells,[223] supported the development of a new class of synthetic angiogenic materials.

Host multinucleated giant cells were identified in scaffolds **P80-2** with and without pre-seeded FBMSCs (Figure 5-37). These cells are part of the host immune response and have functions comparable to osteoclasts in resorption and remodelling,[224] moreover, they are known to trigger vascularisation.[195] VEGFR-2 expression suggested scaffolds **P80-2** pre-seeded with FBMSCs improved the recruitment of endothelial cells, which could enhance vasculogenesis (Figure 5-39). In agreement with our results, an earlier report suggested that primary human osteoblasts guide host multinucleated giant cells and endothelial cells into scaffolds, improving scaffold vascularisation.[195] Therefore, scaffolds pre-cultured with FBMSCs appear to increase vasculogenesis in concert with host immune response.

5.4 Conclusions

An array of 3D polymer scaffolds was used to design a highly functional 3D scaffold which displayed exceptional angiogenesis ability. The array enabled the rapid fabrication and screening of tailored libraries of functional 3D polymer scaffolds *via* freeze-casting and UV photo-polymerisation.

Scaffold microstructure was tuned by modifying the level of the porogenic solvent to provide highly interconnected porous materials with porosities greater than 80% and average pore sizes larger than 150 μm. Moreover, the scaffold mechanical characterisation showed they could be excellent candidates for skeletal repair applications due to their indentation moduli ranging from 10 KPa to 10 MPa and their high capacity for load reduction.

Foetal bone marrow stroma cells (FBMSCs) were used to interrogate the arrays and select two porous candidates, **P80-2** and **P80-3**, which exhibited excellent cell proliferation rate with collagen deposition and ALP expression indicating the progression of osteoblastic cellular differentiation. During the screening process, FBMSCs on porous scaffolds were compared to FBMSCs on scaffolds without pores (P0) and tissue culture plates (TC) to assess how the 3D microenvironment tuned cellular fate.

Biocompatibility and angiogenesis of the 3D polymer scaffolds were analysed *ex vivo* using a chick CAM model and *in vivo* applying a mouse subcutaneous model. Biocompatibility of scaffolds **P80-2** and **P80-3** was evidenced by the CAM assay, which showed significant angiogenesis and host cell recruitment. The **P80-2** scaffolds implanted subcutaneously in mice showed extensive vascularisation within and throughout the synthetic 3D porous polymer, which confirmed its regenerative potential in a mammalian model.

Overall, the array of 3D polymer scaffolds allowed the rapid screening of both multiple polymer combinations and varying physical properties leading to the identification of a new class of osteogenic and angiogenic materials. Furthermore, this remarkable vascularisation potential, a crucial property for tissue regeneration, makes scaffolds of **co-polymer 2**, poly(MTEMA$_{36}$-*co*-IBA$_{36}$-*co*-HDOBA$_{18}$), promising for applications in hard and soft skeletal tissues.

6. Concluding remarks and outlook

Fabrication strategies of 3D polymeric biomaterial to date have focused on exploring how either scaffold composition or scaffold microstructure can promote tissue regeneration. However, fewer examples can be found where both of these characteristics are tuned simultaneously.

Herein, an array of 3D polymer scaffolds was developed to explore the potential of acrylate-based 3D polymers in providing biomimetic microenvironments that support the expansion and differentiation of bone progenitor cells. Freeze-casting with DMSO as the porogenic solvent and UV photo-polymerisation were identified as the best approach to control the 3D microstructure and composition of the scaffolds. This method enabled the fabrication and screening of up to 96 different polymer scaffolds in a convenient platform suitable for the majority of biological settings. 45 different 3D polymers were interrogated with foetal bone marrow stromal cells (FBMSCs) to discover scaffolds that promote cell proliferation and ECM formation, while the array approach using micro-CT allowed the high-content morphological screening of 12 polymer scaffolds in a single scan.

The 3D polymer scaffolds identified *in vitro* were validated *ex vivo*, with a CAM assay, and *in vivo*, with subcutaneous implantation in mice, with the leading 3D polymer showing high biocompatibility, integration in the tissue and vascularisation. Next steps will entail the assessment of the 3D polymer scaffolds in a bone defect model for its ability to integrate with bone tissue and promote osteogenesis.

Although this proof-of-concept strategy has been proven successful in identifying biocompatible 3D polymer scaffolds, there are some aspects that could improve the method. Fine control of cooling gradients using Peltier-based coolers with PID controllers could be employed to enable the fabrication of new porous arrays. Moreover, exploring different porogenic solvents such as water, which has multiple ice crystal structures (e.g. hexagonal, stellar, dendrite) that can be translated to scaffold microstructure, could reveal new structures that can tune cell fate.

7. References

[1] A. Atala, F. Kurtis Kasper, A. G. Mikos, *Sci. Transl. Med.* **2012**, *4*, 1.

[2] In *The Williams Dictionary of Biomaterials*; Williams, D. F., Ed.; Liverpool University Press, 1999.

[3] In *Biomaterials*; Migonney, V., Ed.; Wiley, 2014.

[4] L. L. Hench, J. M. Polak, *Science* **2002**, *295*.

[5] M. Navarro, a Michiardi, O. Castaño, J. a Planell, *J. R. Soc. Interface* **2008**, *5*, 1137.

[6] J. M. Branemark, PI; Breine, U.; Johansson, B.; Roylance, P.J.; Rocker, H.; Yoffey, *Acta Anat* **1964**, *59*, 1.

[7] In *Biosynthetic Polymers for Medical Applications*; Poole-Warren, L.; Martens, P.; Green, R., Eds.; Elsevier, 2016.

[8] E. S. Place, N. D. Evans, M. M. Stevens, *Nat. Mater.* **2009**, *8*, 457.

[9] E. Thomas Pashuck, M. M. Stevens, *Sci. Transl. Med.* **2012**, *4*.

[10] L. Pedraz, G. Orive, E. Santos, R. M. Herna, *Trends Biotechnol.* **2012**, *30*, 331.

[11] K. Duval, H. Grover, L.-H. Han, Y. Mou, A. F. Pegoraro, J. Fredberg, Z. Chen, *Physiology* **2017**, *32*, 266.

[12] A. J. Cavanagh, P.R.; Licata, A.A.; Rice, In *Proceedings of the 20th Annual Meeting of the American Society for Gravitational and Space Biology*; 2005.

[13] D. Tang, R. S. Tare, L. Y. Yang, D. F. Williams, K. L. Ou, R. O. C. Oreffo, *Biomaterials* **2016**, *83*, 363.

[14] A. J. Engler, S. Sen, H. L. Sweeney, D. E. Discher, *Cell* **2006**, *126*, 677.

[15] M. J. P. Biggs, R. G. Richards, N. Gadegaard, C. D. W. Wilkinson, R. O. C. Oreffo, M. J. Dalby, *Biomaterials* **2009**, *30*, 5094.

[16] K. A. Kilian, B. Bugarija, B. T. Lahn, M. Mrksich, *Proc. Natl. Acad. Sci. U. S. A.* **2010**, *107*, 4872.

[17] G. Charras, E. Sahai, *Nat. Rev. Mol. Cell Biol.* **2014**, *15*, 813.

[18] J. Aureille, N. Belaadi, C. Guilluy, *Curr. Opin. Cell Biol.* **2017**, *44*, 59.

[19] J. Nishida, T. Shimamura, *Med. Sci. Monit.* **2008**, *14*, 107.

[20] A. S. Brydone, D. Meek, S. MacLaine, *Proc. Inst. Mech. Eng. Part H J. Eng. Med.* **2010**, *224*, 1329.

[21] P. Zorlutuna, N. Annabi, G. Camci-Unal, M. Nikkhah, J. M. Cha, J. W. Nichol, A. Manbachi, H. Bae, S. Chen, A. Khademhosseini, *Adv. Mater.* **2012**, *24*, 1782.

[22] C. M. Murphy, M. G. Haugh, F. J. O'Brien, *Biomaterials* **2010**, *31*, 461.

[23] Q. Yao, J. G. L. Cosme, T. Xu, J. M. Miszuk, P. H. S. Picciani, H. Fong, H. Sun, *Biomaterials* **2017**, *115*, 115.

[24] E. López-Ruiz, S. Venkateswaran, M. Perán, G. Jiménez, S. Pernagallo, J. J. DÍaz-Mochón, O. Tura-Ceide, F. Arrebola, J. Melchor, J. Soto, G. Rus, P. J. Real, M. DIaz-Ricart, A. Conde-González, M. Bradley, J. A. Marchal, *Sci. Rep.* **2017**, *7*, 1.

[25] G. A. Di Lullo, S. M. Sweeney, J. Körkkö, L. Ala-Kokko, J. D. San Antonio, *J. Biol. Chem.* **2002**, *277*, 4223.

[26] In *Biodegradable and Biocompatible Polymer Composites*; Balaji, A. B.; Pakalapati, H.; Khalid, M.; Walvekar, R.; Siddiqui, H., Eds.; Elsevier, 2018.

[27] F. Nudelman, K. Pieterse, A. George, P. H. H. Bomans, H. Friedrich, L. J. Brylka, P. A. J. Hilbers, G. De With, N. A. J. M. Sommerdijk, *Nat. Mater.* **2010**, *9*, 1004.

[28] D. C. Hay, S. Pernagallo, J. J. Diaz-Mochon, C. N. Medine, S. Greenhough, Z. Hannoun, J. Schrader, J. R. Black, J. Fletcher, D. Dalgetty, A. I. Thompson, P. N. Newsome, S. J. Forbes, J. A. Ross, M. Bradley, J. P. Iredale, *Stem Cell Res.* **2011**, *6*, 92.

[29] S. Pernagallo, O. Tura, M. Wu, K. Samuel, J. J. Diaz-Mochon, A. Hansen, R. Zhang, M. Jackson, G. J. Padfield, P. W. F. Hadoke, N. L. Mills, M. L. Turner, J. P. Iredale, D. C. Hay, M. Bradley, *Adv. Healthc. Mater.* **2012**, *1*, 646.

[30] A. Hansen, H. K. Mjoseng, R. Zhang, M. Kalloudis, V. Koutsos, P. A. de Sousa, M. Bradley, *Adv. Healthc. Mater.* **2014**, *3*, 848.

[31] C. R. E. Duffy, R. Zhang, S.-E. How, A. Lilienkampf, G. Tourniaire, W. Hu, C. C. West, P. de Sousa, M. Bradley, *Biomater. Sci.* **2014**, *2*, 1683.

[32] R. Santoro, S. Venkateswaran, F. Amadeo, R. Zhang, M. Brioschi, A. Callanan, M. Agrifoglio, C. Banfi, M. Bradley, M. Pesce, *Biomater. Sci.* **2018**, *6*, 154.

[33] S. R. Caliari, J. A. Burdick, *Nat. Methods* **2016**, *13*, 405.

[34] Z. Li, X. Guo, S. Matsushita, J. Guan, *Biomaterials* **2011**, *32*, 3220.

[35] G. Jiménez, S. Venkateswaran, E. López-Ruiz, M. Perán, S. Pernagallo, J. J. Díaz-Monchón, R. F. Canadas, C. Antich, J. M. Oliveira, A. Callanan, R. Walllace, R. L. Reis, E. Montañez, E. Carrillo, M. Bradley, J. A. Marchal, *Acta Biomater.* **2019**, *90*, 146.

[36] In *Polymer Synthesis: Theory and Practice*; Braun, D.; Cherdron, H.; Rehahn, M.; Ritter, H.; Voit, B., Eds.; Springer, 2013.

[37] In *Polymeric Hydrogels as Smart Biomaterials*; Kalia, S., Ed.; Springer, 2016.

[38] D. M. Rosenbaum, D. R. Liu, *J. Am. Chem. Soc.* **2003**, *125*, 13924.

[39] K. Matyjaszewski, *Macromolecules* **2012**, *45*, 4015.

[40] S. Perrier, *Macromolecules* **2017**, *50*, 7433.

[41] J. J. Hanak, *J. Mater. Sci.* **1970**, *5*, 964.

[42] B. Healey, *Science* **1995**, *269*, 1078.

[43] S. Brocchini, K. James, V. Tangpasuthadol, J. Kohn, *J. Biomed. Mater. Res.* **1998**, *42*, 66.

[44] J. J. Díaz-Mochón, G. Tourniaire, M. Bradley, *Chem. Soc. Rev.* **2007**, *36*, 449.

[45] D. G. Anderson, S. Levenberg, R. Langer, *Nat. Biotechnol.* **2004**, *22*, 863.

[46] R. Zhang, A. Liberski, R. Sanchez-Martin, M. Bradley, *Biomaterials* **2009**, *30*, 6193.

[47] A. Hansen, R. Zhang, M. Bradley, *Macromol. Rapid Commun.* **2012**, *33*, 1114.

[48] In *Microarray analysis*; Mark Schena, Ed.; Wiley-Liss, 2003.

[49] P. S. Maher, R. P. Keatch, K. Donnelly, R. E. MacKay, J. Z. Paxton, *Rapid Prototyp. J.* **2009**, *15*, 204.

[50] M. Vaezi, H. Seitz, S. Yang, *Int. J. Adv. Manuf. Technol.* **2013**, *67*, 1721.

[51] B. Gao, Q. Yang, X. Zhao, G. Jin, Y. Ma, F. Xu, *Trends Biotechnol.* **2016**, *34*, 1.

[52] H. Kang, S. J. Lee, I. K. Ko, C. Kengla, J. J. Yoo, A. Atala, *Nat. Biotechnol.* **2016**.

[53] K. Satoshi, S. Hong-Bo, T. Tomokazu, T. Kenji, *Nature* **2001**, *412*, 697.

[54] A. Di Luca, K. Szlazak, I. Lorenzo-Moldero, C. A. Ghebes, A. Lepedda, W. Swieszkowski, C. Van Blitterswijk, L. Moroni, *Acta Biomater.* **2016**, *36*, 210.

[55] T. Bhattacharjee, S. M. Zehnder, K. G. Rowe, S. Jain, R. M. Nixon, W. G. Sawyer, T. E. Angelini, *Sci. Adv.* **2015**, *1*, E1500655.

[56] A. Eatemadi, H. Daraee, N. Zarghami, H. M. Yar, A. Akbarzadeh, *Artif. Cells, Nanomedicine Biotechnol.* **2016**, *44*, 111.

[57] K. H. Lee, H. Y. Kim, M. S. Khil, Y. M. Ra, D. R. Lee, *Polymer (Guildf).* **2003**, *44*, 1287.

[58] R. B. Diego, M. P. Olmedilla, Á. S. Aroca, J. L. G. Ribelles, M. M. Pradas, G. G. Ferrer, M. S. Sánchez, *J. Mater. Sci.* **2005**, *40*, 4881.

[59] S. Yu, F. L. Ng, K. C. C. Ma, A. A. Mon, F. L. Ng, Y. Y. Ng, *J. Appl. Polym. Sci.* **2013**, *127*, 2641.

[60] Y. Hu, S. Ma, Z. Yang, W. Zhou, Z. Du, J. Huang, H. Yi, C. Wang, *Colloids Surfaces B Biointerfaces* **2016**, *140*, 382.

[61] F. Dehghani, N. Annabi, *Curr. Opin. Biotechnol.* **2011**, *22*, 661.

[62] K. K. Taek, J. Y. Jun, S. L. Doo, T. G. Park, *Biomaterials* **2006**, *27*, 152.

[63] W. L. Li, K. Lu, J. Y. Walz, *Int. Mater. Rev.* **2011**, *57*, 37.

[64] I. A. Quintero Ortega, J. D. Mota-Morales, E. A. Elizalde Peña, D. G. Zárate-Triviño, Y. A. De Santiago, A. Ortiz, B. García Gaitan, I. C. Sanchez, G. Luna-Bárcenas, *Ind. Eng. Chem. Res.* **2013**, *52*, 706.

[65] H. Bai, D. Wang, B. Delattre, W. Gao, J. De Coninck, S. Li, A. P. Tomsia, *Acta Biomater.* **2015**, *20*, 113.

[66] Y. Zhou, S. Fu, Y. Pu, S. Pan, M. V. Levit, A. J. Ragauskas, *RSC Adv.* **2013**, *3*, 19272.

[67] Y. H. Koh, J. J. Sun, H. E. Kim, *Mater. Lett.* **2007**, *61*, 1283.

[68] K. Araki, J. W. Halloran, *J. Am. Ceram. Soc.* **2005**, *87*, 2014.

[69] R. Chen, C. A. Wang, Y. Huang, L. Ma, W. Lin, *J. Am. Ceram. Soc.* **2007**, *90*, 3478.

[70] National Institute of Standards and Technology, Phase change data Dimethyl Sulfoxide (DMSO). *NIST Chem. Webb.* **2019**.

[71] K. Lu, C. Hammond, J. Qian, *J. Mater. Sci.* **2010**, *45*, 582.

[72] N. Annabi, J. W. Nichol, D. Ph, X. Zhong, C. Ji, **2010**, *16*.

[73] D. L. Elbert, *Acta Biomater.* **2011**, *7*, 31.

[74] D. Wu, F. Xu, B. Sun, R. Fu, H. He, K. Matyjaszewski, *Chem. Rev.* **2012**, *112*, 3959.

[75] B. Thavornyutikarn, N. Chantarapanich, K. Sitthiseripratip, G. A. Thouas, Q. Chen, *Prog. Biomater.* **2014**, *3*, 61.

[76] In *A Companion to Paleopathology*; Grauer, A. L., Ed.; Wiley-Blackwell, 2012.

[77] S. Wu, X. Liu, K. W. K. Yeung, C. Liu, X. Yang, *Mater. Sci. Eng. R* **2014**, *80*, 1.

[78] In *Ortner's Identification of Pathological Conditions in Human Skeletal Remains*; Buikstra, J. E., Ed.; Elsevier, 2019.

[79] H. Ema, H. Nakauchi, *Blood* **2000**, *95*, 2284.

[80] K. A. Hing, *Philos. Trans. Math. Phys. Eng. Sci.* **2004**, *362*, 2821.

[81] B. Wopenka, J. D. Pasteris, *Mater. Sci. Eng. C* **2005**, *25*, 131.

[82] R. Florencio-Silva, G. R. D. S. Sasso, E. Sasso-Cerri, M. J. Simões, P. S. Cerri, *Biomed Res. Int.* **2015**, *2015*.

[83] In *Primer on the Metabolic Bone Diseases and Disorders of Mineral Metabolism*; Bilezikian, J. P., Ed.; Wiley-Blackwell, 2013.

[84] M. Phimphilai, Z. Zhao, H. Boules, H. Roca, R. T. Franceschi, *J. Bone Miner. Res.* **2006**, *21*, 637.

[85] H. C. Anderson, *Curr. Rheumatol. Rep.* **2003**, *5*, 222.

[86] In *Pediatric Bone*; Glorieux, F. H.; Pettifor, J. M.; Juppner, H., Eds.; Elsevier, 2012.

[87] G. Boivin, Y. Bala, A. Doublier, D. Farlay, L. G. Ste-Marie, P. J. Meunier, P. D. Delmas, *Bone* **2008**, *43*, 532.

[88] T. Bellido, *Calcif. Tissue Int.* **2014**, *94*, 25.

[89] D. L. Lopes, C. Martins-Cruz, M. B. Oliveira, J. F. Mano, *Biomaterials* **2018**, *185*, 240.

[90] In *The Ciba collection of medical illustrations*; Netter, F. H., Ed.; CIBA Pharmaceutical Company, 1987.

[91] T. A. Einhorn, L. C. Gerstenfeld, *Nat. Rev. Rheumatol.* **2015**, *11*, 45.

[92] N. M. G. Kurdy, J. B. Weiss, A. Bate, *Injury* **1996**, *27*, 143.

[93] F. Y. I. Lee, Yong Won Choi, F. F. Behrens, D. O. DeFouw, T. A. Einhorn, *J. Orthop. Res.* **1998**, *16*, 144.

[94] M. Melnyk, T. Henke, L. Claes, P. Augat, *Arch. Orthop. Trauma Surg.* **2008**, *128*, 1159.

[95] S. Stegen, N. van Gastel, G. Carmeliet, *Bone* **2015**, *70*, 19.

[96] E. Zelzer, R. Mamluk, N. Ferrara, R. S. Johnson, E. Schipani, B. R. Olsen, *Development* **2004**, *131*, 2161.

[97] M. Bouletreau, Pierre; Warren, Stephen; Spector, Jason; Peled, Ziv;Gerrets, Rene ; Greenwald, Joshua;Longaker, *Plast. Reconstr. Surg.* **2002**, *109*, 2384.

[98] M. M. L. Deckers, M. Karperien, C. Van Der Bent, T. Yamashita, S. E. Papapoulos, C. W. G. M. Löwik, *Endocrinology* **2000**, *141*, 1667.

[99] U. Mayr-wohlfart, J. Waltenberger, H. Hausser, S. Kessler, K. P. Günther, C. Dehio, W. Puhl, R. E. Brenner, *Bone* **2002**, *30*, 472.

[100] R. Blanco, H. Gerhardt, *Cold Spring Harb. Perspect. Med.* **2013**, *3*, 1.

[101] M. Potente, H. Gerhardt, P. Carmeliet, *Cell* **2011**, *146*, 873.

[102] A. Syahrom, M. Al-Fatihhi, M. Szali, J. Muhamad, N. Harun, A. Öchsner, In *Cancellous Bone - Mechanical Characterization and Finite Element Simulation*; Springer, 2018.

[103] O. R. Boughton, S. Ma, S. Zhao, M. Arnold, A. Lewis, U. Hansen, J. P. Cobb, F. Giuliani, R. L. Abel, *PLoS One* **2018**, *13*, 1.

[104] H. Follet, G. Boivin, C. Rumelhart, P. J. Meunier, *Bone* **2004**, *34*, 783.

[105] K. Alvarez, H. Nakajima, *Materials (Basel).* **2009**, *2*, 790.

[106] E. J. Sheehy, D. J. Kelly, F. J. O'Brien, *Mater. Today Bio* **2019**, *3*, 100009.

[107] J. S. Choi, B. A. C. Harley, *Sci. Adv.* **2017**, *3*.

[108] V. Karageorgiou, D. Kaplan, *Biomaterials* **2005**, *26*, 5474.

[109] J. W. Lee, G. Ahn, D. W. Cho, J. Y. Kim, *J. Mater. Sci. Mater. Med.* **2010**, *21*, 3195.

[110] Y. Takahashi, Y. Tabata, *J. Biomater. Sci. Polym. Ed.* **2004**, *15*, 41.

[111] J. L. Simon, S. Michna, J. A. Lewis, E. D. Rekow, V. P. Thompson, J. E. Smay, A. Yampolsky, J. R. Parsons, J. L. Ricci, *J. Biomed. Mater. Res. Part A* **2007**, *83*, 747.

[112] R. A. Perez, G. Mestres, *Mater. Sci. Eng. C* **2016**, *61*, 922.

[113] F. M. Klenke, Y. Liu, H. Yuan, E. B. Hunziker, K. A. Siebenrock, W. Hofstetter, *J. Biomed. Mater. Res. Part A* **2008**, *85*, 777.

[114] M. I. Santos, R. E. Unger, R. A. Sousa, R. L. Reis, C. J. Kirkpatrick, *Biomaterials* **2009**, *30*, 4407.

[115] T. Albrektsson, C. Johansson, *Eur. Spine J.* **2001**, *10*, S96.

[116] In *Rapid Prototyping of Biomaterials: Principles and Applications*; Narayan, R., Ed.; Elsevier, 2014; pp. 176–200.

[117] A. Venturato, G. MacFarlane, J. Geng, M. Bradley, *Macromol. Biosci.* **2016**, *16*, 1864.

[118] R. S. Tare, F. Khan, G. Tourniaire, S. M. Morgan, M. Bradley, R. O. C. Oreffo, *Biomaterials* **2009**, *30*, 1045.

[119] F. Khan, R. S. Tare, R. O. C. Oreffo, M. Bradley, *Angew. Chemie - Int. Ed.* **2009**, *48*, 978.

[120] F. Khan, R. S. Tare, J. M. Kanczler, R. O. C. Oreffo, M. Bradley, *Biomaterials* **2010**, *31*, 2216.

[121] F. Khan, J. O. Smith, J. M. Kanczler, R. S. Tare, R. O. C. Oreffo, M. Bradley, *Adv. Funct. Mater.* **2013**, *23*, 2850.

[122] J. O. Smith, E. R. Tayton, F. Khan, A. Aarvold, R. B. Cook, A. Goodship, M. Bradley, R. O. C. Oreffo, *J. Tissue Eng. Regen. Med.* **2017**, *11*, 1065.

[123] D. F. E. Ker, D. Wang, A. W. Behn, E. T. H. Wang, X. Zhang, B. Y. Zhou, Á. E. Mercado-Pagán, S. Kim, J. Kleimeyer, B. Gharaibeh, Y. Shanjani, D. Nelson, M. Safran, E. Cheung, P. Campbell, Y. P. Yang, *Adv. Funct. Mater.* **2018**, *28*, 1.

[124] S. Yao, X. Lin, Y. Xu, Y. Chen, P. Qiu, C. Shao, B. Jin, Z. Mu, N. A. J. M. Sommerdijk, R. Tang, **2019**, *1900683*.

[125] H. Cheng, R. Chabok, X. Guan, A. Chawla, Y. Li, A. Khademhosseini, H. L. Jang, *Acta Biomater.* **2018**, *69*, 342.

[126] K. Y. Morgan, D. Sklaviadis, Z. L. Tochka, K. M. Fischer, K. Hearon, T. D. Morgan, R. Langer, L. E. Freed, *Adv. Funct. Mater.* **2016**, *26*, 5873.

[127] S. Camarero-Espinosa, B. Rothen-Rutishauser, C. Weder, E. J. Foster, *Biomaterials* **2016**, *74*, 42.

[128] S. Yin, W. Zhang, Z. Zhang, X. Jiang, *Adv. Healthc. Mater.* **2019**, *8*, 1801433.

[129] R. D. Prabha, D. C. E. Kraft, L. Harkness, B. Melsen, H. Varma, P. D. Nair, J. Kjems, M. Kassem, *J. Tissue Eng. Regen. Med.* **2018**, *12*, e1537.

[130] J. Ye, J. Wang, Y. Zhu, Q. Wei, X. Wang, J. Yang, S. Tang, H. Liu, J. Fan, F. Zhang, E. M. Farina, M. K. Mohammed, Y. Zou, D. Song, J. Liao, J. Huang, D. Guo, M. Lu, F. Liu, J. Liu, L. Li, C. Ma, X. Hu, R. C. Haydon, M. J. Lee, R. R. Reid, G. A. Ameer, L. Yang, T. C. He, *Biomed. Mater.* **2016**, *11*, 025021.

[131] L. Ren, Y. Kang, C. Browne, J. Bishop, Y. Yang, *Bone* **2014**, *64*, 173.

[132] L. Wang, H. Fan, Z. Y. Zhang, A. J. Lou, G. X. Pei, S. Jiang, T. W. Mu, J. J. Qin, S. Y. Chen, D. Jin, *Biomaterials* **2010**, *31*, 9452.

[133] M. van Driel, J. P. T. M. van Leeuwen, *Bonekey Rep.* **2014**, *3*, 1.

[134] M. Doube, M. M. Klosowski, I. Arganda-Carreras, F. P. Cordelières, R. P. Dougherty, J. S. Jackson, B. Schmid, J. R. Hutchinson, S. J. Shefelbine, *Bone* **2010**, *47*, 1076.

[135] S. P. Timoshenko, J. N. Goodier, In *Theory of Elasticity*; McGraw-Hill, Ed.; 1951; pp. 1–14.

[136] V. Egorov, S. Tsyuryupa, S. Kanilo, M. Kogit, A. Sarvazyan, *Med. Eng. Phys.* **2008**, *30*, 206.

[137] R. M. Delaine-Smith, S. Burney, F. R. Balkwill, M. M. Knight, *J. Mech. Behav. Biomed. Mater.* **2016**, *60*, 401.

[138] S. D. McCullen, H. Autefage, A. Callanan, E. Gentleman, M. M. Stevens, *Tissue Eng. Part A* **2012**, *18*, 2073.

[139] J. A. M. Steele, S. D. McCullen, A. Callanan, H. Autefage, M. A. Accardi, D. Dini, M. M. Stevens, *Acta Biomater.* **2014**, *10*, 2065.

[140] F. Langenbach, J. Handschel, *Stem Cell Res. Ther.* **2013**, *4*, 117.

[141] C. Fu, D. Luo, M. Yu, N. Jiang, D. Liu, D. He, Y. Fu, T. Zhang, Y. Qiao, Y. Zhou, Y. Liu, *Adv. Healthc. Mater.* **2018**, *7*, e1800705.

[142] J. Rosser, L. Bonewald, In *Bone Research Protocols. Methods in Molecular Biology*; HelfrichStuart, M. H.; Ralston, H., Eds.; Springer, 2012; pp. 67–81.

[143] C. A. Gregory, W. G. Gunn, A. Peister, D. J. Prockop, *Anal. Biochem.* **2004**, *329*, 77.

[144] M. J. C. Moester, M. A. E. Schoeman, I. B. Oudshoorn, M. M. van Beusekom, I. M. Mol, E. L. Kaijzel, C. W. G. M. Löwik, K. E. De Rooij, *Biochem. Biophys. Res. Commun.* **2014**, *443*, 80.

[145] R. Rezakhaniha, A. Agianniotis, J. T. C. Schrauwen, A. Griffa, D. Sage, C. V. C. Bouten, F. N. Van De Vosse, M. Unser, N. Stergiopulos, *Biomech. Model. Mechanobiol.* **2012**, *11*, 461.

[146] S. Park, E. S. Gil, B. B. Mandal, H. Cho, J. A. Kluge, B. Min, D. L. Kaplan, *J. Tissue Eng. Regen. Med.* **2012**, *6*, 24.

[147] J. C. Moses, S. K. Nandi, B. B. Mandal, *Adv. Healthc. mate* **2018**, *7*, e1701418.

[148] *Isolation, Differentiation, and Characterisation of Skeletal Stem Cells from Human Bone Marrow In Vitro and In Vivo*; Helfrich, M. H.; Ralston, S. H., Eds.; Springer, 2012.

[149] D. Gothard, K. Cheung, J. M. Kanczler, D. I. Wilson, R. O. C. Oreffo, *Stem Cell Res. Ther.* **2015**, *6*, 1.

[150] E. M. Czekanska, J. Geng, M. Glinka, K. White, J. Kanczler, N. D. Evans, R. O. C. Oreffo, M. Bradley, *J. Mater. Chem. B* **2018**, *6*, 4437.

[151] H. W. Chalkley, *J. Natl. Cancer Inst.* **1943**, *4*, 47.

[152] S. Hansen, D. A. Grabau, F. B. Sørensen, M. Bak, W. Vach, C. Rose, *Stem Cells* **2003**, *21*, 681.

[153] S. Inglis, K. H. Schneider, J. M. Kanczler, H. Redl, R. O. C. Oreffo, *Adv. Healthc. Mater.* **2019**, *8*, e1800088.

[154] E. L. Smith, J. M. Kanczler, D. Gothard, C. A. Roberts, J. A. Wells, L. J. White, O. Qutachi, M. J. Sawkins, H. Peto, H. Rashidi, L. Rojo, M. M. Stevens, A. J. El Haj, F. R. A. J. Rose, K. M. Shakesheff, R. O. C. Oreffo, *Acta Biomater.* **2014**, *10*, 4186.

[155] L. G. Griffith, M. A. Swartz, *Nat. Rev. Mol. cell Biol.* **2006**, *7*, 211.

[156] M. B. Oliveira, J. F. Mano, *Trends Biotechnol.* **2014**, *32*, 627.

[157] N. N. T. Le, S. Zorn, S. K. Schmitt, P. Gopalan, W. L. Murphy, *Acta Biomater.* **2016**, *34*, 93.

[158] K. Neumann, A. Conde-González, M. Owens, A. Venturato, Y. Zhang, J. Geng, M. Bradley, *Macromolecules* **2017**, *50*, 6026.

[159] P. P. Provenzano, P. J. Keely, *J. Cell Sci.* **2011**, *124*, 1195.

[160] A. K. Gaharwar, A. Arpanaei, T. L. Andresen, A. Dolatshahi-Pirouz, *Adv. Mater.* **2016**, *28*, 771.

[161] A. Dolatshahi-Pirouz, M. Nikkhah, A. K. Gaharwar, B. Hashmi, E. Guermani, H. Aliabadi, G. Camci-Unal, T. Ferrante, M. Foss, D. E. Ingber, A.

Khademhosseini, *Sci. Rep.* **2015**, *4*, 1.

[162] A. Ranga, S. Gobaa, Y. Okawa, K. Mosiewicz, A. Negro, M. P. Lutolf, *Nat. Commun.* **2014**, *5*, 4324.

[163] Y. Yang, D. Bolikal, M. L. Becker, J. Kohn, D. N. Zeiger, C. G. Simon, *Adv. Mater.* **2008**, *20*, 2037.

[164] K. Cheng, Y. Lai, W. S. Kisaalita, *Biomaterials* **2008**, *29*, 2802.

[165] E. M. Czekanska, M. J. Stoddart, J. R. Ralphs, R. G. Richards, J. S. Hayes, *J. Biomed. Mater. Res. - Part A* **2014**, *102*, 2636.

[166] S. Pernagallo, J. J. Diaz-Mochon, M. Bradley, *Lab Chip* **2009**, *9*, 397.

[167] R. Zhang, H. K. Mjoseng, M. a Hoeve, N. G. Bauer, S. Pells, R. Besseling, S. Velugotla, G. Tourniaire, R. E. B. Kishen, Y. Tsenkina, C. Armit, C. R. E. Duffy, M. Helfen, F. Edenhofer, P. a de Sousa, M. Bradley, *Nat. Commun.* **2013**, *4*, 1335.

[168] S. Hemes, G. Desbois, J. L. Urai, B. Schröppel, J. O. Schwarz, *Microporous Mesoporous Mater.* **2015**, *208*, 1.

[169] M. Schmitt, M. Halisch, C. Muller, C. Peres Fernandes, *Solid Earth* **2016**, *7*, 285.

[170] P. Egan, X. Wang, H. Greutert, K. Shea, K. Wuertz-Kozak, S. Ferguson, *3D Print. Addit. Manuf.* **2019**, *6*, 73.

[171] E. Alabort, D. Barba, R. C. Reed, *Scr. Mater.* **2019**, *164*, 110.

[172] H. Bai, Y. Chen, B. Delattre, A. P. Tomsia, R. O. Ritchie, *Sci. Adv.* **2015**, *1*, e1500849.

[173] A. K. Denisin, B. L. Pruitt, *ACS Appl. Mater. Interfaces* **2016**, *8*, 21893.

[174] E. P. Chan, Y. Hu, P. M. Johnson, Z. Suo, C. M. Stafford, *Soft Matter* **2012**, *8*, 1492.

[175] A. A. Zinchik, I. S. Kuryndin, G. K. Elyashevich, *Phys. Solid State* **2017**, *59*,

583.

[176] M. J. Duer, *J. Magn. Reson.* **2015**, *253*, 98.

[177] G. J. Her, H. C. Wu, M. H. Chen, M. Y. Chen, S. C. Chang, T. W. Wang, *Acta Biomater.* **2013**, *9*, 5170.

[178] O. Chaudhuri, L. Gu, D. Klumpers, M. Darnell, S. A. Bencherif, J. C. Weaver, N. Huebsch, H. P. Lee, E. Lippens, G. N. Duda, D. J. Mooney, *Nat. Mater.* **2016**, *15*, 326.

[179] R. O. Navarrete, E. M. Lee, K. Smith, S. L. Hyzy, M. Doroudi, J. K. Williams, K. Gall, B. D. Boyan, Z. Schwartz, *PLoS One* **2017**, *12*, 1.

[180] Y. Ma, M. Lin, G. Huang, Y. Li, S. Wang, G. Bai, T. J. Lu, F. Xu, *Adv. Mater.* **2018**, *30*, e1705911.

[181] M. Prideaux, A. R. Wijenayaka, D. D. Kumarasinghe, R. T. Ormsby, A. Evdokiou, D. M. Findlay, G. J. Atkins, *Calcif. Tissue Int.* **2014**, *95*, 183.

[182] M. L. Bouxsein, S. K. Boyd, B. A. Christiansen, R. E. Guldberg, K. J. Jepsen, R. Müller, *J. Bone Miner. Res.* **2010**, *25*, 1468.

[183] L. S. Fellay, L. A. Fasce, M. P. Suárez, P. M. Frontini, M. Czerner, *Procedia Mater. Sci.* **2015**, *8*, 287.

[184] X. Liang, J. Gao, W. Xu, X. Wang, Y. Shen, J. Tang, S. Cui, X. Yang, Q. Liu, L. Yu, J. Ding, *Biofabrication* **2019**, *11*, 035009.

[185] D. R. Carter, C. W. E., *Trans. Orthop. Res. Soc.* **1983**, *8*, 285.

[186] C. M. M. Fondrk, E. Bahniuk, D. T. Davy, *Biomechanics* **1988**, *21*.

[187] H. Zilch, A. Rohlmann, G. Bergmann, *Arch Orthop Traumat Surg* **1980**, *97*, 257.

[188] D. D. Deligianni, A. Maris, Y. F. Missirlis, *J. Biomech.* **1994**, *27*, 1469.

[189] A. Lau, M. L. Oyen, R. W. Kent, D. Murakami, T. Torigaki, *Acta Biomater.* **2008**, *4*, 97.

[190] T. Moriguchi, K. Yano, S. Nakagawa, F. Kaji, *J. Colloid Interface Sci.* **2003**, *260*, 19.

[191] A. Higuchi, Q.-D. Ling, Y. Chang, S.-T. Hsu, A. Umezawa, *Chem. Rev.* **2013**, *113*, 3297.

[192] M. J. Elliott, C. R. Butler, A. Varanou-Jenkins, L. Partington, C. Carvalho, E. Samuel, C. Crowley, P. Lange, N. J. Hamilton, R. E. Hynds, T. Ansari, P. Sibbons, A. Fierens, C. McLaren, D. Roebuck, C. Wallis, N. Muthialu, R. Hewitt, D. Crabbe, S. M. Janes, P. De Coppi, M. W. Lowdell, M. A. Birchall, *Stem Cells Transl. Med.* **2017**, *6*, 1458.

[193] N. Mitrousis, A. Fokina, M. S. Shoichet, *Nat. Rev. Mater.* **2018**, *3*, 441.

[194] A. Atala, S. B. Bauer, S. Soker, J. J. Yoo, A. B. Retik, *Lancet* **2006**, *367*, 1241.

[195] S. Ghanaati, R. E. Unger, M. J. Webber, M. Barbeck, C. Orth, J. A. Kirkpatrick, P. Booms, A. Motta, C. Migliaresi, R. A. Sader, C. J. Kirkpatrick, *Biomaterials* **2011**, *32*, 8150.

[196] G. Papavasiliou, M. H. Cheng, E. M. Brey, *J. Investig. Med.* **2010**, *58*, 838.

[197] S. Bose, G. Fielding, S. Tarafder, A. Bandyopadhyay, *Trends Biotechnol.* **2013**, *31*, 594.

[198] H. Tian, J. Du, J. Wen, Y. Liu, S. R. Montgomery, T. P. Scott, B. Aghdasi, C. Xiong, A. Suzuki, T. Hayashi, M. Ruangchainikom, K. Phan, G. Weintraub, A. Raed, S. S. Murray, M. D. Daubs, X. Yang, X. B. Yuan, J. C. Wang, Y. Lu, *ACS Nano* **2016**, *10*, 7362.

[199] J. Bejarano, R. Detsch, A. R. Boccaccini, H. Palza, *J. Biomed. Mater. Res. Part A* **2017**, *105*, 746.

[200] L. Krishna, K. Dhamodaran, C. Jayadev, K. Chatterjee, R. Shetty, S. S. Khora, D. Das, Nanostructured scaffold as a determinant of stem cell fate. *Stem Cell Res. Ther.* **2016**, *7*.

[201] K. O'Donoghue, N. M. Fisk, *Best Pract. Res. Clin. Obstet. Gynaecol.* **2004**,

18, 853.

[202] Y. Li, X. S. Sun, *RSC Adv.* **2015**, *5*, 44009.

[203] H. Wu, P. Chen, C. Yan, C. Cai, Y. Shi, *Mater. Des.* **2019**, *171*, 107704.

[204] D. D. Bikle, *Chem. Biol.* **2014**, *21*, 319.

[205] C. Wang, H. Meng, X. Wang, C. Zhao, J. Peng, Y. Wang, *Med. Sci. Monit.* **2016**, *22*, 226.

[206] W. Huang, B. Carlsen, G. Rudkin, M. Berry, K. Ishida, D. T. Yamaguchi, T. A. Miller, *Bone* **2004**, *34*, 799.

[207] A. Zaheer, R. E. Lenkinski, A. Mahmood, A. G. Jones, L. C. Cantley, J. V. Frangioni, *Nat. Biotechnol.* **2001**, *19*, 1148.

[208] I. Moreno-Jiménez, G. Hulsart-Billstrom, S. A. Lanham, A. A. Janeczek, N. Kontouli, J. M. Kanczler, N. D. Evans, R. O. C. Oreffo, *Sci. Rep.* **2016**, *6*, 1.

[209] M. G. Haugh, T. J. Vaughan, C. M. Madl, R. M. Raftery, L. M. McNamara, F. J. O'Brien, S. C. Heilshorn, *Biomaterials* **2018**, *171*, 23.

[210] C. Lin, B. Tao, Y. Deng, Y. He, X. Shen, R. Wang, L. Lu, Z. Peng, Z. Xia, K. Cai, *Biomaterials* **2019**, *217*.

[211] M. J. Butler, M. V. Sefton, *J. Biomed. Mater. Res. Part A* **2007**, *82*.

[212] R. J. Miron, Y. F. Zhang, *J. Dent. Res.* **2012**, *91*, 736.

[213] J. Feng, T. Hu, W. Liu, S. Zhang, Y. Tang, R. Chen, X. Jiang, F. Wei, *J. Pediatr. Surg.* **2001**, *36*, 1770.

[214] S. Provot, E. Schipani, *Biochem. Biophys. Res. Commun.* **2005**, *328*, 658.

[215] R. Marom, I. Shur, R. Solomon, D. Benayahu, *J. Cell. Physiol.* **2005**, *202*, 41.

[216] F. Tortelli, R. Tasso, F. Loiacono, R. Cancedda, *Biomaterials* **2010**, *31*, 242.

[217] S. Takamizawa, Y. Maehata, K. Imai, H. Senoo, S. Sato, R. I. Hata, *Cell Biol. Int.* **2004**, *28*, 255.

[218] P. G. Robey, *Tissue Eng. Part B Rev.* **2011**, *17*, 423.

[219] J. L. Kovar, X. Xu, D. Draney, A. Cupp, M. A. Simpson, D. Michael Olive, *Anal. Biochem.* **2011**, *416*, 167.

[220] W. M. Saltzman, T. R. Kyriakides, *Princ. Tissue Eng.* **2014**, 385.

[221] J. Street, M. Bao, L. DeGuzman, S. Bunting, F. V. Peale Jr, N. van bruggen, P. Redmon, R. Carano, E. Filvaroff, *Proc. Natl. Acad. Sci.* **2001**, *98*, 6027.

[222] J. A. McGovern, M. Griffin, D. W. Hutmacher, *Dis. Model. Mech.* **2018**, *11*, dmm033084.

[223] G. Papavasiliou, M. H. Cheng, E. M. Brey, *J. Investig. Med.* **2010**, *58*, 838.

[224] M. Pereira, E. Petretto, S. Gordon, J. H. D. Bassett, G. R. Williams, J. Behmoaras, *J. Cell Sci.* **2018**, *131*, jcs216267.

[225] NHS Blood and Transplant, *Overview of Organ Donation and Transplantation*; 2019.

[226] Great Britain, Home Office, *Annual statistics of scientific procedures on living animals: Great Britain 2018*; 2019.

[227] M. R. Bart van der Worp, H.; Howells, David W.; Sena, Emily S.; Porrit, Michelle J.; Rewell, Sarah; O'Collins, Victoria; Macleod, *PLoS Med.* **2010**, *7*.

[228] R. M. Plenge, *Sci. Transl. Med.* **2016**, *8*, 1.

[229] Cancer Research UK, Bone sarcoma statistics. *Cancer Res. UK* **2019**.

8. Appendices

A Polymer substrates for bone cell attachment

Microarrays were fabricated using a selection of polymers previously identified in the Bradley group. These polymers were chosen based on their ability to support the growth of suspension cells,[166] endothelia progenitor cells,[29] human embryonic stem cells,[30,167] bone cells[121] or mesenchymal stem cells.[31] 1,6-hexanediol diacrylate and hydroxy-2-methylpropiophenone were used in all the polymers as cross-linker and UV-photoinitiator respectively. Different ratios of monomers were explored (monomer 1 to monomer 2: 0:100, 25:75, 50:50, 75:25 and 100:0) in the case of polymers composed of two acrylate monomers.

Inkjet printing (Scienion S5, Germany) was used to *in situ* fabricate 180 different acrylate polymers (Table 8-1 and Table 8-2) on a single glass microscope slide. Glass slides were acrylate functionalised before printing and three replicates were generated for each polymer including internal controls (see section 3.4 for details of the microarray fabrication). Microarrays (two replicates) were interrogated with SAOS-2 and MG-63 cells and their attachment to the polymers were quantified (number of cells per mm^2 of polymer) after two days of cells culture.

Both cell lines showed good cell attachment on the large number of polymers interrogated (Figure 4-1 and Figure 4-2). The large standard deviation in the screening with SAOS-2 cells (285 ± 184 SAOS-2 cells/mm^2) illustrated that these cells were perhaps more selective to the composition of the polymers than MG-63 cells (256 ± 95 MG-63 cells/mm^2). As such polymer composition were selected based on SAOS-2 cell attachment*.

* Polymers with monomers that produced excessive swelling (e.g. AEtMA-CL, NIPAAm, DMAEMA) were discarded as swelling can disrupt the 3D microstructure. Polymers 43-45, 58, 73-74, 111, 131-132.

Table 8-1. Monomers explored in the microarray fabricated to identify polymer substrates capable of supporting the attachment of SAOS-2 and MG-63 cells.

Abbreviation	Monomer name	CAS
MMA	Methyl methacrylate	80-62-6
St	Styrene	100-42-5
NIPAAm	N-isopropylacrylamide	2210-25-5
AAH	Acrylic acid	79-10-7
DEAEA	2-(diethylamino)ethyl acrylate	2426-54-2
MA-H	Methacrylic acid	79-41-4
GMA	Glycidyl methacrylate	106-91-2
MEMA	2-methoxyethylmethacrylate	6976-93-8
HEMA	2-hydroxyethylmethacrylate	868-77-9
VP4	4-vinylpyridine	100-43-6
VP2	2-vinylpyridine	100-69-6
EMA	Ethyl methacrylate	97-63-2
BMA	Butyl methacrylate	97-88-1
DMAEA	2-(dimethylamino)ethyl acrylate	2439-35-2
HBMA	Hydroxybutyl methacrylate mixture of isomers	29008-35-3
DEAEMA	2-(diethylamino)ethyl methacrylate	105-16-8
DMAEMA	2-(dimethylamino)ethyl methacrylate	2867-47-2
HPMA	Hydroxypropylmethacrylate	27813-02-1
AEtMA-CL	2-(acryloyloxyethyl) trimethylammonium chloride	44992-01-0
DEAA	N,N-Diethyl acrylamide	2675-94-7
DMOBAA	N-(1,1-Dimethyl-3-oxobutyl)acrylamide	2873-97-4
Aam	Acrylamide	79-06-1
DMAA	N,N-Dimethyl acrylamide	2680-03-7
HBA	4-Hydroxybutyl acrylate	2478-10-6
BHA	4-tert-Butylcyclohexyl acrylate	84100-23-2
CEA	2-Carboxyethyl acrylate	24615-84-7
IBA	Isobornyl acrylate	5888-33-5
EGDPEA	Ethylene glycol dicyclopentenyl ether acrylate	65983-31-5
MTEMA	2-(Methylthio)ethyl methacrylate	14216-23-0
AEMA-Cl	2-Aminoethyl methacrylate hydrochloride	2420-94-2
TBAA	N-tert-Butylacrylamide	107-58-4
HPPA	2-Hydroxy-3-phenoxypropyl acrylate	16969-10-1
HDOBA (CL)	1,6-hexanediol diacrylate	13048-33-4

Table 8-2. Composition of the acrylate polymers explored in the microarray fabricated to identify polymer substrate capable of supporting the attachment of SAOS-2 and MG-63 cells. Solutions were prepared in NMP (1 M). 1,6-hexanediol diacrylate was used as cross-linker (incorporated at 18 mol %). Hydroxy-2-methylpropiophenone was used as a UV photo-initiator (10% mol).

Polymer number	Monomer 1	Monomer 2	Polymer number	Monomer 1	Monomer 2
1	BMA (25)	DMAEA (75)	**21**	EMA (75)	DEAEA (25)
2	BMA (50)	DMAEA (50)	**22**	MEMA (25)	HEMA (75)
3	BMA (75)	DMAEA (25)	**23**	MEMA (50)	HEMA (50)
4	HEMA (25)	VP2 (75)	**24**	MEMA (75)	HEMA (25)
5	HEMA (50)	VP2 (50)	**25**	St (25)	NIPAA (75)
6	HEMA (75)	VP2 (25)	**26**	St (50)	NIPAA (50)
7	MMA (25)	DMAEMA (75)	**27**	St (75)	NIPAA (25)
8	MMA (50)	DMAEMA (50)	**28**	MTEMA (25)	BHA (75)
9	MMA (75)	DMAEMA (25)	**29**	MTEMA (50)	BHA (50)
10	MMA (25)	DMAEMA (75)	**30**	MTEMA (75)	BHA (25)
11	MMA (50)	DMAEMA (50)	**31**	MMA (25)	GMA (75)
12	MMA (75)	DMAEMA (25)	**32**	MMA (50)	GMA (50)
13	BHA (25)	BMA (75)	**33**	MMA (75)	GMA (25)
14	BHA (50)	BMA (50)	**34**	BHA (25)	DMAA (75)
15	BHA (75)	BMA (25)	**35**	BHA (50)	DMAA (50)
16	BMA (25)	DEAEA (75)	**36**	BHA (75)	DMAA (25)
17	BMA (50)	DEAEA (50)	**37**	MMA (25)	MAH (75)
18	BMA (75)	DEAEA (25)	**38**	MMA (50)	MAH (50)
19	EMA (25)	DEAEA (75)	**39**	MMA (75)	MAH (25)
20	EMA (50)	DEAEA (50)	**40**	MMA (25)	DEAEA (75)

Polymer number	Monomer 1	Monomer 2	Polymer number	Monomer 1	Monomer 2
41	MMA (50)	DEAEA (50)	**61**	EMA (25)	DEAEMA (75)
42	MMA (75)	DEAEA (25)	**62**	EMA (50)	DEAEMA (50)
43	AEtMACl (25)	DMOBA (75)	**63**	EMA (75)	DEAEMA (25)
44	AEtMACl (50)	DMOBA (50)	**64**	EMA (25)	DMAEMA (75)
45	AEtMACl (75)	DMOBA (25)	**65**	EMA (50)	DMAEMA (50)
46	HBMA (25)	DEAEMA (75)	**66**	EMA (75)	DMAEMA (25)
47	HBMA (50)	DEAEMA (50)	**67**	HPMA (25)	DMAEMA (75)
48	HBMA (75)	DEAEMA (25)	**68**	HPMA (50)	DMAEMA (50)
49	HBMA (25)	DMAEMA (75)	**69**	HPMA (75)	DMAEMA (25)
50	HBMA (50)	DMAEMA (50)	**70**	HPMA (25)	DEAEA (75)
51	HBMA (75)	DMAEMA (25)	**71**	HPMA (50)	DEAEA (50)
52	HBMA (25)	DEAEA (75)	**72**	HPMA (75)	DEAEA (25)
53	HBMA (50)	DEAEA (50)	**73**	HBA (25)	DMAEMA (75)
54	HBMA (75)	DEAEA (25)	**74**	HBA (50)	DMAEMA (50)
55	HBMA (25)	DMAEA (75)	**75**	HBA (75)	DMAEMA (25)
56	HBMA (50)	DMAEA (50)	**76**	HPMA (25)	DEAEMA (75)
57	HBMA (75)	DMAEA (25)	**77**	HPMA (50)	DEAEMA(50)
58	NIPAA (25)	DMAEMA (75)	**78**	HPMA (75)	DEAEMA (25)
59	NIPAA (50)	DMAEMA (50)	**79**	AEtMACl (25)	DEAA (75)
60	NIPAA (75)	DMAEMA (25)	**80**	AEtMACl(50)	DEAA (50)

Polymer number	Monomer 1	Monomer 2	Polymer number	Monomer 1	Monomer 2
81	IBA (50)	MTEMA (50)	**101**	MEMA(50)	DEAEA (50)
82	DMAEMA (25)	DEAA (75)	**102**	MEMA(75)	DEAEA (25)
83	DMAEMA (50)	DEAA (50)	**103**	CEA(25)	IBA (75)
84	DMAEMA (75)	DEAA (25)	**104**	CEA(25)	IBA (75)
85	DEAEA (25)	DMAEMA (75)	**105**	CEA(25)	IBA (75)
86	DEAEA (50)	DMAEMA (50)	**106**	DMOBAA(25)	DMAEMA (75)
87	DEAEA (75)	DMAEMA (25)	**107**	DMOBAA(50)	DMAEMA (50)
88	HEMA (25)	DMAEMA (75)	**108**	DMOBAA(75)	DMAEMA (25)
89	HEMA (50)	DMAEMA (50)	**109**	AEtMACl(25)	DMAEMA (75)
90	HEMA (75)	DMAEMA (25)	**110**	AEtMACl(50)	DMAEMA (50)
91	MEMA (25)	DEAEMA (75)	**111**	AEtMACl(75)	DMAEMA (25)
92	MEMA (50)	DEAEMA (50)	**112**	AAH(25)	DMAEMA (75)
93	MEMA (75)	DEAEMA (25)	**113**	AAH(50)	DMAEMA (50)
94	MEMA (75)	DMAEMA (25)	**114**	AAH(50)	DMAEMA (50)
95	MEMA (50)	DMAEMA (50)	**115**	AAH(25)	DEAEA (75)
96	MEMA (75)	DMAEMA (25)	**116**	AAH(50)	DEAEA (50)
97	DMAEMA (25)	NIPAA (75)	**117**	AAH(75)	DEAEA (25)
98	DMAEMA (50)	NIPAA (50)	**118**	DMAEMA(25)	EGDPEA (75)
99	DMAEMA (75)	NIPAA (75)	**119**	DMAEMA(50)	EGDPEA (50)
100	MEMA (25)	DEAEA (75)	**120**	DMAEMA(75)	EGDPEA (25)

Polymer number	Monomer 1	Monomer 2	Polymer number	Monomer 1	Monomer 2
121	Aam (25)	DMAEMA (75)	**141**	MTEMA (75)	TBAA (25)
122	Aam (50)	DMAEMA (50)	**142**	HPPA (25)	HEMA (75)
123	Aam (75)	DMAEMA (25)	**143**	HPPA (50)	HEMA (50)
124	DMAA (25)	DMAEMA (75)	**144**	HPPA (75)	HEMA (25)
125	DMAA (50)	DMAEMA (50)	**145**	MEMA (25)	EGDPEA (75)
126	DMAA (75)	DMAEMA (25)	**146**	MEMA (50)	EGDPEA(50)
127	DMAA (25)	DEAEA (75)	**147**	MEMA (75)	EGDPEA(25)
128	DMAA (50)	DEAEA (50)	**148**	MMA (100)	-
129	DMAA (75)	DEAEA (25)	**149**	St (100)	-
130	AEtMACl (25)	DEAEA (75)	**150**	NIPAA (100)	-
131	AEtMACl (50)	DEAEA (50)	**151**	AAH (100)	-
132	AEtMACl (75)	DEAEA (25)	**152**	DEAEA (100)	-
133	HEMA (25)	IBA (75)	**153**	MAH (100)	-
134	HEMA (50)	IBA (50)	**154**	GMA (100)	-
135	HEMA (75)	IBA (25)	**155**	MEMA (100)	-
136	HEMA (25)	EGDPEA (75)	**156**	HEMA (100)	-
137	HEMA (50)	EGDPEA (50)	**157**	VP4 (100)	-
138	HEMA (75)	EGDPEA (25)	**158**	VP2 (100)	-
139	MTEMA (25)	TBAA (75)	**159**	EMA (100)	-
140	MTEMA (50)	TBAA (50)	**160**	BMA (100)	-

Polymer number	Monomer 1	Monomer 2	Polymer number	Monomer 1	Monomer 2
161	DMAEA (100)	-	**171**	HBA (100)	-
162	HBMA (100)	-	**172**	BHA (100)	-
163	DEAEMA (100)	-	**173**	CEA (100)	-
164	DMAEMA (100)	-	**174**	IBA (100)	-
165	HPMA (100)	-	**175**	EGDPEA (100)	-
166	AEtMACl (100)	-	**176**	MTEMA (100)	-
167	DEAA (100)	-	**177**	St (100)	-
168	DMOBAA (100)	-	**178**	TBAA (100)	-
169	Aam (100)	-	**179**	HPPA (100)	-
170	DMAA (100)	-	**180**	HDODA (100)	-

B Thermogravimetric analysis

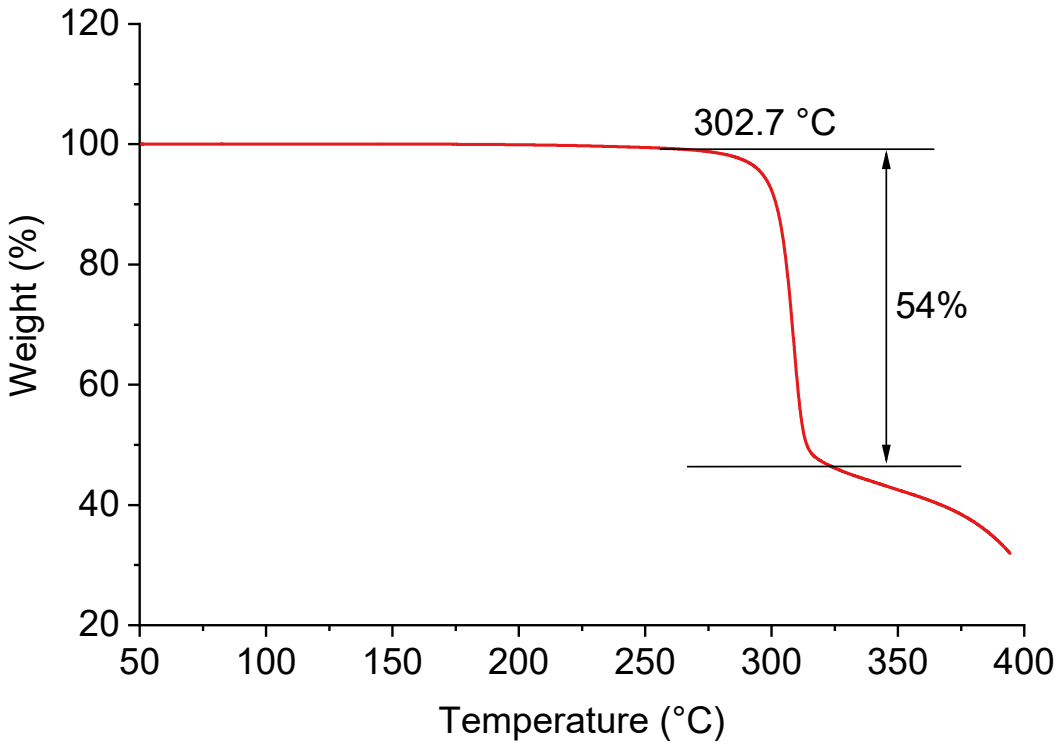

Figure 8-1. Thermal stability of **co-polymer 174** (Table 8-2), poly(IBA_{72}-*co*-$HDOBA_{18}$), with high level of porosity (**P80**). Thermogravimetric analysis showed polymer degradation above 302 °C with about 54% weight loss at 325 °C.

C Analysis of immunofluorescence using the Imaris platform

Image acquisition of the immunostaining (ALP, type I collagen and osteopontin) was carried out using a confocal microscope to obtain images at different heights (z-stack) of the polymer scaffolds. The software Imaris was used to analyse these images to obtain 2D projections of the 3D FMBSC-scaffold assemblies (Figure 8-2). Fluorescence intensity was deconvoluted by channels applying a threshold that separated cell cytoplasm and nuclei from the background. It allowed quantification of the intensity of the antibody staining and counting of cell numbers in addition to construction of 3D models that showed cell distribution across the 3D polymer scaffolds (Figure 8-3).

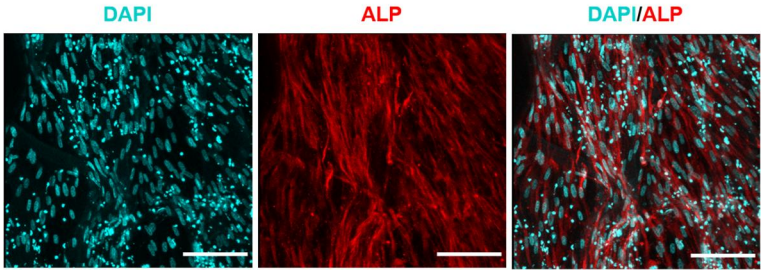

Figure 8-2. Representative 2D image projection of a Z-stack (3D) with ALP stained red and nuclei stained cyan (DAPI nuclear staining) of FBMSCs on scaffolds **P80-2**. Scale bar = 100 µm.

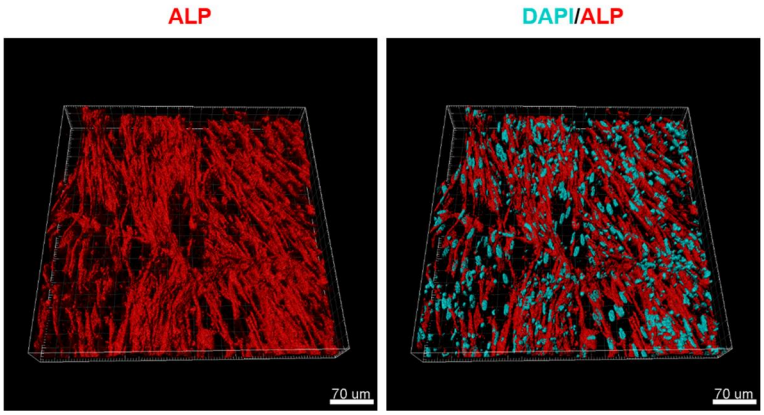

Figure 8-3. Immunofluorescence assessment of FBMSCs ALP expression on a scaffold **P80-2** after 7 days incubation. 3D image with ALP stained red and nuclei stained cyan (DAPI nuclear staining). Scale bar = 70 µm.